

OKINAWA INSTITUTE OF SCIENCE AND TECHNOLOGY
GRADUATE UNIVERSITY

Thesis submitted for the degree

Doctor of Philosophy

Massively parallel split-step Fourier techniques for simulating quantum systems on graphics processing units

A large, abstract graphic on the left side of the page consists of several thick, red, wavy lines that curve and twist in various directions, resembling stylized neurons or complex quantum paths.

by

James Schloss

Supervisor: Thomas Busch

July, 2019

Declaration of Original and Sole Authorship

I, James Schloss, declare that this thesis entitled *Massively parallel split-step Fourier techniques for simulating quantum systems on graphics processing units* and the data presented in it are original and my own work.

I confirm that:

- No part of this work has previously been submitted for a degree at this or any other university.
- References to the work of others have been clearly acknowledged. Quotations from the work of others have been clearly indicated, and attributed to them.
- In cases where others have contributed to part of this work, such contribution has been clearly acknowledged and distinguished from my own work.
- None of this work has been previously published elsewhere, with the exception of the following: (provide list of publications or presentations, or delete this part). (If the work of any co-authors appears in this thesis, authorization such as a release or signed waiver from all affected co-authors must be obtained prior to publishing the thesis. If so, attach copies of this authorization to your initial and final submitted versions, as a separate document for retention by the Graduate School, and indicate on this page that such authorization has been obtained).

Date: July, 2019

Signature:

Abstract

Massively parallel split-step Fourier techniques for simulating quantum systems on graphics processing units

The split-step Fourier method is a powerful technique for solving partial differential equations and simulating quantum systems of various forms. In this body of work, we focus on several variations of this method to allow for simulations of one, two, and three-dimensional quantum systems, along with several notable methods for controlling these systems. In particular, we use quantum optimal control and shortcuts to adiabaticity to study the non-adiabatic generation of superposition states in strongly correlated one-dimensional systems, analyze chaotic vortex trajectories in two dimensions by using rotation and phase imprinting methods, and create stable, three-dimensional vortex structures in Bose–Einstein condensates through artificial magnetic fields generated by the evanescent field of an optical nanofiber. We also discuss algorithmic optimizations for implementing the compressed split-step Fourier method for graphics processing units and multicomponent simulations. All variations present in this work are justified with physical systems where such techniques have been applied and have been incorporated into a state-of-the-art and open-source software suite known as GPUE, which is currently the fastest quantum simulator of its kind.

Acknowledgment

Theses must acknowledge assistance received in any of the following areas:

- Designing the research
- Executing the research
- Analyzing the data
- Interpreting the data/research
- Writing, proofing, or copyediting the manuscript

Abbreviations

All abbreviations used in the thesis should be listed here, with their definitions, in alphabetical order. This includes trivial and commonly used abbreviations (at your own discretion), but not words that have entered into general English usage (such as laser or DNA). In particular, non-standard abbreviations should be presented here. This is an aid to the reader who may not read all sections of the thesis.

BEC Bose–Einstein Condensate

GPGPU General Purpose computation on Graphics Processing Units

GPU Graphics Processing Unit

NLSE Non-linear Schrödinger Equation

Glossary

Dipole Blockade	Phenomenon in which the simultaneous excitation of two atoms is inhibited by their dipolar interaction.
Cavity Induced Transparency	Phenomenon in which a cavity containing two atoms excited with light at a frequency halfway between the atomic frequencies contains the number of photons an empty cavity would contain.

Nomenclature

- c Speed of light ($2.997\ 924\ 58 \times 10^8\ \text{ms}^{-1}$)
 \hbar Planck constant ($1.054\ 572\ 66 \times 10^{-34}\ \text{Js}$)
 k_B Boltzmann constant ($1.380\ 658 \times 10^{-23}\ \text{JK}^{-1}$)
 Z_0 Impedance of free space ($376.730\ 313\ 461\ \Omega$)
 μ_0 Permeability of free-space ($4\pi \times 10^{-7}\ \text{Hm}^{-1}$)

If desired, an optional and short dedication may be
included here.

Contents

Declaration of Original and Sole Authorship	ii
Abstract	iv
Acknowledgment	v
Abbreviations	vi
Glossary	vii
Nomenclature	viii
Contents	x
Introduction	1
1 Introduction to the SSFM for vortex simulations	5
1.1 The SSFM	6
1.2 Introduction to ultracold quantum systems	12
1.2.1 Bose–Einstein condensation and the Gross–Pitaevskii Equation . .	13
1.3 Superfluid systems and vortex dynamics	16
1.3.1 Rotation	21
1.3.2 Phase imprinting	22
1.3.3 Artificial magnetic fields	23

1.4	Modifications to the SSFM for superfluid vortex simulations	27
1.5	Multi-component simulations	29
2	Quantum engineering for one-dimensional quantum systems	31
2.1	Optimization methods	32
2.1.1	Nelder–Mead	33
2.1.2	Chopped random basis optimal control	36
2.2	Shortcuts to adiabaticity	37
2.3	Non-adiabatic generation of NOON states in a Tonks–Girardeau gas	39
2.3.1	Tonks–Girardeau gas	40
2.3.2	NOON states in TG gas	40
2.3.3	Results with optimal control	44
2.3.4	Results with STA protocols	47
2.4	Outlook	54
3	General Purpose computing with Graphics Processing Units and the GPUE codebase	55
3.1	Types of parallelism	56
3.2	General purpose computing with graphics processing units	58
3.2.1	Limitations of GPU computing	59
3.2.2	GPU hardware architecture	59
3.2.3	Comparison between various languages for GPGPU computation	68
3.3	Introduction to the GPUE codebase for n -dimensional simulations of quantum systems on the GPU	70
3.3.1	FFT optimization	71
3.3.2	Dynamic field input and output in GPUE with expression trees	72
3.3.3	GPUE memory footprint	74
3.3.4	Vortex tracking and highlighting	75
3.3.5	Energy calculation for superfluid simulations	79

3.3.6	Similar software packages	81
3.3.7	Future direction and multi-GPU development	81
3.4	DistributedTranspose.jl	82
3.5	Outlook	84
4	Chaotic vortex analysis of two-dimensional superfluid systems for few-vortex systems	85
4.1	Model	87
4.2	Regular and irregular vortex dynamics	88
4.3	Characterizing chaotic vortex dynamics	91
4.4	Outlook	95
5	Generation, control and detection of 3D vortex structures in superfluid systems	97
5.1	Three-dimensional vortex structures	98
5.2	Controlled creation of three-dimensional vortex structures in Bose–Einstein condensates using artificial magnetic fields	100
5.2.1	Bose–Einstein condensate dynamics in the presence of an optical nanofiber	101
5.2.2	Ground state vortex configurations	107
5.2.3	Dynamic vortex detection and scissor modes	111
5.3	Conclusion	114
Conclusion		116
5.4	Overall conclusions	116
5.5	Further development of GPUE	117
5.5.1	Vortex tracking in two and three dimensions	117
5.5.2	General purpose Hamiltonian solver	118
5.5.3	Octree grid	118

5.6 Future simulations of quantum systems	120
A Simple vector additions in CUDA, OpenCL, and JuliaGPU	121
A.1 Vector addition with C++	121
A.2 Vector addition with CUDA	123
A.3 Vector addition with OpenCL	125
A.4 Julia	129
Bibliography	131
Published articles	154

Introduction

Massively parallel methods have become commonplace in High-Performance Computing (HPC) environments that often rely on large networks of distributed computing nodes for performing simulations of various forms. In recent years, it has been found that the Graphics Processing Unit (GPU) can provide a higher bandwidth for highly parallelizable computation because all components are available in a single device that has been developed specifically for the computation of many small actions in parallel. As such, many supercomputers have been transitioning to GPU-based computation, including Summit, currently the fastest supercomputer in the world [1]. For these reasons, General-Purpose GPU (GPGPU) programming methods have become more relevant than ever and many frameworks are beginning to cater to the demand [2–5], with the current state-of-the art platform being NVIDIA’s CUDA (Compute Unified Device Architecture) [6].

Though GPU devices are often faster than their CPU counterparts for simple tasks, there are plenty of drawbacks to using the GPU. For example, each GPU card typically has less available memory than the CPU, and inter-GPU or GPU-CPU communication is an incredibly slow process, thereby encouraging developers to restrict communication between devices as much as possible. In comparison to CPU software, developers need to be more aware of how GPU memory is being used to write optimized code for their specific purpose. In addition, individual GPU computing cores are weaker than those found on the CPU, so iterative tasks are even less optimal and should be avoided when programming for GPUs.

Spectral and pseudo-spectral methods are interesting subsets of problems that are used for large-scale, distributed computation on HPC environments that rely on FFTs (Fast Fourier Transforms) to solve partial differential equations of various forms. Though there are robust FFT libraries, like FFTW [7] to perform distributed FFTs [8], FFTs are still global operations, often requiring memory manipulation on multiple nodes simultaneously and requiring communication between them. For this reason, the FFT is often the com-

putational bottleneck for spectral and pseudo-spectral methods. It is difficult to directly benchmark GPU and CPU software, but it is generally accepted that one-dimensional GPU-based FFTs perform more optimally as the grid size increases; however, for higher-dimensional FFT operations, this performance increase is not as drastic [9]. This leads to an interesting question about whether spectral methods could be faster on distributed networks of GPU devices, as the bulk of the parallelization occurs in a single device and should be faster than a distributed CPU network. Though special care needs to be taken to ensure that GPU memory is properly aligned, a few pseudo-spectral methods have been shown to be both easier to implement and faster than other force integration schemes like Runge-Kutta, and one such method is the Split-Step Fourier Method (SSFM) [10].

The SSFM is known as the primary workhorse for computation of wavepackets in single and multi-mode fiber optic systems and is primarily intended to solve the Non-linear Schrödinger equation, which has obvious applications to many areas of quantum simulation. In particular, the SSFM can be used to solve the Gross-Pitaevskii equation, which is the governing formula for all dynamics of superfluid Bose–Einstein condensates in the mean-field limit. Superfluid systems behave fundamentally differently than classical fluids and there is significant interest in many areas of superfluid research, including methods of vortex generation and their interaction; however, three-dimensional simulations can quickly become computational infeasible. For this reason, it is worth exploring and developing GPU-based libraries for the computation of superfluid dynamics. This work has developed a massively parallel, GPU-based library for the simulation of various quantum phenomenon with the SSFM, with a focus on solving the Gross-Pitaevskii equation for the simulation of superfluid vortex dynamics. I will also discuss and motivate several methods for simulation of quantum engineering on GPU devices. This work was carried out during my time as a PhD student in the Quantum Systems Unit at the Okinawa Institute of Science and Technology Graduate University (OIST).

Introduction to the SSFM for vortex simulations

This work will begin with an introduction to the SSFM, itself, along with the physical target for most of this work: superfluid vortex simulations. As such, it will also discuss methods of vortex generation, including rotation, phase imprinting, and gauge fields, along with modifications to the Gross–Pitaevskii equation for simulating rotating and multi-component systems. This chapter lays the groundwork for all subsequent chapters.

Quantum engineering for one-dimensional quantum systems

This chapter will motivate several methods that are difficult to simulate on GPU architecture, focusing on methods of quantum engineering for a one-dimensional example where macroscopic superposition states are generated in a Tonks–Girardeau gas. In addition, this chapter will highlight methods in quantum optimal control and shortcuts to adiabaticity that will serve as examples of quantum engineering methods physicists might wish to implement for various quantum phenomena that are difficult to perform on GPU architecture. This work has been published in the New Journal of Physics [11].

Introduction to GPGPU and the GPUE codebase

This chapter will introduce the concept of General-Purpose GPU computing and the GPUE (GPU-based Gross-Piteavskii Equation solver) codebase for superfluid vortex simulation. It will also cover GPU architecture in-depth and discuss several optimizations performed in GPUE to enable certain features which could not be done before with other GPU libraries with similar purposes. This chapter will conclude with a discussion of a notoriously difficult problem with GPU hardware that could make spectral and pseudo-spectral methods even more efficient on GPU hardware: an n -dimensional distributed transpose. The GPUE codebase has been published in the Journal of Open Source Software [12].

Vortex analysis of two-dimensional superfluid systems

This chapter will be related to an example of superfluid simulations with GPUE in two-dimensions, where vortices essentially follow the dynamics of point-vortex models. Here, the system is shown to exhibit chaotic dynamics with only a few vortices present. This system highlights the necessity of good post-processing methods for the simulations performed with GPUE, as the Lyapunov exponents are used on the tracked vortex positions to ascertain the degree of chaotic motion. This work has been published in Phys. Rev. Fluids [13].

Generation, control, and detection of 3D vortex structures in superfluid systems

This chapter is another example of superfluid simulations performed with GPUE, this time in three-dimensions. For this system, a novel device is proposed that can generate, control, and detect vortex ring-like structures by coupling the BEC to the light of an optical nanofiber. This system highlights the need for many of the features suggested during GPUE development for minimizing the memory footprint and ensuring fast, dynamic simulations. This work has been submitted to Phys. Rev. Fluids [14].

Outlook

Throughout this text, I will try to motivate future directions at the end of each chapter; however, a global outlook, including new simulations possible with GPUE and other areas of development that could be focused on will be discussed in the end.

Chapter 1

Introduction to the SSFM for vortex simulations

The Split-Step Fourier Method (SSFM) is an essential technique for simulating a variety of physical systems and is particularly useful for simulating the propagation of wave packets in single and multimode fibers [15–18] and in various quantum systems [19–21]. Though other methods, such as explicit and implicit Euler [22], Crank-Nicholson [23], and Runge-Kutta [22], can solve similar differential equations, the SSFM has distinct advantages over these methods. For example, because the SSFM primarily relies on embarrassingly parallel element-wise matrix multiplications and Fast Fourier Transform (FFT) routines that have been optimized for parallel and distributed systems, is often much easier to parallelize than Runge-Kutta [10]. The SSFM also provides a lower error bound than either the Euler or Crank-Nicholson methods, and does not require an implicit or tridiagonal solver [24, 25] which are also not easily parallelizable [26–28]. Though much of this work focuses on using the SSFM to simulate superfluid vortex states, I will not be discussing alternative methods, such as point-vortex [29] or vortex-filament [30] simulations in rigorous detail, as this work focuses primarily on engineering appropriate quantum states, while vortex-point and vortex filament methods focus primarily on vortex structures, themselves.

In the work presented in this chapter, I will be focusing on the application of the

SSFM to superfluid vortex simulations and will use primarily physical arguments to understand the details of the method itself. I will also discuss several numerical techniques for optimally simulating quantum systems on massively parallel Graphics Processing Units (GPUs), along with software developed for this purpose: GPUE, the Graphics Processing Unit Gross-Pitaevskii Equation Solver. More details about General Purpose computing with Graphics Processing Units (GPGPU) and the GPUE simulation software can be found in Chapter 3. There, I will discuss several additional areas of interest for implementing similar solvers on GPUs, including distributed transposes and important considerations for traditional FFT routines for simulating quantum systems on multiple GPU devices.

This chapter will assume familiarity with basic principles of quantum mechanics and focus on considerations for simulating quantum systems with the SSFM. As such, I will also introduce important physical insights for understanding ultracold atomic systems that will be used throughout the rest of this work. In particular, I will focus on understanding superfluid systems created by Bose–Einstein condensation and methods by which vortex structures can be generated and controlled in a Bose–Einstein Condensate (BEC).

1.1 The SSFM

Let us begin with the one-dimensional Schrödinger equation,

$$i\hbar \frac{\partial \Psi(r, t)}{\partial t} = \left(\frac{p^2}{2m} + V_0(\mathbf{r}) \right) \Psi(\mathbf{r}, t) \quad (1.1)$$

where $\hat{p} = -i\hbar \frac{\partial}{\partial x}$ is the canonical momentum operator, m is the mass, $V_0(\mathbf{r})$ is the trapping potential, and $\Psi(r, t)$ is the single-particle wavefunction. In this case, one often replace most of the right-hand side of the equation with a Hamiltonian operator, which for this case would be $\hat{\mathcal{H}} = \frac{p^2}{2m} + V_0(\mathbf{r})$. This noticeably has two components, one acting in position-space, $\hat{\mathcal{H}}_v = V_0(\mathbf{r})$ and another in momentum-space, $\hat{\mathcal{H}}_p = \frac{\hat{p}^2}{2m}$. For consistency, I will denote all variables in momentum-space with a p , and real-space with a v . Additionally,

the wavefunction can be expanded into a complete set of eigenkets of the Hamiltonian, with $\hat{\mathcal{H}} |\Psi_n\rangle = E_n |\Psi_n\rangle$. One can then write

$$|\Psi(\mathbf{r})\rangle = \sum_{n=0}^N c_n e^{-iE_n t} |\psi_n(\mathbf{r})\rangle, \quad (1.2)$$

where N is the total number of states in the system, c_n is a constant for each constituent eigenfunction $\psi_n(\mathbf{r})$.

Simply stated, the SSFM splits the Hamiltonian into separate operators and uses a Fourier transform on the wavefunction to ensure that these operators are applied in the appropriate space. In order to apply the Hamiltonian to the system, one first assumes a formal solution to the Schrödinger equation,

$$\Psi(\mathbf{r}, t + dt) = \left[e^{-\frac{i\hat{\mathcal{H}}_v dt}{\hbar}} \right] \Psi(\mathbf{r}, t) = \left[e^{-\frac{i(\hat{\mathcal{H}}_v + \hat{\mathcal{H}}_p)dt}{\hbar}} \right] \Psi(\mathbf{r}, t), \quad (1.3)$$

where dt is a small timestep. If we assume we are simulating our system by a series of small timesteps, we can split this operation by using the Baker-Campbell-Hausdorff formula,

$$\Psi(\mathbf{r}, t + dt) = \left[e^{-\frac{i\hat{\mathcal{H}}_v dt}{\hbar}} e^{-\frac{i\hat{\mathcal{H}}_p dt}{\hbar}} e^{-\frac{[i\hat{\mathcal{H}}_v, i\hat{\mathcal{H}}_p]dt^2}{2}} \right] \Psi(\mathbf{r}, t). \quad (1.4)$$

If neglected, the commutation of the real and momentum-space components of the Hamiltonian will accrue an error on the order of dt^2 . This is a noticeably high; however, we can decrease the dt^2 error to dt^3 by performing a half-step in position space before doing a full-step in momentum space, through a process called Strang splitting [31],

$$\Psi(\mathbf{r}, t + dt) = \left[e^{-\frac{i\hat{\mathcal{H}}_v dt}{2\hbar}} e^{-\frac{i\hat{\mathcal{H}}_p dt}{\hbar}} e^{-\frac{i\hat{\mathcal{H}}_v dt}{2\hbar}} \right] \Psi(\mathbf{r}, t) + \mathcal{O}(dt^3). \quad (1.5)$$

Strang splitting can be best understood by performing a Taylor series expansion on both $e^{h(\mathbf{A}+\mathbf{B})}$ and $e^{h\mathbf{A}}e^{h\mathbf{B}}$, where \mathbf{A} and \mathbf{B} are matrices and h is a defined step size [32].

When expanded,

$$e^{h(A+B)} \approx \mathbf{I} + h(\mathbf{A} + \mathbf{B}) + \frac{1}{2}h^2(\mathbf{A} + \mathbf{B})^2. \quad (1.6)$$

where \mathbf{I} is the identity matrix. Here, the first-order terms for the expansion in Equation (1.6) is identical to the expansion of $e^{h\mathbf{A}}e^{h\mathbf{B}}$; however, when expanding the last term, we find,

$$\frac{1}{2}h^2(\mathbf{A} + \mathbf{B})^2 = \frac{1}{2} (\mathbf{A}^2 + \mathbf{AB} + \mathbf{BA} + \mathbf{B}^2). \quad (1.7)$$

Here, the \mathbf{BA} term is missing in the expansion of $e^{h\mathbf{A}}e^{h\mathbf{B}}$ because \mathbf{A} always comes before \mathbf{B} . If a symmetric splitting is used instead, it is clear that all the terms up to the second order are the same, such that $e^{h(\mathbf{A}+\mathbf{B})} \approx e^{h\mathbf{A}/2}e^{h\mathbf{B}}e^{h\mathbf{A}/2}$.

Because position and momentum are conjugate domains, after Strang splitting we address each part of this solution in chunks, first in position space, then in momentum space, then in position space again by using Fourier transforms. Which looks something like this:

$$\Psi(\mathbf{r}, t + dt) = \left[\hat{U}_r(dt)\mathcal{F}^{-1} \left[\hat{U}_p(dt)\mathcal{F} \left[\hat{U}_r(dt)\Psi(\mathbf{r}, t) \right] \right] \right] + \mathcal{O}(dt^3) \quad (1.8)$$

where $\hat{U}_r = e^{-\frac{i\hat{\mathcal{H}}_v dt}{2\hbar}}$, $\hat{U}_p = e^{-\frac{i\hat{\mathcal{H}}_p dt}{\hbar}}$, and \mathcal{F} and \mathcal{F}^{-1} indicate forward and inverse Fourier transforms. In practice, these Fourier transforms are performed with Fast Fourier Transforms (FFTs), typically using a variation on the Cooley-Tukey method, which was first discovered by Gauss and later contemporized by Cooley and Tukey when they independently discovered it [33]. This method is not straightforwardly parallelizable; however, FFTs have become so fundamental to signal processing, that they have been incredibly well-optimized with several libraries, including FFTW [7] and CuFFT [3] for distributed and GPU calculations, respectively. I will discuss optimal techniques for using FFTs with the SSFM method in Chapter 3.

Each timestep of the SSFM is essentially composed of the following steps:

1. Multiply the wavefunction in real space with the real-space operator by using a

half-step in position space.

2. Flip to momentum space with an FFT operation on the wavefunction.
3. Multiply the momentum-space wavefunction by the momentum-space operator.
4. Flip to position space with an inverse FFT on the wavefunction.
5. Repeat 1-4 until satisfied.

With the method described so far, we can simulate simple quantum systems. For example, if we use a Gaussian wavefunction which is offset from the center of a simple harmonic oscillator, we can simulate the wavefunction oscillation, as shown in Figure 1.1(a).

In addition to this, we can find the lowest energy state of our system with the SSFM by performing a Wick rotation and using $\tau = it$ for the simulation instead of traditional units of time [34]. This changes the solution from the complex sinusoid shown in Equation (1.4) to an exponential decay,

$$\Psi(\mathbf{r}, \tau + d\tau) = \left[e^{-\frac{\hat{\mathcal{H}}d\tau}{\hbar}} \right] \Psi(\mathbf{r}, \tau) = \sum_{n=0}^N \left[e^{-\frac{(E_n d\tau)}{\hbar}} \right] \Psi_n(\mathbf{r}, \tau). \quad (1.9)$$

This has two notable effects:

1. There will be an exponential decay of all energy states, with higher-energy states decaying faster than the ground-state.
2. We see an exponential decay in the wavefunction density and therefore require renormalization regularly during the imaginary-time evolution.

Let me start with a discussion on the first point, by showing a simulation of the same system as in Figure 1.1(a), but in imaginary time, shown in Figure 1.1(b). Here, we see that the wavefunction density is shifting to the center of the trap, and in Figure 1.1(c), we see the energy decaying to the known ground-state energy of a quantum harmonic oscillator of $\frac{1}{2}\hbar\omega = 3.31 \times 10^{-33}$. This is because all eigenstates of the wavefunction are

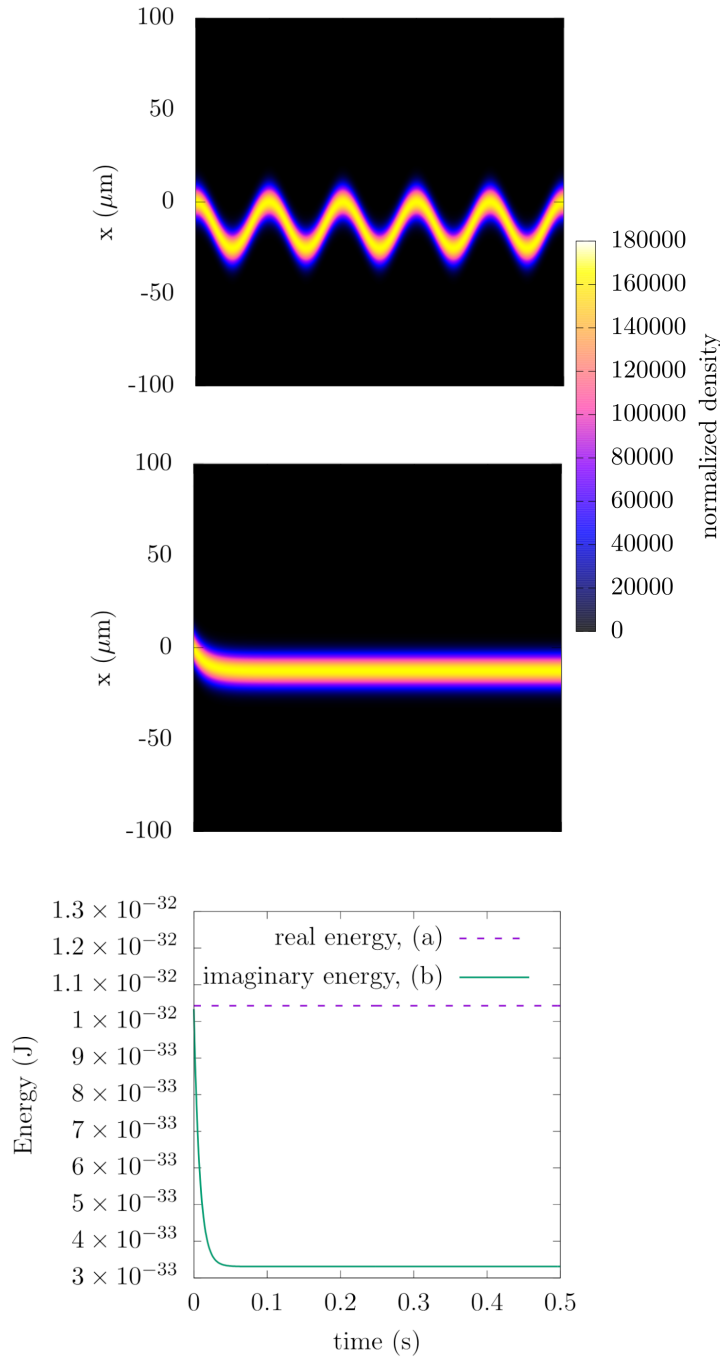


Figure 1.1: Evolution of a simple harmonic oscillator in (a) real, and (b) imaginary time after slightly shifting the trapping potential in the \hat{x} direction. In (c), we see the energy as a function of time and show that the energy of the system when evolving in real time remains constant, but in imaginary time it will decay to the known ground-state energy of the simple harmonic oscillator. The simulated results are from evolution with the SSFM after 10,000 steps. Here, we use a ^{87}Rb atom with $\omega_x = 10\text{Hz}$ on a 256-point grid of size $200\text{ }\mu\text{m}$, where the trap has been shifted by $5\text{ }\mu\text{m}$. The wavefunction has been normalized such that $\int_{-\infty}^{\infty} |\Psi|^2 dx = 1$. This simulation was performed with the GPUE codebase [12].

[WIP]

affected by the exponential decay, with the ground state decaying the slowest, and because renormalization occurs every timestep, only the ground state will survive imaginary time propagation.

Here, the energy is computed as,

$$E = \langle \Psi(\mathbf{r}) | \hat{H} | \Psi(\mathbf{r}) \rangle \quad (1.10)$$

For many systems, we can assume the simulation is in the ground state when the energy converges to a fixed value. More quantitatively, this means that the simulation can be completed when the change in energy every step in imaginary time is below some provided threshold; however, this is not always the best course-of-action. Further discussion on energy calculations performed in this work will be shown in Chapter 3.

Now to discuss the second point, which is problematic from a software perspective. In practice, every step in imaginary time requires a relatively costly renormalization step with

$$\int_{\infty}^{\infty} |\Psi(\mathbf{r}, t)|^2 d\mathbf{r} = 1, \quad (1.11)$$

for a single-particle wavefunction. Computationally, this operation requires a summation, which is not well-optimized for GPU hardware; however, it is possible to perform a parallel reduction (summation), which allows for a considerable improvement on massively parallel systems [35]. Even so, the normalization is still a slow operation and should be used sparingly.

The implementation of the SSFM provided here assumes large-scale element-wise matrix multiplications in position and momentum-space; however, even though this implementation lends itself to parallelization, we will see other methods in Chapter 3 when we discuss the implementation of the SSFM on graphics processing units.

It is important to note that the complexity of the SSFM is similar to the complexity

of a convolution via the convolutional theorem,

$$f * g = (F)^{-1} (\mathcal{F}(f) \cdot \mathcal{F}(g)). \quad (1.12)$$

Here, f and g are arbitrarily chosen functions to be convolved. In fact, interpreting the method as a series of convolutions can lead to important insight as to how the method operates. For example, in imaginary time, the momentum-space operator becomes a Gaussian and the position-space operator becomes a more tightly-confining potential. In this way, every time-step in imaginary time corresponds to a blurring operation with the momentum-space step and strong confinement with the position-space steps. Real-time propagation can be interpreted in a similar way, as the momentum-space operator is similar to the Fourier transform of two Sobel filters, thereby performing two spatial derivatives. In Chapter 3, I will discuss this further in combination with how derivatives can be performed on GPU architecture, but for now I will turn the focus to systems to be simulated via the SSFM throughout this work: ultracold atoms.

1.2 Introduction to ultracold quantum systems

When atomic systems are cooled to temperatures near zero Kelvin, it becomes easier to discern their quantum properties which vary drastically depending on whether the particles are bosonic or fermionic. Because fermions have half-integer spin, they must obey the Pauli exclusion principle and are constrained to Fermi–Dirac statistics at zero temperature. This creates a *Fermi sea*, where the particles fill defined energy levels from the bottom-up with two particles of opposite spin per level. On the other hand, bosons have integer spin and follow Bose–Einstein statistics. They will condense into a single, macroscopic ground state when cooled [36, 37], and this state of matter is known as a Bose–Einstein Condensate (BEC). The BEC has the properties of a superfluid, which will be discussed more completely in the following section.

There are notable exceptions to these rules, such as the highly correlated Tonks–Girardeau gas where bosons may act as spinless, non-interacting fermions [11, 38]. Though there also exists a regime where interacting fermions can condense into a BEC-like system by forming molecules with integer spin [39, 40], we will not discuss fermionic systems further in this work. For now, we will focus on BEC systems, but will also discuss Tonks–Girardeau gas systems later in Chapter 2.

1.2.1 Bose–Einstein condensation and the Gross–Pitaevskii Equation

For this section, we will follow a straightforward derivation using the second quantization [41]. As mentioned in Section 1.2, bosons in a BEC condense into a single ground state, meaning we must introduce a many-body Hamiltonian for the system and take inter-particle interactions into account. Because experimental systems are dilute, we will only consider two-body interactions and assume any interactions between three or more atoms to be unlikely and negligible. We can write the Hamiltonian with two body interactions in the second quantized form as

$$\hat{\mathcal{H}} = \int \hat{\Psi}^\dagger(\mathbf{r}) \left[-\frac{\hbar^2}{2m} \nabla^2 + V_0(\mathbf{r}) \right] \hat{\Psi}(\mathbf{r}) d\mathbf{r} + \frac{1}{2} \int \hat{\Psi}^\dagger(\mathbf{r}) \hat{\Psi}^\dagger(\mathbf{r}') V(\mathbf{r} - \mathbf{r}') \hat{\Psi}(\mathbf{r}') \hat{\Psi}(\mathbf{r}) d\mathbf{r} d\mathbf{r}' \quad (1.13)$$

where \mathbf{r} and \mathbf{r}' are the positions of the two colliding particles, $V(\mathbf{r} - \mathbf{r}')$ is the interaction potential, and $\hat{\Psi}^\dagger(\mathbf{r})$ and $\hat{\Psi}(\mathbf{r})$ are the creation and annihilation operators that follow the bosonic commutation relations,

$$[\hat{\Psi}(\mathbf{r}), \hat{\Psi}^\dagger(\mathbf{r})] = \delta(\mathbf{r} - \mathbf{r}') \quad (1.14)$$

$$[\hat{\Psi}^\dagger(\mathbf{r}), \hat{\Psi}^\dagger(\mathbf{r}')] = 0 \quad (1.15)$$

$$[\hat{\Psi}(\mathbf{r}), \hat{\Psi}(\mathbf{r}')] = 0. \quad (1.16)$$

In the case of a BEC at $T \approx 0$, we may perform a Bogoliubov expansion [42, 43]

$$\hat{\Psi}(\mathbf{r}, t) = \Phi(\mathbf{r}, t) + \delta\hat{\Phi}(\mathbf{r}, t), \quad (1.17)$$

where $\Phi(\mathbf{r}, t) \equiv \langle \hat{\Psi}(\mathbf{r}, t) \rangle$ is the wavefunction of the condensate known as the order parameter and $\delta\hat{\Phi}(\mathbf{r}, t)$ represents fluctuations of the BEC system. For Equation (1.17) I have used the Heisenberg representation for field operators [43]. As a note, the condensate density is defined as

$$n(\mathbf{r}, t) = |\Phi(\mathbf{r}, t)|^2. \quad (1.18)$$

Now we may use the Heisenberg equation of motion,

$$i\hbar \frac{\partial}{\partial t} \hat{\Psi}(\mathbf{r}, t) = [\hat{\Psi}, \hat{H}], \quad (1.19)$$

to determine the time evolution of the field operator $\hat{\Psi}(\mathbf{r}, t)$ as

$$\frac{\partial}{\partial t} \hat{\Psi}(\mathbf{r}, t) = \frac{1}{i\hbar} \left[-\frac{\hbar^2}{2m} \nabla^2 + V_0(\mathbf{r}) + \int d\mathbf{r}' \hat{\Psi}^\dagger(\mathbf{r}', t) V(\mathbf{r}' - \mathbf{r}) \hat{\Psi}(\mathbf{r}', t) \right] \hat{\Psi}(\mathbf{r}, t), \quad (1.20)$$

which follows from Equation (1.13) after integrating over \mathbf{r} . If we assume that two bosons will only interact with a contact potential of the form

$$V(\mathbf{r}' - \mathbf{r}) = g\delta(\mathbf{r}' - \mathbf{r}), \quad (1.21)$$

which has a strength given by

$$g \equiv \frac{4\pi\hbar^2 a_s}{m}, \quad (1.22)$$

where a_s is the species and state-dependent s-wave scattering length, we may write the time-dependent Schrödinger equation as

$$i\hbar \frac{\partial}{\partial t} \Phi(\mathbf{r}, t) = \left(-\frac{\hbar^2}{2m} \nabla^2 + V_0(\mathbf{r}) + g|\Phi(\mathbf{r}, t)|^2 \right) \Phi(\mathbf{r}, t). \quad (1.23)$$

This is the Gross–Pitaevskii Equation (GPE), which is known as a governing equation for the physics of BEC systems. When written in the time-independent form it determines the chemical potential μ of the condensate system [44, 45]

$$\mu\Phi(\mathbf{r}) = \left(-\frac{\hbar^2}{2m}\nabla^2 + V_0(\mathbf{r}) + g|\Phi(\mathbf{r})|^2 \right) \Phi(\mathbf{r}). \quad (1.24)$$

This equation allows us to determine the full dynamics of a BEC system and the numerical solutions will be discussed in subsequent chapters. Similar derivations of the GPE can be found in many introductory texts on BEC physics [37, 46, 47]. The main difference between this equation and the Schrödinger equation is the non-linear interaction term of $g|\Psi|^2$, that accounts for the fact that BECs typically consist of 10^3 to 10^6 particles. When solving this system in a simple harmonic oscillator in the limit where interactions are significant, we will find a slightly different distribution for the wavefunction density, known as a Thomas–Fermi distribution, shown in Figure 1.2 for a single dimension and varying interaction strengths.

In this case, the Thomas–Fermi distribution can be derived from the time-independent GPE in the limit where there are a large number of bosons in the condensate ($N \gg 1$) as [48]

$$\Psi_{\text{TF}}(\mathbf{r}) = \sqrt{\frac{[\mu - V(\mathbf{r})]\Theta(\mu - V(\mathbf{r}))}{g}} \quad (1.25)$$

where Θ is the Heaviside step function that ensures the condensate stays positive and $\Psi(\mathbf{r})_{\text{TF}}$ is the wavefunction in the Thomas–Fermi limit. The shape of this function is similar to that of an inverted parabola for a harmonic trap, and the radius in any direction from the center can be found to be

$$R_{\text{TF}} = \sqrt{\frac{2\mu}{m\omega_i^2}} \quad (1.26)$$

where R_{TF} is the Thomas–Fermi radius and ω_i is the trapping frequency in the i th direction. In the case of multiple particles, the normalization condition becomes $\int_{-\infty}^{\infty} |\Psi(\mathbf{r}, t)|^2 =$

N , where N is the total number of particles. By using this normalization condition, we find that the Thomas–Fermi chemical potential is

$$\mu_{\text{TF}} = \frac{\hbar\omega_i}{2} \left(\frac{15Na_s}{a} \right)^{2/5}, \quad (1.27)$$

where $a = \sqrt{\hbar/m\bar{\omega}}$ and $\bar{\omega}$ is the average of all the harmonic trapping frequencies. Using Equations (1.27) and (1.26) we find that

$$R_{\text{TF}} = a \left(\frac{15Na_s}{a} \right)^{1/5} \frac{\bar{\omega}}{\omega_i} \quad (1.28)$$

This approximation is valid for stationary condensate solutions in simple harmonic oscillator trapping geometries.

It is important to note that a BEC acts like a superfluid, which is a state of matter that is similar to a classical fluid without viscosity. This means that once a superfluid is set in motion, there is no retarding force to keep it from flowing. There are a few known systems in which superfluidity can exist, such as ^4He (sometimes called Helium II when in its superfluid phase) [49], neutron stars [50], or BEC systems [36, 51]. BEC systems are generally cleaner experimental systems to create, as they do not have a classical fluid fraction, like ^4He . As stated, we will focus on BEC systems in this work, but it is important to note that any results shown in this body of work for BEC systems may have applications beyond cold, atomic physics.

1.3 Superfluid systems and vortex dynamics

Here, I will focus here on the differences between vortex dynamics in classical and superfluid systems before continuing to discuss three methods of vortex generation in superfluid systems: rotation, phase imprinting and artificial magnetic fields. By rotating a fluid, it is possible to create a vortex around the axis of rotation; however, because of the viscosity of a classical fluid, the vortex will eventually disappear without constant driving. In a

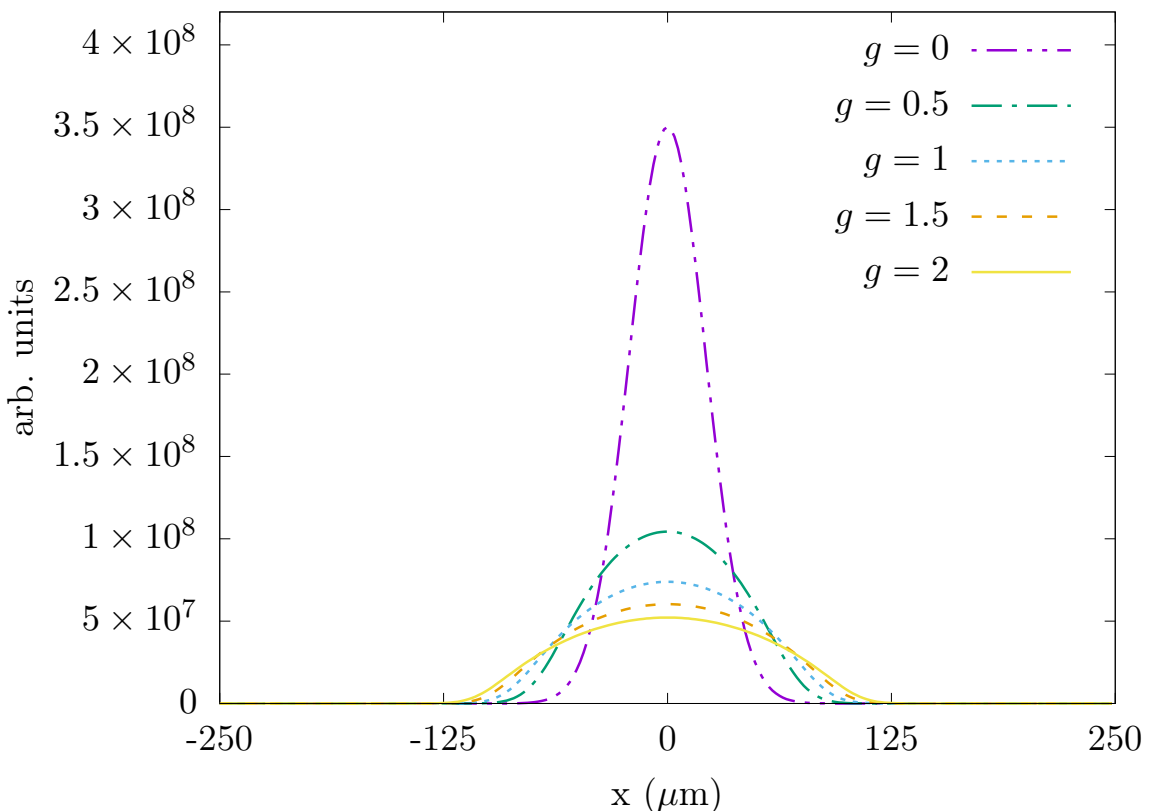


Figure 1.2: Ground state of simple harmonic oscillator for the Schrödinger equation (purple, dashed) and the GPE with varying interaction strengths (all other lines). Here, we see that the GPE solution follows a Thomas-Fermi distribution, while the Schrödinger equation is Gaussian. This simulation was performed with GPUE [12] for a two-dimensional grid of 256^2 elements of size $250\mu m$ with a trapping potential of $\omega_x = \omega_y = 1$, and 5×10^4 particles.

superfluid, this is not necessarily the case. For this discussion, it is worthwhile to discuss the hydrodynamic description of a BEC, following the text of Pethick and Smith [46]. To start, I will treat the condensate wavefunction as

$$\Psi(\mathbf{r}, t) = \sqrt{\rho(\mathbf{r}, t)} e^{i\phi(\mathbf{r}, t)}, \quad (1.29)$$

with

$$\rho(\mathbf{r}, t) = \Psi(\mathbf{r}, t)^* \Psi(\mathbf{r}, t) = |\Psi(\mathbf{r}, t)|^2. \quad (1.30)$$

where $\phi(\mathbf{r}, t)$ is the BEC phase. By multiplying the GPE by $\Psi^*(\mathbf{r}, t)$ and subtracting out the complex conjugate of the result, one can obtain the continuity equation [46],

$$\frac{\partial}{\partial t} \rho(\mathbf{r}, t) + \nabla \cdot \mathbf{J}(\mathbf{r}, t) = 0, \quad (1.31)$$

where \mathbf{j} is the current density of the condensate, defined as,

$$\mathbf{j}(\mathbf{r}, t) = \frac{-i\hbar}{2m} (\Psi^*(\mathbf{r}, t) \nabla \Psi(\mathbf{r}, t) - \Psi(\mathbf{r}, t) \nabla \Psi^*(\mathbf{r}, t)). \quad (1.32)$$

By substituting Equation (1.29) into Equation (1.32), we find the form of the current density for the GPE to be,

$$\mathbf{j}(\mathbf{r}, t) = |\Psi(\mathbf{r}, t)|^2 \frac{\hbar}{m} \nabla \phi(\mathbf{r}, t). \quad (1.33)$$

The velocity of the superfluid is defined as a ratio of the current density to the density, itself, which is

$$\mathbf{v}(\mathbf{r}, t) = \frac{\mathbf{j}(\mathbf{r}, t)}{\rho(\mathbf{r}, t)} = \frac{\hbar}{m} \nabla \phi(\mathbf{r}, t). \quad (1.34)$$

this can be interpreted to mean that the gradient of the phase determines the velocity of atoms in the BEC, indicating that the system is irrotational ($\nabla \times \mathbf{v} = 0$). Because the

condensate is single-valued,

$$\oint \mathbf{v} \cdot d\ell = \frac{\hbar}{m} 2\pi\ell. \quad (1.35)$$

Here, ℓ is an integer charge of circulation, and Equation (1.35) shows the quantized nature of circulation in a superfluid with each vortex hosting multiples of 2π charge. Every singly-charged vortex in a BEC will have a 2π phase winding, and an example simulation with one vortex in a two-dimensional condensate and its corresponding phase can be seen in Figure 1.3 (a and c). Equation (1.35) also indicates that the phase is not defined at the center of the vortex; however, at this point, the density has also dropped to zero. The density dip from the normal condensate density to zero happens over the scale of the healing length, which is

$$\xi = \frac{1}{\sqrt{8\pi\rho_b a_s}} \quad (1.36)$$

for repulsive interactions, where ρ_b is the bulk density of the condensate.

In a cylindrically symmetric condensate with a single vortex at its center, the wavefunction can be written as

$$\Psi(\mathbf{r}) = |\Psi(\mathbf{r})| e^{i\ell\phi} \quad (1.37)$$

And when substituting this in to Equation (1.10) for the GPE, we find

$$E = \int_{-\infty}^{\infty} \frac{\hbar^2}{2m} \left(|\nabla\Psi(\mathbf{r})|^2 + \frac{|\Psi(\mathbf{r})|^2 \ell^2 m \mathbf{v}^2}{2} \right) + V_0(\mathbf{r}) |\Psi(\mathbf{r})|^2 + \frac{g}{2} |\Psi(\mathbf{r})|^4. \quad (1.38)$$

Because $E \propto \ell^2$, as a superfluid is spun faster beyond a critical angular velocity, a vortex will not grow or shrink in angular momentum, but multiple vortices will spawn instead [46]. In other words, it is energetically favorable for two vortices of smaller angular momentum to form instead of a single vortex with a large amount of angular momentum. As angular momentum increases and more vortices are introduced into the system, they will eventually arrange themselves in a triangular lattice structure known as an Abrikosov lattice [52, 53]. This behavior is identical to that of type II superconductors under the effects of a magnetic field, and the size of each vortex is described by a physical scale

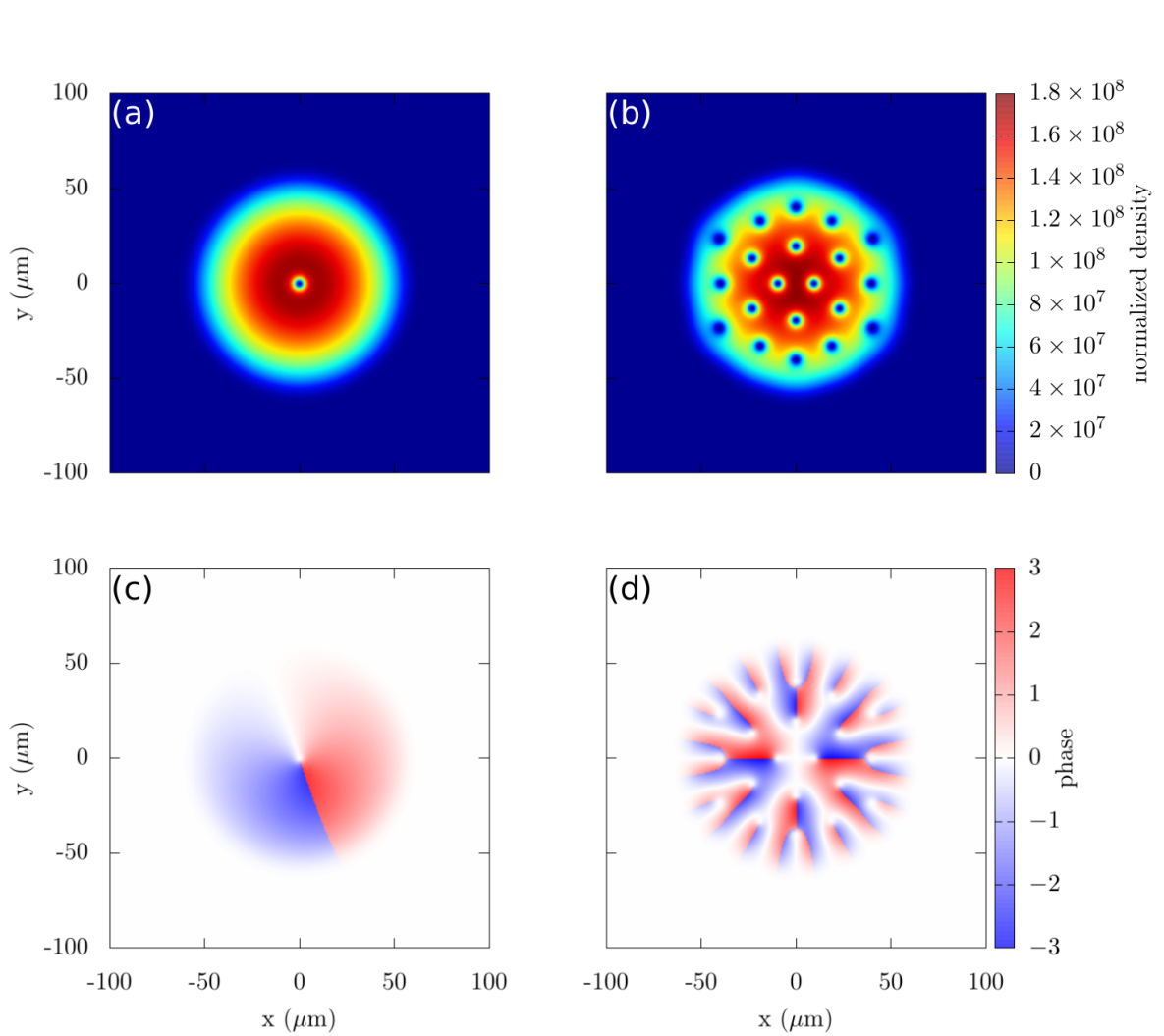


Figure 1.3: Simulation of rotation with a single vortex (a, b) and a vortex lattice (c, d). The wavefunction density is shown in a and c, while the corresponding phase is shown in b and d. A rotation of $\Omega = 0.35\omega_x$ was used for a and b, while a rotation of $\Omega = 0.99\omega_x$ was used for c and d. Here, we use a ^{87}Rb atom with $\omega_x = 2\pi\text{Hz}$ on a 512-point grid of size $200\ \mu\text{m}$. This simulation was performed with the GPUE codebase [12], and the phase plots are created by multiplying the phase by the wavefunction density to remove anomalous noise beyond the BEC boundary. [WIP]

known as the healing length. An example of a vortex lattice and its phase can be seen in Figure 1.3 (b and d).

Until now, I have focused primarily on vortex structures in two-dimensions; however, the three-dimensional properties of vortices in superfluid systems are also peculiar when compared to their classical counterparts. Here, vortex lines are formed that must either end at the end of the condensate [54] or reconnect in the form of vortex rings or other, more complicated vortex structures [55, 56]. Because the circulation around superfluid vortices is quantized, when two vortices approach each other with different velocity fields, they may reconnect into smaller, more energetically favorable vortex structures. During this reconnection, the abrupt change in energy will create a sound wave at the reconnection site [57].

Three dimensional vortex structures of non-trivial topology have been notoriously difficult to controllably generate experimentally, but we will discuss an experimentally viable method to generate, control, and detect vortex ring-like structures in superfluid BEC systems in Chapter 5. In that chapter, I will also further discuss three-dimensional vortex motion. In Chapter 4, I will also discuss important aspects of simulating two-dimensional condensate systems. For now, we will begin discussing the three primary processes to generate vortex structures in superfluid systems: rotation, phase imprinting, and artificial magnetic fields.

1.3.1 Rotation

Rotation of a BEC system will provide vortex lines that follow the axis of rotation and start and end on the BEC boundary. To simulate the effects of rotation, we simply need to append the angular momentum operator $L_z = -i\hbar(xp_y - yp_x)$ to the GPE,

$$i\hbar \frac{\partial \Psi(\mathbf{r}, t)}{\partial t} = \left(\frac{p^2}{2m} + V_0 + g|\Psi(\mathbf{r}, t)|^2 - \Omega L_z \right) \Psi(\mathbf{r}, t), \quad (1.39)$$

where Ω is the rotation frequency.

In order to generate a vortex via rotation in a harmonic trap, we must rotate faster than the critical velocity of $\Omega_c \approx 0.7\omega_{\perp}$, where ω_{\perp} is the trapping frequency perpendicular to the axis of rotation [47]. In addition, if the rotation frequency is greater than the trapping frequency, the atoms will no longer be bound by the trap due to centripetal forces. As such, finding the appropriate rotation frequency for creating vortex lattices in BEC systems is a precarious balancing act. Even so, large scale vortex lattices have been generated both experimentally and theoretically [58–61].

Experimentally, rotation for a small number of vortices can be generated in a number of ways, such as a “rotating bucket” approach that has been extended to bosonic systems [62]. For this method, bosons are confined to a magnetic trap and an anisotropic potential is superimposed that rotates with the desired angular velocity [54, 60, 63, 64]. For rotation velocities near the harmonic trapping frequency, additional methods must be used to ensure the atoms remain in-place. These methods include adding an extra confining potential [65], or the evaporative spin-up technique, where atoms with less angular momentum are evaporated such that the remaining atoms have a higher rotation speed [61, 66].

In this work, we use rotation in a qualitatively similar way to Equation (1.39); however, we will later introduce artificial magnetic fields, which is a broader framework that encompass rotation and will be used in all our simulations moving forward. We will discuss this in more detail in Section 1.4.

1.3.2 Phase imprinting

Phase imprinting is a powerful tool to allow for the generation of various structures in atomic systems, including vortices [67–71]. To generate vortices in a BEC, this technique relies on imprinting a 2π phase winding onto a ground state condensate wavefunction. Experimentally, phase imprinting can be done in a number of ways. As an example, the phase could be imprinted with a Raman two-photon process to transfer orbital angular momentum to atoms from a Laguerre–Gaussian beam [68, 72]. Another method is through

pulsing a spatially dependent potential for a short time when compared to the trapping frequency, which will imprint the potential energy onto the phase of the system [73] and can be used to generate solitons [70], vortices [74], or other states with quantized circulation [67]. Phase imprinting has also been used in theoretical studies to create a defect in a large vortex lattice by flipping the phase (and therefore rotation direction) of a selected vortex by imprinting a -4π phase at the vortex's location [59]. Note that if a phase greater than $|2\pi|$ is imprinted onto the system, the vortices are likely to decay into multiple vortices of $|2\pi|$ phase [75].

For the purposes of this work, we will only consider imprinting vortex lines along the transverse plane by applying phase imprinting operations to our condensate, such that

$$\Psi_{\text{IMP}}(x, y, t) = |\Psi(x, y, t)| e^{i(\theta(x, y, t) + \theta_{\text{IMP}}(x, y))}, \quad (1.40)$$

where $\Psi_{\text{IMP}}(x, y, t)$ is the condensate wavefunction after phase imprinting. This method allows us to apply a phase mask to any location in the transverse plane. This technique will be applied further in Chapter 4.

Phase imprinting has allowed for the generation of many interesting vortex topologies in theoretical and experimental studies [76, 77]; however, it is a dynamical process that does not create eigenstates of the system. As such, it is not as useful for engineering stable vortex structures, but is instead useful for dynamical studies, such as those found in Chapter 4.

1.3.3 Artificial magnetic fields

Magnetic fields are capable of generating rotational effects in charged systems through the Lorentz force, $F_l = q(\mathbf{E} + \mathbf{v} \times \mathbf{B})$, where q is the charge of the system, \mathbf{E} is the electric field, \mathbf{B} is the magnetic field, and \mathbf{v} is the velocity of the particle. This effect allows for the creation of vortices in type II superconductors; however, it is not directly applicable to BEC systems, because BECs are composed of neutral atoms. Even so, it is possible to

generate artificial magnetic fields with similar effects, and these artificial magnetic fields have been shown to create vortices experimentally [78]. In addition, artificial magnetic fields create a broader framework that encompasses rotational effects previously shown in Section 1.3.1, and we will use this framework instead of rotation for simulations in this work. As such, a detailed introduction, similar to that given by Dalibard in [79], will be presented below.

If written in the Hamiltonian formalism, the Lorentz force law becomes

$$\hat{\mathcal{H}} = \frac{(\hat{\mathbf{p}} - q\mathbf{A}(\mathbf{r}))^2}{2m} \quad (1.41)$$

where \mathbf{A} is a vector potential such that $\mathbf{B} = \nabla \times \mathbf{A}$ and q is the charge of the particle. Because cold atoms are neutral, we must find ways to simulate the effects of magnetic fields instead of using magnetic fields, themselves.

Firstly, let us describe how rotation can be considered to be an artificial vector potential and thus generate vortex structures in BEC systems. Imagine a plane rotating with an angular velocity Ω around the z -axis ($\boldsymbol{\Omega} = \Omega \hat{z}$). In this case, the Coriolis force is defined as

$$\mathbf{F}_{\text{Coriolis}} = 2m\mathbf{v} \times \boldsymbol{\Omega}, \quad (1.42)$$

which is formally similar to the Lorentz force law. By applying the transformation $\hat{\mathcal{H}} = \hat{\mathcal{H}}_0 - \Omega \hat{L}_z$, where $\hat{L}_z = x\partial_y - y\partial_x$, we find [80]

$$\begin{aligned} \hat{\mathcal{H}} &= -\frac{\hbar^2}{2m}\nabla^2 + \frac{1}{2}m\omega^2(x^2 + y^2) - \frac{\hbar\Omega}{i}(x\partial_y - y\partial_x) \\ &= \frac{1}{2m}\left(\frac{\hbar}{i}\nabla - m(\boldsymbol{\Omega} \times \mathbf{r})\right)^2 + \frac{m}{2}(\omega^2 - \Omega^2)r^2 \\ &= \frac{(\hat{\mathbf{p}} - m\mathbf{A}(\mathbf{r}))^2}{2m} + V_0(\mathbf{r}), \end{aligned} \quad (1.43)$$

where ω is the trapping frequency for a symmetric two-dimensional harmonic trap, $\mathbf{A} \equiv \boldsymbol{\Omega} \times \mathbf{r}$, and $V_0 = m/2(\omega^2 - \Omega^2)r^2$. The final form is similar to that of the Lorentz force law and coincides with an effective magnetic field of $2\boldsymbol{\Omega} \propto \mathbf{B}$. In this way, we may recreate

the rotation expected from the Lorentz force law in a cold atomic system with an artificial magnetic field [54, 60, 81]. Artificial magnetic fields provide a powerful tool to researchers who wish to generate and control complex vortex structures, and because of this, it is worth discussing them in further detail. Important implementation details for how to use artificial magnetic fields with the SSFM will be discussed in Section 1.4 and further discussions of how these modifications can be applied on GPU architecture can be found in Chapter 3.

Geometric Gauge Fields

As I have already described how rotation can act as an artificial Lorentz force, we now turn our attention towards methods that might allow us to generate more general rotational effects and vortex structures. In particular, we will discuss the adiabatic motion of free atoms undergoing geometric phase transformations through the Berry phase. For this, we assume that our system has an external parameter λ such that

$$\hat{H}(\lambda) |\psi_n(\lambda)\rangle = E_n(\lambda) |\psi_n(\lambda)\rangle, \quad (1.44)$$

where the set of eigenstates $\{|\psi_n(\lambda)\rangle\}$ allows us to define the time evolution of our system such that

$$|\psi(t)\rangle = \sum_n c_n(t) |\psi_n(\lambda(t))\rangle, \quad (1.45)$$

and we consider λ to evolve slowly with time. If we consider the system to begin with

$$c_l(0) = 1, \quad c_n(0) = 0, \quad \text{for all } n \neq l \quad (1.46)$$

the state of the system is proportional to $|\psi_l(\lambda(t))\rangle$. In this case, $c_l(t)$ is determined by the equation

$$i\hbar \dot{c}_l = [E_l(t) - \dot{\lambda} \cdot \mathbf{A}_l(\lambda)] c_l, \quad (1.47)$$

where

$$\mathbf{A}_l(\lambda) = i\hbar \langle \psi_l | \nabla \psi_l \rangle. \quad (1.48)$$

This quantity is called the Berry connection, which is considered a vector potential, such that we can define a new artificial magnetic field, the Berry curvature as

$$\mathbf{B}_l = \nabla \times \mathbf{A}_l. \quad (1.49)$$

Now imagine that the λ parameter follows the closed contour C such that $\lambda(T) = \lambda(0)$.

By integrating Equation (1.47) above, we find

$$c_l(t) = e^{i\Phi_{\text{dyn}}(t)} e^{i\Phi_{\text{B}}(T)} c_l(0), \quad (1.50)$$

where

$$\begin{aligned} \Phi_{\text{dyn}}(T) &= -\frac{1}{\hbar} \int_0^T E_l(t) dt \\ \Phi_{\text{Berry}}(T) &= \frac{1}{\hbar} \int_0^T \dot{\lambda} \cdot \mathbf{A}_l(\lambda) dt = \frac{1}{\hbar} \oint \mathbf{A}_l(\lambda) \cdot d\lambda \end{aligned} \quad (1.51)$$

In this case Φ_{Berry} is called the Berry phase and it only depends on the motion path of λ . It should be mentioned that both of the exponential terms in Equation (1.50) are gauge invariant and thus remain unchanged when $|\psi_n(\lambda)\rangle$ is multiplied by a phase factor. The Berry phase allows us to transfer angular momentum into our BEC and generate a vortex geometry like those formed in the 2009 experiment by Lin *et al.* [78]. As a note, the vortex structures generated in this way follow the magnetic fields lines, thus providing the capability to generate complex vortex structures beyond vortex lines. A method to generate these gauge fields in an experimentally realizable way with the evanescent field of a dielectric system undergoing total internal reflection will be described in Chapter 5, but for now we should discuss how these fields can be implemented in the SSFM, with an emphasis on their effects for superfluid simulations.

1.4 Modifications to the SSFM for superfluid vortex simulations

As shown above, in order to simulate the effects of artificial magnetic fields on BEC systems, we must slightly modify the Hamiltonian, such that

$$\hat{\mathcal{H}} = \frac{(p - m\mathbf{A})^2}{2m} + V_0 + g|\Psi(\mathbf{r}, t)|^2, \quad (1.52)$$

where \mathbf{A} is an artificial vector potential. As a note, some texts absorb the mass term into the artificial vector potential, but here we are stating it explicitly for clarity. When expanded, we note that the gauge field has a component in position space, $\frac{m\mathbf{A}^2}{2}$, which couples with the trapping potential, and another component that is partially in both position and momentum space, $-\left(\frac{p\mathbf{A} + \mathbf{A}p}{2}\right)$.

Firstly, let us discuss the component purely in position space. Here, we see that it is important to properly balance the trapping potential and the artificial vector potential when simulating BEC systems with artificial vector potentials, otherwise, the trapping geometry will become warped. In the case of rotation, this is effectively balanced by the centripetal force; however, in the case of arbitrarily chosen vector potentials, this can create rather unusual potential geometries, as shown in Figure 5.7 for a Gaussian \mathbf{A}_x and \mathbf{A}_y . Though we might be able to balance this warping with a centripetal force tailored to the gauge fields we introduce, we did not consider this for the simulations within this work.

The components of the artificial vector potential that are partially in position and momentum space are somewhat difficult to consider numerically. For many physical examples, such as rotation, $\frac{\partial \mathbf{A}_i}{\partial i} = 0$ for $i \in x, y, z$, which means the only relevant term is $-\frac{\mathbf{A}_i p_i}{2}$. This will effectively create a variable that resides in both position and momentum space, and multiplication with this operator can be performed with a one-dimensional FFT across n -dimensional data on the wavefunction first. This means that if we have

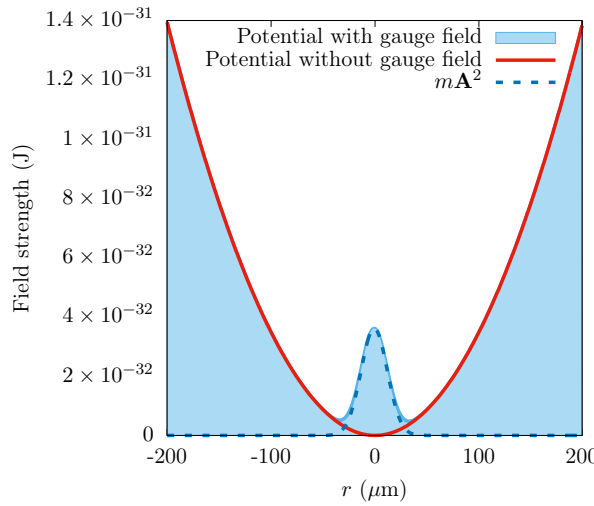


Figure 1.4: Simulation of GPE with an arbitrarily chosen Gaussian artificial vector potential. For this simulation, we have removed the pA term to focus on the warped potential, itself.

three operators, $\mathbf{A}_x p_x \hat{x}$, $\mathbf{A}_y p_y \hat{y}$, and $\mathbf{A}_z p_z \hat{z}$, we will need to perform an FFT on our wavefunction in the \hat{x} , \hat{y} , and \hat{z} dimensions, respectively, before performing an element-wise multiplication. As I will discuss in Chapter 3, this has significant performance penalties if we do not consider the massively parallel GPU architecture. This also requires the usage of more intricate FFT plans for the FFTW or CuFFT libraries, which are non-trivial for three-dimensional simulations.

If $\frac{\partial \mathbf{A}_i}{\partial i} \neq 0$, then the other operator, $-\frac{p_i \mathbf{A}_i}{2}$, must also be considered. To perform this operation, a derivative must be performed on \mathbf{A} before application to the wavefunction. This operation doubles the complexity of the application of artificial magnetic fields to the system and should be avoided unless necessary.

At this point, I have discussed all the relevant physics to understand subsequent chapters; however, it is worth noting additional physics that will become relevant when motivating future work.

1.5 Multi-component simulations

Until now, the discussion has been oriented around single-component condensates; however, in recent years, there has been a significant amount of theoretical and experimental interest in multiple BEC components in the same system [82–84]. When simulating such systems, the GPE must be modified to take interactions between components into account and each wavefunction must be evolved separately, such that

$$i\hbar \frac{\partial \Psi_i(\mathbf{r}, t)}{\partial t} = \left(\frac{(p - mA)^2}{2m} + V_0 + \sum_{j=1}^C g_{ij} |\Psi_j(\mathbf{r}, t)|^2 \right) \Psi_i(\mathbf{r}, t) \quad (1.53)$$

where C is the total number of components being simulated, $\Psi_i(\mathbf{r}, t)$ for $i \in 0, \dots, C$ is the wavefunction for a unique component being evolved, and g_{ij} is the interaction strength between components i and j . The interaction matrix is symmetric, such that $g_{ji} = g_{ij}$, and there are generally three mixing regimes in which multi-component condensates can be found:

No interaction In this regime, $g_{ij} = 0$, while $g_{ii} = 1$. This creates an interaction matrix that is identical to the identity matrix and can be understood as a simulation of C GPE components without interaction. It is rare that these simulations will be performed, simply because the additional components will produce identical results unless the atomic species is modified, and there is no reason to perform a non-interacting multi-component simulation rather than multiple single-component simulations.

Miscible In this regime, $0 < g_{ij} < 1$ and the C components mix in some fashion. This means that there will be some differentiation between components, but they can still exist in the same physical space.

Immiscible In this regime, $g_{ij} \geq 1$ and the C components no longer mix and therefore cannot exist in the same physical locations as other components.

ADD FIGURE

In Figure ??, I show simulations for a two-component condensate in each of these three regimes for a rotating system. These simulations are memory-intensive, but we will discuss several methods to minimize the memory footprint of single-component simulations in Chapter 3. These methods also apply to multicomponent simulations and allow for simulations with a higher component number.

At this point, I have discussed the SSFM, itself, along with the primary system we will be simulating in this work; however, we have yet to discuss key techniques in quantum engineering that are necessary to motivate several design decisions. As such, we will consider two dynamic methods for quantum state engineering in the following chapter: shortcuts to adiabaticity and quantum optimal control.

Chapter 2

Quantum engineering for one-dimensional quantum systems

Until recently, methods involving dynamic control protocols to engineer specific quantum states have been difficult to perform on GPU devices without full control of the software, itself. This meant that researchers wishing to engineer specific quantum states by using GPU simulations would be required to have domain-specific knowledge in both software design and quantum mechanics, neither of which are trivial to understand. This chapter serves as motivation for several methods to be discussed in Chapter 3 to allow for the simulation of quantum control methods on GPU devices, with a particular focus on quantum optimal control [85] and Shortcuts to Adiabaticity (STA) [86]. Both of these control protocols will be used in a physical example for the non-adiabatic generation of superposition states in a one-dimensional Tonks–Girardeau (TG) gas [11]. To start, I will discuss the field of optimization algorithms before moving to STA protocols and a physical system using both in practice.

The work in this chapter has been published in New Journal of Physics [11], and in this publication, I performed all calculations for all the figures generated and focused on optimal control methods. The STA protocol was devised by Jérémie Gillet, and the research was supervised by Albert Benseny and Thomas Busch.

2.1 Optimization methods

Optimization algorithms have become essential to many areas of modern computing and focus on either minimizing or maximizing a cost function by modifying several control parameters [87]. The number of control parameters create an n -dimensional space to traverse, and optimization algorithms are tasked at finding the global minimum or maximum of this domain. For certain domains, it is difficult to find a global optimization strategy and many methods instead get caught by local minima while attempting to find the appropriate solution. Because generalized optimization is such a fundamental problem, there are many known optimal control methods, such as gradient descent [88], the Nelder–Mead or simplex method [89], genetic algorithms [90], and many more. Of these, gradient descent is often considered to be one of the easiest to implement with favorable complexity and convergence guarantees, and because of this, it has become ubiquitous in many areas such as machine learning, which is of particular interest for GPU engineering. Even so, there are limitations to gradient descent, such as its dependence on calculating the gradient of the cost function’s solution domain along with lengthy convergence times for high-precision solutions.

For this work, I am primarily interested in the area of quantum optimal control, which is a method typically used to determine the optimal time-dependent control parameters necessary to transform an initial state to a final, desired state [85]. This means that one will often be maximizing the fidelity between states, defined as $\mathcal{F} = |\langle \psi | \phi \rangle|^2$, where ψ is the engineered quantum state and ϕ is the state one is attempting to replicate. This problem can be re-framed as an attempt to find the maximum of a fidelity *landscape*, where each point in the domain is a calculation of the fidelity, itself. This means that each point in the fidelity landscape necessarily involves solving the Schrödinger equation for chosen control parameters. For this reason, I will be introducing a gradient-less (derivative-free) optimization algorithm, the Nelder–Mead (simplex) method, which is often used as a heuristic approach to this problem and there are several known optimizations for this

method [89, 91, 92]. This method is also the recommended optimization algorithm for the chosen quantum optimal control method of the physical example later discussed in this chapter, Chopped RAndom Basis (CRAB) optimal control. This will be further discussed in Section 2.1.2.

2.1.1 Nelder–Mead

The Nelder–Mead method is one of the most commonly implemented gradient-less optimization algorithms to-date and relies heavily on the concept of a simplex, which is a generalization of the three-dimensional tetrahedron to n -dimensions. For example, a 0-simplex is a point, a 1-simplex is a line, a 2-simplex is a triangle, a 3-simplex is a tetrahedron, and so on. If the Nelder–Mead method is attempting to optimize a cost function with n control parameters, an $n + 1$ point simplex will be created, and the points of this simplex will be manipulated until they have converged to a minimum or maximum in the domain. For this section, I will focus on the method introduced in the original work by Nelder and Mead in 1965 while working at the National Vegetable Research Station in Warwick, England [89].

For $P_i \in i = \{0, \dots, n\}$ simplex points with heights of $y_i \in i = \{0, \dots, n\}$, the Nelder–Mead method is tasked at minimizing all points such that $\sqrt{\sum(y_i - \bar{y})^2/n} < \eta$, where \bar{y} denotes the height of the centroid location of the simplex, and η is some pre-defined convergence threshold value. This convergence criteria assumes that if all points have converged with this method, the final location must be the minimum of the optimization domain; however, as mentioned in the previous section, this method may become trapped in a local minima. At every step in the Nelder–Mead method, the points with the highest and lowest values are determined and denoted as P_h and P_l , respectively. In addition, the centroid location is found as \bar{P} . This method then performs up to three basic operations on the simplex, itself:

Reflection For this operation, P_h is flipped across \bar{P} , such that the new location,

$$P^* = (1 + \alpha)\bar{P} - \alpha P_h. \quad (2.1)$$

Here, $\alpha > 0$ is a constant known as the reflection coefficient. After this operation, the new height is compared to y_l . If it is lower, the method proceeds to an expansion step. Otherwise, the method checks whether the new height is lower than some other $y_i \in \{0, \dots, n\}, n \neq \{l, h\}$, and if it is, the point is kept and the method continues to find the new simplex ordering. If it is found that the reflected point, P^* , is higher in value than all other points, the method then keeps whichever point corresponds to the lowest height between the reflected and previous highest point and proceeds to the contraction step.

Expansion For this operation, an expansion is performed, such that the new location,

$$P^{**} = \gamma P^* + (1 - \gamma)\bar{P}. \quad (2.2)$$

Here, $\gamma > 1$ is a constant known as the expansion coefficient. If the new height is less than the previously lowest point, the expanded point, P^{**} , is kept, otherwise the reflected point is kept.

Contraction For this operation, a contraction is performed, such that the new location,

$$P^{**} = \beta P_h + (1 - \beta)\bar{P}. \quad (2.3)$$

Here, $0 < \beta < 1$ is a constant known as the contraction coefficient. If the contracted point, P^{**} , is lower than the previous highest point, the contracted point is kept, otherwise, we contract the entire simplex closer to the lowest point with $P_i = (P_i + P_l)/2$.

Each step in the Nelder–Mead method begins with a proposed reflection of the least

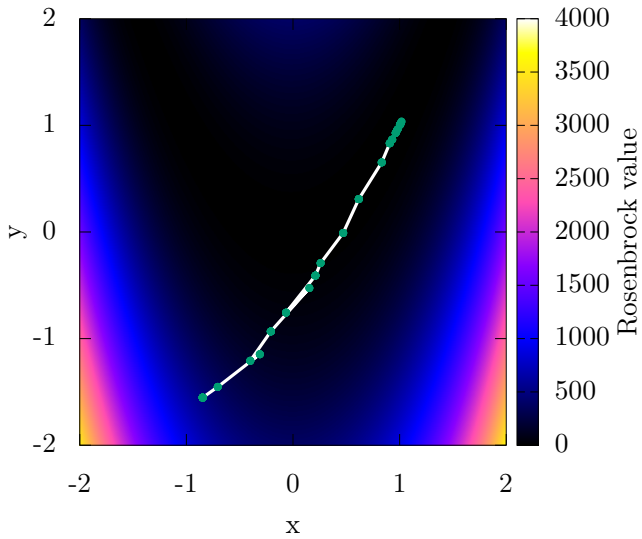


Figure 2.1: Plot of the centroid locations (green dots connected with white line) for the Nelder–Mead method while optimizing the Rosenbrock banana function, $f(x, y) = (a - x)^2 + b(y - x^2)^2$, with $a = 1$ and $b = 100$. Here, we see the centroid locations starting at $(-0.851, -1.553)$ and end at the known minimum of $(1, 1)$ in 19 iterations. Here, $\alpha = 1$, $\beta = 0.5$, and $\gamma = 1.5$.

optimal point about its centroid position. From there, the method follows the protocol described above. The choice of α , β , and γ is somewhat arbitrary and should be optimized by-hand. An example of the centroid locations for minimization using this method with the Rosenbrock banana function [93] can be seen in Figure 2.1.

Even though the Nelder–Mead method is a heuristic approach and can become stuck in a local minimum, as long a sufficient number of random simplexes are chosen at the start of the simulation, it can be used to find an adequately optimal solution. Ultimately, any gradient-less optimization algorithm can be used to traverse the fidelity landscape for quantum optimal control, and in the next section, I will discuss a common method used in the field: the Chopped RAndom Basis (CRAB) optimal control method.

2.1.2 Chopped random basis optimal control

The CRAB technique works by modifying a control parameter for a given system, Γ , with a multiplicative term as

$$\Gamma^{\text{CRAB}}(t) = \Gamma^0(t)\gamma(t), \quad (2.4)$$

where $\Gamma^0(t)$ is an initial guess, and the function $\gamma(t)$ is written as a sum of $2J$ sinusoidal functions,

$$\gamma(t) = 1 + \frac{1}{\lambda(t)} \sum_{j=1}^J (A_j \sin(\nu_j t) + B_j \cos(\nu_j t)). \quad (2.5)$$

Here, $\lambda(t)$ is usually defined by the system, such that Γ^{CRAB} and Γ^0 coincide at initial and final times. This means that $\lim_{t \rightarrow 0} \lambda(t) = \lim_{t \rightarrow T} \lambda(t) = \infty$, where T is the final time of evolution. As such, any smooth function may be chosen with these constraints. For example, we might use

$$\lambda(t) = \frac{T^2}{4t(t-T)}, \quad (2.6)$$

which satisfies the provided conditions. This then transforms the optimal control problem into an optimization of the space spanning $\{A_j, B_j, \nu_j\}$, which can be done by using Nelder–Mead with a simplex of random initial points. As an example, if $J = 10$, a thirty-dimensional space would be created and a thirty-one simplex would be formed to traverse this space. It is important to remember that each new simplex and simplex-operation requires re-solving the Schrödinger equation for those values, and as such, this is a computational costly technique. Even though higher J values will produce a more accurate result, lower values should be chosen, if possible.

This method is a general-purpose computational tool for determining the optimal pulse to ensure the generated state is as close to the desired state as possible, and I will show an example of it being used later in this chapter. As such, it is sometimes worthwhile to attempt to devise analytical frameworks that serve a similar purpose, and for certain

systems, this can be done with Shortcuts To Adiabaticity (STA).

2.2 Shortcuts to adiabaticity

STA protocols are semi-analytical methods that allow for quantum state generation while retaining the effects of adiabatic movement. Here, adiabatic processes are defined as actions by which slow changes in the control parameters leave particular properties invariant, such as the quantum number [86]. The ultimate goal of STA protocols is to achieve adiabatic motion in sub-adiabatic time, and this can be done in a number of ways; however, in this section, I will introduce only the invariant-based inverse-engineering approach using Lewis–Riesenfeld invariants [94]. In particular, I will focus on the specific methods necessary for the example to be introduced later in this chapter and much of this section will follow traditional derivations from various sources [11, 86, 94].

With the method of Lewis–Riesenfeld invariants, the theory for relating different eigenstates of a time-dependent, Hermitian invariant to the solutions to the Schrödinger equation [95] can be applied to systems with time-dependent Hamiltonians, such that

$$\frac{d}{dt} = i\hbar \frac{\partial I(t)}{\partial t} - [\hat{\mathcal{H}}, I(t)] = 0, \quad (2.7)$$

where $I(t)$ is the invariant. This ensures that the expectation values for the states driven by $\hat{\mathcal{H}}$ are constant in time. It is possible to expand the state of the system $|\Psi(t)\rangle$ into the orthonormal basis of the invariant with,

$$|\Psi(t)\rangle = \sum_n^{\infty} c_n |\psi_n(t)\rangle \quad (2.8)$$

$$|\psi_n(t)\rangle = e^{i\alpha_n(t)} |\phi_n(t)\rangle, \quad (2.9)$$

where c_n are time-independent amplitudes for each state, and $|\phi_n(t)\rangle$ are orthonormal

eigenvectors of the invariant, such that

$$I(t) = \sum_n^{\infty} |\phi_n(t)\rangle \lambda_n \langle \phi_n(t)|. \quad (2.10)$$

Here, the λ_n are real constants, and the phase is defined as [95]

$$\alpha_n(t) = \frac{1}{\hbar} \int_0^t \langle \phi_n(t') | i\hbar \frac{\partial}{\partial t'} - \hat{\mathcal{H}}(t') | \phi_n(t') \rangle dt'. \quad (2.11)$$

From here, inverse engineering can be used to create the desired time-dependent Hamiltonian, by imposing some dynamics on the system. The phases, $\alpha_n(t)$ may be chosen as arbitrary functions to create a time-dependent, unitary evolution operator,

$$U = \sum_n^{\infty} e^{i\alpha_n(t)} |\phi_n(t)\rangle \langle \phi_n(0)|, \quad (2.12)$$

that obeys $i\hbar \dot{U} = \hat{\mathcal{H}}(t)U$ and the dot is a time-derivative. If one considers Hamiltonians of the Lewis and Leach variety [96],

$$\hat{\mathcal{H}} = \frac{p^2}{2m} - F(t)x + \frac{m}{2}\omega^2(t)x^2 + \frac{1}{\rho(t)^2}U \left[\frac{x - x_c}{\rho(t)} \right] + f(t), \quad (2.13)$$

there will be an invariant that is quadratic in momentum,

$$I = \frac{1}{2m}[\rho(p - mx_c) - m\dot{\rho}(x - x_c)]2 + \frac{1}{2}m\omega_0^2 \left(\frac{x - x_c}{\rho} \right)^2 + U \left(\frac{x - x_c}{\rho} \right). \quad (2.14)$$

These equations are valid so long as ρ , x_c , ω , and F satisfy

$$\ddot{\rho} + \omega^2(t)\rho = \frac{\omega_0^2}{\rho^3} \quad (2.15)$$

$$\ddot{x}_c + \omega^2(t)x_c = F(t)/m \quad (2.16)$$

with ω_0 as a defined constant whose physical interpretation depends on the system. As in

the case of quantum optimal control, additional constraints must be considered to ensure the Hamiltonian and its invariant commute at initial and final times t_0 and T .

The obvious drawbacks to STA methods are the strengths of quantum optimal control. Where shortcuts can only be used on a specific subset of problems we wish to evolve adiabatically and that are amenable to the analytical methods used, quantum optimal control is a more general tool for a wider variety of systems. On the other hand, STA protocols are semi-analytical and if such protocols can be found, they greatly reduce the computational cost to engineering particular quantum states. Now that I have provided specific examples of methods used in quantum engineering, it is time to put them into practice with an example of creating large-scale superposition states non-adiabatically in the highly-correlated Tonks–Girardeau (TG) gas regime.

2.3 Non-adiabatic generation of NOON states in a Tonks–Girardeau gas

For this example application of quantum optimal control and STA protocols, we are interested in generating the maximally entangled $|N, 0\rangle + |0, N\rangle$ (NOON) state, which is composed of two modes where all particles can be found exclusively in one or the other. Recently, Hallwood *et al.* proposed an experimentally realistic method to generate NOON states in a gas of strongly interacting, neutral bosons on a one-dimensional ring. In this system, different rotational states can be coupled by breaking the rotational symmetry and it is possible to create superposition states with rotating and non-rotating components. Because the atoms are considered to be in the strongly correlated TG gas regime, this process results in a macroscopically-entangled state. It is worth discussing the TG gas in further detail before discussing the precise method of NOON state generation for this example.

2.3.1 Tonks–Girardeau gas

As mentioned in Chapter 1, the TG gas consists of a number of bosons that have the properties of spinless, non-interacting fermions. This is a particular case of the one-dimensional Schrödinger equation where $g \rightarrow \infty$. In this case, the bosons cannot pass each other and cannot be at the same location, which acts formally similar to the Pauli-exclusion principle for fermionic systems. In this case, the Hamiltonian can be solved by the Bose–Fermi mapping theorem [97, 98], which replaces the interaction terms in the Hamiltonian with a boundary condition on the many-body bosonic wavefunction.

$$\Psi_B(x_1, x_2, \dots, x_N) = 0, \quad \text{if} \quad x_i - x_j = 0 \quad \text{with} \quad i \neq j. \quad (2.17)$$

The Bose–Fermi mapping theorem allows us to replace strongly interacting bosons by spinless, non-interacting fermions, on which one can use the Slater determinant [99],

$$\Psi_F(x_1, x_2, \dots, x_N) = \frac{1}{\sqrt{N}} \det \left[\psi_n(x_j) \right]_{n,j=1}^N. \quad (2.18)$$

where $\psi_n(x_j)$ are the single-particle eigenstates of the trapping potential V_0 . Because the Fermionic many-body wavefunction is anti-symmetric, this needs to be symmetrized for bosonic states as,

$$\Psi_B(x_1, x_2, \dots, x_N) = \prod_{i < j} \operatorname{sgn}(x_i - x_j) \Psi_F(x_1, x_2, \dots, x_N) \quad (2.19)$$

which means that calculating the time evolution of a TG gas requires evolving single-particle states, governed by a much simpler Hamiltonian.

2.3.2 NOON states in TG gas

Similar to other ring systems introduced in the literature [100, 101], the system suggested by Hallwood *et al.* considers a gas of N interacting bosons of mass m on a one-dimensional

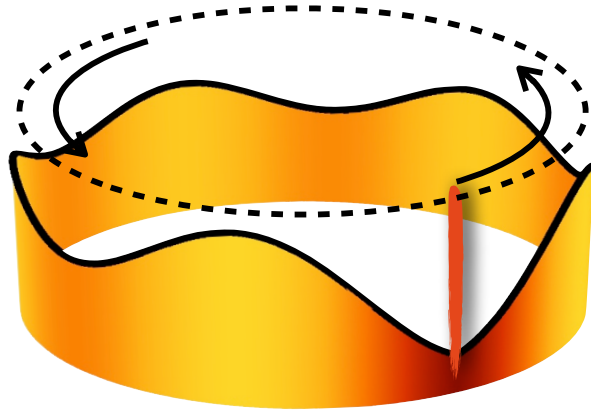


Figure 2.2: Schematic of the system described by Hallwood *et al.* [102]. Here, the density profile for five atoms in a TG gas is shown being stirred by a highly localized potential, indicated by the vertical line.

ring with circumference L [102]. In addition, this system includes a potential barrier, modeled by a Dirac δ function that rotates with an angular frequency Ω , as shown in Figure 2.2. In the rotating frame, the scaled Hamiltonian of the system is given by [102]

$$H^{(N)} = \sum_{i=1}^N \left[\frac{1}{2} \left(-i \frac{\partial}{\partial x_i} - \Omega \right)^2 + b\delta(x_i) + g \sum_{i < j}^N \delta(x_i - x_j) \right], \quad (2.20)$$

where b is the height of the barrier (in units of \hbar^2/mL^2), $x_i \in [-1/2, 1/2]$ is the position of the i -th particle (in units of L) and g (in units of \hbar^2/mL^2) is the effective interaction strength between the atoms. As discussed in the previous section, the evolution of a TG gas requires the evolution of single-particle states, and in the case of this system, the Hamiltonian becomes,

$$H = -\frac{1}{2} \frac{\partial^2}{\partial x^2} + b\delta[x - x_0(t)], \quad (2.21)$$

where x_0 is the position of the barrier at time t .

The energy spectrum of this system is shown in Figure 2.3 as a function of the rotational frequency $\Omega \equiv \dot{x}_0/L$ of the system. In Figure 2.3(a) it is shown that in the absence of a barrier, the eigenstates of $\hat{\mathcal{H}}$ are plane waves with quantized angular momentum in

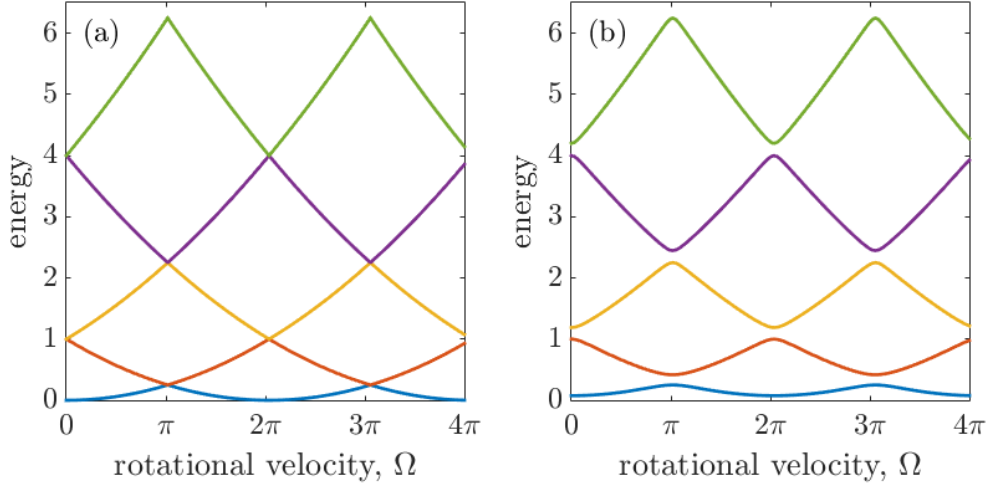


Figure 2.3: Single-particle energy spectrum as a function of Ω for a barrier height of (a) $b = 0$ and (b) $b = 2$. When a barrier is present in the system, avoided crossings appear in the energy spectrum which grow as the barrier strength increases.

integer multiples of 2π ; however when $b > 0$ (Figure 2.3(b)), the rotational symmetry is broken and avoided crossings appear in the energy spectrum. This makes transitions between different manifolds possible [103].

By adiabatically accelerating the barrier's rotational frequency from 0 to π , a particle will enter a superposition between two rotational states, and in the case of the TG gas, this will create a macroscopic NOON superposition state between successive values of angular momentum [102]. Any non-adiabatic behavior around the rotational frequencies of the avoided crossing can lead to a transition to a higher energy state and destroy the NOON state. For this reason, the condition for adiabaticity must depend on the gap size, which is dictated by the barrier strength [104]; however, for a delta barrier, the gap size stays relatively constant to first-order approximation [105].

Because this system requires adiabatic movement to properly generate the NOON state, it is difficult to efficiently generate it experimentally. For this reason, it is a perfect example of a system where quantum optimal control and STA protocols can be used to rapidly engineer the appropriate states. For quantum optimal control in this system, a non-adiabatic rotational frequency $\Omega(t)$ must be found, for which we will use the CRAB

technique with an initial condition of $\Omega = 0$ and final condition of $\Omega = \pi$. For each simulation in the fidelity landscape, we will be modifying this pulse with procedurally generated sinusoidal functions, calculating the fidelity, and then using the Nelder–Mead method to optimize the result. This will allow one to determine an optimal pulse that maximizes the fidelity of our generated state when compared to the expected NOON state in a pre-set amount of time. For this system, I will show the optimal pulse for the cases where we manipulate the rotational velocity, the barrier height, and both.

For STA protocols, the acceleration process will be split into two, one that breaks the rotational symmetry and another that accelerates the atoms. At the end of the protocol, the potential is lowered to restore rotational symmetry. Here, it is worth mentioning that a FAst, QUasi-ADiabatic (FAQUAD) shortcut for the creation of superposition states in a TG gas has also been created with some similarities [106].

For both of these methods, instead of calculating the fidelity, itself, I calculate the *infidelity*, which is simply $1 - \mathcal{F} = 1 - |\langle \Psi | \Phi \rangle|^2$, as the function to minimize. It is also worth mentioning that the fidelity between two many-particle states in a TG gas can be calculated by using the method of mode projections [107, 108],

$$\begin{aligned} \langle \Psi | \Phi \rangle &= \frac{1}{N!} \sum_{\eta, \mu \in P} \epsilon_\eta \epsilon_\mu \langle \psi_{\eta_1}(x_1) | \phi_{\mu_1}(x_1) \rangle \cdots \langle \psi_{\eta_N}(x_N) | \phi_{\mu_N}(x_N) \rangle \\ &= \det \left[\langle \psi_i | \phi_j \rangle \right]_{i,j=1}^N \end{aligned} \quad (2.22)$$

which follows directly from the form of the TG state [38]

$$\Psi(x_1, x_2, \dots, x_N) = \frac{1}{\sqrt{N!}} \prod_{i < j} \text{sign}(x_i - x_j) \sum_{\eta \in P} \epsilon_\eta \psi_{\eta_1}(x_1) \cdots \psi_{\eta_N}(x_N). \quad (2.23)$$

Here P represents the set of all permutations of N elements, ϵ_η represents the anti-symmetric tensor of the permutation η , and ψ_i represent the orbitals. Now I will discuss our findings with both optimal control and STA protocols.

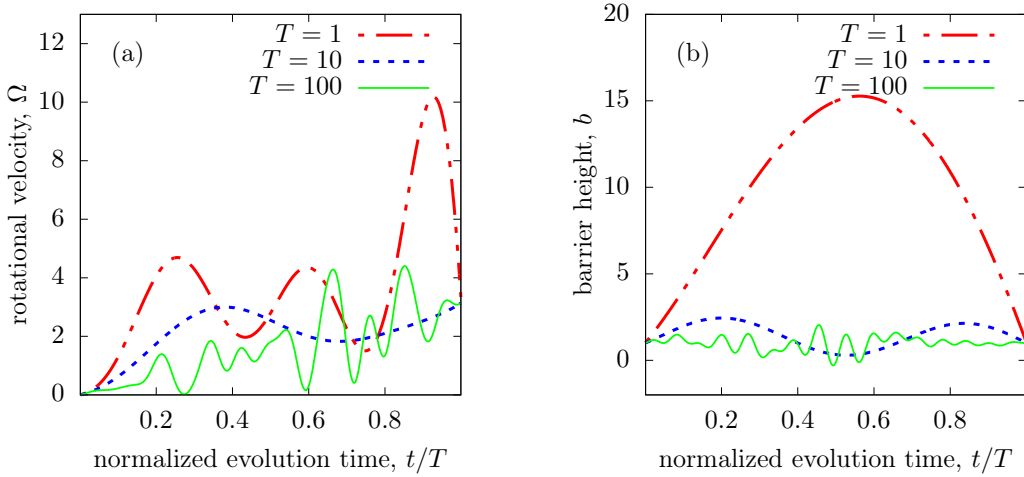


Figure 2.4: Accelerating a single particle from the ground state with $J = 15$. (a) Optimal rotational velocity pulses for $T = 1$, 10, and 100 for fixed barrier height $b = 1$. (b) Optimal barrier height for a linearly increasing rotational velocity, $\Omega = \pi t/T$ for $T = 1$, 10, and 100.

2.3.3 Results with optimal control

First, I will focus on the acceleration of a single particle, initially in the ground state of the system. Figure 2.4 (a) shows the results of this simulation if the barrier height is kept constant and we assume an initial unmodified pulse that corresponds to a linear ramp from $\Omega = 0$ to π for a preset total time, T . For longer evolution times, there are many local maxima for the fidelity, and as such, longer evolution times effectively produce noisy signals and the Nelder–Mead method converges on one of many local minima. For shorter evolution times, the pulse greatly affects the system and the shapes vary greatly from the initial linear ramp. The infidelities for the linear guess pulse and its corresponding optimized pulse can be found in Figure 2.6, and one can see an improvement of several orders of magnitude. Here, we see that for longer evolution times, the initial linear pulse is a reasonable method to generate NOON states with an infidelity of 10^{-2} because it is close to adiabaticity by definition; however, even in this case, the NOON state generation fidelity is better with optimization. For all optimal control results in this Chapter, the

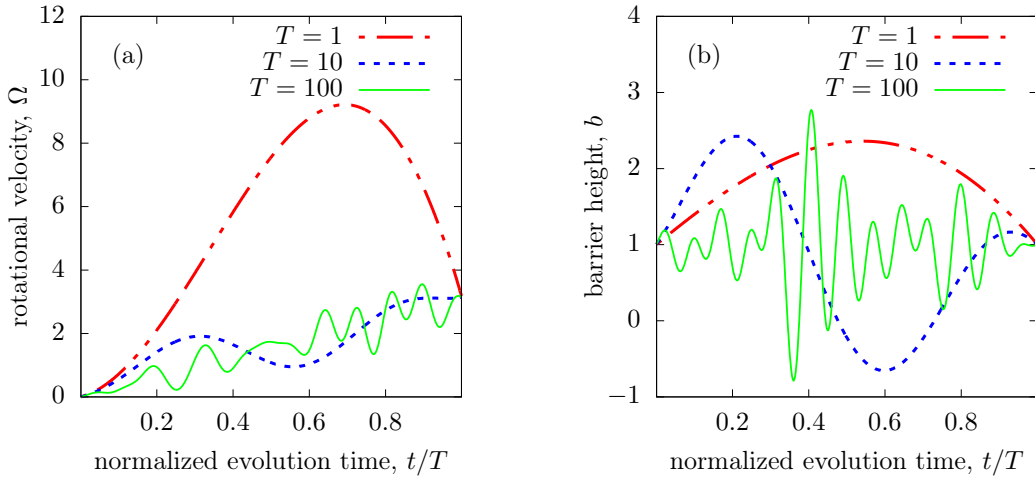


Figure 2.5: Optimal pulses to accelerate a single particle initially in the ground state of the trap for $T = 1$, 10, and 100 for the (a) rotational velocity and (b) barrier height when optimizing over both simultaneously.

CRAB method was run 100 times and the data with the highest fidelity was kept.

For optimizations of the barrier strength, simple linear ramp for Ω and an initial final height for the barrier at $b = 1$ were chosen. The optimal pulses for the barrier height for $T = 1$, 10, and 100 are shown in Figure 2.4(b) and shorter evolution times similarly produce larger deviations from the initial pulse. Again these pulses lead to significant improvements in the fidelity shown in Figure 2.6.

With the CRAB method, it is possible to optimize over as many control parameters as one would like, and as such, it is possible to optimize over both the barrier strength and rotational frequency, and the results can be seen in Figure 2.5, where (a) is the modified rotational frequency and (b) is the barrier height. When comparing to the previous cases, similar trends emerge. In particular, shorter evolution times result in less noisy optimizations when compared to longer evolution. Even so, all sets of pulses are radically different when compared to optimizations over a single variable. When comparing the fidelities in Figure 2.6, it is clear that optimizations over rotation, alone provide the simplest method to optimize the fidelity. It is likely that each run of the CRAB method

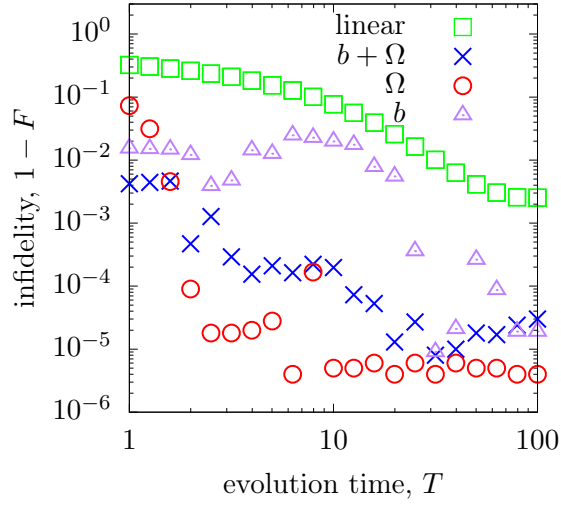


Figure 2.6: Infidelities as a function of the overall process time for optimally controlled rotational acceleration, barrier height, or both. Here, 'linear' refers to an unoptimized linear acceleration from $\Omega = 0$ to π while keeping the barrier height fixed at $b = 1$.

is stuck in a local minima in the fidelity landscape at some point and that optimization over both variables can provide the same optimization as rotating, alone.

Finally, it is worth discussing the dynamics of a TG gas with 3 and 5 particles. Because of the Bose–Fermi mapping theorem, the evolution of an N -particle TG gas can be calculated by evolving a gas of N spinless fermions. In the zero-temperature limit, the fermions in the initial and target state create a Fermi sea by filling the lowest N energy levels. In this case, only atoms near the Fermi edge can transition into empty states and it is thus crucial to optimize the dynamics of the overall gas with respect to the particle with highest energy [106]. In Figure 2.7, I show the fidelity for the particle closest to the Fermi edge and the entire TG gas for $N = 3$ and 5. In this figure, one can see that by performing the optimization for the atoms near the Fermi edge, one can increase the fidelity of the entire gas for certain regimes; however, in contrast to Figure 2.6, there seems to be no fidelity increase from a linear pulse for short evolution times. There also seems to be a crossover regime where optimizations of the particle at the Fermi edge seem to fail, but evolution of the entire gas is still slightly better than the linear pulse. It is

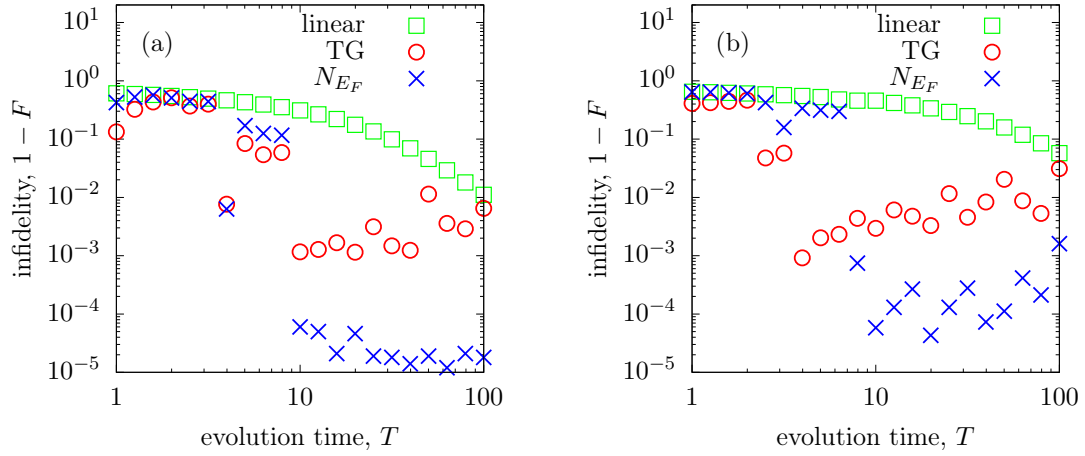


Figure 2.7: Infidelities for the evolution of a TG gas with (a) $N = 3$ and (b) $N = 5$ particles using the CRAB optimal control technique. The optimal pulses were determined for the particle at the Fermi edge (blue crosses), and applied to the whole gas (red circles). Here, the green squares show the fidelity of a linear pulse for the atom closest to the Fermi edge. A clear range where the CRAB algorithm is effective for generating NOON states with multiple particles can be clearly identified.

clear that the CRAB method creates highly effective pulses; however, for very short and long evolution times, the fidelity increase from a linear pulse is not as drastic.

2.3.4 Results with STA protocols

In this section, I will describe an STA protocol to generate NOON states in this system non-adiabatically, and though this was mentioned briefly in Section 2.3.2, it will be described more rigorously here. For this method, the rotational symmetry must be broken by introducing a time-dependent external potential that is removed in the end. This requires a slight modification of the system proposed by Hallwood *et al.* to allow for a barrier that is not a δ function, but instead a harmonic or sinusoidal potential along the ring.

The protocol consists of five steps:

1. Adiabatic raising of a weak harmonic or sinusoidal potential around the ring.

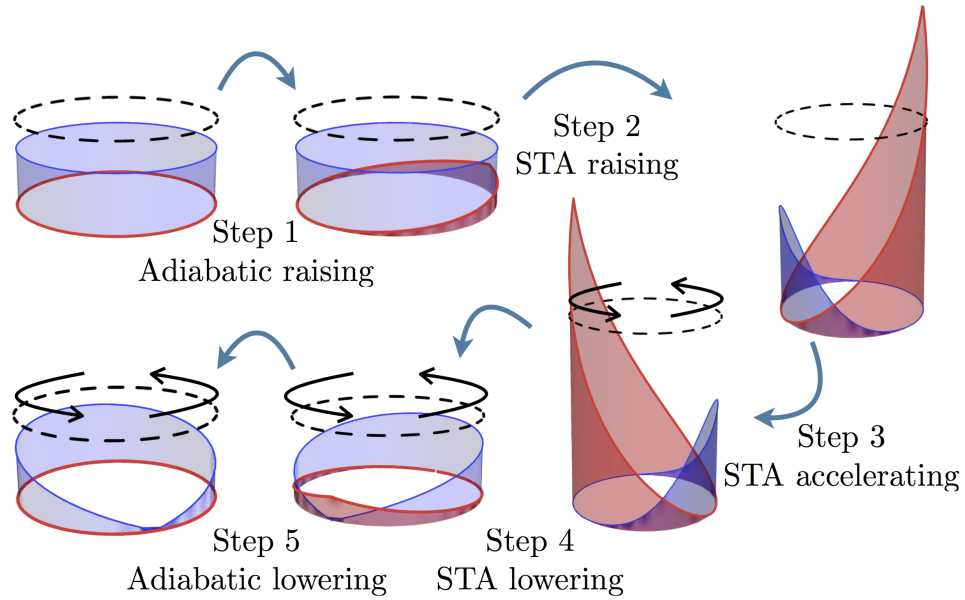


Figure 2.8: Scheme for the acceleration of a single atom using STA. In this example, the ground state of free space gets localized, accelerated and released at the angular velocity of $\Omega = \pi$ into the state $(\exp(i2\pi x) + 1) / \sqrt{2}$. The atomic density is indicated in blue and the potential is in red.

2. Fast tightening of this potential to localize the particles.
3. Accelerating the particles by moving the center of the potential.
4. Lowering the potential by reversing step 2.
5. Adiabatic lowering of the harmonic or sinusoidal potential.

A schematic of this process is shown in Figure 2.8. For steps 2-4, pre-existing STA protocols can be used, and these will be discussed in this section. The full protocol for the TG ring example will follow the STA methods outlined above with Lewis–Riesenfeld invariants and in our case, one needs to fulfill boundary conditions such that $\hat{\mathcal{H}}(t_0) = \hat{\mathcal{H}}(T) = p^2/2m$. To be clear, the NOON states created with the STA protocol are slightly different those generated with quantum optimal control, as the STA variant does not rely on a δ barrier.

One of the two shortcuts being used for this system involves raising and lowering a harmonic potential [109, 110]. For this shortcut, we need a stationary harmonic potential

and can set F , x_c , and U from Equation (2.13) to zero, leading to

$$\hat{\mathcal{H}} = -\frac{1}{2} \frac{\partial^2}{\partial x^2} + \frac{1}{2} \omega^2(t) x^2. \quad (2.24)$$

To change the frequency while keeping the commutation relations and $\omega(t)$ continuous the following conditions must be imposed:

$$\begin{aligned} \rho(t_0) &= 1, & \rho(t_f) &= \gamma = \sqrt{\omega_0/\omega_f}, \\ \dot{\rho}(t_0) &= 0, & \dot{\rho}(t_f) &= 0, \\ \ddot{\rho}(t_0) &= 0, & \ddot{\rho}(t_f) &= 0. \end{aligned} \quad (2.25)$$

As long as the conditions, Equations (2.15) and (2.25) are obeyed, any form of ρ can be chosen, and a good choice is the polynomial,

$$\rho(s) = 6(\gamma - 1)s^5 - 15(\gamma - 1)s^4 + 10(\gamma - 1)s^3 + 1, \quad (2.26)$$

where $s = (t - t_0)/(t_f - t_0)$ allows one to numerically find a solution for $\omega(t)$ that leads to the squeezing or expansion of the particle wavefunction with high fidelity in a short time. As an important note, small values for ω_0 , Equation (2.15) can provide purely imaginary values for $\omega(t)$, corresponding to repulsive potentials. In order to avoid this and because the final states of this protocol require the external potential to be absent, the first and final steps in the protocol for this system involves adiabatically raising and lowering a potential to a suitable ω_0 value.

Once the potential has been raised, it is time to accelerate the particles to the chosen frequency, and a shortcut for this process with a harmonic trap exists [111–113]. In the rotational shortcut, the trapping frequency is held constant and the position of the potential is modified. This means that $U = 0$, $F = \omega_0^2 x_0(t)$, and

$$H = -\frac{1}{2} \frac{\partial^2}{\partial x^2} + \frac{1}{2} \omega_0^2(x - x_0(t))^2. \quad (2.27)$$

Here, Equation (2.16) becomes the only relevant auxiliary equation,

$$\ddot{x}_c + \omega_0^2(x_c - x_0) = 0. \quad (2.28)$$

Conditions are then imposed on x_c , such that

$$\begin{aligned} x_c(t_0) &= x_0(t_0), & x_c(t_f) &= d, \\ \dot{x}_c(t_0) &= 0, & \dot{x}_c(t_f) &= \Omega_f, \\ \ddot{x}_c(t_0) &= 0, & \ddot{x}_c(t_f) &= 0, \end{aligned} \quad (2.29)$$

where d is the final position of the potential minimum and Ω_f is its final velocity. For most applications of this shortcut, d is important, and Ω_f is set to zero; however, this case is the opposite.

Like the shortcut for raising the potential, the exact form of x_c can be chosen somewhat arbitrarily, and a convenient choice is

$$x_c(s) = (6d - 3\Omega_f)s^5 - (15d - 7\Omega_f)s^4 + (10d - 4\Omega_f)s^3 + x_0(t_0), \quad (2.30)$$

where, as above, s is the normalized time. The value of Ω_f can then be chosen to be odd multiples of π to generate the desired NOON states.

Unlike the shortcut to raise the potential, this shortcut is only approximate and works best when ω is large so that the particles are highly localized. Both of these shortcuts rely on the presence of a harmonic potential of the form

$$V_H(x, t) = \frac{1}{2}\omega^2(t)(x - x_0(t))^2, \quad (2.31)$$

where ω is the frequency of the trap (in units of \hbar/mL^2) and x_0 the position of its minimum. In the case of the TG ring, the potential must be symmetric around x_0 , such that it is continuous at $x = \pm 1/2$; therefore, the real form of $(x - x_0)$ must be $(x - x_0 + 1/2)(\text{mod } 1) - 1/2$. The potential V_H is then continuous everywhere on the ring,

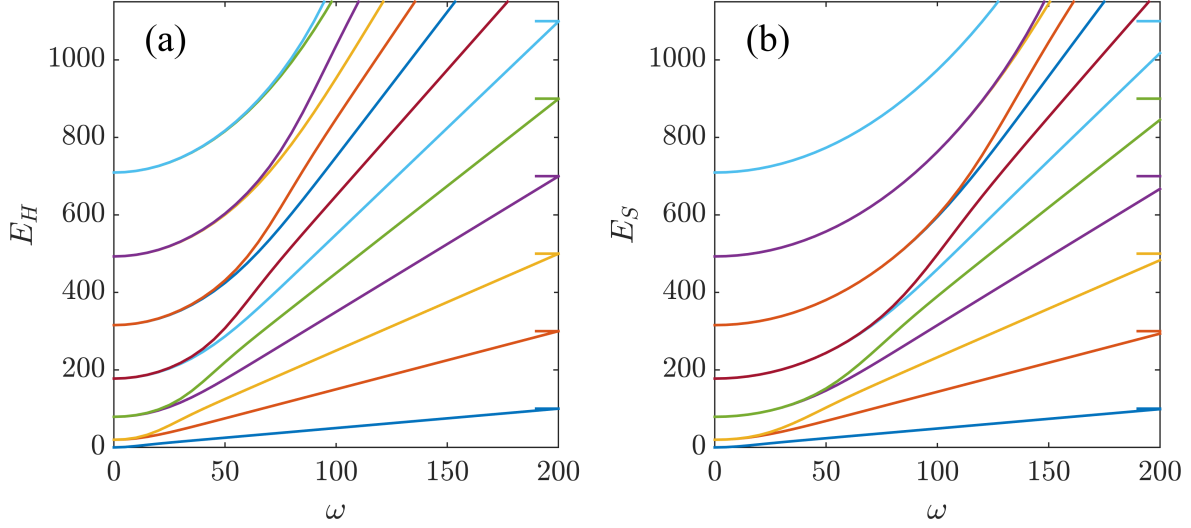


Figure 2.9: Energy eigenspectrum of the system with (a) a harmonic or (b) a sinusoidal potential as a function of ω . The eigenstates continuously change from angular momentum states of energy $E_k = 2\pi^2 k^2$ (with $k = 0, \pm 1, \dots$) at $\omega = 0$, towards harmonic-oscillator states of energy $E_n = \omega(n + 1/2)$ (with $n = 0, 1, \dots$) for large ω . For comparison, the horizontal lines on the right vertical axis give the energy levels in a harmonic potential with $\omega = 200$.

but its derivative is discontinuous at $x = x_0 + 1/2$ because this position is diametrically opposite to x_0 . Though V_H is ideal theoretically, it is not necessarily experimentally realistic, so a sinusoidal potential is also considered [114, 115],

$$V_S(x, t) = \frac{\omega^2(t)}{2\pi^2} \sin^2(\pi(x - x_0(t))), \quad (2.32)$$

where the notation is the same as before. Here, prefactors are chosen such that V_H is an approximation of V_S around x_0 .

In Figure 2.9 I show the difference between the two potentials by computing the energy spectra of both Hamiltonians. Here, the eigenstates at $\omega = 0$ are the angular momentum states $e^{i2\pi kx}$, with degenerate clockwise and counterclockwise momentum states of opposite quantum number k . As ω is increased, the degeneracy ceases and the spectrum asymptotically approaches that of a harmonic oscillator. For the sinusoidal case, the difference with the harmonic spectrum increases with the quantum number n .

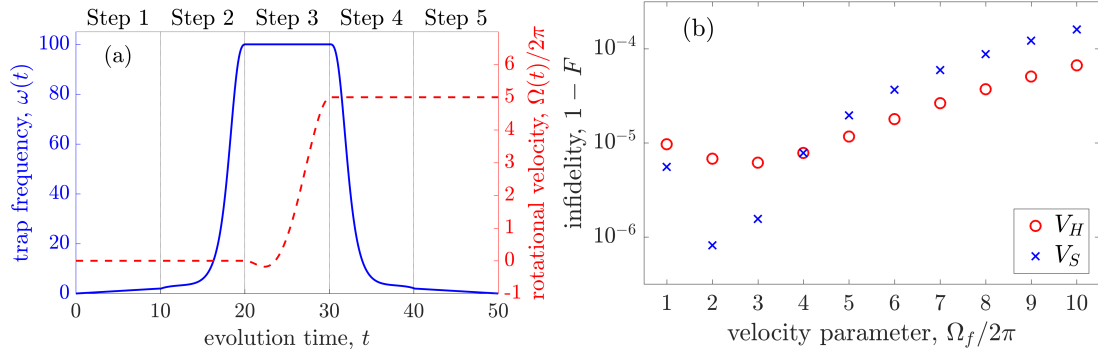


Figure 2.10: (a) Plot of the parameters $\omega(t)$ and the angular velocity $\Omega(t)$ for the entire protocol. The parameters are $\omega_0 = 2$, $\omega_f = 100$, $d = 100$, each step is executed in $t_f - t_0 = 10$, and Ω_f is picked depending on the desired output state (here, $\Omega_f = 5 \times 2\pi$). (b) Final infidelities for $\Omega_f = 1, 2, \dots, 10 \times 2\pi$ for V_H (dotted blue line) and V_S (solid red line). The rest of parameters are as shown in (a).

Like the case of quantum optimal control, I will first show the single-particle results. In Figure 2.10(a), the values for $\omega(t)$ and $\Omega(t)$ are shown, and in Figure 2.10(b), the infidelities for the state preparation of plane waves $e^{i\Omega_f x}$ with $\Omega_f = 1 \dots 10 \times 2\pi$ are shown. Here, it is clear that even for a large amount of angular momentum, the fidelities remain high for both the harmonic and sinusoidal potentials.

For a multi-particle case in the TG regime, the initial states for the particles will be eigenstates of free space, which are simply plane waves $e^{i2\pi kx}$ with integer k . Because the states with $\pm k$ are degenerate, it is equally valid to consider the initial eigenstates

$$\phi_0^i(x) = 1, \quad (2.33)$$

$$\phi_{2l-1}^i(x) = \frac{1}{\sqrt{2}} (e^{i2\pi lx} - e^{-i2\pi lx}) = i\sqrt{2} \sin(2l\pi x), \quad (2.34)$$

$$\phi_{2l}^i(x) = \frac{1}{\sqrt{2}} (e^{i2\pi lx} + e^{-i2\pi lx}) = \sqrt{2} \cos(2l\pi x), \quad (2.35)$$

for $l = \{1, 2, \dots\}$. These states have a total angular momentum of zero and are well-suited for the provided STA protocol because when an odd number of particles occupies the lower eigenstates, the sin/cos pairs are guaranteed to be populated.

For $\Omega_f = \pi$, the plane wave of quantum numbers $k+1$ and $-k$ are degenerate and we

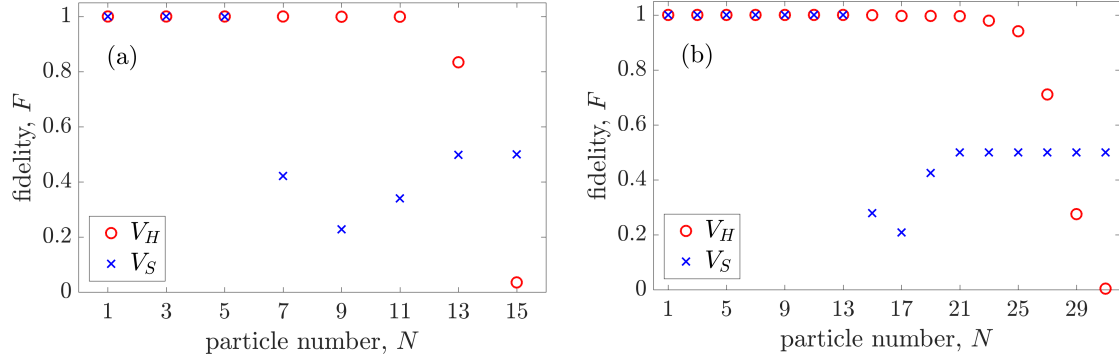


Figure 2.11: Final fidelities F of TG states of increasing particle number for the protocol shown in Figure 2.10(a) with $\Omega_f = \pi$ for V_H (red circle) and V_S (blue cross). Plot (a) shows the fidelity of the protocol with $\omega_f = 100$ and (b) with $\omega_f = 200$.

can construct the target states

$$\phi_{2l}^t(x) = \frac{1}{\sqrt{2}} (e^{i2\pi(l+1)x} + e^{-i2\pi l x}) = \sqrt{2} \cos[(2l+1)\pi x] e^{i\pi x}, \quad (2.36)$$

$$\phi_{2l+1}^t(x) = \frac{1}{\sqrt{2}} (e^{i2\pi(l+1)x} - e^{-i2\pi l x}) = i\sqrt{2} \sin[(2l+1)\pi x] e^{i\pi x}, \quad (2.37)$$

for $l = 0, 1, 2, \dots$. The states with total angular momentum π are similar to NOON states.

Any initial state $|\phi_l^i\rangle$ can be brought to the target state $|\phi_l^t\rangle$ with high fidelity with the proposed protocol, and the process also works for TG gases. In Figure 2.11(a), the harmonic potential fidelities are shown to remain high for $N \leq 11$ after which they decrease due to a finite maximum height of the potential enforced by periodic boundary conditions. The fidelities can be improved by increasing the maximum trapping frequency ω_f as we demonstrate in Figure 2.11(b) where the value of ω_f is doubled and the fidelities remain high until $N \leq 21$. When using the sinusoidal potential, the fidelity drops for smaller particle numbers compared to the harmonic potential (although it also increases with ω_f), due to the lower height V_S has compared to V_H .

2.4 Outlook

In this chapter, quantum optimal control and STA protocols were introduced to optimize quantum engineering tasks. I introduced a physical system to generate NOON states in a TG gas non-adiabatically with both methods, and they were shown to be highly effective. Such dynamical evolution techniques require time-dependent control parameters, such as rotation frequency or barrier height, and allowing for these dynamic operations has hitherto been a difficult task on GPU hardware. In the following chapter, we will discuss GPU hardware in-depth and also tackle this issue, along with several others noted in Chapter 1.

Chapter 3

General Purpose computing with Graphics Processing Units and the GPUE codebase

The Graphics Processing Unit (GPU) is a computing card that typically connects to the motherboard through a Peripheral Component Interconnect (PCI) slot. As the name implies, the GPU is designed to rapidly manipulate memory to create images or graphics that are sent to a display device, such as a monitor. Because individual pixels in images are independent of each other and modern computers require updating all pixels on the display device quickly, the GPU has been developed as a massively parallel computing device, capable of efficiently performing simple tasks (such as pixel generation or manipulation) rapidly by distributing the computation among many computing cores. This design methodology starkly contrasts the few, powerful cores on the Central Processing Unit (CPU), which is the default computing device on modern desktop systems. Due to this difference in hardware design, there are also several optimizations to consider when programming for massively parallel GPU devices, and several of these techniques will be covered in this chapter.

As GPU technology grew, other areas of computational science became increasingly

hungry for computing power, specifically in the area of scientific computing on High-Performance Computing (HPC) systems. Historically, HPC systems were often developed as large, distributed networks of computing nodes intended for CPU-based computation. As such, these systems facilitated the development of highly parallel and distributed numerical methods to perform scientific computation.

With new, parallel algorithms being developed for HPC systems and GPU technology advancing rapidly to perform more computation in parallel to satiate the consumer demands for high-quality videos and graphics for video games and other media, it became possible to use the GPU as a scientific computing device as well with a new technique called General Purpose computing on Graphics Processing Units (GPGPU). Modern HPC design often incorporates the GPU into each computing node, thereby increasing the throughput of the system, overall, and the fastest known supercomputer today (Summit, ORNL [1]), is almost entirely composed of GPU nodes with NVIDIA Tesla V100 cards (32 GB of available RAM), connected with NVlink and IBM's power architecture. In addition to the utility of GPGPU for scientific computing, GPU technology has also been rapidly developed for AI and related fields.

In this chapter, I will discuss the design methodology for the hardware and software related to GPGPU before proceeding to the development of GPUE, the GPU-based Gross-Pitaevskii Equation solver, which will be used for the remainder of this work. To start, I will first look into different types of parallelism and how these affect different hardware and software practices.

3.1 Types of parallelism

Older CPU architecture with a single core was designed as SISD (Single Instruction, Single Data) according to Flynn's taxonomy [116]. This simply means that no parallelism exists in the instructions or data. Even now, most code is naïvely written as if it is to be executed on SISD architecture, even though it is rare to find such a system in

modern environments. For capable devices, there are two separate methods to parallelize computation: *Task parallelism* and *data parallelism*.

Task parallelism allows programmers to split their computation along separate, non-interacting *tasks* or instructions, where each core performs its designated computation before moving on. On the other hand, data parallelism allows programmers to perform the same, repetitive task along a large data set by distributing worker threads across the data. Task parallelism is often better for dealing with a large number of specific actors, while data parallelism is often better for dealing with a large number of similar tasks on the same data, such as operations on a large matrix. If a computing architecture allows for multiple instructions, but only a single data stream, it is considered to be MISD (Multiple Instruction, Single Data) by Flynn’s taxonomy; meanwhile, if the architecture allows for multiple data streams with only a single instruction, it is considered to be SIMD (Single Instruction, Multiple Data). Most modern HPC systems are designed to be MIMD (Multiple Instruction, Multiple Data), and both task and data parallelism is exploited by developers; however, for GPU computation, data parallelism is often used more frequently.

In the realm of data parallelism, there is an extreme case where the data is *embarrassingly parallel*. Here, there could be a large matrix of data to manipulate, but no single element depends on any other. This means that when distributing computation along this matrix, we can simply assign tasks to each core without considering interactions with the rest of the data set. In this way, it is embarrassingly easy to parallelize, and hence the term *embarrassingly parallel*. As a note, element-wise matrix multiplications are embarrassingly parallel operations; however, FFTs are not [117]. As such, the SSFM is not overall embarrassingly parallel; however, because the FFTs are handled by the CuFFT library, programmers do not often need to consider task parallelism at all when developing SSFM code. Even so, understanding all the features of GPUE and its future directions requires a strong understanding of GPGPU, and this will be discussed in the following section.

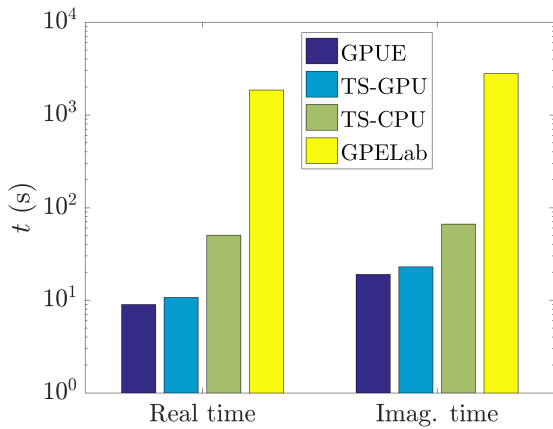


Figure 3.1: Comparison between GPUE (CUDA), Trotter-Suzuki on both GPU (CUDA) and CPU (C++), and GPElab (Matlab). Here, it is shown that GPUE is marginally faster than Trotter-Suzuki, but both GPU implementations are faster than the CPU-based variants. Both software packages are much faster than GPElab.

3.2 General purpose computing with graphics processing units

GPGPU programming is a relatively new development to the computing world and is generally much faster than CPU-based computation for tasks that can be easily parallelized in a SIMD-like fashion. Though benchmarks vary greatly depending programming languages, code quality, and intent of the software being benchmarked, our GPUE codebase is often 5 to 10 times faster than well-optimized C/C++ code and 100-200 times faster than Matlab code that is simulating the same system [118]. This is shown in Figure 3.1, where a comparison between GPUE, GPElab [119], and Trotter-Suzuki [120] are shown. These benchmarks are consistent with other GPGPU programs [121–123].

As it is possible to massively increase the performance of certain programs by using GPU hardware, it is important to discuss the differences between GPGPU and CPU-based computation, along with important optimizations for GPU computing that will be used throughout this work. For the remainder of this work, I will use the term *host* interchangeably with CPU and *device* with GPU.

3.2.1 Limitations of GPU computing

GPGPU and massively parallel computation are best suited for embarrassingly parallel systems and there are several problems that are poorly suited to parallelization. For example, any task that is inherently iterative (such as summation) or recursive (such as tree traversal) is not suited for parallel computation. Even so, there are methods to reframe these problems such that they are better optimized for massively parallel devices, and these will be covered when relevant to the development of GPUE.

In addition to these algorithmic limitations, GPU cards have several notable drawbacks in terms of available memory on individual cards, which is often much less than the amount available on the host. As such, when simulating a large system on the GPU, one often limits the resolution to what can fit onto GPU memory. In addition the data transfer between GPUs and between the GPU and CPU through the PCI port is a slow process. Until recently, these limited the size of the simulated wavefunction with GPUE to roughly 512³ on a single Tesla K80 card. Higher resolution simulations could be performed with more recent cards (such as the Tesla V100) or by using multiple cards; however, because it takes time to transfer data between GPUs, it is preferred to use a single card where possible. At this point, it is worthwhile to fully discuss GPU hardware and software ideologies, with particular focus on areas relevant to the development of GPUE. We will discuss important methods used in the development of GPUE to overcome shortcomings in GPGPU afterward in Section 3.3.

3.2.2 GPU hardware architecture

Even though several programming frameworks exist with the capability of running code on the GPU, most of these hide necessary optimizations from the user. As such, I have chosen to focus exclusively on programming frameworks that expose the hardware for software developers, such as CUDA, OpenCL, and Julia. Though the following discussion will primarily focus on CUDA, a brief discussion of OpenCL and Julia can be found in

Listing 3.1: An example of vector addition performed in C or C++ for a , b , and c , all of size n

```
1 for (int i = 0; i < n; ++i){  
2     c[i] = a[i] + b[i];  
3 }
```

Section 3.2.3, and example code for both languages can be found in the Appendix A. For the purposes of this discussion, I will cover only the GPU memory architecture of NVIDIA GPU devices as these are the most common computing devices for HPC systems.

This topic is easiest to describe by dividing it into two parts: an introduction to the software interface as defined by the CUDA API, followed by a discussion of the memory and thread hierarchy of GPU devices. Throughout these sections, I will discuss performance tips to ensure maximum GPU utilization, memory throughput, and instruction throughput.

Introduction to CUDA software interface

The CUDA parallel computing platform bares the hardware of the GPU to software developers. This means that important elements of this programming interface will appear in subsequent sections regarding hardware limitations and performance guidelines. Much of this discussion can be found in the *CUDA C Programming Guide* [6], while other sources will be cited as necessary. Full code for this discussion can be found in the Appendix A.

I will show a simple example where we would like to add two vectors such that $\mathbf{a} + \mathbf{b} = \mathbf{c}$. This can be done with a simple loop in C, shown in Listing 3.1. In this case, we take each element with a specified ID in \mathbf{a} and \mathbf{b} and add them to the appropriate ID \mathbf{c} . In some parallel programming models (OpenACC [124], OpenMP [125], GPUifyLoops.jl, and many others), parallelization of this method is possible by adding a macro to the start of the loop to specify that the operation is to be performed in parallel; however, this obscures GPU hardware for the user and does not always have the same performance guarantees [2]. As such, CUDA takes a slightly different approach by encouraging software developers

Listing 3.2: An example of a vector addition kernel in CUDA

```

1 --global__ void vecAdd(double *a, double *b, double *c){
2
3     // Global Thread ID
4     int id = threadIdx.x;
5
6     c[id] = a[id] + b[id];
7 }
```

to write *kernels*, specific to the computation at hand. An example CUDA kernel for vector addition is shown in Listing 3.2, which has a number of notable differences to the loop in C in Listing 3.2. This kernel is already remarkably different than an expected function on the CPU, and it is worth comparing Listings 3.1 and 3.2 in detail for a better understanding of GPU hardware.

The first peculiarity appears in line 1 with the `--global__` function specifier. This is a necessary element of all CUDA kernels that specifies where and when this kernel is capable of being called. A `--global__` kernel can be called by either host (with a standard CPU function) or the device (with a GPU kernel). A `--host__` kernel is exactly the same as a CPU function and can only be called by other CPU functions. Finally, a `--device__` kernel can only be called by other `--device__` or `--global__` kernels. As a note `--global__` kernels are incapable of returning vectors or other variables, and must instead mutate the variables, themselves. This is why the `--global__ vecAdd(...)` kernel does not return *c*, but instead assumes it is a pre-allocated variable.

Another peculiarity appears on line 6, where the addition, itself, occurs. Though there was a necessity for a loop in Listing 3.1, there does not seem to be one at all in Listing 3.2. This is because the GPU is performing this task in parallel and handling the parallelism behind the scenes on line 4 with the `int id = threadIdx.x` command. In this line, we are identifying which element of the array we are operating on with the CUDA-specific `threadIdx.x` variable.

Here, each *thread* is an individual instructional element acted on in parallel with

other threads in the same *block*, which is further subdivided into *grids*. All threads in the same block have a *shared memory* resource, while all three structures have access to *global memory*. In general, it is important to use shared memory when possible, as it has a lower latency than global memory, and this will be discussed further in subsequent sections. As a note, threads often work without feedback from other threads; moreover, it may be necessary to stop thread execution until all other threads have caught up. This can be done with the `__syncthreads()` function in CUDA.

Threads, blocks, and grids are all `dim3` variables with *x*, *y*, and *z* attributes. The way in which these threads and blocks are allocated are defined by the user before kernel execution. Often times, a thread number of 1024 is chosen, and the number of blocks is decided based on the size of the input array. If there are more elements to compute than threads in a block, one then need to use the `blockDim.x` and `blockIdx.x` variables to access the appropriate threads for computation. All threads are indexed as one-dimensional vectors even in a multidimensional space, as shown in Figure 3.2. Even though threads are rarely acted on sequentially, the thread ID has important ramifications that will be discussed further with other performance tips.

As another note, CUDA will execute code on unallocated memory if one does not tell it to otherwise. As such, if one had failed to set the number of threads in the block to the number of elements in the array in Listing 3.2, the kernel would exhibit undefined behavior. For this reason, one needs to take into account potential out-of-bounds computation. If one takes the above example of vector addition, assuming that the thread count is higher than can fit in one block and take into consideration potential out-of-bounds behavior, the kernel would instead look like Listing 3.3.

Finally, I need to discuss how software developers call these CUDA kernels in host code. This requires the developer to allocate space on the device for use in the CUDA kernel via a `cudaMalloc(...)` command. Often times, arrays on the host must also be established and transferred to the device with `cudaMemcpy(...)` functions as well. In addition, the kernel must be configured before running with `<<<grid, threads,...>>>`.

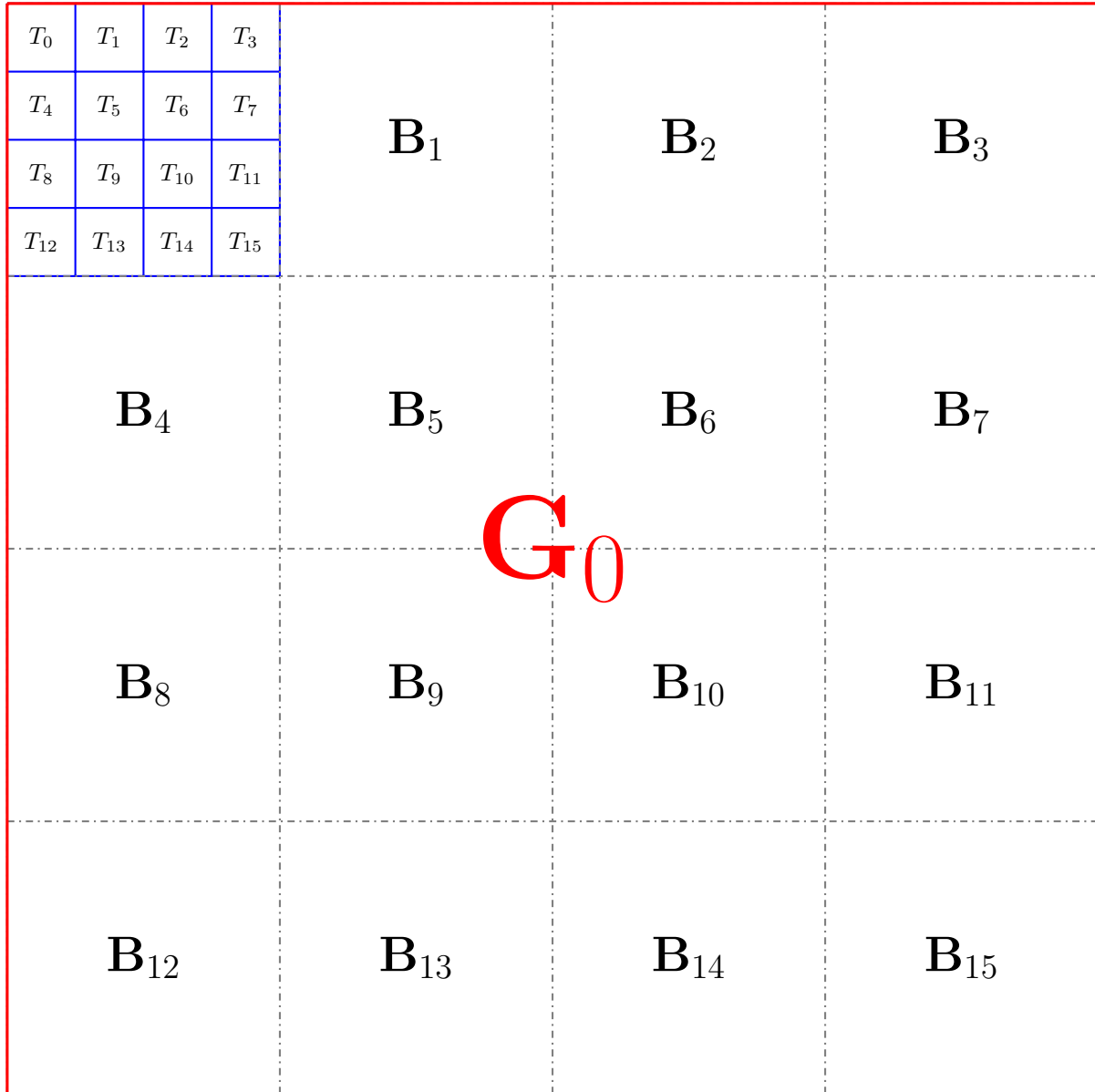


Figure 3.2: Each grid is subdivided into multiple blocks, which is further subdivided into threads for computation. Each thread has a specified ID, which acts as a one-dimensional array, even in a two or three-dimensional system. Here, all areas outlined in red have access to global memory, and any area outlined in blue has access to shared memory. [slight modification necessary to show 1D indexing!]

Listing 3.3: An example of a vector addition kernel in CUDA using blocks and threads, and ensuring no computation happens beyond the size of the array, n .

```
1 --global__ void vecAdd(double *a, double *b, double *c, int n){
2
3     // Global Thread ID
4     int id = blockDim.x * blockIdx.x + threadIdx.x;
5
6     if (id < n){
7         c[id] = a[id] + b[id];
8     }
9 }
```

When everything is considered, the host code might look like what is shown in Listing 3.4

All said, vector addition is often known as the “Hello World!” of GPU programming as it is the first application that shows the parallelism of GPU devices; however, even here, a distinction between users and developers can be seen. As more complex software is developed, it becomes more important to write software in such a way that users do not directly interface with CUDA code, and the full ramifications of this will be discussed in later in this chapter. In addition, this discussion highlights the important distinction between host and device code, including the concept of threads and blocks, shared memory, and the ability to transfer data from the host to the device, all of which are essential to understanding particular design decisions of GPUE. For now, I will continue this discussion by moving to GPU hardware, focusing on thread and memory hierarchy.

Discussion of GPU thread and memory hierarchy

Every time host code invokes a CUDA kernel call (as shown in Listing 3.4), the data is mapped to a scalable array of multiprocessors on GPU hardware. Multiple blocks might be distributed to the same multiprocessor, but blocks are always distributed contiguously. Each multiprocessor is designed to execute hundreds of threads in parallel by using a unique SIMT (Single Instruction, Multiple Threads) architecture, which is similar to SIMD and can be used as such for most cases; however, there are performance benefits to optimizing instruction-level parallelism at the thread level. Each multiprocessor dis-

Listing 3.4: An example of host code to run Listing 3.3.

```

1 int main(){
2
3     int n = 1024;
4
5     // Initializing host vectors
6     double *a, *b, *c;
7     a = (double*) malloc(sizeof(double)*n);
8     b = (double*) malloc(sizeof(double)*n);
9     c = (double*) malloc(sizeof(double)*n);
10
11    // Initializing all device vectors
12    double *d_a, *d_b, *d_c;
13
14    cudaMalloc(&d_a, sizeof(double)*n);
15    cudaMalloc(&d_b, sizeof(double)*n);
16    cudaMalloc(&d_c, sizeof(double)*n);
17
18    // Initializing a and b
19    for (size_t i = 0; i < n; ++i){
20        a[i] = i;
21        b[i] = i;
22        c[i] = 0;
23    }
24
25    cudaMemcpy(d_a, a, sizeof(double)*n, cudaMemcpyHostToDevice);
26    cudaMemcpy(d_b, b, sizeof(double)*n, cudaMemcpyHostToDevice);
27
28    dim3 threads, grid;
29
30    // threads are arbitrarily chosen
31    threads = {100, 1, 1};
32    grid = {(unsigned int)ceil((float)n/threads.x), 1, 1};
33    vecAdd<<<grid, threads>>>(d_a, d_b, d_c, n);
34
35    // Copying back to host
36    cudaMemcpy(c, d_c, sizeof(double)*n, cudaMemcpyDeviceToHost);
37
38    // Check to make sure everything works
39    for (size_t i = 0; i < n; ++i){
40        if (c[i] != a[i] + b[i]){
41            std::cout << "Yo. You failed. What a loser! Ha\n";
42            exit(1);
43        }
44    }
45
46    std::cout << "You passed the test, congratulations!\n";
47
48    free(a);
49    free(b);
50    free(c);
51
52    cudaFree(d_a);
53    cudaFree(d_b);
54    cudaFree(d_c);
55 }
```

tributes its parallel processes into *warps*, which are units of 32 threads that execute a single common operation at a time. Notably, the way a block is distributed into warps is always the same, so it is important to ensure that the input data is in powers of 32 to avoid wasting unnecessary computation. Outside of this, developers can often ignore SIMD behavior as long as they do not allow threads in a warp to have separate operations.

Understanding GPU memory architecture is essential to properly using GPU hardware, and as such, it is worth discussing in-detail. There are three forms of GPU memory that are useful for most applications of GPGPU for scientific computation: global memory, shared memory, and texture memory. As described above, global memory is shared between all grids, blocks, and threads and is considered to be the slowest memory bank. As such, whenever a warp accesses global memory, it tries to perform as few accessing operations as possible, which is made easier if the warp needs to access contiguous memory blocks. If the warp is required to access non-contiguous blocks, more accesses will be necessary and thus performance will take a relatively large hit. For this reason, it is important to make sure all data accesses are *coalesced*, which ensures that the warp will access consecutive elements as depicted in Figure 3.2.

For optimal memory throughput, shared memory is an essential tool to understand and use appropriately. As described, shared memory is on-chip memory that is shared between all threads in a block. The amount of shared memory available is hardware-dependent and configurable on kernel execution. In general, it is worthwhile to transfer data with a large number of accesses to shared memory for performance. Shared memory is split into several memory banks which can be accessed simultaneously. If two memory accesses are required of the same bank, there will be a conflict (known as a bank conflict) and the operation can no longer be performed in parallel. It is sometimes necessary to pad variables to prevent bank conflicts from occurring [126].

Of the three types of memory mentioned, texture memory is the least-often used and is primarily on the GPU for graphics computation and focuses on performance for two-dimensional structures. Texture memory has a relatively long write time, but is quick to

read. It is also faster than global memory for non-coalesced access patterns and therefore can be useful for certain tasks with slowly varying operators. In principle, this is the case for the momentum-space operator in the SSFM; however, because texture memory uses single-precision, it will not be used further in this work.

In addition to appropriate usage of memory on GPU architecture, it is also essential to minimize data transfers between the device and host and even between devices in multi-GPU setups. The data transfer between the host and device or between devices must send data through the PCI slot on the motherboard, which is a slow operation. For data transfer between devices, this transfer time can be slightly alleviated on Power architecture where NVlink technology can directly transfer data from device to device [127], but the data transfer between devices will still likely be the slowest part of the computation. In addition, CUDA-aware MPI for multi-GPU setups may add a huge burden on software development time [128, 129]. As such, developers often try to keep all of their computation on a single card, if possible, and several optimization strategies are used when multiple GPU cards are needed. These strategies will be covered on a case-by-case basis as they arise in this work.

As a final note, one optimization strategy for CUDA code that will not be discussed in-depth in this work is the maximization of instruction throughput. The simplest optimizations here involve increasing the number of instructions performed over a specified period by trading precision for speed and minimizing thread synchronization. Because we are performing high-precision superfluid simulations, we cannot perform a trade-off between precision and computational speed. When optimizing the instruction throughput for GPU devices, it is important to discuss conditionals, like `if` and `switch` statements. Here, programmers need to be careful not to accidentally cause the operation executed on threads in a warp to diverge.

3.2.3 Comparison between various languages for GPGPU computation

As one might expect, specialized programming languages are necessary to write code that compiles and runs on GPU architecture. There are several known libraries to extend modern programming languages such as Matlab, python, and C++ to GPU devices; however, we will limit this discussion to common programming methods that allow fine-grained control of GPU memory and could be used for the development of GPUE. We will briefly discuss the advantages and disadvantages of three competing languages considered here: CUDA, OpenCL, and Julia, and as a simple example, vector addition in these languages is shown in Appendix A.

CUDA

CUDA is a computing API provided by NVIDIA for interfacing with NVIDIA GPUs and is the industry standard for GPGPU programming. CUDA is primarily limited by the NVIDIA-specific hardware it runs on, and although NVIDIA currently produces the most common GPUs for GPGPU programming, AMD GPU devices are also available and often cheaper for a similar level of computational power. In addition, CUDA support has recently ceased for MacOS systems as NVIDIA cards are no longer bundled with current generation Mac computers, so CUDA code can only be used on Windows and Linux devices with NVIDIA cards. GPUE was written entirely in CUDA; however, due to the aforementioned limitations, there has been some consideration to re-writing the software in OpenCL or Julia.

OpenCL

Though CUDA is the industry-standard for GPGPU programming, OpenCL (Open Compute Language) is largely competitive in terms of performance and has the benefit of being compatible with both NVIDIA and AMD GPU devices. OpenCL is also completely open-

source and works as additional libraries to C or C++, which allows developers to compile OpenCL code with traditional compilers like `gcc` or `clang`. OpenCL has nearly similar structure to CUDA with slightly more verbose syntax, and thus provides all necessary functionality to develop and maintain scientific software. It should be mentioned that OpenCL also has the capability of running on a large variety of other computing architectures, such as FPGA and is a more general-purpose computing library than CUDA. In addition, compute kernels are compiled at run-time, meaning that users can potentially modify kernels without recompiling the code. This could be a huge boon for developers writing software for users who may need to quickly simulate a slightly modified system. Unfortunately, OpenCL has a rather cumbersome interface and has less support than CUDA for GPGPU. As such, it is not often used for scientific computing software.

In the end, although OpenCL does provide the ability to more easily construct dynamic kernels, the increased engineering time necessary to write software in OpenCL is often not worth the cost; however, further advances in compiler design for heterogeneous architecture has been made in the past few years [130], which has provided the unique opportunity for computer scientists to write maintainable and fast code in new languages, like Julia.

Julia

Julia is a new language to scientific computing, but boasts promising results. It claims to be as usable as Python, but as performant as C [131], which is a huge boon for maintainability of HPC software. In addition, Julia’s runtime is comparable to CUDA C for GPGPU computation and allows for similar hardware optimizations [4, 132], while also allowing users to edit the compiler implementations at will. This is an important point that will be discussed in more detail in Section 3.3.2.

In addition, because Julia is much easier to write than C for new programmers, GPU-based Julia code could allow developers to provide fast, efficient code with a usable interface for scientists and engineers. The trade off between performance and readability

in programming has been described as the “two-language” problem, as most scientific computing solutions to this point have required using two languages: a fast language for the back-end and a readable language for the user interface. Julia succeeds in bridging the gap between the languages, effectively solving the two-language problem and allowing scientists and engineers to write efficient code that is also compilable on the GPU. For these reasons, we have begun porting our CUDA code to Julia, as it will lead to simpler and more maintainable code in the future. This will be further discussed in the outlook of this work, Chapter 5.4. In Chapters 4 and 5, I will also introduce systems that could benefit from a Julia interface.

3.3 Introduction to the GPUE codebase for n -dimensional simulations of quantum systems on the GPU

At this point, all the motivation and background necessary has been provided to discuss GPUE, the GPU-based Gross-Pitaevskii Equation solver. This codebase will be used for all remaining simulations performed in this work and its development has also inspired the development of other computational libraries such as the `DistributedTranspose.jl` package, which will also be discussed in Section 3.4. Some additional information on prior development of GPUE can be found in other sources [133]. The GPUE codebase was published in the Journal of Open Source Software in 2018 [12] and was originally designed by Lee O’riordan with the capability of simulating large-scale Abrikosov lattices in superfluid BECs. My focus with GPUE development has been to simulate three-dimensional systems and optimize the software for dynamic studies on GPU hardware. For this section, I will first describe the FFT optimizations used in GPUE for three-dimensional simulations, followed by additional features necessary for dynamic simulations on GPU architecture.

3.3.1 FFT optimization

As mentioned in Chapter 1 and previously in this chapter, the SSFM is primarily limited by the complexity of the FFT operations. For a three dimensional simulation with gauge fields in the \hat{x} , \hat{y} , and \hat{z} directions, one set of global FFTs and three sets of one-dimensional FFTs must be performed. This is equivalent to two three-dimensional FFT operations, which become much undesirable when scaling to multiple GPU devices [117]. The CuFFT API provides an option for computing FFT's on separate batches of an array in GPU memory with the `cufftPlanMany(...)` command; however, if this command is repurposed for one-dimensional FFT operations, it does not provide the necessary functionality for FFTs across the \hat{y} or \hat{z} dimensions. With the CuFFT library, all FFT operations performed with this plan must follow an indexing pattern, such that

```
input[b*idist + x*istride]
output[b*odist + x*ostride]
```

where `b` is the batch ID, `x` is the element ID, `idist` and `odist` are the distances between batches for the input and output array, respectively, and `istride` and `ostride` are the strides between consecutive elements for computation with the input and output array, respectively. On the other hand, if data is transferred to the GPU, it is often re-indexed as a one-dimensional array, such that

```
array[i,j,k] = array[i + j*xDim + k*xDim*yDim]
```

where `i`, `j`, and `k` are iterable variables in the \hat{x} , \hat{y} , and \hat{z} directions, and `xDim`, `yDim`, and `zDim` are the dimensions in \hat{x} , \hat{y} , and \hat{z} , respectively. As such, it is not possible to use the `cufftPlanMany` functionality to perform one-dimensional FFTs in \hat{y} and \hat{z} ; however, if we increase the number of batches to `xDim*yDim*zDim`, set the distance between each stride to 1, and assume the stride between each element is `xDim*yDim`, we can recreate the functionality of the FFT in the \hat{z} direction. For the \hat{y} FFT operations, we need an external loop that iterates over each xy slab, performing `xDim` operations on each slab, and this greatly hampers performance.

[Will add image, if time permits.]

With this considered, only one-third of the necessary FFT operations are appropriately coalesced in memory for three dimensional simulations. Because FFTs are global operations that are best performed on contiguous chunks of memory, multi-GPU simulations with the SSFM are even less optimal. This has motivated the development of other packages to allow for memory coalescence with FFT operations, such as the distributed transpose, which will be described in Section 3.4. Even though the three-dimensional FFT operations are the biggest bottleneck in the GPUE codebase, it is not easy to avoid usage of the `cufftPlanMany(...)` operation while still using CUDA. This is why optimizations to GPUE FFT operations will be performed exclusively in GPUE.jl. Next, I will focus on another feature that was inhibited by the CUDA framework, but is nevertheless possible: methods to enable dynamic quantum engineering with expression trees.

3.3.2 Dynamic field input and output in GPUE with expression trees

As mentioned in Chapter 2, quantum engineering typically requires some form of time-dependent variables, along with evolution in real time. This means that the user must be able to input a time-dependent equation to GPUE, often for $V(t)$, $g(t)$, or $\mathbf{A}(t)$. Because GPUE is written in CUDA, there is no straightforward method for the user to input time-dependent fields without recompiling the source code and modifying CUDA kernels at will, which is unnecessarily cumbersome for the user. As such, we have provided a method for users to input the fields of their choosing as strings, which will be compiled into a set of operations to perform on the GPU through expression trees, which are similar to Abstract Syntax Trees (ASTs) in compiler design [134, 135].

An example of an expression tree can be seen in Figure 3.3. These are evaluated depth-first to follow the traditional order of operations. With this method, a user can type in a string, like " $V = m*\omega*\omega*x*x*t$ ", and this will be parsed into a set of

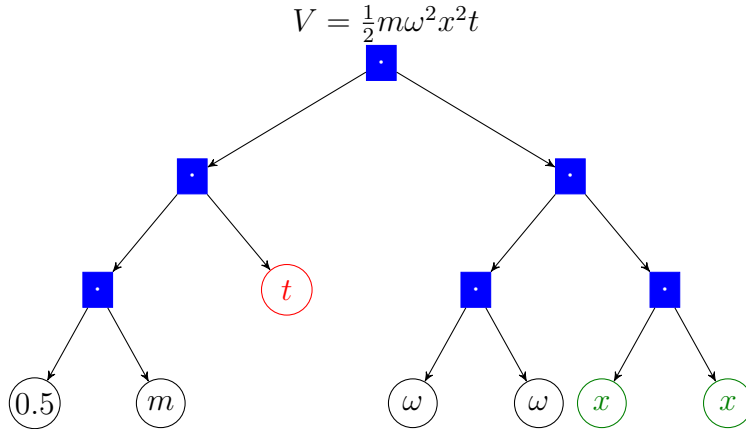


Figure 3.3: Example of expression tree for $V = \frac{1}{2}m\omega^2x^2t$. Blue, filled nodes are operations, leaf nodes are variables, time has been highlighted in red, and spatially-dependent variables are in green. This visualization was modified from a form provided by Xadisten during a Twitch livestream.

operations to be performed on-the-fly by the GPU. After parsing user-provided equations, certain leaf nodes are designated as either spatially or temporally dynamic. In the case of spatially dynamic variables (*x*, *y*, and *z*), values are taken from constituent vectors based on their `threadIdx.xyz` values, and for any equation that is dependent on *t*, a stored `time` variable is used. This operation necessitates the usage of a dictionary data structure to hold all variables on the host in some fashion, which inhibits host performance; however, because the bulk of the computation is performed on the GPU, this does not significantly impact GPUE performance, overall. On the GPU, each necessary variable can be stored in a shared memory buffer, and even though we are replacing the embarrassingly parallel element-wise matrix multiplications with these expression trees, the performance is not severely impacted; however, because parsing expression trees is an inherently iterative process, the longer the expression, the less optimal using this method is. Ultimately, more work could be done in the future to maximize instruction throughput with our implementation of GPU-accelerated expression trees.

Not only do expression trees allow for STA and quantum optimal control methods to be used with GPUE, but they also eliminate the need to store any operators in GPU memory, effectively increasing the available memory by a factor of 5 for each three-dimensional

simulation, as V , K , A_x , A_y , and A_z no longer need to be stored. This allows one to perform higher-resolution simulations and could allow for dynamical turbulence studies in the future; however, in order to scale beyond this limit, either multiple GPUs must be used or we must find some way to compress the wavefunction. This will be discussed further in Section 3.3.7. As a final note, this feature can be implemented easier in other GPU frameworks, such as OpenCL and Julia.

The implementation of expression trees in GPUE effectively decreases the memory footprint of our simulations and allows for dynamical studies on the GPU; however, dynamical studies also require a large amount of fileIO. Next, I will briefly discuss efforts to curtail the memory and storage footprint of GPUE simulations.

3.3.3 GPUE memory footprint

For the simulations to be shown in Chapter 4, roughly 50 TB were used of storage was used for relatively simple two-dimensional, dynamic simulations; however, at the time of that study, there was no compression performed on the output data. It is clear that some level of compression is necessary for three-dimensional, dynamic studies and that this level of compression is likely beyond what can be performed with higher-dimensional, compressed data formats like HDF5. For many vortex studies, it is possible to output only the vortex locations with proper vortex tracking methods, and these methods will be discussed in Section 3.3.4. Though HDF5 is now fully supported by GPUE, this section will focus on other methods that could allow for compressed SSFM simulations.

Initially, the Compressed Split-Step Fourier Method (CSSFM) [19] was considered to compress the size of our wavefunction. The CSSFM attempts to compress the wavefunction into a basis where it is sparse and then performs the SSFM on this compressed wavefunction with operators that have been transformed into the appropriate spaces. After CSSFM operation, the wavefunction is then reconstructed to an effectively higher resolution with compressed sensing [136], and in the original work by Bayindir [19], one-dimensional simulations of soliton dynamics were performed. This provided a considerable

improvement in both performance and memory usage for a wide range of potential resolutions. After attempting to use this method with GPUE, this method was found to be unsuitable for two and three-dimensional vortex simulations, because compressed sensing does not provide adequate compression for simulations of this nature.

In addition to this, an octree-based grid reduction scheme has been considered for two and three-dimensional simulations with the SSFM. This method creates an octree grid based on the Sobel filter of the density with the intent of creating a higher-resolution simulation at locations where the condensate density fluctuates. Further discussion of this system can be found in the Conclusion 5.4.

3.3.4 Vortex tracking and highlighting

In order to analyze the motion of vortices in a superfluid system, some form of vortex tracking must be implemented, and the current vortex tracking methods used in GPUE for two dimensions can be found in prior work [133] or the GPUE documentation [137]. It is important to describe two dimensional vortex-tracking first before continuing to three-dimensional vortex analysis, which is a much more complicated process.

At a first glance, one might assume that vortices are located at areas of low density in a superfluid system; however, this is not always the case. Because a condensate simulated with GPUE often inhomogeneously trapped and does not necessarily extend to the edges of the simulated domain, there will be large areas of zero density outside our condensate. In addition, sound waves and other perturbations with minimal density can occur. As such, locations of low density should only be used as educated guesses as to where actual vortices are located, but should not be used as the final predictor.

Instead, the phase can be used to uniquely identify vortex locations, as shown in Figure 4.1. In the highlighted region, all elements sum to a value of 2π . In this way, vortex tracking essentially transforms into the task of locating all the 2π phase windings in the simulated domain via minimization routines where we attempt to find any four grid elements whose sum is 2π . This process also necessitates a mask for regions outside of the

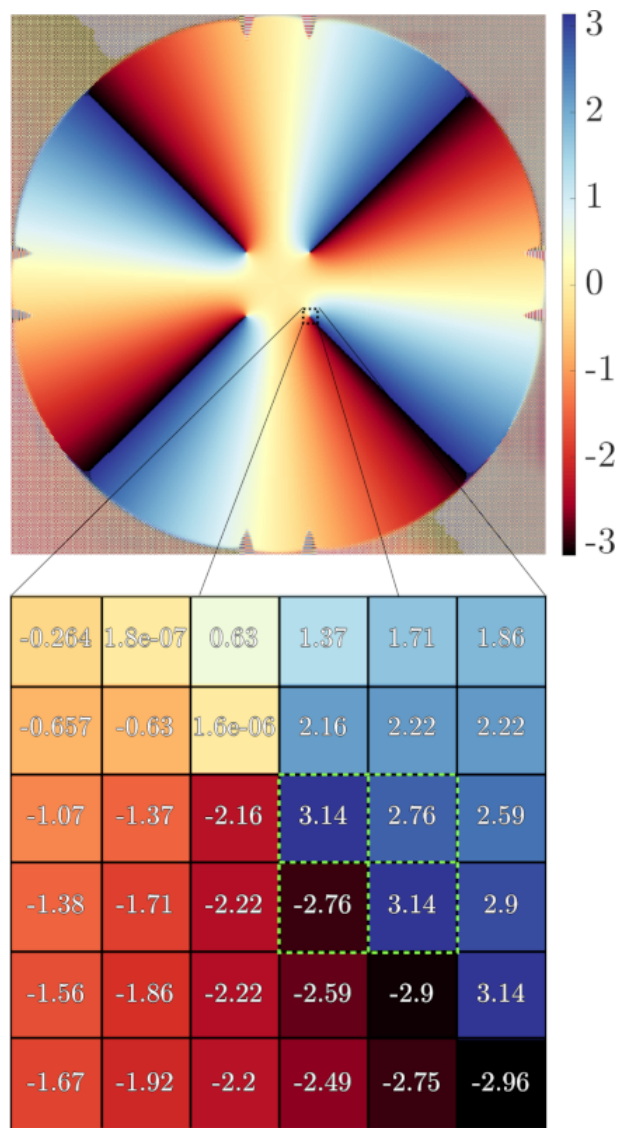


Figure 3.4: An example phase plot of a condensate with four vortices. The inset shows the values of the grid around each vortex location and highlights where the sum is 2π for vortex tracking.

BEC domain, as these regions create spurious 2π phase windings because of the density is roughly zero outside of the condensate region. Further discussion on how to refine this position can be found in previous work [133, 137].

In three dimensions, vortices are no longer confined to a plane and can extend in any direction, so long as the vortex lines either end at the end of the superfluid or re-connect in the form of vortex rings or more complicated vortex structures. Tracking three-dimensional vortices is a much more difficult problem which does not have many solutions in superfluid simulations where the superfluid does not fill the simulation domain. The current state-of-the-art solution has been proposed by Villois *et al* [138], and requires finding density dips in the superfluid as initial guesses as to where a vortices might exist. From there, a vorticity plane is determined and the entire vortex is discovered by moving perpendicularly to the vorticity plane at each gridpoint. This is a tedious and time-consuming process that does not lend itself well to GPGPU computation without communication between the host and device. Because some systems simulated with GPUE do not fill the contents of our simulation domain, the proposed method will not work without some modification. We could still use the method if we have some understanding of the trapping geometry to mask out regions beyond the condensate density; however, as we discussed in Chapter 1, this is not always the case with gauge fields. As such, we are currently seeking a more computationally efficient method for tracking vortices in three dimensions, and some thoughts on how this could be done can be found in the Conclusion 5.4.

For these reasons, instead of focusing on vortex *tracking*, I have instead implemented a simple vortex *highlighting* scheme for three dimensions. This can be done with a Sobel filter on the condensate density, and can easily create crisp visualizations like those found in the computer graphics literature [139]. An example of a vortex highlighted wavefunction density, along with an isosurface of both the density and the highlighted density can be seen in Figure 3.5. In this figure, we show that the density after being Sobel filtered can be more easily used to isolate vortex structures without the background BEC. Though

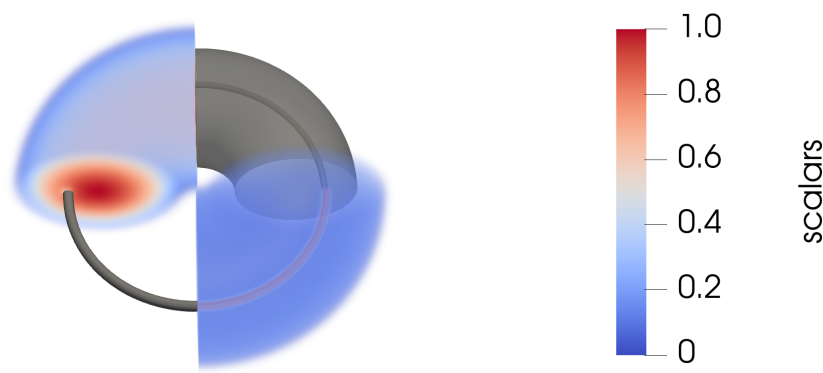


Figure 3.5: An example of vortex highlighting with a Sobel filter. The upper left quadrant is the superfluid density with no modifications and the upper right quadrant is an isosurface of the density with an opacity of 0.6. Note here that if there is no opacity set, it is not possible to see the vortex because it is obscured by the outside boundary of the BEC. The lower right quadrant is the superfluid density after Sobel filtering and the bottom left quadrant is an isosurface on the Sobel filtered density. Here, we can easily create isosurfaces of vortices that would be occluded when using the density, alone. The scale varies depending on whether it is coloring the normalized wavefunction density or the filtered density.

it would be possible to use further edge detection methods, such as the Canny edge detector [140], this would add a significant computational overhead and thus was not implemented in the current work. The problem of efficiently tracking vortex skeletons in three-dimensions is a difficult problem that requires further study; however, vortex highlighting is enough for most three dimensional vortex simulations. In Chapter 5, we show an example simulation where vortex highlighting has been used to determine the vortex isosurfaces.

3.3.5 Energy calculation for superfluid simulations

As discussed in Chapter 1, energy calculations can play an essential role in SSFM simulations and can be used to help understand vortex dynamics in certain simulations. More importantly, energy calculations lie at the heart of convergence criteria for imaginary time propagation. Essentially, in order to avoid unnecessary computation, many SSFM implementations will cease simulating the system in imaginary time when the change in energy every timestep drops below a certain threshold value. Though this option is available in GPUE, it is not a native feature for at least three important reasons:

1. Certain systems, such as large vortex lattices with high rotation, have a seemingly degenerate ground state with different vortex configurations [58, 59, 133].
2. GPUE is often run on a computing cluster where the maximum simulation time is set before-hand. For this, the user must be able to estimate the duration of their simulation, and this is not straightforward if imaginary-time propagation finishes at an unknown time.
3. The energy calculation is memory and operation-intensive and requires at least one additional object of the size of the wavefunction to be created and stored on GPU memory.

The first and second of these are somewhat self-explanatory, but the third requires further

elucidation.

Energy calculations in GPUE are essentially composed of the following operation,

$$E = \langle \Psi | \hat{\mathcal{H}} | \Psi \rangle \quad (3.1)$$

The first problem with this operation is that it requires a summation for the final energy value, and as discussed, this is a poorly-suited problem for GPU hardware. Even though a robust implementation of parallel reduction has been implemented in GPUE, this is still a slow process. The next problem comes from the nature of the Hamiltonian, itself. As described in Chapter 1, the Hamiltonian is essentially composed of three separate components for vortex simulations:

$$\hat{\mathcal{H}}_v = V_0 + g|\Psi|^2 + \frac{m\mathbf{A}^2}{2} \quad (3.2)$$

$$\hat{\mathcal{H}}_p = \frac{p^2}{2m} \quad (3.3)$$

$$\hat{\mathcal{H}}_{pv} = p\mathbf{A} \quad (3.4)$$

where $\hat{\mathcal{H}}_v$, $\hat{\mathcal{H}}_p$, and $\hat{\mathcal{H}}_{pv}$ are the Hamiltonians in position-space, momentum-space, and mixed-space, respectively. These operations can be considered with expression trees; however, for three-dimensional simulations they still require either a set of forward and inverse FFT's or a derivative function with fixed stride along with the parallel reduction operation. This ultimately amounts to the same number of operations required for a single step of imaginary-time evolution; however, because the simulated wavefunction cannot be influenced by the energy calculation, the operation requires at least one additional allocation of a wavefunction-sized array. Due to the computational time required for each energy calculation, users are requested to input the set of timesteps they would like to compute the energy for before-hand. In addition, at certain points, it is impossible to run GPUE with the energy calculation, simply because there is not enough memory available

on the device.

Though finding the energy of the wavefunction is a useful feature for certain simulations, it should not be used regularly for memory-limited tasks or tasks that should be performed quickly. Even so, for most applications of GPUE on HPC environments, there should be no problem running the energy-calculation alongside the simulation, itself.

3.3.6 Similar software packages

[Discuss other software here, like XMDS]

3.3.7 Future direction and multi-GPU development

At this point, I would consider GPUE to be close to feature-complete. It is capable of simulating a wide-variety of quantum systems and can even perform dynamic quantum engineering studies with minimal fileIO. Though more work can be done to maximize instruction throughput, this will not significantly improve the performance of the code because it relies heavily on double-precision.

The next logical step for GPUE development is scaling to larger simulations. This means that we either need to increase the number of GPUs used for the simulation or decrease the size of the wavefunction, itself. Though the CSSFM method [19] should allow for the latter, it was ultimately found unsuitable for general-purpose simulations. As such, the next logical progression is to scale GPUE to multiple GPU devices; however, as I hope to have impressed by now, this is not a trivial task. Even though the CuFFT library can support multiple GPU devices, this comes with a huge performance penalty, especially for the `cufftPlanMany(...)` functionality. To scale to multiple GPU devices efficiently, while still using the SSFM, a large-scale, in-place, multi-GPU transpose is required to ensure proper memory coalescence for FFT routines, which eliminated the need for `cufftPlanMany(...)` in GPUE.

For this reason, development of GPUE.jl has begun, which has similar performance

to GPUE, but is currently lacking the expression tree functionality. Once GPUE.jl is at feature parity with GPUE, it will become the primary software package for future development. Ultimately, the Julia language allows for the development of GPUE in a much more maintainable fashion, and also allows for the accessing of GPU hardware in a more convenient way. In addition to this, Julia allows for more modular development of certain features, such as the DistributedTranspose.jl package that should allow for multi-GPU transposes when fully developed.

3.4 DistributedTranspose.jl

At its heart, the two-dimensional transpose is a straightforward operation consisting of a swapping of all row and column elements. Unsurprisingly, this is a difficult task to ensure memory coalescence, but it is possible to perform a two-dimensional transpose at the same performance as a simple copy, so long as the operation is out-of-place in memory, the operation is performed on shared memory tiles, and bank conflicts are avoided by padding the data structure being transposed [126] The transpose becomes even more difficult to create when we wish to transpose large three-dimensional matrices, potentially spanning across multiple GPU devices, while also ensuring the operation is in-place in memory.

In principle, there are three types of three-dimensional transposes:

Simple Copy A benchmark for other transpositions,

$$A_{xyz} \rightarrow A_{xyz} \tag{3.5}$$

Involution A transpose where a two-dimensional transpose is operated on a three-

dimensional data structure,

$$A_{xyz} \rightarrow A_{xzy} \quad (3.6)$$

$$A_{xyz} \rightarrow A_{xyz} \quad (3.7)$$

$$A_{xyz} \rightarrow A_{zyx} \quad (3.8)$$

Rotation A fully three-dimensional transpose,

$$A_{xyz} \rightarrow A_{yzx} \quad (3.9)$$

$$A_{xyz} \rightarrow A_{zxy} \quad (3.10)$$

It has been shown that for out-of-place transpositions, it is possible to perform all of these operations as efficiently as a simple copy; however, in-place rotational transposes can only attain 60-70% of the performance based on currently known methods [141?]. In addition, distributed transposes of this nature have not been discussed except for on an out-of-place array [142].

At its current state, the `DistributedTranspose.jl` package is able to do out-of-place, distributed transposes; however, when feature-complete, it should allow for the implementation of new distributed methods for such computation. It should be mentioned that this package has potential to be used by many other software packages that require using spectral methods on multiple GPU devices. Often, HPC engineers prefer finite-element or difference methods when computing large-scale fluid flow because these methods scale much better across distributed systems; however, with an appropriate distributed transpose methods, it might be more optimal to perform spectral simulations in certain regimes over other methods.

3.5 Outlook

In this chapter, I presented the fundamentals of GPGPU, along with the GPUE codebase for simulating superfluid vortex systems. It is important to note that GPU architecture is best at embarrassingly parallel tasks, and as such, the SSFM is severely limited by its FFT routines; however, because one-dimensional FFT operations on GPU devices are often faster for larger matrix sizes than their CPU-based counter-parts [9], it seems that the SSFM is better suited for GPU architecture. In this chapter, I also discussed important optimizations done in GPUE to ensure proper utilization of GPU architecture for dynamic simulations of dynamic superfluid vortex simulations in two and three dimensions, including expression trees, FFT optimizations, vortex tracking and highlighting, methods used to decrease GPUE's storage footprint, and GPUE.jl. Finally, I discussed the future development of the DistributedTranspose.jl package, which should allow for large-scale spectral methods to be suitable for distributed GPU systems, often found in HPC environments.

For Chapters 4 and 5, I will discuss two physical examples that were enabled by the GPUE codebase, also highlighting future physical directions and re-enforcing the future directions discussed here.

Chapter 4

Chaotic vortex analysis of two-dimensional superfluid systems for few-vortex systems

Here, we show an application of the GPUE codebase by simulating a two-dimensional chaotic system with few vortices. In addition, this chapter intends to display the dependence of post-processing metrics such as the Lyapunov exponent to dynamical studies of superfluid systems.

Chaotic evolution is typically identified by a significant divergence in trajectory based on a small change in the initial conditions [143], and it is possible to find such an environment in turbulent flow [144, 145]. For classically turbulent flow, the degree of chaos depends on the Reynolds number [146]; however, the nature of quantum chaos for superfluid flow is still an active area of research [76]. Because superfluid vortices have well defined strength and quantized winding numbers, they can be considered less complex when compared to classical vortices where circulation is continuous, there has also been significant interest in the differences between classical and quantum turbulence [147–150]. In spite of the differences between the fluid models, vortex dynamics in superfluid systems are remarkably similar to classical point-vortex models and key features of classical tur-

bulence, such as the Kolmogorov spectrum have been shown to exist for large, turbulent, quantum systems [151–154].

It is known that it is not possible to excite chaotic behavior in large vortex lattices, as these systems have been proven to be stable to external perturbations [133]. For this reason, it is interesting to probe classical chaos with a small number of vortices, such that quantum turbulent effects are not excited. Chaotic, few-vortex systems have been studied previously by Aref and Pumphrey [155–157], who showed that chaos can be excited in systems with as few as four vortices in an infinite plane [155]. Unlike classical chaos, the onset of chaos in quantum systems seems to appear with fewer vortices present, and few-vortex systems have been explored experimentally for two, three, and four vortices in harmonically trapped BECs [150]. When analyzed with a reduced Hamiltonian approach, harmonically trapped BECs seem to exhibit chaotic effects with as few as three vortices, two co-rotating vortices and an anti-vortex rotating in the other direction [148, 149].

Experimentally, it is now possible to detect vortex circulation [158] and image vortices *in-situ* [159]. It is also possible to probe vortex dynamics at different times within a single experiment [160, 161]. Because quantum vortices are simple and BECs are highly controllable experimental systems in two-dimensions, there has been significant interest in two-dimensional quantum turbulent systems as well [75, 162]. Additional effects, such as the Kármán vortex street [163] and Onsager vortex clusters [164, 165] have already been shown to exist experimentally.

Because chaotic events require very small changes in the initial conditions of the system, it is important to create a system with well-controlled initial conditions. For this, I will start with a small vortex lattice of four vortices, and then create a defect in this lattice using phase imprinting, as described in Chapter 1. This process will controllably induce chaotic vortex dynamics in an experimentally feasible way. We also show that the chaotic dynamics are enhanced by the close approach of vortices. By using phase imprinting in this way on a larger number of vortices in a vortex lattice, it might be possible to induce chaotic events there as well, which might enable studying a set of vortex trajectories that

is chaotic at specific points, but stable overall.

4.1 Model

The physics simulated in this Chapter is purely two-dimensional, so it is appropriate to begin this section with a disclaimer about the dimensionality of the system I will be simulating. In principle, all real-world physics is three-dimensional, but just as a one-dimensional cigar-shaped BEC can be created, a pancake-like geometry can also be constructed by increasing the trapping frequency in the \hat{z} (perpendicular) direction with respect to the \hat{x} and \hat{y} (transverse) directions. With this geometry, one can assume that the condensate is in the ground state along the \hat{z} dimension so long as there are no energy excitations in the \hat{z} direction that compare with the chemical potential. One can then rewrite the wavefunction as $\Psi(\mathbf{r}, t) = \Psi(x, y, t)\phi(z)$, where $\Psi(x, y, t)$ is the wavefunction in the transverse plane and $\phi(z) = (m\omega_z/(\pi\hbar))\exp(z^2m\omega_z/(2\hbar))$ is the ground state along the \hat{z} dimension. By integrating over \hat{z} , the interaction strength is modified for a two-dimensional condensate to be

$$g_{2D} = g\sqrt{\frac{m\omega_z}{2\pi\hbar}}. \quad (4.1)$$

For the GPUE codebase, $g_{2D} = 6.8 \times 10^{-40}$. With these changes, one can simulate two-dimensional settings with the GPUE codebase [13, 58, 59, 133]. This chapter will apply several of the techniques mentioned in Chapters 1 and 3 to a rotating two-dimensional BEC system for a small number of vortices and was published in *Phys. Rev. Fluids* 4(5):054701, 2019 [13].

For this study, a condensate with $N = 10^6$ ^{87}Rb atoms and an s-wave scattering length of $a_s = 4.76 \times 10^{-9}\text{m}$ in a pancake geometry with typical trapping frequencies of $(\omega_\perp, \omega_z) = (2\pi, 32\pi)\text{Hz}$ will be considered. Here, the effective two-dimensional interaction strength is $g = 6.8 \times 10^{-40} \text{ m}^4\text{kg/s}^2$. These simulations were performed on a grid of $2^{10} \times 2^{10}$ points and covering an extent of $700\mu\text{m} \times 700\mu\text{m}$

First, ground-state evolution was performed with a low rotation frequency of $\Omega = 0.3 \times$

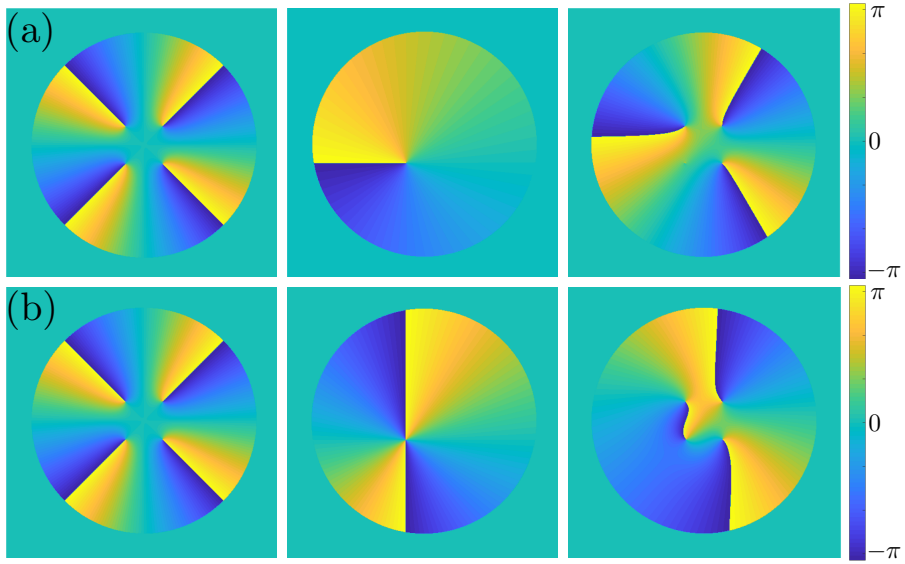


Figure 4.1: Phase distribution of the initial four co-rotating vortex system is shown at the left. In the center is the applied phase mask of -2π for (a) and -4π for (b), and the resulting phase distribution is shown on the right. By applying a -2π phase winding, a vortex is erased from the system, and by applying a -4π phase winding, the vortex is flipped, creating an anti-vortex.

2π Hz via GPUE [12]. Although large rotational frequencies will create a triangular lattice, for smaller frequencies, other configurations are known [166], and I will focus on the regime where the ground state is composed of four vortices in a square configuration [167]. Once this configuration is achieved, a vortex is manipulated via phase imprinting, such that three co-rotating vortices and one anti-vortex exist in the system. Examples of phase imprinting on this system can be seen in Figure 4.1, where the top row shows a simple vortex annihilation and the bottom row shows a vortex flip.

4.2 Regular and irregular vortex dynamics

It is known that a lattice of vortices with the same direction of rotation will exhibit regular dynamics [60], and in Figure 4.2(a), we confirm this for this system. In this figure, we show a histogram of the vortex trajectories over 20 seconds of evolution when removing and then re-imprinting a vortex of the same rotational direction at the same

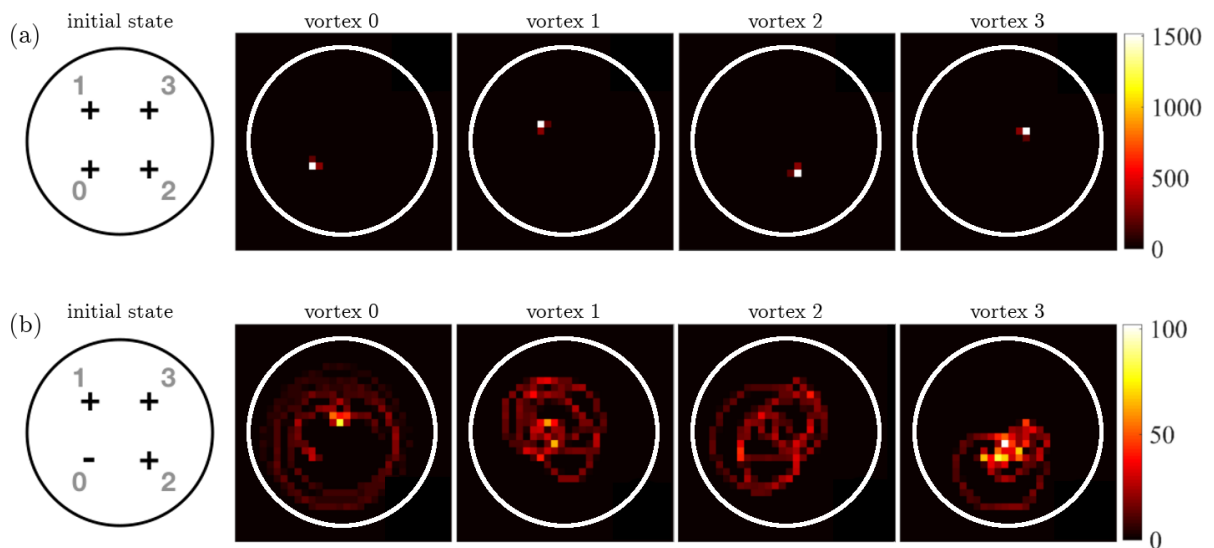


Figure 4.2: Histograms of the positions of each vortex in the transversal plane for 20 seconds in the co-rotating frame. The lower left vortex has been annihilated and reimprinted with (a) the same and (b) the opposite direction of rotation, exactly on the location of the previous vortex. The area of each plot is $400\mu(m) \times 400\mu(m)$, and the white circles correspond to iso-lines at 40% of the maximum density to highlight the extent of the vortex motion. In (a), if all four vortices are co-rotating, regular trajectories appear, but in (b), flipping the rotation direction of a single vortex creates disordered trajectories.

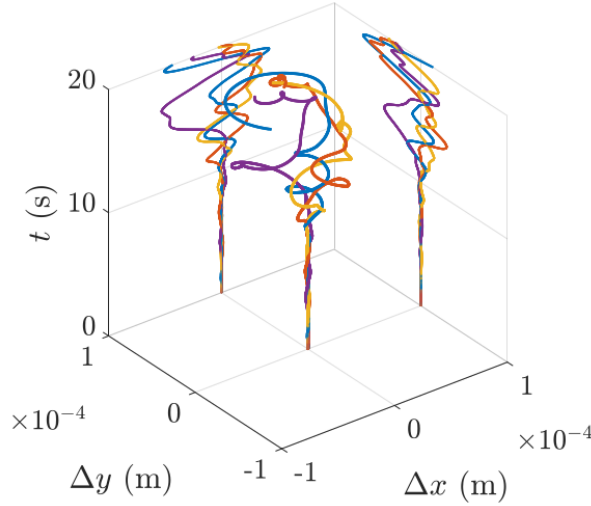


Figure 4.3: Evolution of the difference in trajectories $\Delta\mathbf{r}_i = \mathbf{r}_i - \mathbf{r}'_i$ with \mathbf{r} corresponding to the position of the i th vortex from the center of the condensate and $i \in \{0, 1, 2, 3\}$ labelling each individual vortex for the four-vortex system as shown in Fig. 4.2. A small change in the initial position of the anti-vortex arises from a phase-imprint at (x_0, y_0) and $(x_0 - \xi/3, y_0)$ where (x_0, y_0) denotes the pre-existing co-rotating vortex core position. The curves show that even though the onset of disorder is immediate, a strong divergence of trajectories is observed at about $t \approx 10$ s (see projections onto the x - t and y - t planes). The difference in trajectory of the anti-vortex, $\Delta\mathbf{r}_0$, is shown in blue, while yellow, orange, and purple lines depict the three co-rotating vortices.

location. Even though a small residual movement appears, potentially due to phonon excitations that were not fully removed from the imaginary time evolution, the vortices remain stationary. In Figure 4.2(b), we also show that if the re-imprinted rotation is of the opposite direction, the vortex dynamics become more disordered, with vortices traversing a larger width of the condensate. It is worth mentioning that similar histograms can be constructed experimentally with available imaging techniques [159, 160].

Even though the introduction of the anti-vortex creates disordered trajectories, it could be entirely possible that these trajectories are still stable. To uniquely identify chaotic behavior, one needs to show that any small perturbation in the vortex location will also provide a significantly different trajectory. To check this, I compare two sets of vortex trajectories with slightly different shifts in the initial position of the anti-vortex, \mathbf{r}_0 and \mathbf{r}'_0 , where $\mathbf{r}_0 - \mathbf{r}'_0 = \xi/3$ and ξ is the healing length. In Figure 4.3, I show the

differences in trajectories, defined as $\Delta\mathbf{r}_i(t) = \mathbf{r}_i(t) - \mathbf{r}'_i(t)$, where \mathbf{r}_i refers to the position of the i th vortex from the center of the condensate and $i \in \{1, 2, 3\}$ corresponds to the vortex number. The unique ID for each vortex is shown in Figure 4.2. Here, one sees that the difference in trajectories is initially small, but diverges significantly at around $t \approx 10$ seconds, which is a strong indication of chaotic behavior.

After closely inspecting the vortex dynamics (shown in the supplementary movie [168]), one sees that this strong divergence in vortex trajectories seems to be accelerated when all four vortices come in close proximity. Because the velocity fields of each vortex decays as $1/\mathbf{r}$, where \mathbf{r} is the distance from the vortex's core, the vortices experience stronger velocity fields when they are closer; therefore, the point of minimal separation can be seen as a highly nonlinear multi-vortex scattering event that accelerates the divergence shown in Figure 4.3. In Figure 4.4 we study this further by showing snapshots of the condensate density before ($t = 6$ s), at ($t = 10$ s), and after ($t = 15$ s) the scattering event in (a) and (b) for the non-shifted and shifted initial anti-vortex locations. The differences between position of each vortex and the anti-vortex is also shown (c) for the case where the anti-vortex is shifted by $\xi/3$. Here, there is a clear minimum at $t \approx 10$ seconds, which is the same time at which the trajectories begin to diverge in Figure 4.3. In order to characterize this divergence in trajectory, one must analyze the vortex dynamics in more detail and calculate the Lyapunov exponent.

4.3 Characterizing chaotic vortex dynamics

To characterize the degree of chaos for the shown vortex dynamics, I have chosen to use Lyapunov exponents, which give the rates of divergence for nearby orbits in phase space [169]. With this measure, one can track two trajectories in phase space and assume that the divergence between the two trajectories will either exponentially converge or

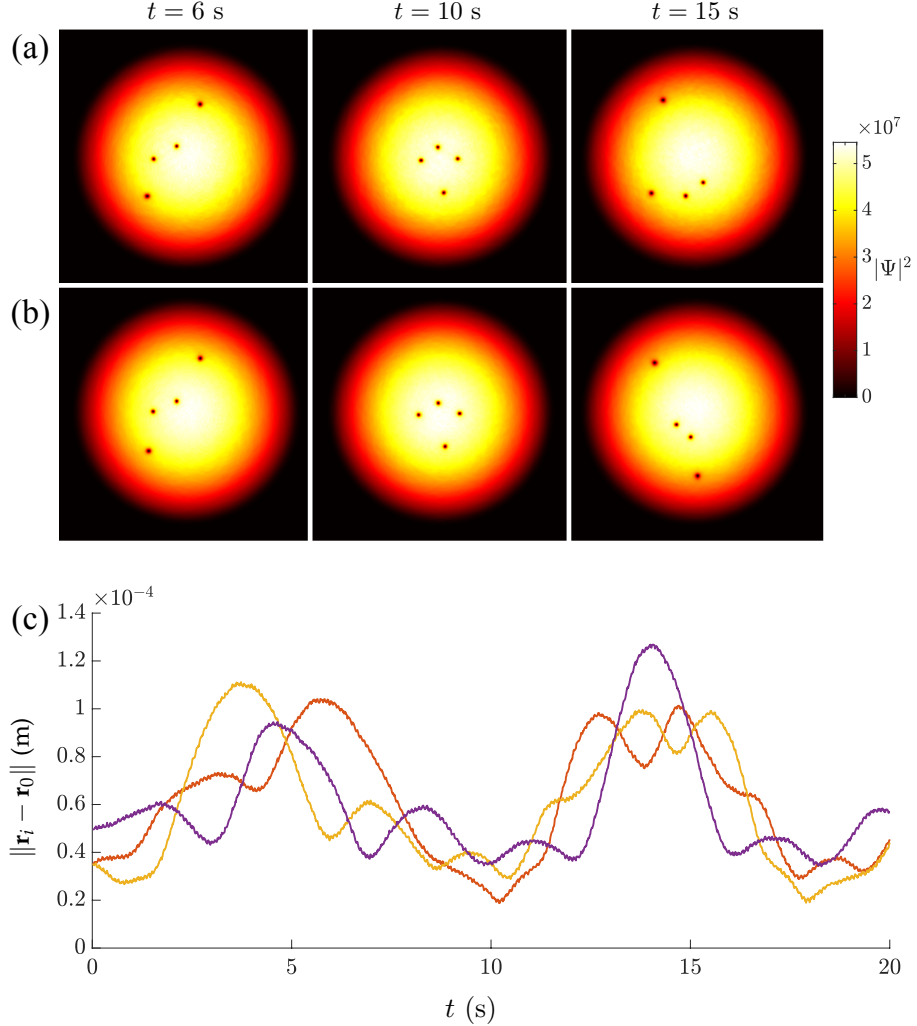


Figure 4.4: Density plots of condensate for (a) $\Delta x = 0$ and (b) $\Delta x = \xi/3$ at times $t = \{6, 10, 15\}$ s. The densities before the scattering event differ only on small scales (see $t = 6$ s), whereas for times after the event, large deviations are visible (see $t = 15$ s). At $t = 10$ seconds the vortices make their closest approach. The area plotted is $500\mu\text{m} \times 500\mu\text{m}$. (c) Distances between the vortices at positions \mathbf{r}_i with \mathbf{r} corresponding to the position of the i th vortex from the center of the condensate and $i \in \{1, 2, 3\}$ corresponding to the vortex number as shown in Fig. 4.2 and anti-vortex at \mathbf{r}_0 for $\Delta x = 0$. A minimum around $t = 10$ seconds is clearly visible.

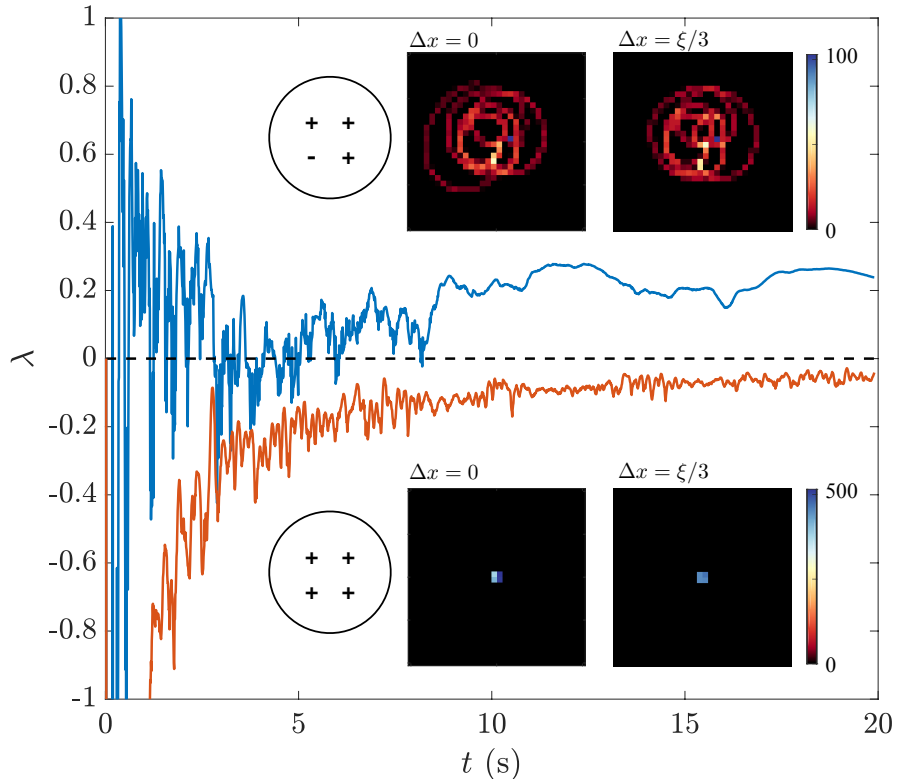


Figure 4.5: The insets show the histograms of the COM trajectories calculated over 20 seconds of evolution for the system of four vortices when the position of a single vortex has been shifted by $\Delta x = 0\xi$ and $\Delta x = \xi/3$. The upper two panels depict the corresponding trajectories after the direction of rotation of a single vortex has been reversed, whereas the lower row displays the trajectories for the case where all vortices co-rotate. The main curve plots the corresponding Lyapunov exponents, calculated from the shown COM trajectories. The negative Lyapunov exponents (orange) indicate that shifting the vortex about the initial position still ensures the stability of vortex trajectories. Reversing the direction of circulation of a single vortex (blue) however leads to fluctuations about zero, eventually leading to a fully positive exponent.

diverge, which can be modeled with

$$|\delta\mathbf{Z}(t)| \approx e^{\lambda t} |\delta\mathbf{Z}_0|. \quad (4.2)$$

Here, $\delta\mathbf{Z}_0$ is the initial separation between the trajectories and λ is a quantity known as the Lyapunov exponent. If the exponent is negative, this means that the trajectories tend to converge, but if it is positive, the trajectories will diverge, thus indicating chaotic motion. The rate of divergence is determined by the value of the exponent.

For this simulation, I model the trajectories in four-dimensional phase-space with $\mathbf{P}(t) = (x(t), y(t), v_x(t), v_y(t))$ and $\mathbf{P}'(t) = (x'(t), y'(t), v'_x(t), v'_y(t))$. The separation is then defined to be $\delta\mathbf{P}(t) = (\delta x(t), \delta y(t), \delta v_x(t), \delta v_y(t))$ where $\delta x(t) = x(t) - x'(t)$, etc. The exponent can then be calculated as

$$\lambda = \lim_{t \rightarrow \infty} \frac{1}{t} \ln \frac{||\delta\mathbf{P}(t)||}{||\delta\mathbf{P}(0)||} \quad (4.3)$$

where $||\cdot||$ denotes the Euclidean norm.

In this case, each vortex is tracked with the methods outlined in Chapter 3, and use both the position and velocity of the vortex. To determine whether the total system is chaotic, beyond its constituent vortices, I use a center of mass (COM) variable, defined as $\mathbf{R}_M = \frac{1}{n+1} \sum_{i=0}^n r_i$, where $n+1$ is the number of vortices. Similarly, the center of velocity is defined as $\mathbf{v}_M = \frac{1}{n+1} \sum_{i=0}^n v_i$. These values are then used with Equation (4.3), and the results are shown in Figure 4.5. The insets in Figure 4.5 show the histograms of the COM trajectories for the case where an anti-vortex is and is not present.

As expected, the exponent spectrum calculated in Figure 4.5 shows that the regular, co-rotating system always shows a negative (converging) exponential value, but the system with the anti-vortex is largely positive (diverging). During the scattering event shown in Figures 4.4 and 4.3, the exponent becomes positive for the remaining duration of the simulation. It is worth noting that other global measurements could be used instead of the COM, such as the center of charge [148], but these were found to provide similar

qualitative results to those shown here.

4.4 Outlook

With this study, I have shown that it is possible to induce chaotic vortex dynamics in few-vortex systems by using phase imprinting to flip the rotational direction of a vortex in two dimensions. We also show that a scattering event seems to be correlated to a positive Lyapunov exponent and an acceleration of chaotic behavior. This behavior is radically different to the behavior of large scale vortex lattices, as similar techniques for these systems have been shown to only cause local disturbances [59]. Further exploration of the crossover from regular to turbulent dynamics, and the crossover from chaotic to stable dynamics for large-scale vortex lattices remains an interesting extension for future work.

This study shows that there is strong utility in simulating two-dimensional quantum gases and highlights dynamic measures, such as the Lyapunov exponent. Here, it is obvious that fast vortex tracking methods are essential to dynamical turbulence and chaos modelling, and a major limitation to performing similar studies in three dimensions is the computational hurdle of vortex tracking in this area. As such, most three-dimensional studies of quantum chaos rely on other methods, such as vortex filament methods which provide vortex skeletons during the simulation, itself. As mentioned in Chapter 1, these methods cannot simulate the underlying dynamics of the condensate, and are thus removed from experimental application. Further extensions of this work in three dimensions would also allow for studies on the movement of the vortex lines, themselves, which were projected onto two-dimensional point-vortices in this model.

It is important to note the utility of the GPUE codebase in this study. Throughout the process, highly-resolved (up to 2048×2048) wavefunction densities were generated in the ground state via imaginary time propagation and dynamics were determined with real-time evolution. For a typical run of 1024×1024 with 1×10^6 steps, with a time

resolution of 1×10^{-5} and outputting every 1000 steps, the simulation can be completed within an hour. This metric includes vortex tracking on every output step, which is a computational intensive task, as discussed in Chapter 3. Because of the computational speed of GPUE, this study performed hundreds of individual runs with slightly varying initial conditions to provide a strong indication of chaotic behavior. Because this study very heavily relied on post-processing metrics, such as vortex tracking and the calculation of the Lyapunov exponent, it is apparent that it is ideal to provide an interface to the GPUE codebase in a language that more easily provides the functionality expected by researchers for data manipulation. Such an interface is possible with GPUE.jl and further motivates this development.

For the next study, I will transition into a discussion of three-dimensional vortex dynamics and show an experimentally realistic system to allow for the generation, control, and detection of vortex ring-like systems with artificial magnetic fields.

Chapter 5

Generation, control and detection of 3D vortex structures in superfluid systems

In this chapter, I will discuss another application of the GPUE codebase, this time to the controlled creation of vortex structures in three dimensions with artificial magnetic fields generated by an optical nanofiber. To the best of my knowledge, this is the first time an experimentally realizable device to generate vortex ring-like structures with a dielectric system has been suggested and investigated, and I also provide a method to detect whether a vortex ring is present in an elliptic-toroidal condensate. This project encompasses three-dimensional vortices and coupled light-matter systems, so to begin, I will briefly discuss vortices in three-dimensional systems, followed by the model used for this project, where I will describe how the light from an optical nanofiber can generate and control vortex structures in BEC systems. As a note, even though vortex dynamics are not shown in this study, GPUE is more than capable of simulating these effects, and potential applications of vortex ring dynamics will be discussed in the outlook of this chapter. The contents of this chapter have recently been submitted to Phys. Rev. Fluids ???. In this study, I performed all simulations, with exception of vortex states generated in Figures ?? and ??, which were performed under my supervision by Peter Barnett. I also designed the GPUE codebase to allow for these simulations and visualized all data. This project

was supervised overall by Thomas Busch and Rashi Sachdeva.

5.1 Three-dimensional vortex structures

As mentioned in Chapter 1, in BEC systems with large amounts of angular momentum and a single axis of rotation, the vortices will create a triangular, Abrikosov lattice [52, 60]. This regular structure is a direct consequence of the quantization of angular momentum in quantum mechanics, and in Chapter 4, I discussed a small vortex lattice in two-dimensions by integrating out the \hat{z} direction. In this chapter, I will discuss fully three-dimensional vortex structures in BEC systems. In three dimensions, BEC systems have been shown to support a large variety of flow-related excitations, such as vortex lines and rings [40, 54, 60, 170–174]. There are many interesting features to superfluid vortices in three dimensions, many of which follow from classical fluid dynamic theory [47], which is a well-studied field and covered in many texts [175–178].

By modifying the axis of rotation or inducing a vortex structure with either artificial magnetic fields or phase imprinting, one may create three-dimensional topologies, like the vortex ring. This structure is also common in large, three dimensional modelling of superfluid systems and is a direct consequence of the required connections of vortex lines. The stability of vortex rings is ensured by Kelvin’s theorem [179], which means that unstable excitations may decay into vortex rings or objects with ring-like topology [171].

In the case of multiple, interacting vortex rings, one can expect to find many similar features in superfluids to what has been found previously in classical, viscous fluids. If two vortex rings are generated in the same plane and in close proximity, it could be possible for the two velocity fields to interact, causing one ring to expand and slow down while the other contracts and speeds up. Under the right conditions, the lagging ring can pass the forward ring through a process known as *leapfrogging* [180, 181]. This behavior can be extended to vortex ring bundles, in such systems the entire bundle will turn in on itself while moving in its self-induced velocity field[There’s a Barenghi paper I cannot find...].

In addition to leapfrogging, vortex rings can interact through direct collisions [182]. In superfluid ^4He , some of the earliest experiments on vortex collisions with vortex rings were performed by Schwarz in 1968 [183]. In the case of a head-on collision, two identical, moving vortex rings will first grow in size before dispersing into a series of smaller vortex rings around their common circumference [184]. These smaller rings are created by vortex reconnections, which can occur any time vortex lines are facing anti-parallel directions and it is energetically favorable to do so.

Finally, I will briefly discuss vortex reconnections, themselves. As predicted by Feynman in 1955, vortex reconnections in a dissipative superfluid systems lead to larger vortices continually reconnecting into smaller ones until the loops become small enough to decay from dissipation or from interactions with boundaries. [57]. These reconnections produce sound waves when vortices directly interact and Kelvin waves when vortices indirectly interact [185]. When a vortex ring structure is not pinned by either gauge fields or rotation, it will evolve naturally by reconnecting into smaller and smaller vortex rings when in a turbulent system [186]. This means that one would expect to see vortex reconnections in any sufficiently complicated vortex tangle [56].

Though these dynamics are expected in superfluid systems, it is difficult to devise experimental systems systematically generate the desired behavior. In practice, complex three-dimensional structures cannot be easily created by stirring or rotating a BEC because vortex lines generated in this way must follow the axis of rotation, thus even vortex rings can be a challenge to create, control, and detect experimentally. In most cases, including in most theoretical proposals, vortex ring generation in BEC systems relies on dynamic processes that do not create eigenstates of the system, such as the decay of dark solitons in multicomponent condensates [171] with the snake instability [187], the collision of symmetric defects [188], or direct density engineering [189, 190]. There are other theoretical proposals that consider interfering two BEC systems [186], using Feschbach resonances [191], or phase imprinting methods [187]. As a note, in inhomogeneously trapped BEC systems, vortex ring structures are known to be unstable, which has

led to difficulties in their experimental observation [192]. In addition, imaging techniques employed for BECs are not suited to identify whether three-dimensional vortex structures are present.

To consistently control and generate more complex three-dimensional structures, methods beyond rotation must be used, and there are only a few known experimental systems that can do so [171, 174]. There is also a large amount of interest in generating more complicated vortex structures, such as vortex knots [77, 193, 194]. Artificial magnetic fields seem to be a promising method for the generation of complex three-dimensional vortex structures in BEC systems [195], and in this chapter, I will present a method to generate vortex rings, ring-lattices, and other vortex structures in three dimensions by using the artificial magnetic field generated by an optical nanofiber.

5.2 Controlled creation of three-dimensional vortex structures in Bose–Einstein condensates using artificial magnetic fields

One method to create artificial magnetic fields involves the interaction between an atomic system in a dressed state and an electric field that is tuned near an atomic resonance frequency [196]. In practice, this means that one can create a configurable artificial magnetic field with an appropriately tuned electric field that varies strongly over short distances, such as those found in the near-field regime on the surface of a dielectric system when light undergoes total internal reflection [197]. One such system that suits this purpose and can be used to generate vortex ring structures in BEC systems is the optical nanofiber, which has several propagation modes to facilitate the generation of configurable artificial magnetic fields.

Optical nanofiber systems can be created by heating and stretching optical fibers until their thinnest region is roughly hundreds of nanometers in diameter [198, 199]. At this

scale, the wavelength of light is larger than the diameter of the fiber and the strength of the evanescent field is significantly enhanced [200]. The form of the evanescent field varies significantly depending on the optical modes propagating through the nanofiber, and I will show that this can be used to generate interesting and tunable artificial magnetic fields.

Optical nanofibers are already used in many different experiments with ultracold atoms [201–206], and trapping potentials around 200nm from the fiber surface can be created with two differently detuned input fields [114, 207]. Our proposed device will allow for the creation of vortex rings in BEC systems that are trapped toroidally around the nanofiber at roughly the same distance as nanofiber systems by coupling the BEC to the evanescent field created by different modes propagating through the nanofiber [208]. A schematic of this system is depicted in Figure 5.1

With this same device, it is also possible to detect whether a vortex ring is present in the system by exciting the scissors mode in an elliptic-toroidal trapping geometry [209–211]. This can be done by tilting the trap radially from the center of the torus, which will cause the BEC to oscillate in and out in the new potential, similar to the oscillation shown in Chapter 1 for a simple harmonic oscillator. Without a vortex present, this oscillation possesses a single frequency, whereas in the presence of a vortex ring, it will contain two frequencies that average to the vortex-less oscillation frequency, similar to scissors mode oscillations in a two-dimensional, elliptically-trapped BEC [212–214].

5.2.1 Bose–Einstein condensate dynamics in the presence of an optical nanofiber

As discussed in Chapter 1, in the presence of an artificial magnetic field, the GPE becomes,

$$i\hbar \frac{\partial \Psi}{\partial t} = \left[\frac{(p - m\mathbf{A}(\mathbf{r}))^2}{2m} + V_{\text{trap}}(\mathbf{r}) + g|\Psi|^2 \right] \Psi. \quad (5.1)$$

Here, all values are defined as before. The artificial vector potential can take many forms,

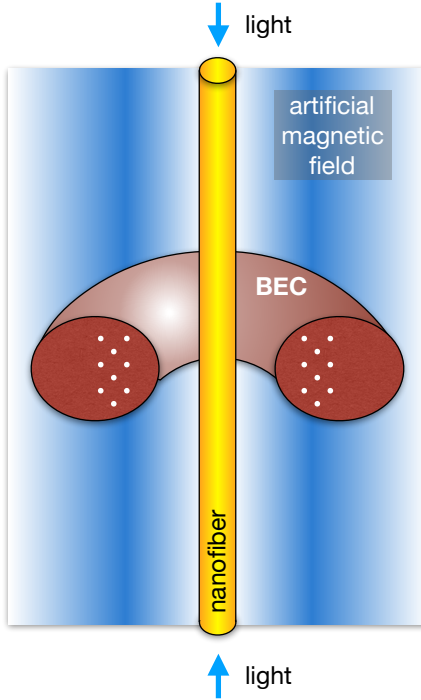


Figure 5.1: Schematic of the system. Blue or red-detuned light is sent into the nanofiber (yellow), creating an evanescent field and artificial magnetic field (blue) that influences the BEC (maroon) held by a toroidal trapping potential. If the artificial magnetic field strength is greater than a threshold value, vortex rings (white) will appear and begin to arrange themselves into a triangular lattice.

but for here, I will again choose a description based on Berry's connection [196],

$$\mathbf{A} = i\hbar \langle \Psi_l | \nabla \Psi_l \rangle, \quad (5.2)$$

where Ψ_l is the atomic wavefunction in some dressed state l .

Considering a dressed, two-state atoms in the presence of an optical field, these states

can be written within the rotating wave approximation as [197],

$$|\Psi_1(\mathbf{r})\rangle = \begin{pmatrix} \cos[\Phi(\mathbf{r})/2] \\ \sin[\Phi(\mathbf{r})/2]e^{i\phi(z)} \end{pmatrix}, \quad (5.3)$$

$$|\Psi_2(\mathbf{r})\rangle = \begin{pmatrix} -\sin[\Phi(\mathbf{r})/2]e^{-i\phi(z)} \\ \cos[\Phi(\mathbf{r})/2] \end{pmatrix}, \quad (5.4)$$

where $\phi(z)$ is the phase of the optical field and $\Phi(\mathbf{r}) = \arctan(|\kappa(\mathbf{r})|/\Delta)$, with $\Delta = \omega_0 - \omega$ being the detuning and $\kappa(\mathbf{r}) = \mathbf{d} \cdot \mathbf{E}(\mathbf{r})/\hbar$ being the Rabi frequency. The atomic dipole moment is given by \mathbf{d} and $\mathbf{E}(\mathbf{r})$ is the electric field. Here the form of \mathbf{A} follows the form of the optical fields, and the artificial magnetic field is given by $\mathbf{B} = \nabla \times \mathbf{A}$; therefore, it is possible to influence the magnetic field and vortex structures generated with this system by modifying the optical profile of the nanofiber.

For optical nanofibers, one can determine which modes will propagate in the system by calculating the V -number, with $V = k_0 a \sqrt{n_1^2 - n_2^2}$, where a is the fiber radius, n_1 is the refractive index of the fiber, n_2 is the refractive index of the cladding, and $k_0 = \omega/c$ with ω being the frequency of the input light beam. The V number can be easily chosen by modifying the radius of the fiber, and the way in which light propagates through the fiber for each mode is characterized by the modal propagation constant, β . In addition, the effective refractive index of the fiber is $n_{\text{eff}} = \beta/\kappa_0$. In figure 5.2, a plot of n_{eff} vs V number is shown in (a) and it can be seen that certain modes cannot propagate until certain threshold values are reached. In (b) and (c), the simulated and experimental images of the fiber output are shown as the LP_{11} group, which is a combination of the $\text{HE}_{21\text{even}}$, $\text{HE}_{21\text{odd}}$, TE_{01} and the TM_{01} modes. For the system considered in this chapter, the fiber has been tapered such that the cladding is the vacuum, itself, with $n_2 = 1$; therefore, higher order modes can only be sustained if $V > V_c \simeq 2.405$. Below this value, only the fundamental mode can propagate in the system.

Using cylindrical coordinates, the evanescent field of the $\text{HE}_{\ell m}$ mode with circular

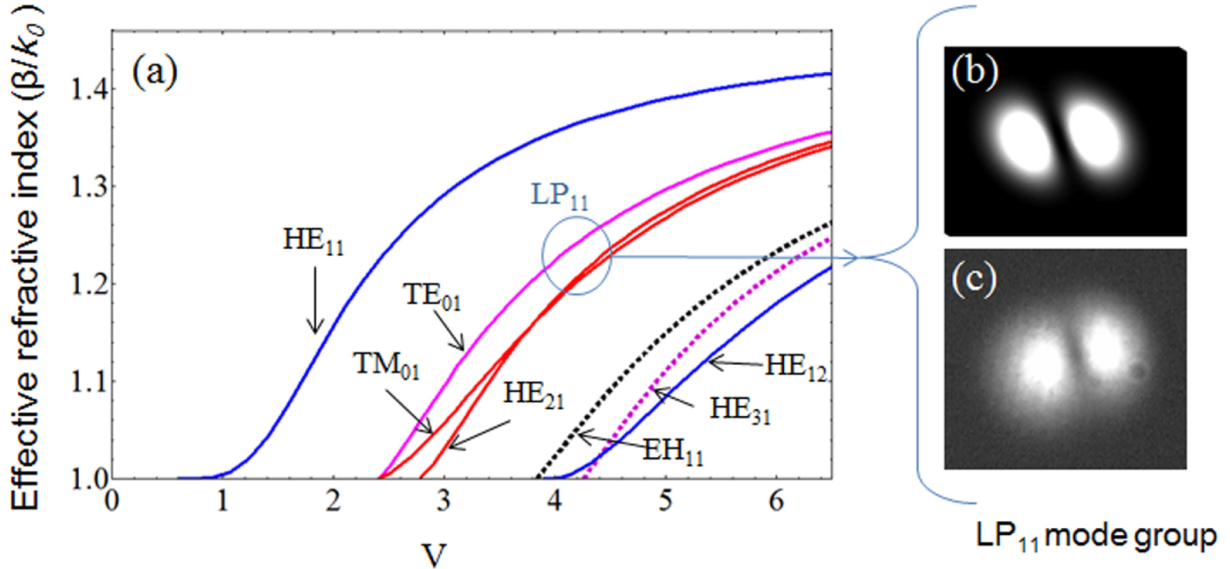


Figure 5.2: (a) Plot of effective refractive index and V number of an optical fiber. The circle indicates the LP_{11} group, which is the first higher-order group composed of the $HE_{21\text{even}}$, $HE_{21\text{odd}}$, TE_{01} and the TM_{01} modes. (b) Simulated and (c) experimental images of the output from the LP_{11} group are also shown. Reproduced from [203, 206].

polarization is [215],

$$E_r = iC[(1-s)K_{\ell-1}(qr) + (1+s)K_{\ell+1}(qr)]e^{i(\omega t - \beta z)}, \quad (5.5)$$

$$E_\phi = -C[(1-s)K_{\ell-1}(qr) - (1+s)K_{\ell+1}(qr)]e^{i(\omega t - \beta z)}, \quad (5.6)$$

$$E_z = 2C(q/\beta)K_\ell(qr)e^{i(\omega t - \beta z)}, \quad (5.7)$$

where

$$s = \frac{1/h^2 a^2 + 1/q^2 a^2}{J'_\ell(ha)/[haJ_\ell(ha)] + K'_\ell(qa)/[qaK_\ell(qa)]}, \quad (5.8)$$

$$C = \frac{\beta}{2q} \frac{J_\ell(ha)/K_\ell(qa)}{\sqrt{2\pi a^2(n_1^2 N_1 + n_2^2 N_2)}}, \quad (5.9)$$

and

$$N_1 = \frac{\beta^2}{4h^2} \left[(1-s)^2 [J_{\ell-1}^2(ha) + J_\ell^2(ha)] + (1+s)^2 [J_{\ell+1}^2(ha) - J_\ell(ha)J_{\ell+2}(ha)] \right] + \frac{1}{2} [J_\ell^2(ha) - J_{\ell-1}(ha)J_{\ell+1}(ha)], \quad (5.10)$$

$$N_2 = \frac{J_\ell^2(ha)}{2K_\ell^2(qa)} \left(\frac{\beta^2}{4q^2} \left[(1-s)^2 [K_{\ell-1}^2(qa) - K_\ell^2(qa)] - (1+s)^2 [K_{\ell+1}^2(qa) - K_\ell(qa)K_{\ell+2}(qa)] \right] \right. \\ \left. [K_\ell^2(qa) + K_{\ell-1}(qa)K_{\ell+1}(qa)] \right). \quad (5.11)$$

The mode geometry is given by $J_n(x)$, the Bessel function of the first kind, $K_n(x)$, the modified Bessel function of the second kind, and β , the propagation constant of the fiber. The scaling factors are given by $q = \sqrt{\beta^2 - n_2^2 k_0^2}$ and $h = \sqrt{n_1^2 k_0^2 - \beta^2}$, the normalization constant is C and s is a dimensionless parameter.

When the input light field is linearly polarized, it is convenient to write the Cartesian components of the evanescent electric field as

$$E_x = \sqrt{2}C \left[(1-s)K_{\ell-1}(qr) \cos(\phi_0) + (1+s)K_{\ell+1}(qr) \cos(2\phi - \phi_0) \right] e^{i(\omega t - \beta z)}, \quad (5.12)$$

$$E_y = \sqrt{2}C \left[(1-s)K_{\ell-1}(qr) \sin(\phi_0) + (1+s)K_{\ell+1}(qr) \sin(2\phi - \phi_0) \right] e^{i(\omega t - \beta z)}, \quad (5.13)$$

$$E_z = 2\sqrt{2}iC(q/\beta)K_\ell(qr) \cos(\phi - \phi_0) e^{i(\omega t - \beta z)}. \quad (5.14)$$

Here ϕ_0 determines the orientation of polarization, with $\phi_0 = 0$ being along the x axis and $\pi/2$ being along the y axis. The artificial vector potential produced by such evanescent fields around an optical nanofiber is then given by [208]

$$\mathbf{A} = \hat{z}\hbar\kappa_0(n_1 + 1)\tilde{s} \left[\frac{|d_r E_r + d_\phi E_\phi + d_z E_z|^2}{1 + \tilde{s}^2 |d_r E_r + d_\phi E_\phi + d_z E_z|^2} \right], \quad (5.15)$$

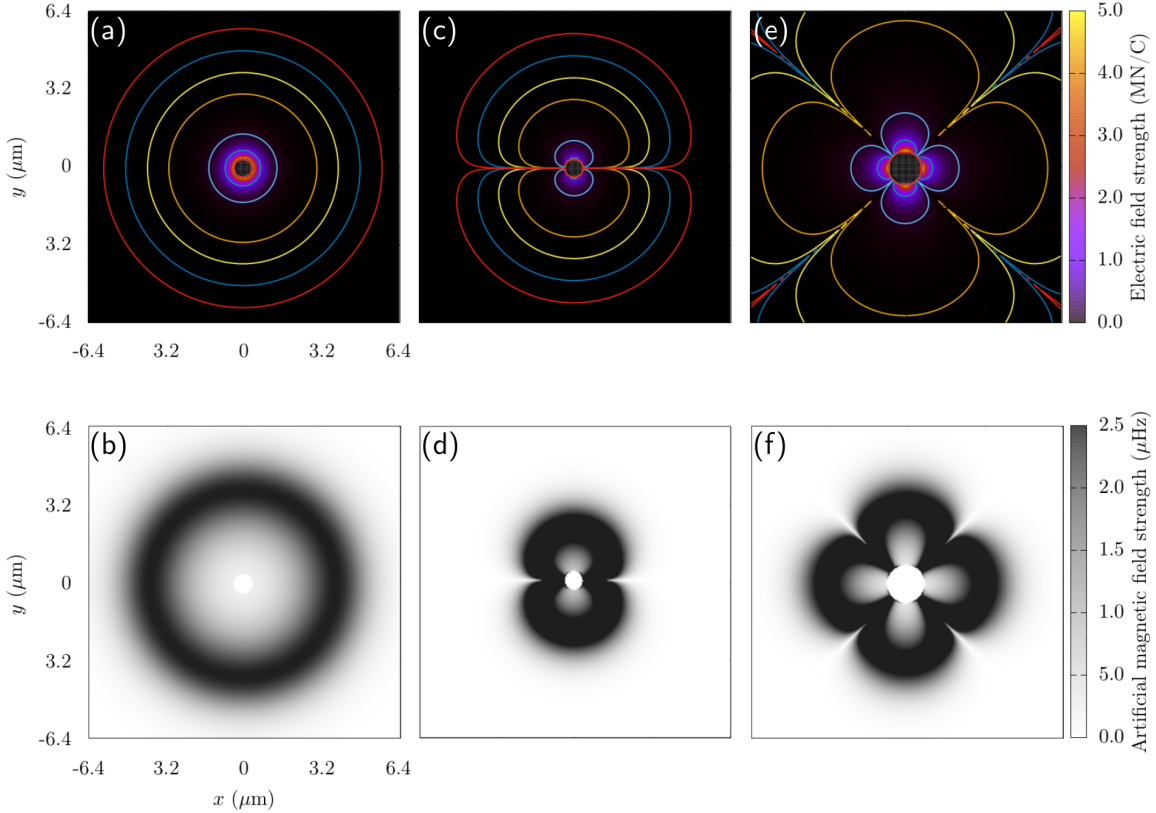


Figure 5.3: Images of electric and artificial magnetic field profiles for [(a) and (b)] the fundamental HE_{11} mode with circular polarization, [(c) and (d)] the HE_{11} mode with linear polarization, and [(e) and (f)] the HE_{21} mode with linear polarization. For these calculations, the input power is 372 nW in (a) and (b) , 16 nW in (c) and (d), and 418 nW in (e) and (f). For the HE_{11} mode, the nanofiber radius is 200 nm with blue-detuned light of 700 nm, and for the HE_{21} mode, the nanofiber radius is 400 nm with red-detuned light of 980 nm

where $\tilde{s} = \frac{|\mathbf{d} \cdot \mathbf{E}|}{\hbar |\Delta|}$ and the corresponding magnetic field $\mathbf{B} = \nabla \times \mathbf{A}$ can be calculated to be

$$\begin{aligned} \mathbf{B} = & \frac{\hbar \kappa_0 s^2 (n_1 + 1)}{(1 + \tilde{s}^2 |d_r E_r + d_\phi E_\phi + d_z E_z|^2)^2} \\ & \times \left[\hat{\phi} \frac{\partial}{\partial r} |d_r E_r + d_\phi E_\phi + d_z E_z|^2 \right. \\ & \left. - \hat{r} \frac{1}{r} \frac{\partial}{\partial \phi} |d_r E_r + d_\phi E_\phi + d_z E_z|^2 \right]. \end{aligned} \quad (5.16)$$

This shows that the \mathbf{B} field has only components in the $\hat{\phi}$ and \hat{r} directions, which means that all field lines lie in the horizontal plane if the fiber is aligned along the vertical \hat{z}

direction.

This also means that a BEC trapped toroidally around the nanofiber would facilitate vortex structures that wrap around the nanofiber and potentially close on themselves in the form of vortex rings; however, other vortex structures are possible as well. In addition, the value of \tilde{s} governs the amplitude and range of the magnetic field, and as such, it is possible to manipulate the size and shape of the generated vortex rings by changing the detuning and intensity of the electric field [208].

For the purposes of this project, I will consider the fundamental HE_{11} mode with circular polarization, the HE_{11} mode with linear polarization, and the HE_{21} mode with linear polarization. Though even higher-order modes may be generated by the optical nanofiber, increasing the V -number to facilitate these modes also requires increasing the fiber radius beyond what is experimentally achievable. It is also possible to create even more complex field configurations by interfering different modes; however, the chosen modes will still demonstrate a range of possible magnetic field profiles. The electric field configurations and their corresponding magnetic field profiles can be seen in Figure 5.3. Here, the circularly polarized HE_{11} mode will create a cylindrically symmetric electric (a) and magnetic (b) field profiles; however, linearly polarized light will create a lobed structure for both (c and d). When using the linearly-polarized HE_{21} mode, four petals appear in the electric and magnetic field profiles, which suggest unusual vortex structures. Now I will discuss what types of vortex structures can be generated with this system, including the possibility of generating vortex ring lattices.

5.2.2 Ground state vortex configurations

We will use GPUE [12] to describe a ^{87}Rb condensate with 1×10^5 atoms with a scattering length of $a_s = 4.76 \times 10^{-9}$ m on a three-dimensional grid of 256^3 points with a spatial resolution of 50 nm, with a toroidal trapping potential around the fiber given by,

$$V_{\text{trap}} = m(\omega_r^2(r - \eta)^2 + \omega_z^2 z^2), \quad (5.17)$$

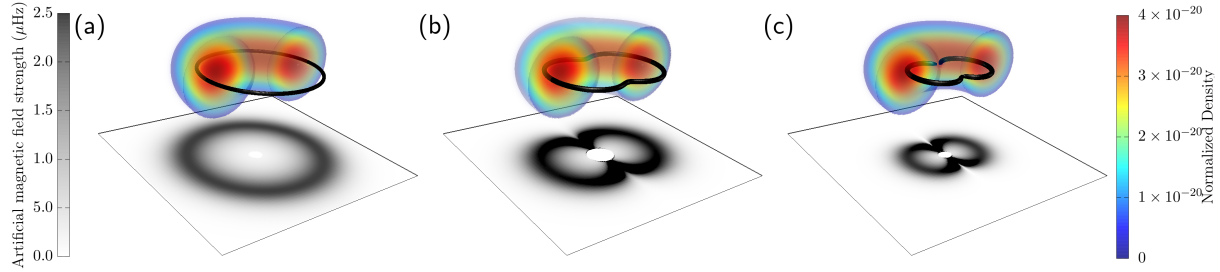


Figure 5.4: Vortex configurations for different magnetic field profiles from the nanofiber for the fundamental HE₁₁ mode with (a) circular polarization, (b) elliptical polarization, and (c) linear polarization along the \hat{y} direction. The vortex distributions have been found via an isosurface on the Sobel filtered wavefunction density for a ⁸⁷Rb BEC and all optical fiber fields are normalized and for a nanofiber of 200 nm in radius with blue-detuned light of 700nm. The magnetic field profiles shown in the shaded region beneath wavefunction density are similar to those in Figure 5.3(b) and (d).

where the frequencies in the \hat{r} and \hat{z} directions are chosen to be $\omega_r = \omega_z = 7071\text{Hz}$ to match typical experimental conditions in fiber trapping [201]. Here, η describes the distance of the center of the torus from the center of the fiber and is chosen such that the atoms are trapped beyond the van-der-Waals potential of the fiber. For the HE₁₁ mode, the fiber radius is 200 nm and $\eta = 3.20\text{\mu m}$, creating a toroidal BEC with an inner radius of roughly 300 nm from the fiber surface. For the HE₂₁ mode, the fiber radius is increased to 400 nm, but keep all other parameters the same, creating a toroidal BEC with an inner radius of roughly 150 nm.

As shown in Figure 5.4(a), when simulating the HE₁₁ mode with these parameters, one can see a vortex line that wraps around the fiber and reconnect in the form of a single vortex ring as the ground state solution. In contrast, the linearly polarized HE₁₁ mode in Figure 5.4(c) shows a ground state where the vortex lines bend toward the center of the torus, creating two vortex lobes. As a note, the vortex lines do not follow the magnetic field lines exactly, but instead reconnect to the neighboring lobe when approaching each other within a healing length. If elliptically polarized light is considered, one can see a hybrid ground state between the circularly and linearly polarized modes, shown in Figure 5.4(b). Finally, I show a four-petal ground-state solution when using the HE₂₁ linearly polarized

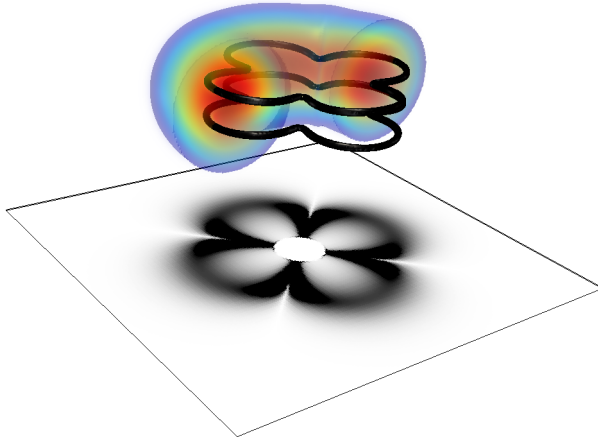


Figure 5.5: Vortex configuration for the HE₂₁ mode with linear polarization along the \hat{y} direction. The magnetic field profile is similar to the one shown in Figure 5.3(f), and has been calculated for a nanofiber of 400 nm in radius with red-detuned light of 980 nm.

mode in Figure 5.5. Here, I also show that it is possible to generate multiple vortex structures in-line with themselves by increasing the intensity of the artificial magnetic field.

This indicates that it is possible to generate interesting vortex ring lattice structures in three-dimensions by sufficiently increasing the artificial magnetic field. To study the control of multiple vortex structures with this system, I first simulated a system with low artificial magnetic field strength and showed that this simulation will cause all vortex rings to line up at peaks in the magnetic field in Figure 5.6(a and b). As the magnetic field is increased from this point, the vortex rings begin to pack together and form an Abrikosov-like lattice in-line with peaks in the artificial magnetic field, shown in Figure 5.6(a and c). If other magnetic field profiles are used, it could be possible to generate different Abrikosov-like ring lattice configurations. This system could allow for studies of bulk vortex-ring movement, thereby potentially creating a vortex ring lattice that rotates in a leapfrogging manner and moves based on individual vortices self-induced velocity.

The optical nanofiber seems to provide unprecedented control over the vortex geometries generated in a toroidally-trapped BEC system, and one can control the shape of each vortex structure by manipulating the optical fields input into the nanofiber. In addition,

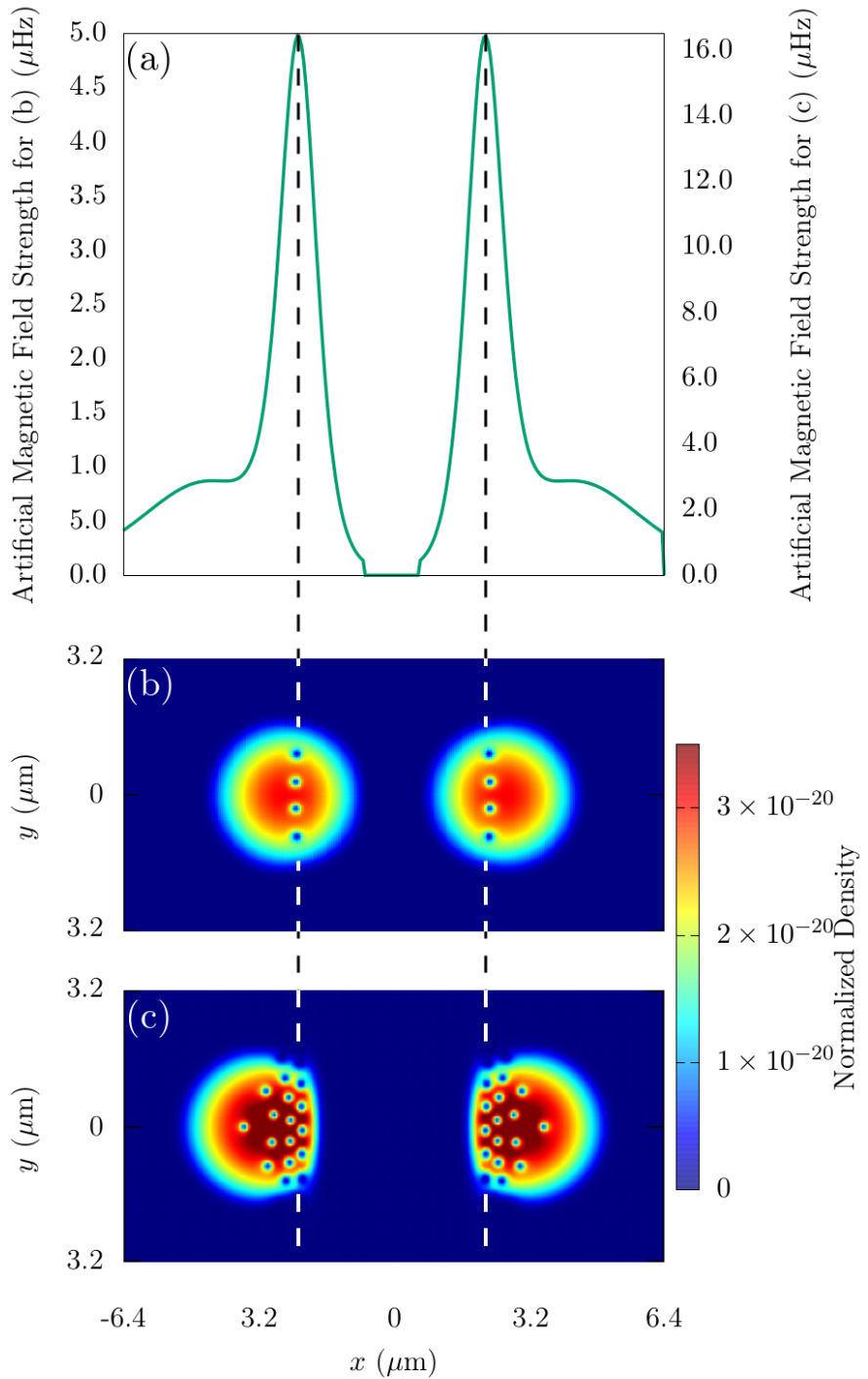


Figure 5.6: (a) The magnetic field profile along the x -direction for the fundamental HE_{11} mode with circular polarization outside a fiber of 200 nm radius. Note that for this mode and polarization the whole system is azimuthally symmetric. For weak fields (see (b)) this leads to a small number of vortices that align along the line at which the magnetic field is maximal and for larger fields (see (c)) more vortex rings appear that form the beginning of an Abrikosov lattice. The optical fiber field and wavefunction density have been normalized and are for a nanofiber of 200 nm in diameter with blue-detuned light of 700nm and a ^{87}Rb BEC respectively.

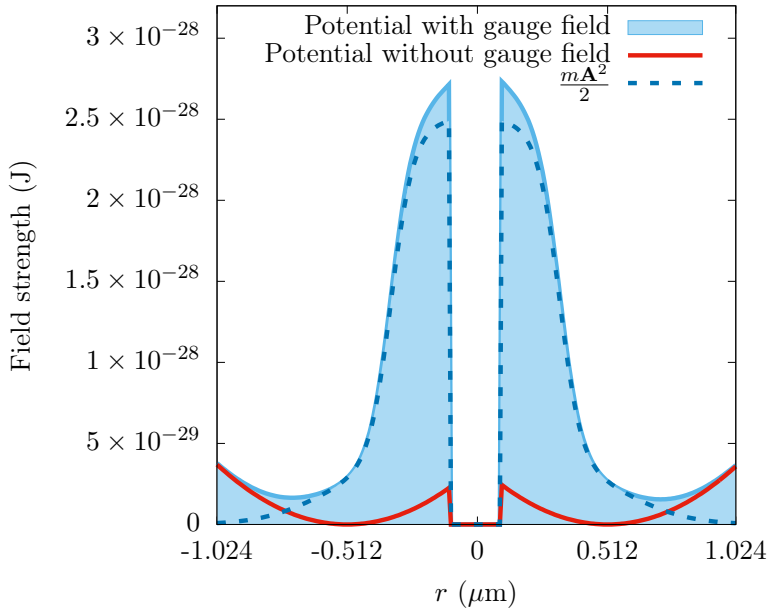


Figure 5.7: Visualization of the change in potential due to the effects of the artificial magnetic field for Figure 5.6. Here, the experienced potential is shown in the blue shaded region, the scaled artificial vector potential is shown as a dotted, dark blue line, and the original trap is shown in red.

because the optical fields could be time-dependent, this system could be used in the future to probe dynamical effects of vortices. In this case, one must consider the effects of high artificial magnetic fields on the distribution of atoms, themselves, because (as described in Chapter 1), the external potential V_{trap} will be modified by a term proportional to \mathbf{A}^2 . In Figure 5.7, I show this modification for the artificial magnetic fields shown in Figure 5.6(c). Dynamical studies in which the gauge field is switched off in a finite time will thus lead to phonon excitations in the condensate, which will also influence the vortex lines, themselves, and this is an area of future work.

5.2.3 Dynamic vortex detection and scissor modes

Observing the presence of vortex rings in a three dimensional BEC is a difficult problem, as absorption spectroscopy usually only provides a picture of an integrated two-dimensional density. However, due to the unique geometry of this system, one can identify whether

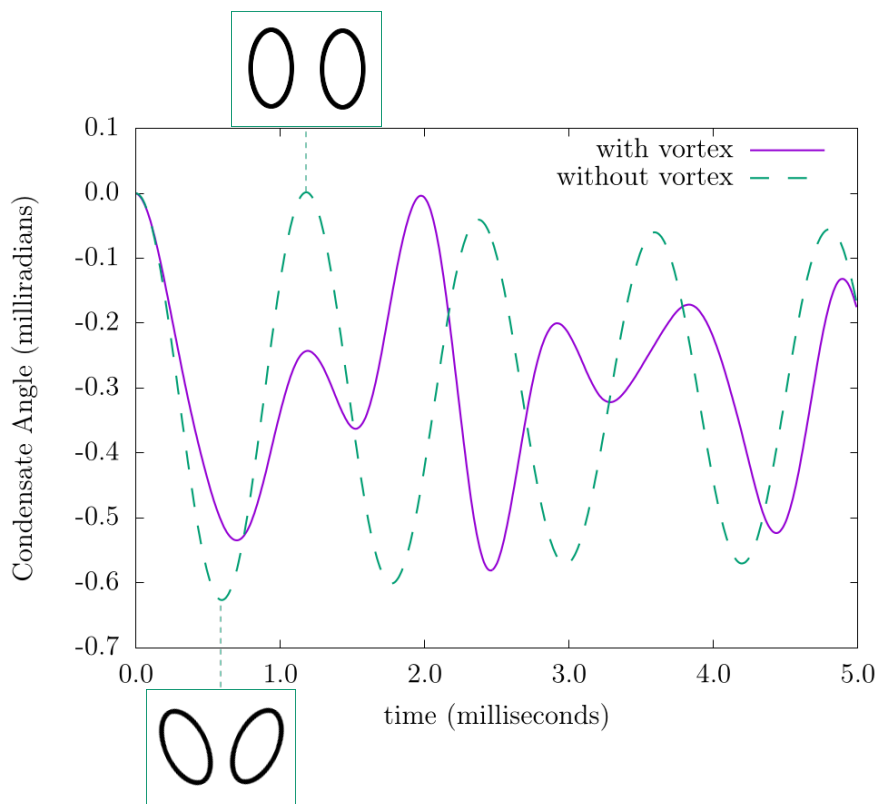


Figure 5.8: Angle of the condensate axis after excitation of the toroidal scissors mode for an elliptic-toroidal BEC with a single vortex ring (purple, solid) and without a vortex present (cyan, dashed). Depictions of two dimensional slices for the scissors mode without a vortex are shown in the insets. Here, the scissors mode causes oscillation in and out towards the center of the system, and that two distinct frequencies are present in the curve for the condensate carrying a vortex ring.

vortex rings are present by exciting the scissors mode of the condensate [209–211]. For an elliptic-toroidal geometry ($\omega_z < \omega_r$), the scissors mode can be excited by modifying the external potential with a rotation in the rz -plane,

$$V = V_{\text{trap}}(r, \theta, z) - m\omega_0^2\alpha r z, \quad (5.18)$$

where $\alpha = 2\epsilon\theta$ is a coefficient related to the tilting angle, ϵ is the deformation of the trap in the rz plane and θ is the angle at which the original trap was aligned at. For a small initial angle of θ_0 this change in the potential causes a BEC without rotation to oscillate back and forth in the trap with a frequency given by [214]

$$\omega_{\text{scissors}} = \sqrt{\omega_r^2 + \omega_z^2}. \quad (5.19)$$

If, however, this mode is excited for a BEC that contains a vortex line, the oscillation will be strongly influenced by the currents inside the condensate and two different frequencies (ω_+ and ω_-) appear in the oscillation [212–214]. When the splitting frequency is small compared to the scissors mode frequency, it can be written as [213]

$$\omega_+ - \omega_- = \frac{\langle l_z \rangle}{m\langle r^2 + z^2 \rangle}, \quad (5.20)$$

where $\langle l_z \rangle$ is the average angular momentum per particle. Calculating these values for the system for $\omega_r = 4242\text{Hz}$, and $\omega_z = 2828\text{Hz}$ then leads to $\omega_{\text{scissors}} = 5090\text{Hz}$, $\omega_- = 3765\text{Hz}$, and $\omega_+ = 6415\text{Hz}$, which are very close to the values observed in the numerical simulations shown in Fig. 5.8. However, one can also see from this figure that the oscillation is not perfect and seems to decay over time. This is due to the above mentioned modification of the trapping potential by the artificial vector potential, which leads to a deviation from the perfect elliptical toroidal shape used in the derivation of Equation (5.20).

It is worth noting that this method cannot be used to detect a vortex ring inside a simply connected condensate, as in this situation the flow around the vortex line has no

preferred direction. However, in the toroidal shape, each radial slice can be seen as a two-dimensional elliptical BEC with a single vortex, and the system will therefore exhibit the scissors mode frequency as expected. While in principle the excitation of the scissors mode can also be used to detect Abrikosov vortex-ring lattice, the fact that the inhomogeneous artificial magnetic field leads to an inhomogeneous vortex ring distribution will have an effect on the expected oscillation frequencies.

5.3 Conclusion

In this application of the GPUE codebase, I have shown that it is possible to create and control vortex rings and more complicated vortex structures by using the artificial magnetic field generated by the optical nanofiber. There is currently no other known method to generate the structures created by the linearly polarized modes, shown in Figure 5.4(b,c) and 5.5. We have also shown that the scissors mode can be used to detect whether a vortex ring is present in an elliptic toroidal trap. These fiber-generated structures could allow for experimental systems to study complicated superfluid mechanisms, like the kelvin-mode cascade, superfluid turbulence, or reconnection events between superfluid vortex lines. These structures might also be the first step in creating knotted vortex lines around an optical nanofiber; however, to generate these structures, the magnetic field must have a dependence on \hat{z} , which is not present in this model.

This project leaves several open fields of study for future work and future simulations with GPUE, including the study of dynamic field effects on vortex structures, the generation of vortex knots in superfluid systems with this device, and studies of vortex ring lattice movement in BEC systems. For both of these cases, significant work must be performed both theoretically and computationally.

To generate vortex knots with this system, a magnetic field with \hat{z} must be created. Such fields might be possible with fiber Bragg gratings [?] or other methods to change the evanescent profile of the fiber. Such simulations would require FEM or FDTD simulations

of the optical fiber, itself, which makes the problem an intricate engineering process of generating the right field with an optical nanofiber. In addition, a z-dependent gauge field requires analysis of the other gauge field term, $\frac{p_z \mathbf{A}_z}{2}$, which is not considered in this work because the derivative along the \hat{z} direction for the fiber field is 0. This leads to interesting questions about how BEC systems behave in the presence of such artificial magnetic fields.

For the movement of dynamic vortex ring tangles generated with this system, vortex tracking methods in three-dimensions should be employed. As described in Chapter 3, this is not a trivial task and I will discuss methods that could be used to do this in the Conclusion 5.4. It is also interesting to see what happens if the HE₂₁ vortex structures are evolved in real-time and whether scissors modes can be used to detect such vortex structures as well. With a sharp magnetic field, it is also possible to create a phase separation along a vortex line for multicomponent condensate simulations.

Conclusion

5.4 Overall conclusions

This thesis has presented my efforts to create a massively parallel SSFM codebase for the simulation of superfluid vortex dynamics in Bose–Einstein Condensates (BECs). Starting from the SSFM and a discussion on the dynamics of ultracold atomic systems, I motivated the dynamic quantum engineering by introducing quantum optimal control and shortcuts to adiabaticity. Both of these methods were used to show that it is possible to generate macroscopic superposition states in a Tonks–Girardeau gas when on a ring with a barrier to break rotational symmetry. From there, I introduced the GPGPU and the GPUE codebase, emphasizing existing challenges in the field and the methods I used to overcome them. In the process, I also briefly mentioned the challenging problem of memory coalescence when using spectral methods on GPU hardware and proposed an additional software package as method to further optimize the FFT operations with a distributed, multi-GPU transpose. After this, I introduced an example physical system that showed it is possible to generate chaotic vortex dynamics in few-vortex systems and emphasized the need for vortex tracking methods and post-processing methods, by calculating the Lyapunov exponent on the vortex trajectories. Finally, I introduced a three-dimensional example system that generates, controls, and detects vortex ring-like geometries in a toroidally-trapped BEC coupled to the artificial magnetic field generated by an optical nanofiber.

Throughout this work, I attempted to highlight all future directions when relevant to

the chapter. I will continue the discussion on future research pursuits here, while also presenting new directions not yet considered in this work.

5.5 Further development of GPUE

Though the GPUE codebase is roughly feature complete, there are several directions for future development, many of which were described in Chapter 3. In particular, a re-write of GPUE in Julia along with developing an n -dimensional, distributed, GPU transpose are currently being worked on. The former will allow for GPUE to be more maintainable and require less development time in the future. The latter is applicable to a wide range of spectral methods and might allow for several methods to become relevant on new HPC environment. As both of these were discussed at length in Chapter 3, I will not discuss them further here; however, there are future directions where proper development has not begun, such as new vortex tracking methods and potentially using expression trees for general-purpose Hamiltonian solutions.

5.5.1 Vortex tracking in two and three dimensions

The GPUE codebase currently has the capability of tracking vortices in two dimensions and highlighting vortices in three; however, vortex tracking has yet to be implemented as there are no reliable and general methods for tracking three dimensional vortex structures in superfluid simulations. In addition, the vortex tracking method in GPUE is currently unstable for non-harmonic traps in two dimensions, and in many cases, the user does not know the precise geometry of the trapping system and thus cannot mask out the phase outside the condensate surface. Though it is possible to create mask out areas without a vortex by multiplying the phase domain by the condensate density, this has not yet been implemented in GPUE. As such, a generalized vortex tracking methods for two and three-dimensional simulations is desirable.

In 2016, a method for three dimensional vortex tracking was proposed by Villois

et. al. [138]; however, this method has no computational complexity bound, assumes periodic boundary conditions, and required a large amount of communication between the device and host. This method begins to search for vortex locations by creating a Boolean domain of locations to search through by locating where the density is below a threshold. After the Boolean matrix is defined, the search is refined by locating phase plaquettes within this domain and iteratively locating a vortex skeleton. For the case where the condensate does not extend to the edges of the simulated domain, this method needs further refinement, and I have considered developing a similar method that leverages the vortex highlighting scheme to create three-dimensional vortex skeletons for vortex tracking in two and three dimensions. In this case, rather than simply searching for locations where the density is low, we could search for locations between peaks in the Sobel-filtered density, which correspond to likely vortex locations. This method could be easily re-worked for two-dimensional simulations as well, creating a dynamic mask every timestep for vortex tracking, thereby eliminated the current, unstable masking procedure.

5.5.2 General purpose Hamiltonian solver

As GPUE can perform multi-component simulations and can also parse expression trees, it is possible to simulate a wide variety of physical systems beyond the GPE. One such extension involves using the expression tree parser to solve arbitrarily provided Hamiltonians. This project would require significant software engineering time apart from GPUE-specific development, as the SSFM is not always the most optimal choice for solving certain quantum systems. In addition, expression trees can be much more easily created and used in other software frameworks, such as Julia.

5.5.3 Octree grid

Though the CSSFM method [19] does not provide adequate compression for vortex-based simulations, there is still an interesting open question about whether any grid compression

schemes might work with the SSFM. One such method that has been suggested is an octree-based grid, where each grid element is determined in a finite-volume fashion based on the Sobel filter of the density. This would allow for higher resolution in areas that have the greatest change in condensate density, which would be around the condensate edges, vortices, and perturbations, such as sound waves. One advantage of using an octree for this purpose is that FFTs may be performed with small modifications on the grid, thereby allowing for the SSFM with dynamic grids; however, the regridding operation is still computationally intensive and even though it is entirely possible to perform an FFT on this system, such functionality is beyond the scope of CuFFT. Therefore, significant engineering time must be devoted to either developing a CuFFT competitor for this case or for finding some method to allow CuFFT to be used in this way. Because the primary advantage of SSFM over other methods is the speed of FFT-based operations, there is likely little reason to use this method over FEM solutions.

GPUE.jl

In Chapter 3, I discussed the advantages of re-writing GPUE in Julia, and in Chapters 4 and 5, I discussed applications of GPUE and suggested areas where Julia could improve the software. In these chapters, I mentioned that post-processing operations, such as vortex tracking, calculating of the Lyapunov exponent spectrum, and calculation of the scissors mode oscillation angle, require processing output data from GPUE, and though vortex tracking and highlighting is already in-built to GPUE, it is still computationally complex operation. For this reason, it would be useful for both the timestepping method and all necessary post-processing tools to be available in the same language, and in Julia, this is possible with littler performance loss. This would also allow for a modular development and maintenance of GPUE in the future, where the timestepping methods remain unchanged as users develop post-processing methods when required.

In addition to these, there are many computer science researchers who are using Julia as a testing-bed for new ideas for software engineering and certain operations, such as

GPU-enabled automatic differentiation [216] could be a useful tool for future quantum simulations like those presented in this work. At the current data, the GPUE.jl package competes with GPUE (CUDA) in GPU performance; however, expression trees have not been completely implemented. Even so, as the development of the DistributedTranspose.jl package is in Julia, future development of GPUE.jl should quickly surpass the functionality of its CUDA-based variant.

5.6 Future simulations of quantum systems

In addition to further developments of GPUE and related software packages, there are also several new simulations that can be performed now on GPU hardware, such are multicomponent simulations with gauge fields and dynamic studies of the system introduced in Chapter 5. Because GPUE allows for the simulation of dynamic control processes through expression trees, further three-dimensional STA studies can also be performed.

Ultimately, this work has provided a toolbox for the simulation of various quantum phenomenon that were computational intractable before now, including the three-dimensional simulations of superfluid turbulence without relying on vortex-filament methods, and simulations of multicomponent systems with gauge fields. It has also developed novel methods for maximizing the size of the simulated domain with the SSFM, along with tools like the DistributedTranspose.jl that allow for spectral methods to be more widely used in HPC environments.

[Add other physics futures]

Appendix A

Simple vector additions in CUDA, OpenCL, and JuliaGPU

This is a compilation of an introductory GPGPU example in three languages (CUDA, OpenCL, and Julia) to show the differences in different approaches to GPGPU computation and the necessary abstractions required by users in order to perform basic tasks using GPGPU

A.1 Vector addition with C++

Firstly, a simple vector addition without GPGPU as a baseline:

```
#include <iostream>

int main(){
    int n = 1024;

    // Initializing host vectors
    double *a, *b, *c;
    a = (double*)malloc(sizeof(double)*n);
    b = (double*)malloc(sizeof(double)*n);
```

```
c = (double*)malloc(sizeof(double)*n);

// Initializing a and b
for (size_t i = 0; i < n; ++i){
    a[i] = i;
    b[i] = i;
    c[i] = 0;
}

// Vector Addition
for (size_t i = 0; i < n; ++i){
    c[i] = a[i] + b[i];
}

// Check to make sure everything works
for (size_t i = 0; i < n; ++i){
    if (c[i] != a[i] + b[i]){
        std::cout << "Yo. You failed. What a loser! Ha\n";
        exit(1);
    }
}

std::cout << "You passed the test, congratulations!\n";

free(a);
free(b);
free(c);
}
```

A.2 Vector addition with CUDA

Now for vector addition with CUDA. Here, it is important to note that it is not practical to ask users to write CUDA kernels, as they are not skilled in GPGPU. In addition, direct kernel manipulation would require a recompilation every run, which is cumbersome for most users along with dedicated directories for differently built binaries if running multiple GPUE simulations simultaneously. As such additional techniques are used in GPUE to allow users to write their own functions without recompiling the GPUE codebase every run, and these methods are discussed in Chapter ??

```
#include <iostream>
#include <math.h>
#include <chrono>

__global__ void vecAdd(double *a, double *b, double *c, int n){

    // Global Thread ID
    int id = blockIdx.x*blockDim.x + threadIdx.x;

    // Check to make sure we are in range
    if (id < n){
        c[id] = a[id] + b[id];
    }
}

int main(){

    int n = 1024;

    // Initializing host vectors
    double *a, *b, *c;
    a = (double*)malloc(sizeof(double)*n);
    b = (double*)malloc(sizeof(double)*n);
}
```

```
c = (double*)malloc(sizeof(double)*n);

// Initializing all device vectors
double *d_a, *d_b, *d_c;

cudaMalloc(&d_a, sizeof(double)*n);
cudaMalloc(&d_b, sizeof(double)*n);
cudaMalloc(&d_c, sizeof(double)*n);

// Initializing a and b
for (size_t i = 0; i < n; ++i){
    a[i] = i;
    b[i] = i;
    c[i] = 0;
}

cudaMemcpy(d_a, a, sizeof(double)*n, cudaMemcpyHostToDevice);
cudaMemcpy(d_b, b, sizeof(double)*n, cudaMemcpyHostToDevice);

dim3 threads, grid;

// threads are arbitrarily chosen
threads = {100, 1, 1};
grid = {(unsigned int)ceil((float)n/threads.x), 1, 1};
vecAdd<<<grid, threads>>>(d_a, d_b, d_c, n);

// Copying back to host
cudaMemcpy(c, d_c, sizeof(double)*n, cudaMemcpyDeviceToHost);

// Check to make sure everything works
for (size_t i = 0; i < n; ++i){
    if (c[i] != a[i] + b[i]){
        std::cout << "Yo. You failed. What a loser! Ha\n";
    }
}
```

```

    exit(1);
}

}

std::cout << "You passed the test, congratulations!\n";

free(a);
free(b);
free(c);

cudaFree(d_a);
cudaFree(d_b);
cudaFree(d_c);

}

```

A.3 Vector addition with OpenCL

Vector addition with OpenCL has notable advantages to CUDA, namely that users can update the kernels without recompilation. Though it is tempting to use OpenCL due to this, it is notably more cumbersome to write OpenCL code than CUDA, and it we lack the engineering resources to develop an OpenCL variant of GPUE. In addition, Julia provides similar benefits to OpenCL with much higher maintainability.

```

#define __CL_ENABLE_EXCEPTIONS

#include <CL/cl.hpp>
#include <iostream>
#include <vector>
#include <math.h>

// OpenCL kernel
const char *kernelSource =
"#pragma OPENCL EXTENSION cl_khr_fp64 : enable

```

```
"__kernel void vecAdd( __global double *a,          \n" \
"                      __global double *b,          \n" \
"                      __global double *c,          \n" \
"                      const unsigned int n){ \n" \
"                          \n" \
"      // Global Thread ID          \n" \
"      int id = get_global_id(0); \n" \
"                          \n" \
"      // Remain in boundaries          \n" \
"      if (id < n){ \n" \
"          c[id] = a[id] + b[id]; \n" \
"      } \n" \
"} \n" ;\n\nint main(){\n    unsigned int n = 1024;\n\n    double *h_a, *h_b, *h_c;\n\n    h_a = new double[n];\n    h_b = new double[n];\n    h_c = new double[n];\n\n    for (size_t i = 0; i < n; ++i){\n        h_a[i] = 1;\n        h_b[i] = 1;\n    }\n\n    cl::Buffer d_a, d_b, d_c;\n\n    cl_int err = CL_SUCCESS;\n    try{\n        std::vector<cl::Platform> platforms;
```

```
cl::Platform::get(&platforms);

if(platforms.size() == 0){
    std::cout << "Platforms size is 0\n";
    return -1;
}

cl_context_properties properties[] =
{ CL_CONTEXT_PLATFORM, (cl_context_properties)(platforms[0])(), 0 };

cl::Context context(CL_DEVICE_TYPE_GPU, properties);
std::vector<cl::Device> devices = context.getInfo<CL_CONTEXT_DEVICES>();

cl::CommandQueue queue(context, devices[0], 0, &err);

d_a = cl::Buffer(context, CL_MEM_READ_ONLY, n*sizeof(double));
d_b = cl::Buffer(context, CL_MEM_READ_ONLY, n*sizeof(double));
d_c = cl::Buffer(context, CL_MEM_WRITE_ONLY, n*sizeof(double));

queue.enqueueWriteBuffer(d_a, CL_TRUE, 0, n*sizeof(double), h_a);
queue.enqueueWriteBuffer(d_b, CL_TRUE, 0, n*sizeof(double), h_b);

cl::Program::Sources source(1,
    std::make_pair(kernelSource, strlen(kernelSource)));
cl::Program program_ = cl::Program(context, source);
program_.build(devices);

cl::Kernel kernel(program_, "vecAdd", &err);

kernel.setArg(0, d_a);
kernel.setArg(1, d_b);
kernel.setArg(2, d_c);
kernel.setArg(3, n);
```

```
    cl::NDRange localSize(64);

    cl::NDRange globalSize((int)(ceil(n/(float)64)*64));

    cl::Event event;
    queue.enqueueNDRangeKernel(
        kernel,
        cl::NullRange,
        globalSize,
        localSize,
        NULL,
        &event
    );

    event.wait();
    queue.enqueueReadBuffer(d_c, CL_TRUE, 0, n*sizeof(double), h_c);
}

catch(cl::Error err){
    std::cerr << "ERROR: " << err.what() << "(" << err.err() << ")\n";
}

// Check to make sure everything works
for (size_t i = 0; i < n; ++i){
    if (h_c[i] != h_a[i] + h_b[i]){
        std::cout << "Yo. You failed. What a loser! Ha\n";
        exit(1);
    }
}

std::cout << "You passed the test, congratulations!\n";

delete(h_a);
delete(h_b);
```

```
    delete(h_c);
}
```

A.4 Julia

Julia is a relatively new language, but boasts the performance of CUDA without as much bulk. In addition, Julia allows users to more easily look at the AST for compilation, thus rendering GPUE's AST process obsolete. Here is vector addition in Julia.

```
using CUDAnative, CUDAdrv, CuArrays, Test

function kernel_vadd(a, b, c)
    i = (blockIdx().x-1) * blockDim().x + threadIdx().x
    j = (blockIdx().y-1) * blockDim().y + threadIdx().y
    @inbounds c[i,j] = a[i,j] + b[i,j]
    return nothing
end

function main()
    res = 1024

    # CUDAdrv functionality: generate and upload data
    a = round.(rand(Float32, (1024, 1024)) * 100)
    b = round.(rand(Float32, (1024, 1024)) * 100)
    d_a = CuArray(a)
    d_b = CuArray(b)
    d_c = similar(d_a) # output array

    # run the kernel and fetch results
    # syntax: @cuda [kwargs...] kernel(args...)
    @cuda threads = (128, 1, 1) blocks = (div(res, 128), res, 1)
        kernel_vadd(d_a, d_b, d_c)
```

```
# CUDAdrv functionality: download data
# this synchronizes the device
c = Array(d_c)
a = Array(d_a)
b = Array(d_b)

@test isapprox(a+b, c)

end
```

Bibliography

- [1] J. A. Kahle, J. Moreno, and D. Dreps. 2.1 summit and sierra: Designing ai/hpc supercomputers. In *2019 IEEE International Solid-State Circuits Conference - (ISSCC)*, pages 42–43, Feb 2019.
- [2] Ruymán Reyes, Iván López-Rodríguez, Juan J Fumero, and Francisco De Sande. accull: an openacc implementation with cuda and opencl support. In *European Conference on Parallel Processing*, pages 871–882. Springer, 2012.
- [3] Massimiliano Fatica, P LeGresley, I Buck, J Stone, J Phillips, S Morton, and P Mikaevicius. High performance computing with cuda. *SC08*, 2008.
- [4] Tim Besard, Pieter Verstraete, and Bjorn De Sutter. High-level gpu programming in julia. *arXiv preprint arXiv:1604.03410*, 2016.
- [5] Aaftab Munshi, Benedict Gaster, Timothy G Mattson, and Dan Ginsburg. *OpenCL programming guide*. Pearson Education, 2011.
- [6] John Cheng, Max Grossman, and Ty McKercher. *Professional Cuda C Programming*. John Wiley & Sons, 2014.
- [7] Matteo Frigo and Steven G Johnson. Fftw: An adaptive software architecture for the fft. In *Proceedings of the 1998 IEEE International Conference on Acoustics, Speech and Signal Processing, ICASSP'98 (Cat. No. 98CH36181)*, volume 3, pages 1381–1384. IEEE, 1998.

- [8] Doru Thom Popovici, Tze Meng Low, and Franz Franchetti. Large bandwidth-efficient ffts on multicore and multi-socket systems. In *2018 IEEE International Parallel and Distributed Processing Symposium (IPDPS)*, pages 379–388. IEEE, 2018.
- [9] HUGH Merz. Cufft 1.1/2.0 vs fftw 3.1. 2 (x86_64) vs fftw 3.2 (cell) comparison, 2016.
- [10] Marius Brehler, Malte Schirwon, Dominik G  ddecke, and Peter M Krummrich. A gpu-accelerated fourth-order runge–kutta in the interaction picture method for the simulation of nonlinear signal propagation in multimode fibers. *Journal of Lightwave Technology*, 35(17):3622–3628, 2017.
- [11] James Schloss, Albert Benseny, J  r  mie Gillet, Jacob Swain, and Thomas Busch. Non-adiabatic generation of noon states in a tonks–girardeau gas. *New Journal of Physics*, 18(3):035012, 2016.
- [12] James R Schloss and Lee J Riordan. Gpue: Graphics processing unit gross-pitaevskii equation solver. *J. Open Source Software*, 3(32):1037, 2018.
- [13] Tiantian Zhang, James Schloss, Andreas Thomasen, Lee James O’Riordan, Thomas Busch, and Angela White. Chaotic few-body vortex dynamics in rotating bose-einstein condensates. *Physical Review Fluids*, 4(5):054701, 2019.
- [14] James Schloss, Peter Barnett, Rashi Sachdeva, and Thomas Busch. Controlled creation of three-dimensional vortex structures in bose–einstein condensates using artificial magnetic fields, 2019.
- [15] Govind P Agrawal. Nonlinear fiber optics. In *Nonlinear Science at the Dawn of the 21st Century*, pages 195–211. Springer, 2000.
- [16] O. V. Sinkin, R. Holzlöhner, J. Zweck, and C. R. Menyuk. Optimization of the split-

- step fourier method in modeling optical-fiber communications systems. *Journal of Lightwave Technology*, 21(1):61–68, Jan 2003.
- [17] T. T. Meirelles, A. A. Rieznik, and H. L. Fragnito. Study on a new split-step fourier algorithm for optical fiber transmission systems simulations. In *SBMO/IEEE MTT-S International Conference on Microwave and Optoelectronics, 2005.*, pages 100–102, July 2005.
- [18] Rao Min, Sun Xiao-Han, and Zhang Ming-De. A modified split-step fourier method for optical pulse propagation with polarization mode dispersion. *Chinese Physics*, 12(5):502–506, apr 2003.
- [19] Cihan Bayindir. Compressive split-step fourier method. *arXiv preprint arXiv:1512.03932*, 2015.
- [20] JAC Weideman and BM Herbst. Split-step methods for the solution of the nonlinear schrödinger equation. *SIAM Journal on Numerical Analysis*, 23(3):485–507, 1986.
- [21] Hanquan Wang. Numerical studies on the split-step finite difference method for nonlinear schrödinger equations. *Applied Mathematics and Computation*, 170(1):17–35, 2005.
- [22] John Charles Butcher. *Numerical methods for ordinary differential equations*. John Wiley & Sons, 2016.
- [23] John Crank and Phyllis Nicolson. A practical method for numerical evaluation of solutions of partial differential equations of the heat-conduction type. In *Mathematical Proceedings of the Cambridge Philosophical Society*, volume 43, pages 50–67. Cambridge University Press, 1947.
- [24] Samuel Daniel Conte and Carl De Boor. *Elementary numerical analysis: an algorithmic approach*, volume 78. SIAM, 2017.

- [25] Llewellyn Thomas. Elliptic problems in linear differential equations over a network: Watson scientific computing laboratory. *Columbia Univ., NY*, 1949.
- [26] Dominik Goddeke and Robert Strzodka. Cyclic reduction tridiagonal solvers on gpus applied to mixed-precision multigrid. *IEEE Transactions on Parallel and Distributed Systems*, 22(1):22–32, 2010.
- [27] HH Wang. A parallel method for tridiagonal equations. *ACM Transactions on Mathematical Software (TOMS)*, 7(2):170–183, 1981.
- [28] Roland A Sweet. A cyclic reduction algorithm for solving block tridiagonal systems of arbitrary dimension. *SIAM Journal on Numerical Analysis*, 14(4):706–720, 1977.
- [29] R Benzi, M Colella, M Briscolini, and Paolo Santangelo. A simple point vortex model for two-dimensional decaying turbulence. *Physics of Fluids A: Fluid Dynamics*, 4(5):1036–1039, 1992.
- [30] KW Schwarz. Three-dimensional vortex dynamics in superfluid he 4: Homogeneous superfluid turbulence. *Physical Review B*, 38(4):2398, 1988.
- [31] Gilbert Strang. On the construction and comparison of difference schemes. *SIAM journal on numerical analysis*, 5(3):506–517, 1968.
- [32] Shev MacNamara and Gilbert Strang. Operator splitting. In *Splitting Methods in Communication, Imaging, Science, and Engineering*, pages 95–114. Springer, 2016.
- [33] James W Cooley and John W Tukey. An algorithm for the machine calculation of complex fourier series. *Mathematics of computation*, 19(90):297–301, 1965.
- [34] Gian Carlo Wick. Properties of bethe-salpeter wave functions. *Physical Review*, 96(4):1124, 1954.
- [35] Mark Harris et al. Optimizing parallel reduction in cuda. *Nvidia developer technology*, 2(4):70, 2007.

- [36] A. B. Migdal. Quantum theory of the monatomic ideal gas, part II. *Physikalisch-mathematische Klasse*, 1:3, 1925.
- [37] Alexander L. Fetter and John Dirk Walecka. *Quantum Theory of Many-Particle Systems*. Dover Publications, 2003.
- [38] Marvin Girardeau. Relationship between systems of impenetrable bosons and fermions in one dimension. *Journal of Mathematical Physics*, 1(6):516–523, 1960.
- [39] P. Nozières and S. Schmitt-Rink. Bose condensation in an attractive fermion gas: From weak to strong coupling superconductivity. *Journal of Low Temperature Physics*, 59(3):195–211, 1985.
- [40] Aurel Bulgac, Michael McNeil Forbes, Michelle M Kelley, Kenneth J Roche, and Gabriel Wlazłowski. Quantized superfluid vortex rings in the unitary fermi gas. *Physical review letters*, 112(2):025301, 2014.
- [41] Alan Aversa. The gross-pitaevskii equation: A non-linear schrödinger equation, 2008.
- [42] N. N. Bogoliubov. On the theory of superfluidity. *J. Phys. (USSR)*, 11:23–32, 1947.
- [43] Franco Dalfovo, Stefano Giorgini, Lev P. Pitaevskii, and Sandro Stringari. Theory of Bose-Einstein condensation in trapped gases. *Rev. Mod. Phys.*, 71:463–512, Apr 1999.
- [44] E. P. Gross. Structure of a quantized vortex in boson systems. *Il Nuovo Cimento (1955-1965)*, 20(3):454–477, 1961.
- [45] L. Pitaevskii. Vortex lines in an imperfect bose gas. *Zh. Eksp. Teor. Fiz.*, 40:646, 1961.
- [46] C. J. Pethick and H. Smith. *Bose-Einstein Condensation in Dilute Gases*. Cambridge University Press, 2002.

- [47] Alexander L. Fetter. Rotating trapped bose-einstein condensates. *Rev. Mod. Phys.*, 81:647–691, May 2009.
- [48] Masahito Ueda. *Fundamentals and new frontiers of Bose-Einstein condensation*. World Scientific, 2010.
- [49] J. Allen and A. Misener. Flow of liquid Helium II. *Nature*, 142:643, 1938.
- [50] A. B. Migdal. A phenomenological approach to the theory of the nucleus. *Soviet Physics JETP*, 10:176, 1960.
- [51] M. H. Anderson, J. R. Ensher, M. R. Matthews, C. E. Wieman, and E. A. Cornell. Observation of Bose–Einstein condensation in a dilute atomic vapor. *Science*, 269(5221):198–201, 1995.
- [52] AA Abrikosov. The magnetic properties of superconducting alloys. *Journal of Physics and Chemistry of Solids*, 2(3):199–208, 1957.
- [53] Alexander L Fetter and Anatoly A Svidzinsky. Vortices in a trapped dilute bose-einstein condensate. *Journal of Physics: Condensed Matter*, 13(12):R135, 2001.
- [54] KW Madison, F Chevy, W Wohlleben, and Jl Dalibard. Vortex formation in a stirred bose-einstein condensate. *Physical review letters*, 84(5):806, 2000.
- [55] Matthew D. Reichl and Erich J. Mueller. Vortex ring dynamics in trapped Bose–Einstein condensates. *Phys. Rev. A*, 88:053626, Nov 2013.
- [56] Carlo F. Barenghi, Ladislav Skrbek, and Katepalli R. Sreenivasan. Introduction to quantum turbulence. *PNAS*, 111:4647, 2014.
- [57] R. P. Feynman. *Progress in Low Temperature Physics: Chapter II, Application of Quantum Mechanics to Liquid Helium*, volume 1. Interscience Publishers Inc, 1955.
- [58] LJ O’Riordan, AC White, and Th Busch. Moiré superlattice structures in kicked bose-einstein condensates. *Physical Review A*, 93(2):023609, 2016.

- [59] Lee James O’Riordan and Thomas Busch. Topological defect dynamics of vortex lattices in bose-einstein condensates. *Physical Review A*, 94(5):053603, 2016.
- [60] JR Abo-Shaeer, C Raman, JM Vogels, and Wolfgang Ketterle. Observation of vortex lattices in bose-einstein condensates. *Science*, 292(5516):476–479, 2001.
- [61] V. Schweikhard, I. Coddington, P. Engels, V. P. Mogendorff, and E. A. Cornell. Rapidly rotating Bose-Einstein condensates in and near the lowest landau level. *Phys. Rev. Lett.*, 92:040404, Jan 2004.
- [62] F Chevy and J Dalibard. Rotating bose-einstein condensates. *Europhysics News*, 37(1):12–16, 2006.
- [63] E Hodby, G Hechenblaikner, SA Hopkins, OM Marago, and CJ Foot. Vortex nucleation in bose-einstein condensates in an oblate, purely magnetic potential. *Physical review letters*, 88(1):010405, 2001.
- [64] PC Haljan, I Coddington, Peter Engels, and Eric A Cornell. Driving bose-einstein-condensate vorticity with a rotating normal cloud. *Physical review letters*, 87(21):210403, 2001.
- [65] Vincent Bretin, Sabine Stock, Yannick Seurin, and Jean Dalibard. Fast rotation of a bose-einstein condensate. *Physical review letters*, 92(5):050403, 2004.
- [66] Peter Engels, I Coddington, PC Haljan, Volker Schweikhard, and Eric A Cornell. Observation of long-lived vortex aggregates in rapidly rotating bose-einstein condensates. *Physical review letters*, 90(17):170405, 2003.
- [67] Avinash Kumar, Romain Dubessy, Thomas Badr, Camilla De Rossi, Mathieu de Goér de Herve, Laurent Longchambon, and Hélène Perrin. Producing superfluid circulation states using phase imprinting. *Physical Review A*, 97(4):043615, 2018.

- [68] Stuart Moulder, Scott Beattie, Robert P. Smith, Naaman Tammuz, and Zoran Hadzibabic. Quantized supercurrent decay in an annular bose-einstein condensate. *Phys. Rev. A*, 86:013629, Jul 2012.
- [69] S. Burger, K. Bongs, S. Dettmer, W. Ertmer, K. Sengstock, A. Sanpera, G. V. Shlyapnikov, and M. Lewenstein. Dark solitons in bose-einstein condensates. *Phys. Rev. Lett.*, 83:5198–5201, Dec 1999.
- [70] J Denschlag, Je E Simsarian, Di L Feder, Charles W Clark, La A Collins, J Cubizolles, Lu Deng, Edward W Hagley, Kristian Helmerson, William P Reinhardt, et al. Generating solitons by phase engineering of a bose-einstein condensate. *Science*, 287(5450):97–101, 2000.
- [71] Biao Wu, Jie Liu, and Qian Niu. Controlled generation of dark solitons with phase imprinting. *Physical review letters*, 88(3):034101, 2002.
- [72] C. Ryu, M. F. Andersen, P. Cladé, Vasant Natarajan, K. Helmerson, and W. D. Phillips. Observation of persistent flow of a bose-einstein condensate in a toroidal trap. *Phys. Rev. Lett.*, 99:260401, Dec 2007.
- [73] Mark Kasevich and Steven Chu. Atomic interferometry using stimulated raman transitions. *Phys. Rev. Lett.*, 67:181–184, Jul 1991.
- [74] M Gajda, M Lewenstein, K Sengstock, G Birkl, W Ertmer, et al. Optical generation of vortices in trapped bose-einstein condensates. *Physical Review A*, 60(5):R3381, 1999.
- [75] Yong-il Shin, Michele Saba, Mukund Vengalattore, TA Pasquini, Christian Sanner, AE Leanhardt, Mara Prentiss, DE Pritchard, and Wolfgang Ketterle. Dynamical instability of a doubly quantized vortex in a bose-einstein condensate. *Physical review letters*, 93(16):160406, 2004.

- [76] Angela C White, Brian P Anderson, and Vanderlei S Bagnato. Vortices and turbulence in trapped atomic condensates. *Proceedings of the National Academy of Sciences*, 111(Supplement 1):4719–4726, 2014.
- [77] F Maucher, SA Gardiner, and IG Hughes. Excitation of knotted vortex lines in matter waves. *New Journal of Physics*, 18(6):063016, 2016.
- [78] Y.-J. Lin, R. L. Compton, K. Jimenez-Garcia, J. V. Porto, and I. B. Spielman. Synthetic magnetic fields for ultracold neutral atoms. *Nature*, 462(7273):628–632, Dec 2009.
- [79] J. Dalibard. Introduction to the physics of artificial gauge fields. *ArXiv e-prints*, April 2015.
- [80] Rajiv Bhat. *Bosons in rotating optical lattices*. PhD thesis, Indian Institute of Technology Kanpur, 2001.
- [81] A. Tonomura M. Peshkin. *The Aharonov–Bohm Effect*, volume 340. Springer-Verlag, 1989.
- [82] Kenichi Kasamatsu, Makoto Tsubota, and Masahito Ueda. Vortices in multicomponent bose-einstein condensates. *International Journal of Modern Physics B*, 19(11):1835–1904, 2005.
- [83] Weizhu Bao. Ground states and dynamics of multicomponent bose-einstein condensates. *Multiscale Modeling & Simulation*, 2(2):210–236, 2004.
- [84] Peter Mason. Ground states of two-component condensates in a harmonic plus gaussian trap. *The European Physical Journal B*, 86(11):453, 2013.
- [85] J Werschnik and EKU Gross. Quantum optimal control theory. *Journal of Physics B: Atomic, Molecular and Optical Physics*, 40(18):R175, 2007.

- [86] D Gu  ry-Odelin, A Ruschhaupt, A Kiely, E Torrontegui, S Mart  nez-Garaot, and JG Muga. Shortcuts to adiabaticity: concepts, methods, and applications. *arXiv preprint arXiv:1904.08448*, 2019.
- [87] Frank L Lewis, Draguna Vrabie, and Vassilis L Syrmos. *Optimal control*. John Wiley & Sons, 2012.
- [88] Sebastian Ruder. An overview of gradient descent optimization algorithms. *arXiv preprint arXiv:1609.04747*, 2016.
- [89] J. A. Nelder and R. Mead. A Simplex Method for Function Minimization. *The Computer Journal*, 7(4):308–313, 01 1965.
- [90] John R Koza. Genetic programming. 1997.
- [91] Tamara G Kolda, Robert Michael Lewis, and Virginia Torczon. Optimization by direct search: New perspectives on some classical and modern methods. *SIAM review*, 45(3):385–482, 2003.
- [92] Robert Michael Lewis, Anne Shepherd, and Virginia Torczon. Implementing generating set search methods for linearly constrained minimization. *SIAM Journal on Scientific Computing*, 29(6):2507–2530, 2007.
- [93] Hartmut Pohlheim. Examples of objective functions. *Retrieved*, 4(10):2012, 2007.
- [94] Erik Torrontegui, Sara Ib  ez, Sofia Mart  nez-Garaot, Michele Modugno, Adolfo del Campo, David Gu  ry-Odelin, Andreas Ruschhaupt, Xi Chen, and Juan Gonzalo Muga. Shortcuts to adiabaticity. In *Advances in atomic, molecular, and optical physics*, volume 62, pages 117–169. Elsevier, 2013.
- [95] H Ralph Lewis Jr and WB Riesenfeld. An exact quantum theory of the time-dependent harmonic oscillator and of a charged particle in a time-dependent electromagnetic field. *Journal of Mathematical Physics*, 10(8):1458–1473, 1969.

- [96] H Ralph Lewis and PGL Leach. A direct approach to finding exact invariants for one-dimensional time-dependent classical hamiltonians. *Journal of Mathematical Physics*, 23(12):2371–2374, 1982.
- [97] M. D. Girardeau, E. M. Wright, and J. M. Triscari. Ground-state properties of a one-dimensional system of hard-core bosons in a harmonic trap. *Phys. Rev. A*, 63:033601, Feb 2001.
- [98] M. D. Girardeau and E. M. Wright. Measurement of one-particle correlations and momentum distributions for trapped 1d gases. *Phys. Rev. Lett.*, 87:050403, Jul 2001.
- [99] John C Slater. The theory of complex spectra. *Physical Review*, 34(10):1293, 1929.
- [100] Kunal K. Das, M. D. Girardeau, and E. M. Wright. Interference of a thermal tonks gas on a ring. *Phys. Rev. Lett.*, 89:170404, Oct 2002.
- [101] M. D. Girardeau and A. Minguzzi. Motion of an impurity particle in an ultracold quasi-one-dimensional gas of hard-core bosons. *Phys. Rev. A*, 79:033610, Mar 2009.
- [102] David W. Hallwood, Thomas Ernst, and Joachim Brand. Robust mesoscopic superposition of strongly correlated ultracold atoms. *Phys. Rev. A*, 82:063623, Dec 2010.
- [103] C Schenke, A Minguzzi, and FWJ Hekking. Probing superfluidity of a mesoscopic tonks-girardeau gas. *Physical Review A*, 85(5):053627, 2012.
- [104] Andreas Nunnenkamp, Ana Maria Rey, and Keith Burnett. Generation of macroscopic superposition states in ring superlattices. *Phys. Rev. A*, 77:023622, Feb 2008.
- [105] David W Hallwood, Keith Burnett, and Jacob Dunningham. The barriers to producing multiparticle superposition states in rotating bose-einstein condensates. *Journal of Modern Optics*, 54(13-15):2129–2148, 2007.

- [106] S. Martínez-Garaot, A. Ruschhaupt, J. Gillet, Th. Busch, and J. G. Muga. Fast quasiadiabatic dynamics. *Phys. Rev. A*, 92:043406, Oct 2015.
- [107] A. del Campo. Long-time behavior of many-particle quantum decay. *Phys. Rev. A*, 84:012113, Jul 2011.
- [108] K. Lelas, T. Šeba, and H. Buljan. Loschmidt echo in one-dimensional interacting bose gases. *Phys. Rev. A*, 84:063601, Dec 2011.
- [109] Xi Chen and J. G. Muga. Transient energy excitation in shortcuts to adiabaticity for the time-dependent harmonic oscillator. *Phys. Rev. A*, 82:053403, Nov 2010.
- [110] Xi Chen, A. Ruschhaupt, S. Schmidt, A. del Campo, D. Guéry-Odelin, and J. G. Muga. Fast optimal frictionless atom cooling in harmonic traps: Shortcut to adiabaticity. *Phys. Rev. Lett.*, 104:063002, Feb 2010.
- [111] Shumpei Masuda and Katsuhiro Nakamura. Fast-forward of adiabatic dynamics in quantum mechanics. *Proceedings of the Royal Society A: Mathematical, Physical and Engineering Sciences*, 466(2116):1135–1154, 2009.
- [112] E. Torrontegui, S. Ibáñez, Xi Chen, A. Ruschhaupt, D. Guéry-Odelin, and J. G. Muga. Fast atomic transport without vibrational heating. *Phys. Rev. A*, 83:013415, Jan 2011.
- [113] Shumpei Masuda. Acceleration of adiabatic transport of interacting particles and rapid manipulations of a dilute bose gas in the ground state. *Phys. Rev. A*, 86:063624, Dec 2012.
- [114] C.F. Phelan, T. Hennessy, and Th. Busch. Shaping the evanescent field of optical nanofibers for cold atom trapping. *Opt. Express*, 21(22):27093–27101, Nov 2013.
- [115] Shumpei Masuda, Katsuhiro Nakamura, and Adolfo del Campo. High-fidelity rapid ground-state loading of an ultracold gas into an optical lattice. *Phys. Rev. Lett.*, 113:063003, Aug 2014.

- [116] JR Gurd. A taxonomy of parallel computer architectures. In *1988 International Specialist Seminar on the Design and Application of Parallel Digital Processors*, pages 57–61. IET, 1988.
- [117] Kenneth Czechowski, Casey Battaglino, Chris McClanahan, Kartik Iyer, P-K Yewng, and Richard Vuduc. On the communication complexity of 3d ffts and its implications for exascale. In *Proceedings of the 26th ACM international conference on Supercomputing*, pages 205–214. ACM, 2012.
- [118] P Wittek. Comparing three numerical solvers of the gross-pitaevskii equation, 2016.
- [119] Xavier Antoine and Romain Duboscq. Gpelab, a matlab toolbox to solve gross–pitaevskii equations i: Computation of stationary solutions. *Computer Physics Communications*, 185(11):2969–2991, 2014.
- [120] Peter Wittek and Fernando M Cucchietti. A second-order distributed trotter–suzuki solver with a hybrid cpu–gpu kernel. *Computer Physics Communications*, 184(4):1165–1171, 2013.
- [121] Michael Garland, Scott Le Grand, John Nickolls, Joshua Anderson, Jim Hardwick, Scott Morton, Everett Phillips, Yao Zhang, and Vasily Volkov. Parallel computing experiences with cuda. *IEEE micro*, 28(4):13–27, 2008.
- [122] Victor W Lee, Changkyu Kim, Jatin Chhugani, Michael Deisher, Daehyun Kim, Anthony D Nguyen, Nadathur Satish, Mikhail Smelyanskiy, Srinivas Chennupaty, Per Hammarlund, et al. Debunking the 100x gpu vs. cpu myth: an evaluation of throughput computing on cpu and gpu. *ACM SIGARCH computer architecture news*, 38(3):451–460, 2010.
- [123] John Nickolls and William J Dally. The gpu computing era. *IEEE micro*, 30(2):56–69, 2010.

- [124] Sandra Wienke, Paul Springer, Christian Terboven, and Dieter an Mey. Openacc—first experiences with real-world applications. In *European Conference on Parallel Processing*, pages 859–870. Springer, 2012.
- [125] Rohit Chandra, Leo Dagum, David Kohr, Ramesh Menon, Dror Maydan, and Jeff McDonald. *Parallel programming in OpenMP*. Morgan kaufmann, 2001.
- [126] Mark Harris. An efficient matrix transpose in cuda c/c++. *Retrieved July, 26:2018*, 2013.
- [127] Denis Foley and John Danskin. Ultra-performance pascal gpu and nvlink interconnect. *IEEE Micro*, 37(2):7–17, 2017.
- [128] Vladimir Lončar, Luis E Young-S, Srdjan Škrbić, Paulsamy Muruganandam, Sadhan K Adhikari, and Antun Balaž. Openmp, openmp/mpi, and cuda/mpi c programs for solving the time-dependent dipolar gross–pitaevskii equation. *Computer Physics Communications*, 209:190–196, 2016.
- [129] Hao Wang, Sreeram Potluri, Devendar Bureddy, Carlos Rosales, and Dhabaleswar K Panda. Gpu-aware mpi on rdma-enabled clusters: Design, implementation and evaluation. *IEEE Transactions on Parallel and Distributed Systems*, 25(10):2595–2605, 2013.
- [130] Tim Besard, Valentin Churavy, Alan Edelman, and Bjorn De Sutter. Rapid software prototyping for heterogeneous and distributed platforms. *Advances in Engineering Software*, 132:29–46, 2019.
- [131] Jeff Bezanson, Alan Edelman, Stefan Karpinski, and Viral B Shah. Julia: A fresh approach to numerical computing. *SIAM review*, 59(1):65–98, 2017.
- [132] Tim Besard, Christophe Foket, and Bjorn De Sutter. Effective extensible programming: unleashing julia on gpus. *IEEE Transactions on Parallel and Distributed Systems*, 30(4):827–841, 2018.

- [133] Lee James O’Riordan. *Non-equilibrium vortex dynamics in rapidly rotating Bose-Einstein condensates*. PhD thesis, Okinawa Institute of Science and Technology Graduate University, 2017.
- [134] Robert F Cohen and Roberto Tamassia. Dynamic expression trees and their applications. In *SODA*, pages 52–61, 1991.
- [135] Ruymán Reyes and Francisco de Sande. Automatic code generation for gpus in llc. *The Journal of Supercomputing*, 58(3):349–356, 2011.
- [136] Mark A Davenport, Marco F Duarte, Yonina C Eldar, and Gitta Kutyniok. Introduction to compressed sensing. *Compressed sensing: theory and applications*, 105:106, 2012.
- [137] James Schloss and Lee O’riordan.
- [138] Alberto Villois, Giorgio Krstulovic, Davide Proment, and Hayder Salman. A vortex filament tracking method for the gross–pitaevskii model of a superfluid. *Journal of Physics A: Mathematical and Theoretical*, 49(41):415502, 2016.
- [139] Yulong Guo, Xiaopei Liu, Chi Xiong, Xuemiao Xu, and Chi-Wing Fu. Towards high-quality visualization of superfluid vortices. *IEEE transactions on visualization and computer graphics*, 24(8):2440–2455, 2018.
- [140] John Canny. A computational approach to edge detection. *IEEE Transactions on pattern analysis and machine intelligence*, (6):679–698, 1986.
- [141] Jose L Jodra, Ibai Gurrutxaga, and Javier Muguerza. Efficient 3d transpositions in graphics processing units. *International Journal of Parallel Programming*, 43(5):876–891, 2015.
- [142] Gregory Ruetsch and Massimiliano Fatica. *CUDA Fortran for scientists and engineers: best practices for efficient CUDA Fortran programming*. Elsevier, 2013.

- [143] Steven H Strogatz. *Nonlinear dynamics and chaos: with applications to physics, biology, chemistry, and engineering*. CRC Press, 2018.
- [144] EA Spiegel. Chaos: a mixed metaphor for turbulence. *Proceedings of the Royal Society of London. A. Mathematical and Physical Sciences*, 413(1844):87–95, 1987.
- [145] Luca Biferale, Guido Boffetta, A Celani, BJ Devenish, A Lanotte, and Federico Toschi. Lagrangian statistics of particle pairs in homogeneous isotropic turbulence. *Physics of Fluids*, 17(11):115101, 2005.
- [146] Arjun Berera and Richard DJG Ho. Chaotic properties of a turbulent isotropic fluid. *Physical review letters*, 120(2):024101, 2018.
- [147] SK Nemirovskii and W Fiszdon. Chaotic quantized vortices and hydrodynamic processes in superfluid helium. *Reviews of Modern Physics*, 67(1):37, 1995.
- [148] Nikos Kyriakopoulos, Vassilis Koukouloyannis, Charalampos Skokos, and Panayotis G Kevrekidis. Chaotic behavior of three interacting vortices in a confined bose-einstein condensate. *Chaos: An Interdisciplinary Journal of Nonlinear Science*, 24(2):024410, 2014.
- [149] Vassilis Koukouloyannis, George Voyatzis, and Panayotis G Kevrekidis. Dynamics of three noncorotating vortices in bose-einstein condensates. *Physical Review E*, 89(4):042905, 2014.
- [150] R Navarro, R Carretero-González, PJ Torres, PG Kevrekidis, DJ Frantzeskakis, MW Ray, E Altuntas, and DS Hall. Dynamics of a few corotating vortices in bose-einstein condensates. *Physical review letters*, 110(22):225301, 2013.
- [151] Caroline Nore, Malek Abid, and ME Brachet. Kolmogorov turbulence in low-temperature superflows. *Physical review letters*, 78(20):3896, 1997.
- [152] Steven R Stalp, L Skrbek, and Russell J Donnelly. Decay of grid turbulence in a finite channel. *Physical review letters*, 82(24):4831, 1999.

- [153] Tsunehiko Araki, Makoto Tsubota, and Sergey K Nemirovskii. Energy spectrum of superfluid turbulence with no normal-fluid component. *Physical review letters*, 89(14):145301, 2002.
- [154] Julien Salort, Christophe Baudet, Bernard Castaing, Benoît Chabaud, François Daviaud, Thomas Didelot, Pantxo Diribarne, Bérengère Dubrulle, Yves Gagne, Frédéric Gauthier, et al. Turbulent velocity spectra in superfluid flows. *Physics of Fluids*, 22(12):125102, 2010.
- [155] Hassan Aref and N Pomphrey. Integrable and chaotic motions of four vortices. i. the case of identical vortices. *Proceedings of the Royal Society of London. A. Mathematical and Physical Sciences*, 380(1779):359–387, 1982.
- [156] Hassan Aref and Neil Pomphrey. Integrable and chaotic motions of four vortices. *Physics Letters A*, 78(4):297–300, 1980.
- [157] Hassan Aref. Integrable, chaotic, and turbulent vortex motion in two-dimensional flows. *Annual Review of Fluid Mechanics*, 15(1):345–389, 1983.
- [158] Sang Won Seo, Bumsuk Ko, Joon Hyun Kim, and Yong-il Shin. Observation of vortex-antivortex pairing in decaying 2d turbulence of a superfluid gas. *Scientific reports*, 7(1):4587, 2017.
- [159] Kali E Wilson, Zachary L Newman, Joseph D Lowney, and Brian P Anderson. In situ imaging of vortices in bose-einstein condensates. *Physical Review A*, 91(2):023621, 2015.
- [160] DV Freilich, DM Bianchi, AM Kaufman, TK Langin, and DS Hall. Real-time dynamics of single vortex lines and vortex dipoles in a bose-einstein condensate. *Science*, 329(5996):1182–1185, 2010.
- [161] Simone Serafini, Luca Galantucci, Elena Iseni, Tom Bienaimé, Russell N Bisset, Carlo F Barenghi, Franco Dalfovo, Giacomo Lamporesi, and Gabriele Ferrari. Vor-

- tex reconnections and rebounds in trapped atomic bose-einstein condensates. *Physical Review X*, 7(2):021031, 2017.
- [162] TW Neely, AS Bradley, EC Samson, SJ Rooney, Ewan M Wright, KJH Law, R Carretero-González, PG Kevrekidis, MJ Davis, and Brian P Anderson. Characteristics of two-dimensional quantum turbulence in a compressible superfluid. *Physical review letters*, 111(23):235301, 2013.
- [163] Woo Jin Kwon, Geol Moon, Jae-yoon Choi, Sang Won Seo, and Yong-il Shin. Relaxation of superfluid turbulence in highly oblate bose-einstein condensates. *Physical Review A*, 90(6):063627, 2014.
- [164] Guillaume Gauthier, Matthew T Reeves, Xiaoquan Yu, Ashton S Bradley, Mark Baker, Thomas A Bell, Halina Rubinsztein-Dunlop, Matthew J Davis, and Tyler W Neely. Negative-temperature onsager vortex clusters in a quantum fluid. *arXiv preprint arXiv:1801.06951*, 2018.
- [165] Shaun P Johnstone, Andrew J Groszek, Philip T Starkey, Christopher J Billington, Tapiro P Simula, and Kristian Helmerson. Order from chaos: Observation of large-scale flow from turbulence in a two-dimensional superfluid. *arXiv preprint arXiv:1801.06952*, 2018.
- [166] Amandine Aftalion and Qiang Du. Vortices in a rotating bose-einstein condensate: Critical angular velocities and energy diagrams in the thomas-fermi regime. *Physical Review A*, 64(6):063603, 2001.
- [167] Alexandra V Zampetaki, R Carretero-González, PG Kevrekidis, FK Diakonos, and DJ Frantzeskakis. Exploring rigidly rotating vortex configurations and their bifurcations in atomic bose-einstein condensates. *Physical Review E*, 88(4):042914, 2013.

- [168] Tiantian Zhang, James Schloss, Andreas Thomasen, Lee James O’Riordan, Thomas Busch, and Angela White.
- [169] Alan Wolf, Jack B Swift, Harry L Swinney, and John A Vastano. Determining lyapunov exponents from a time series. *Physica D: Nonlinear Phenomena*, 16(3):285–317, 1985.
- [170] Daniel H Wacks, Andrew W Baggaley, and Carlo F Barenghi. Large-scale superfluid vortex rings at nonzero temperatures. *Physical Review B*, 90(22):224514, 2014.
- [171] B. P. Anderson, P. C. Haljan, C. A. Regal, D. L. Feder, L. A. Collins, C. W. Clark, and E. A. Cornell. Watching dark solitons decay into vortex rings in a bose-einstein condensate. *Phys. Rev. Lett.*, 86:2926–2929, Apr 2001.
- [172] Mark JH Ku, Biswaroop Mukherjee, Tarik Yefsah, and Martin W Zwierlein. Cascade of solitonic excitations in a superfluid fermi gas: From planar solitons to vortex rings and lines. *Physical review letters*, 116(4):045304, 2016.
- [173] Michael Robin Matthews, Brian P Anderson, PC Haljan, DS Hall, CE Wieman, and Eric A Cornell. Vortices in a bose-einstein condensate. *Physical Review Letters*, 83(13):2498, 1999.
- [174] Tarik Yefsah, Ariel T Sommer, Mark JH Ku, Lawrence W Cheuk, Wenjie Ji, Waseem S Bakr, and Martin W Zwierlein. Heavy solitons in a fermionic superfluid. *Nature*, 499(7459):426, 2013.
- [175] T. E. Faber. *Fluid Dynamics for Physicists*. Cambridge University Press, 1995.
- [176] Ira M. Cohen David R. Dowling, Pijush K. Kundu. *Fluid Mechanics*. Academic Press, Boston, fifth edition edition, 2012.
- [177] D. J. Tritton. *Physical Fluid Dynamics*. Oxford University Press, 1988.
- [178] L. D. Landau and E. M. Lifshitz. *Fluid Mechanics*. Butterworth-Heinemann, 1987.

- [179] R. Donnelly. *Quantized Vortices in Helium II*. Cambridge University Press, 1991.
- [180] A. Sommerfield. *Mechanics of Deformable Bodies: Lectures of Theoretical Physics*, volume 2. Academic Press, 1960.
- [181] R. M. Caplan, J. D. Talley, and P. G. Carretero-González, R. and Kevrekidis. Scattering and leapfrogging of vortex rings in a superfluid. *Physics of Fluids*, 26(9), 2014.
- [182] K Shariff and A Leonard. Vortex rings. *Annual Review of Fluid Mechanics*, 24(1):235–279, 1992.
- [183] K. W. Schwarz. Interaction of quantized vortex rings with quantized vortex lines in rotating he II. *Phys. Rev.*, 165:323–334, Jan 1968.
- [184] T. T. Lim and T. B. Nickels. *Fluid Vortices*. Springer Netherlands, Dordrecht, 1995.
- [185] Matthew S. Paoletti and Daniel P. Lathrop. Quantum turbulence. *Annual Review of Condensed Matter Physics*, 2(1):213–234, 2011.
- [186] B. Jackson, J. F. McCann, and C. S. Adams. Vortex line and ring dynamics in trapped Bose–Einstein condensates. *Phys. Rev. A*, 61:013604, Dec 1999.
- [187] J. Ruostekoski and J. R. Anglin. Creating vortex rings and three-dimensional skyrmions in Bose–Einstein condensates. *Phys. Rev. Lett.*, 86:3934–3937, Apr 2001.
- [188] Naomi S Ginsberg, Joachim Brand, and Lene Vestergaard Hau. Observation of hybrid soliton vortex-ring structures in bose-einstein condensates. *Physical review letters*, 94(4):040403, 2005.
- [189] I Shomroni, E Lahoud, S Levy, and J Steinhauer. Evidence for an oscillating soliton/vortex ring by density engineering of a bose-einstein condensate. *Nature Physics*, 5(3):193, 2009.

- [190] Janne Ruostekoski and Zachary Dutton. Engineering vortex rings and systems for controlled studies of vortex interactions in bose-einstein condensates. *Physical Review A*, 72(6):063626, 2005.
- [191] Florian Pinsker, Natalia G Berloff, and Víctor M Pérez-García. Nonlinear quantum piston for the controlled generation of vortex rings and soliton trains. *Physical Review A*, 87(5):053624, 2013.
- [192] M. Abad, M. Guilleumas, R. Mayol, and M. Pi. Vortex rings in toroidal Bose-Einstein condensates. *Laser Physics*, 18(5):648–652, 2008.
- [193] Dustin Kleckner, Louis H Kauffman, and William TM Irvine. How superfluid vortex knots untie. *Nature Physics*, 12(7):650, 2016.
- [194] Renzo L Ricca, David C Samuels, and Carlo F Barenghi. Evolution of vortex knots. *Journal of Fluid Mechanics*, 391:29–44, 1999.
- [195] Callum W Duncan, Calum Ross, Niclas Westerberg, Manuel Valiente, Bernd J Schroers, and Patrik Öhberg. Linked and knotted synthetic magnetic fields. *Physical Review A*, 99(6):063613, 2019.
- [196] J Dalibard and F Gerbier. Juzeliunas, and p. öhberg. *Rev. Mod. Phys*, 83:1523, 2011.
- [197] M. Mochol and K. Sacha. Artificial magnetic field induced by an evanescent wave. *Scientific Reports*, 5, Jan 2015. Article.
- [198] Jonathan M Ward, Danny G O’Shea, Brian J Shortt, Michael J Morrissey, Kieran Deasy, and Sile G Nic Chormaic. Heat-and-pull rig for fiber taper fabrication. *Review of scientific instruments*, 77(8):083105, 2006.
- [199] Limin Tong, Rafael R Gattass, Jonathan B Ashcom, Sailing He, Jingyi Lou, Mengyan Shen, Iva Maxwell, and Eric Mazur. Subwavelength-diameter silica wires for low-loss optical wave guiding. *Nature*, 426(6968):816, 2003.

- [200] Amnon Yariv et al. *Optical electronics in modern communications*, volume 1. Oxford University Press, USA, 1997.
- [201] E Vetsch, D Reitz, G Sagué, R Schmidt, ST Dawkins, and A Rauschenbeutel. Optical interface created by laser-cooled atoms trapped in the evanescent field surrounding an optical nanofiber. *Physical review letters*, 104(20):203603, 2010.
- [202] C Lacroûte, KS Choi, A Goban, DJ Alton, D Ding, NP Stern, and HJ Kimble. A state-insensitive, compensated nanofiber trap. *New Journal of Physics*, 14(2):023056, 2012.
- [203] Thomas Nieddu, Vandna Gokhroo, and Sile Nic Chormaic. Optical nanofibres and neutral atoms. *Journal of Optics*, 18(5):053001, 2016.
- [204] G Sagué, E Vetsch, W Alt, D Meschede, and A Rauschenbeutel. Cold-atom physics using ultrathin optical fibers: Light-induced dipole forces and surface interactions. *Physical review letters*, 99(16):163602, 2007.
- [205] Laura Russell, Kieran Deasy, Mark J Daly, Michael J Morrissey, and Sile Nic Chormaic. Sub-doppler temperature measurements of laser-cooled atoms using optical nanofibres. *Measurement Science and Technology*, 23(1):015201, 2011.
- [206] Ravi Kumar, Vandna Gokhroo, Kieran Deasy, Aili Maimaiti, Mary C Frawley, Ciarrán Phelan, and Sile Nic Chormaic. Interaction of laser-cooled ^{87}rb atoms with higher order modes of an optical nanofibre. *New Journal of Physics*, 17(1):013026, 2015.
- [207] Fam Le Kien, V. I. Balykin, and K. Hakuta. Atom trap and waveguide using a two-color evanescent light field around a subwavelength-diameter optical fiber. *Phys. Rev. A*, 70:063403, Dec 2004.
- [208] Rashi Sachdeva and Thomas Busch. Creating superfluid vortex rings in artificial magnetic fields. *Physical Review A*, 95(3):033615, 2017.

- [209] Marco Cozzini, Sandro Stringari, Vincent Bretin, Peter Rosenbusch, and Jean Dalibard. Scissors mode of a rotating bose-einstein condensate. *Physical Review A*, 67(2):021602, 2003.
- [210] D Guéry-Odelin and S Stringari. Scissors mode and superfluidity of a trapped bose-einstein condensed gas. *Physical review letters*, 83(22):4452, 1999.
- [211] OM Marago, SA Hopkins, J Arlt, E Hodby, G Hechenblaikner, and CJ Foot. Observation of the scissors mode and evidence for superfluidity of a trapped bose-einstein condensed gas. *Physical review letters*, 84(10):2056, 2000.
- [212] NL Smith, WH Heathcote, JM Krueger, and CJ Foot. Experimental observation of the tilting mode of an array of vortices in a dilute bose-einstein condensate. *Physical review letters*, 93(8):080406, 2004.
- [213] Francesca Zambelli and Sandro Stringari. Quantized vortices and collective oscillations of a trapped bose-einstein condensate. *Physical review letters*, 81(9):1754, 1998.
- [214] S Stringari. Superfluid gyroscope with cold atomic gases. *Physical review letters*, 86(21):4725, 2001.
- [215] Vladimir Georgievich Minogin and Síle Nic Chormaic. Manifestation of the van der waals surface interaction in the spontaneous emission of atoms into an optical nanofiber. *Laser Physics*, 20(1):32–37, 2010.
- [216] Jarrett Revels, Tim Besard, Valentin Churavy, Bjorn De Sutter, and Juan Pablo Vielma. Dynamic automatic differentiation of gpu broadcast kernels. *arXiv preprint arXiv:1810.08297*, 2018.

Published articles

New Journal of Physics

The open access journal at the forefront of physics

Deutsche Physikalische Gesellschaft  DPG

IOP Institute of Physics

Published in partnership
with: Deutsche Physikalische
Gesellschaft and the Institute
of Physics



PAPER

OPEN ACCESS

RECEIVED
29 December 2015

REVISED
1 March 2016

ACCEPTED FOR PUBLICATION
3 March 2016

PUBLISHED
22 March 2016

Non-adiabatic generation of NOON states in a Tonks–Girardeau gas*

James Schloss, Albert Benseny, Jérémie Gillet, Jacob Swain and Thomas Busch

Quantum Systems Unit, Okinawa Institute of Science and Technology, 904-0495 Okinawa, Japan

E-mail: james.schloss@oist.jp

Keywords: NOON states, optimal control, quantum engineering, strongly correlated quantum states, shortcuts to adiabaticity, Tonks–Girardeau gas

Abstract

Adiabatic techniques can be used to control quantum states with high fidelity while exercising limited control over the parameters of a system. However, because these techniques are slow compared to other timescales in the system, they are usually not suitable for creating highly unstable states or performing time-critical processes. Both of these situations arise in quantum information processing, where entangled states may be isolated from the environment only for a short time and where quantum computers require high-fidelity operations to be performed quickly. Recently it has been shown that techniques like optimal control and shortcuts to adiabaticity can be used to prepare quantum states non-adiabatically with high fidelity. Here we present two examples of how these techniques can be used to create maximally entangled many-body NOON states in one-dimensional Tonks–Girardeau gases.

Original content from this work may be used under the terms of the [Creative Commons Attribution 3.0 licence](#).

Any further distribution of this work must maintain attribution to the author(s) and the title of the work, journal citation and DOI.



1. Introduction

Macroscopic superposition states, such as the maximally entangled $|N, 0\rangle + |0, N\rangle$ (NOON) state, are of great interest for fundamental studies of quantum mechanics and for applications in quantum information and quantum metrology. A NOON state is composed of two modes where all particles in the system can be found exclusively in either one or the other. Until now, experimental NOON state generation has been limited to photonic states generated by mixing classical states with down-converted photon pairs [1], and with such techniques it has been possible to create NOON states with around five photons [2]. A theoretical proposal for an experimentally realistic setup for creating NOON states for a large number of ultracold atoms was recently presented by Hallwood *et al* [3], who considered a gas of strongly interacting bosons in a one-dimensional ring. In this proposed system, different angular momentum states were coupled by breaking the rotational symmetry, and the authors showed how to accelerate the atoms into a superposition state of rotating and non-rotating components. Since the atoms were considered to be in the strongly correlated (Tonks–Girardeau) regime [4], this process results in a macroscopically entangled state.

In order to successfully generate NOON states on a ring of strongly correlated ultracold atoms, it is crucial to rotationally accelerate the system slowly, as otherwise unwanted excitations may drive the system out of the desired state. This is especially important close to the avoided crossings where the NOON state lives and where states with different angular momentum quantum numbers are coupled. For larger particle numbers and finite width coupling barriers, the energy gaps at these positions become exponentially small [5], and therefore slower and slower driving is necessary. However, slow processes are not particularly suitable for applications in quantum information, where algorithms must be performed quickly, or for creating states that are highly unstable. Techniques which can speed up the creation process while maintaining high fidelities are therefore of large interest.

Here we present two examples of such techniques that can accelerate the technique for NOON-state preparation suggested by Hallwood *et al* [3]. The first is the chopped random basis (CRAB) optimal control

* Dedicated to the memory of Marvin D Girardeau.

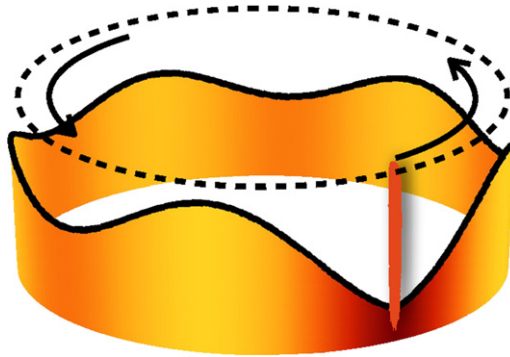


Figure 1. Schematic of the system described by Hallwood *et al* [3]. Shown is the density profile for five atoms in the TG regime which are stirred by a highly localised potential (indicated by the vertical line).

technique [6], where we numerically optimise the angular acceleration and the height of a barrier. The second technique combines two well-known shortcuts to adiabaticity (STA) protocols [7] which we adapt to the ring geometry. In both cases we show that it is possible to drive the system into a NOON state on timescales much faster than required by adiabaticity.

The paper is organised as follows: in section 2 we briefly review the ring system of strongly correlated ultracold atoms. This is followed in section 3 by a detailed description of how to use the optimal control CRAB algorithm to create NOON states non-adiabatically and in section 4 we show how STA can be used to create the same NOON state with high fidelity in a similar system. We finish with the conclusions in section 5.

2. Creating a NOON state on a ring

Let us begin by briefly summarising the protocol suggested by Hallwood *et al* [3] for creating a NOON state in a gas of strongly correlated bosons. For this we consider a gas of N interacting bosons of mass m on a one-dimension ring with circumference L , similar to ring systems previously introduced in literature [8, 9]. This system includes a potential barrier, modelled by a Dirac δ function, that rotates with an angular frequency Ω (see schematic in figure 1). In the rotating frame, the Hamiltonian of the system is given by [3]

$$H^{(N)} = \sum_{i=1}^N \left[\frac{1}{2} \left(-i \frac{\partial}{\partial x_i} - \Omega \right)^2 + b\delta(x_i) + g \sum_{i < j}^N \delta(x_i - x_j) \right], \quad (1)$$

where b is the height of the barrier (in units of \hbar^2/mL^2), $x_i \in [-1/2, 1/2]$ is the position of the i -th particle (in units of L) and g (in units of \hbar^2/mL^2) is the effective interaction strength between the atoms.

In the strongly correlated Tonks–Girardeau (TG) limit ($g \rightarrow \infty$), the Hamiltonian $H^{(N)}$ can be solved by using the Bose–Fermi mapping theorem [10, 11], which requires replacing the interaction terms in the Hamiltonian with a boundary condition on the many-body bosonic wavefunction

$$\Psi_B(x_1, x_2, \dots, x_N) = 0, \quad \text{if} \quad x_i - x_j = 0 \quad \text{with} \quad i \neq j. \quad (2)$$

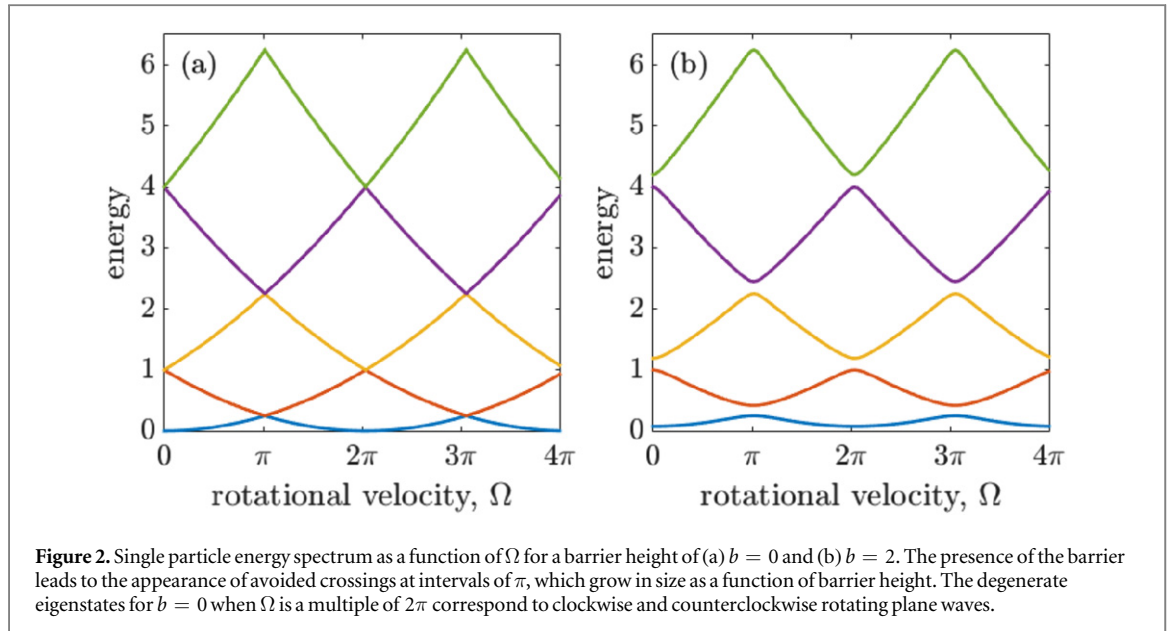
In this so-called hard-core limit, two bosons cannot be at the same point in space, which is formally similar to the Pauli principle for fermions. The Bose–Fermi mapping theorem therefore allows us to replace strongly interacting bosons by non-interacting fermions, for which the many-body wavefunction can be calculated as

$$\Psi_F(x_1, x_2, \dots, x_N) = \frac{1}{\sqrt{N!}} \det [\psi_n(x_j)]_{n,j=1}^N. \quad (3)$$

Here the $\psi_n(x_j)$ are the single particle eigenstates of the trapping potential V_0 . However, as the fermionic many-body wavefunction is an antisymmetric function, it needs to be symmetrised to describe the bosonic states by

$$\Psi_B(x_1, x_2, \dots, x_N) = \prod_{i < j} \operatorname{sgn}(x_i - x_j) \Psi_F(x_1, x_2, \dots, x_N). \quad (4)$$

Calculating the time evolution of the entire strongly interacting gas therefore only requires evolving single-particle states, which are governed by the laboratory-frame Hamiltonian



$$H = -\frac{1}{2} \frac{\partial^2}{\partial x^2} + b\delta[x - x_0(t)], \quad (5)$$

where x_0 is the position of the barrier at time t .

The energy spectrum of this system is shown in figure 2 as a function of the rotational velocity $\Omega \equiv \dot{x}_0/L$ (in units of \hbar/mL) of the system. In the absence of barrier, $b = 0$ (figure 2(a)), the eigenstates of H are plane waves with quantised angular momentum in units of integer multiples of 2π and manifolds of fixed angular momentum are uncoupled due to the existence of rotational symmetry. However, when $b > 0$ (figure 2(b)) this symmetry is broken and transitions between different manifolds become possible [12], resulting in the avoided crossings visible in the energy spectrum.

By adiabatically accelerating the barrier from $\Omega = 0$ to π , a particle initially in an eigenstate of H will enter a superposition state of two angular momentum eigenstates, and in the TG limit, where the strongly correlated many-particle wavefunction can be directly calculated from the single particles ones, this will create a macroscopic NOON state between different values of angular momentum [3]. However, any non-adiabatic behaviour will lead to transitions to higher or lower lying states in the vicinity of the gaps which would degrade the fidelity of the superposition state. The condition for adiabaticity of the system must therefore be chosen with respect to the smallest gap size, which in general decreases exponentially for higher energies [13]. For a delta barrier, however, the gap size can be shown to stay constant to first order [5].

From an experimental standpoint it would be desirable if the restrictions set by the adiabatic condition could be avoided, and in the following we discuss two strategies with which this can be achieved. The first one makes use of an optimal control technique, which determines an optimal form ('pulse') of the non-adiabatic rotational velocity $\Omega(t)$ which will generate the desired final state with high fidelity through brute-force computational methods. For this we have implemented the CRAB optimal control technique [6], which starts by initially assuming a constant acceleration of the angular barrier velocity from $\Omega = 0$ to π and iterates on this by including procedurally generated sinusoidal variations. After each iteration, the fidelity is calculated and the Nelder–Mead method [14] is used to find the pulse that gives a final state closest to the desired one. This ultimately leads to a form of the rotational velocity that maximises the fidelity for reaching the NOON state in a preset amount of time. In a similar way, we also find optimal pulses for the barrier height, and for a combination of both, the rotational velocity and the barrier height.

The second strategy we consider combines two known results from the area of STA [7]. In order to implement these, we assume that a harmonic or sinusoidal potential can be raised along the perimeter of the ring, and then split the acceleration process into two processes: a first one which breaks the rotational symmetry (raising of a potential), and a second which accelerates the atoms. In order to maximise the fidelity for reaching the NOON state, the rotational symmetry is restored by lowering the potential at the end. It is worth mentioning that a fast quasi-adiabatic shortcut for creating a TG gas superposition state as described above was recently suggested [15].

To quantify the success of our protocols, we use the fidelity $F = |\langle \psi | \phi \rangle|^2$, where $|\psi\rangle$ is the achieved state and $|\phi\rangle$ is the target state. When F is close to one, it is convenient to also define the infidelity as $1 - F$. The fidelity between two many-particle TG states, $|\Psi\rangle$ and $|\Phi\rangle$, can be calculated by using the mode by mode projections

[16, 17]

$$\begin{aligned}\langle \Psi | \Phi \rangle &= \frac{1}{N!} \sum_{\eta, \mu \in P} \epsilon_\eta \epsilon_\mu \langle \psi_{\eta_1}(x_1) | \phi_{\mu_1}(x_1) \rangle \cdots \langle \psi_{\eta_N}(x_N) | \phi_{\mu_N}(x_N) \rangle \\ &= \det[\langle \psi_i | \phi_j \rangle]_{i,j=1}^N\end{aligned}\quad (6)$$

which follows directly from the form of the TG state [4]

$$\Psi(x_1, x_2, \dots, x_N) = \frac{1}{\sqrt{N!}} \prod_{i < j} \text{sign}(x_i - x_j) \sum_{\eta \in P} \epsilon_\eta \psi_{\eta_1}(x_1) \cdots \psi_{\eta_N}(x_N). \quad (7)$$

Here P represents the set of all permutations of N elements, ϵ_η represents the antisymmetric tensor of the permutation η , and ψ_i represent the orbitals. These definitions will be used to measure how close the final state of our finite-time algorithms comes to the perfect NOON state.

3. Optimal control

To examine the possibility for using an optimal control approach to generate a NOON state for the TG gas on the ring, we have implemented the CRAB optimal control algorithm [6] for systems of up to five particles. The CRAB technique works by modifying a control parameter of a given system, Γ , with a multiplicative term as

$$\Gamma^{\text{CRAB}}(t) = \Gamma^0(t) \gamma(t), \quad (8)$$

where $\Gamma^0(t)$ is an initial guess, and the function $\gamma(t)$ is written as a sum of $2J$ sinusoidal functions

$$\gamma(t) = 1 + \frac{1}{\lambda(t)} \sum_{j=1}^J (A_j \sin(\nu_j t) + B_j \cos(\nu_j t)). \quad (9)$$

To ensure that $\Gamma^{\text{CRAB}}(t)$ and $\Gamma^0(t)$ coincide at the initial and final times, $\lambda(t)$ is defined such that $\lim_{t \rightarrow 0} \lambda(t) = \lim_{t \rightarrow T} \lambda(t) = \infty$. In our implementation we chose

$$\lambda(t) = \frac{T^2}{4t(t-T)}. \quad (10)$$

The optimisation process then reduces to finding the optimal values for $\{A_j, B_j, \nu_j\}$, which can be achieved by initially assigning random values and then numerically maximising the fidelity by using an algorithm such as the Nelder–Mead method [14]. While it is clear that this process will lead to more accurate outcomes for larger J , the fact that the maximisation has to be carried over a larger number of degrees of freedom also increases the computational complexity. In our case, $\Gamma(t)$ can be chosen to be the rotational angular frequency or the barrier height, which means that we may optimise over the rotation frequency while keeping the barrier height constant, optimise over the barrier height while keeping the rotation acceleration constant, or optimise over both of them simultaneously. These three possibilities will be discussed in the following.

3.1. Optimising over the rotational velocity

Before we discuss the optimal pulse for the full TG, we will focus on the acceleration of a single particle, initially in the ground state of the trap. For this we assume a fixed barrier height and start with a guess pulse that increases linearly from $\Omega = 0$ to π in a preset total time T . The results for $J = 15$ and for $T = 1, 10$, and 100 are shown in figure 3(a). For longer evolution times, a linear pulse is a reasonable method to adiabatically generate the macroscopic superposition state with high fidelity and the modifications stemming from the optimal control process for $T = 100$ can be seen to be weak in magnitude. Shorter evolution times, however, require pulse shapes that strongly influence the system and which therefore differ dramatically from the initial linear guess. From the infidelities for the linear guess pulse and the optimised pulse, shown in figure 5, one can see an improvement of several orders of magnitude on all timescales.

3.2. Optimising over the barrier height

To optimise over the barrier height, we choose a guess pulse which is constant at $b = 1$ while the rotational velocity of the barrier is set to increase linearly from $\Omega = 0$ to π over a total time T . The optimised pulses for the barrier heights for $T = 1, 10$, and 100 for $J = 15$ are shown in figure 3(b), and, similar to the case of varying Ω , shorter evolution times require larger deviations from the initial guess. As in the previous case, these pulses also lead to significant improvements in the final fidelity, shown in figure 5.

3.3. Optimising over rotational velocity and barrier height

With the CRAB algorithm, it is possible to optimise over multiple parameters at the same time. In figure 4, we show the optimal pulses for simultaneously changing the rotational velocity and barrier height. Compared to the

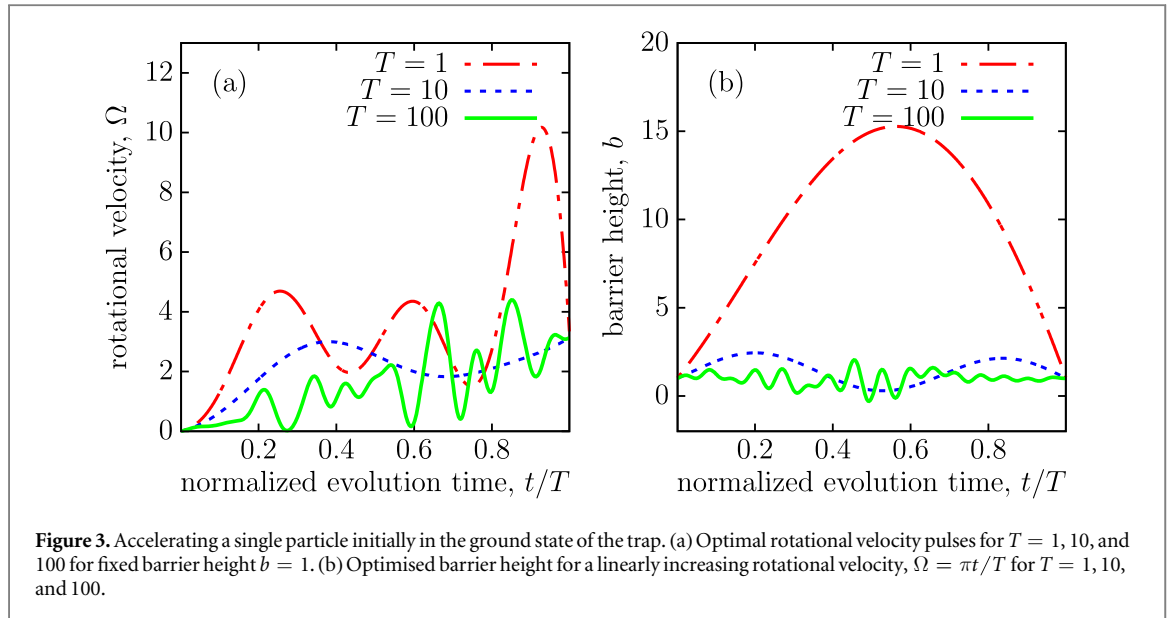


Figure 3. Accelerating a single particle initially in the ground state of the trap. (a) Optimal rotational velocity pulses for $T = 1, 10$, and 100 for fixed barrier height $b = 1$. (b) Optimised barrier height for a linearly increasing rotational velocity, $\Omega = \pi t/T$ for $T = 1, 10$, and 100 .

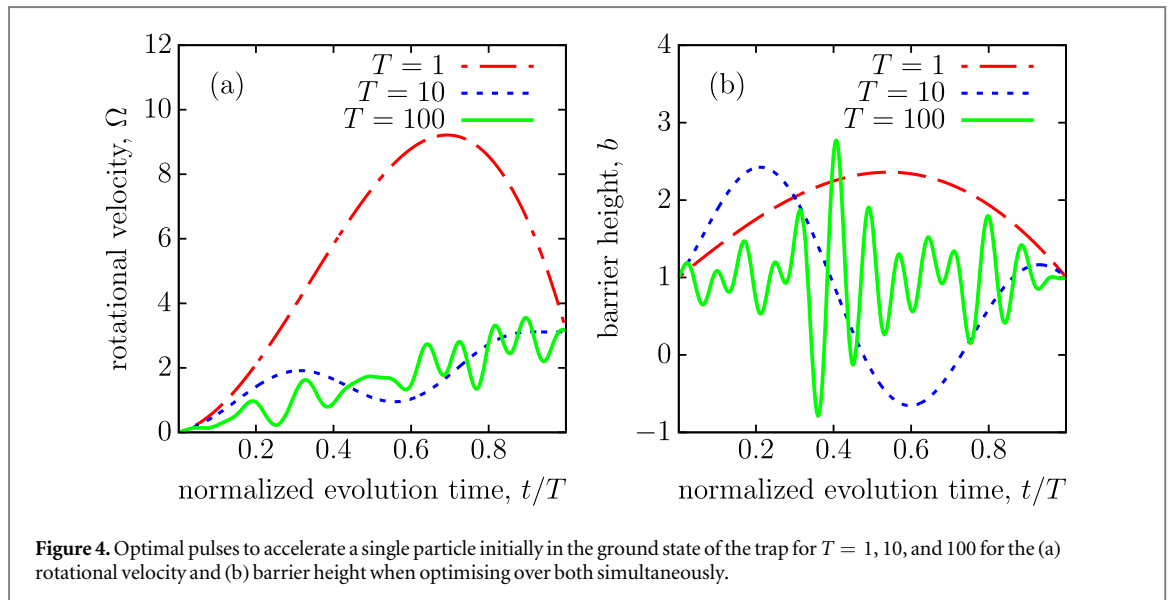


Figure 4. Optimal pulses to accelerate a single particle initially in the ground state of the trap for $T = 1, 10$, and 100 for the (a) rotational velocity and (b) barrier height when optimising over both simultaneously.

previous cases, where only one parameter was optimised, one can see that for longer evolution times the resulting pulse shapes are similar. For shorter times, they differ significantly (compare the red lines in figures 3 and 4). However, the final fidelity is not drastically different from the one stemming from optimising only over the rotation of the barrier (see Figure 5), which is of interest when considering experimental realisations.

3.4. TG gas acceleration

Due to the Bose–Fermi mapping theorem, the evolution of an N -particle TG gas can be calculated by evolving a gas of N spin-polarised independent fermions. Here we only consider the zero temperature limit, in which the fermions in the initial and the target state create a Fermi sea by filling the lowest N energy levels. During the dynamics the atoms close to the Fermi edge can make transitions into empty states, which will affect the global fidelity, and it is therefore most crucial to optimise the dynamics of the overall gas with respect to the particle with the highest energy [15]. In figure 6 we show the fidelity for both, the particle closest to the Fermi edge and the entire TG gas (for $N = 3$ and 5), and one can see that that CRAB algorithm used in this way gives highly effective pulses. Note however, that for very short and long evolution times no significant fidelity increase due to the CRAB algorithm exists for a TG gas.

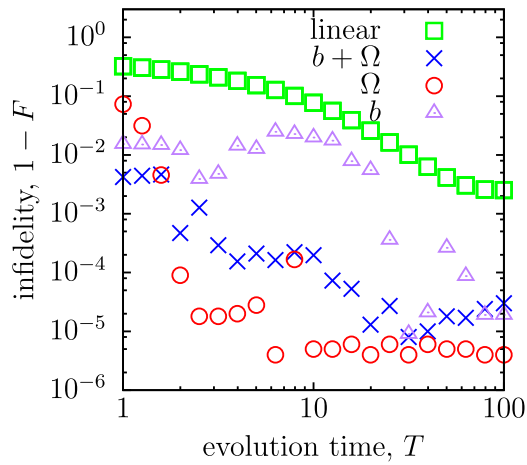


Figure 5. Infidelities as a function of the overall process time for optimally controlled rotational acceleration, barrier height, or both. Here, ‘linear’ refers to an unoptimised linear acceleration from $\Omega = 0$ to π while keeping the barrier height fixed at $b = 1$.

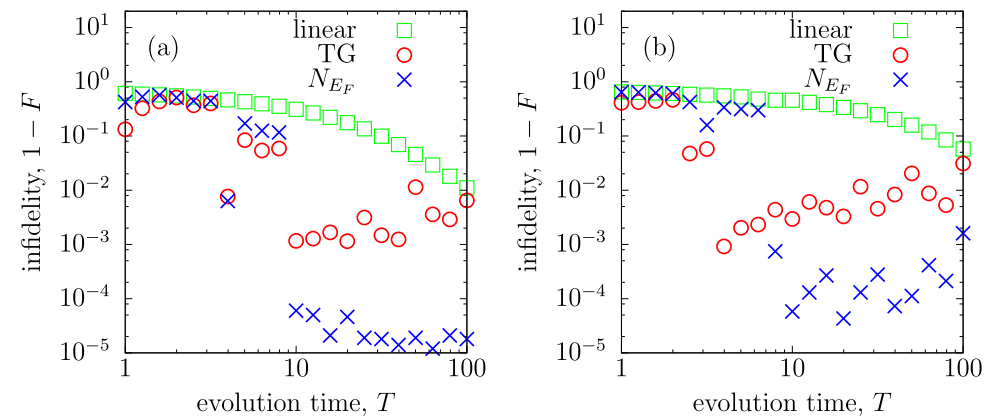


Figure 6. Infidelities for the evolution of a TG gas with (a) $N = 3$ and (b) $N = 5$ particles using the CRAB optimal control technique. The optimal pulses were determined for the particle at the Fermi edge (blue crosses), and applied to the whole gas (green squares). Here, the green squares show the fidelity of a linear pulse for the atom closest to the Fermi edge. A clear range where the CRAB algorithm is effective for generating NOON states with multiple particles can be clearly identified.

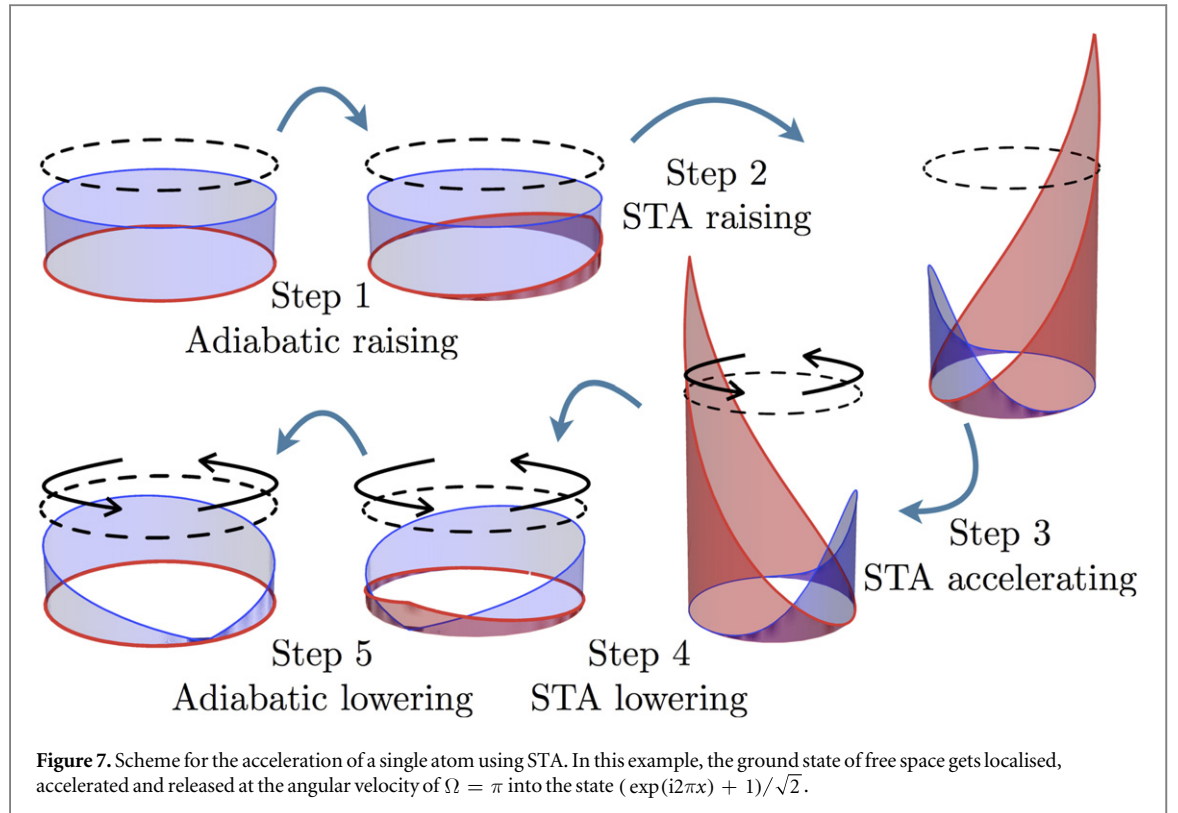
4. Shortcuts to adiabaticity

In the following we will discuss the possibility of creating the NOON state by using STA techniques [7]. For this we break the rotational symmetry of the ring system by introducing a time-dependent external potential that we remove again at the end. At variance with the set-up proposed by Hallwood *et al* [3], this scheme can prepare the system in a NOON state without requiring a narrow potential barrier. Instead, we consider the use of a harmonic potential, or a more experimentally realistic sinusoidal potential.

The protocol we suggest consists of five steps, (1) adiabatically raising a weak harmonic potential wrapped around the ring, (2) quickly tightening this potential via a shortcut to localise the particle, (3) accelerating the particle by moving the centre of the harmonic potential via another shortcut, (4) lowering the potential via the reverse process of step (2) to delocalise it again, and (5) adiabatically removing the harmonic potential. A schematic of this process is shown in figure 7. In the next section, we will briefly review the general framework of the STA formalism [7] and detail the differences of our protocol with respect to existing ones.

4.1. Lewis–Riesenfeld invariants

STA methods based on the Lewis–Riesenfeld invariant inverse-engineering approach [18–20] make use of the existence of invariants. A one-dimensional Hamiltonian has an invariant quadratic in momentum p if and only if it can be expressed in the following manner



$$H = \frac{p^2}{2m} - F(t)q + \frac{m}{2}\omega^2(t)q^2 + \frac{1}{\rho(t)^2}U\left(\frac{q - q_c(t)}{\rho(t)}\right), \quad (11)$$

where U is an arbitrary function and q is the position operator. The variables ρ , q_c , ω , and F are arbitrary functions of time satisfying the auxiliary equations

$$\ddot{\rho} + \omega^2(t)\rho = \frac{\omega_0^2}{\rho^3}, \quad (12)$$

$$\ddot{q}_c + \omega^2(t)q_c = F(t)/m, \quad (13)$$

where ω_0 is a constant. The physical interpretation of the constant and functions depends on the underlying system. Additional constraints have to be considered to insure that the Hamiltonian and its invariants commute at initial and final times t_0 and t_f , which in our case results in $H(t_0) = H(t_f) = p^2/2m$.

4.2. Shortcut for raising/lowering the potential

One of the two shortcuts being used in the protocol above involves raising or lowering of a harmonic potential [19, 21]. For this we only need a stationary harmonic potential and can set F , q_c and U from equation (11) to zero, which leads to

$$H = -\frac{1}{2}\frac{\partial^2}{\partial x^2} + \frac{1}{2}\omega^2(t)q^2, \quad (14)$$

complemented by the single auxiliary equation (12). To change the frequency from $\omega(t_0) = \omega_0$ to $\omega(t_f) = \omega_f$ while keeping the commutation relations and $\omega(t)$ continuous, we impose the conditions

$$\begin{aligned} \rho(t_0) &= 1, & \rho(t_f) &= \gamma = \sqrt{\omega_0/\omega_f}, \\ \dot{\rho}(t_0) &= 0, & \dot{\rho}(t_f) &= 0, \\ \ddot{\rho}(t_0) &= 0, & \ddot{\rho}(t_f) &= 0. \end{aligned} \quad (15)$$

This means that as long as the conditions (12) and (15) are obeyed, we are free to choose any specific form of ρ . A good choice is a simple polynomial of the form

$$\rho(s) = 6(\gamma - 1)s^5 - 15(\gamma - 1)s^4 + 10(\gamma - 1)s^3 + 1, \quad (16)$$

where $s = (t - t_0)/(t_f - t_0)$, which, when inserted into equation (12), allows us to numerically find a solution for $\omega(t)$. This solution leads to the necessary squeezing or expansion of the particle wavefunction with perfect fidelity in an arbitrarily short time $t_f - t_0$, although in practice a shorter squeezing time involves a faster

variation of ω , which may be limited by technical capabilities. Note that even though this shortcut was not specifically built for systems with periodic boundaries, it can also be used in a ring, as the symmetry of the potential is never broken during the time evolution.

It is also important to note that the initial frequency ω_0 can be chosen arbitrarily small as long as it is non-zero. Furthermore, the solution of equation (12) for very small values of ω_0 can yield purely imaginary values of $\omega(t)$, which corresponds to inverted (repulsive) potentials. While changing potentials between attractive and repulsive is technically possible, such a procedure is often associated with very fast changes with large amplitudes, which may not be easy to realise experimentally. As our final states require the external potential to be absent, i.e. $\omega = 0$, the first step of our protocol raises ω from 0 to a suitable ω_0 adiabatically slowly before the shortcut protocol can be used. In a similar manner, the last step of lowering the potential to $\omega = 0$ after having accelerated the particle has to be done adiabatically.

4.3. Shortcut for the acceleration

Once the potential has been raised, the next step is to accelerate the particles. A shortcut for this process using a harmonic trap exists [22–24], which keeps the trapping frequency constant and only requires a change in the position of the potential. We can therefore set $U = 0$ and $F = \omega_0^2 x_0(t)$ which leaves

$$H = -\frac{1}{2} \frac{\partial^2}{\partial x^2} + \frac{1}{2} \omega_0^2 (q - x_0(t))^2, \quad (17)$$

and condition (13) becomes the only relevant auxiliary equation

$$\ddot{q}_c + \omega_0^2 (q_c - x_0) = 0. \quad (18)$$

We once again impose conditions on q_c such that all boundary conditions are satisfied

$$\begin{aligned} q_c(t_0) &= x_0(t_0), & q_c(t_f) &= d, \\ \dot{q}_c(t_0) &= 0, & \dot{q}_c(t_f) &= \Omega_f, \\ \ddot{q}_c(t_0) &= 0, & \ddot{q}_c(t_f) &= 0, \end{aligned} \quad (19)$$

where d is the final position of the potential minimum and Ω_f is its final velocity. For transport schemes, d is the important parameter and Ω_f is set to 0, but in our case the opposite occurs as we want the particles to accumulate kinetic energy before being released from the potential (so that they keep revolving at constant speed Ω_f after t_f). The final position d plays no significant role in the evolution of the states.

The exact form of q_c can again be chosen arbitrarily and we pick the polynomial

$$q_c(s) = (6d - 3\Omega_f)s^5 - (15d - 7\Omega_f)s^4 + (10d - 4\Omega_f)s^3 + x_0(t_0), \quad (20)$$

where, as above, s is the normalised time. The value of Ω_f can be chosen as a multiple of 2π to create a plane wave after release, or as an odd multiple of π to prepare superpositions between states of different angular momentum.

Note that this transport scheme is usually applied to an open, infinite space, whereas our system has periodic boundary conditions. Since translational symmetry is broken, the shortcut is no longer guaranteed to work perfectly, as the potential has a finite height and therefore higher-lying states are no longer trapped. Unlike the potential raising shortcut, this accelerating shortcut is only approximate and works best when ω is large (the particle is highly localised) and the rotational velocity, \dot{q}_c , is not too high (the harmonic well is not moving too fast).

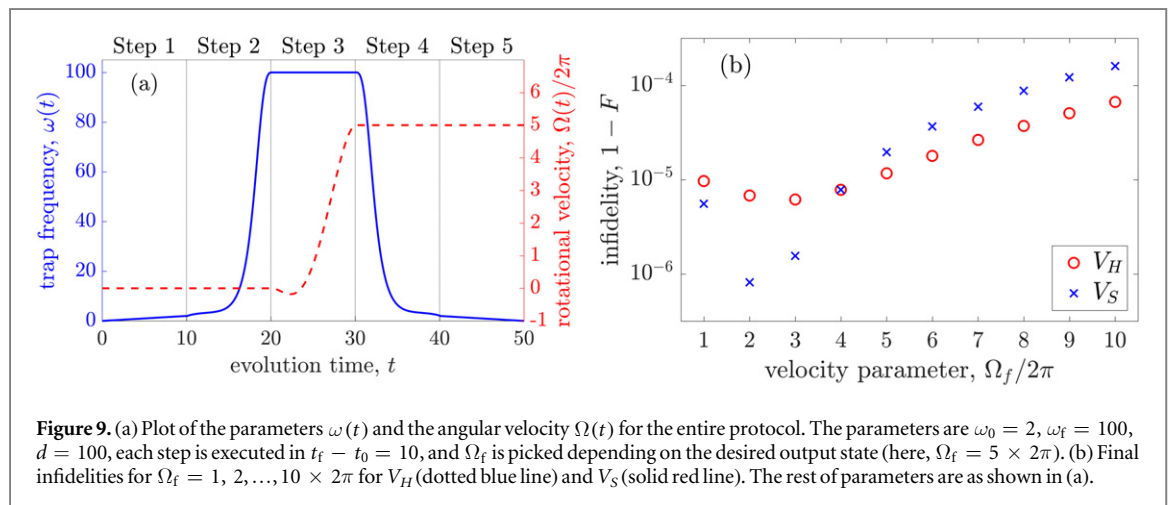
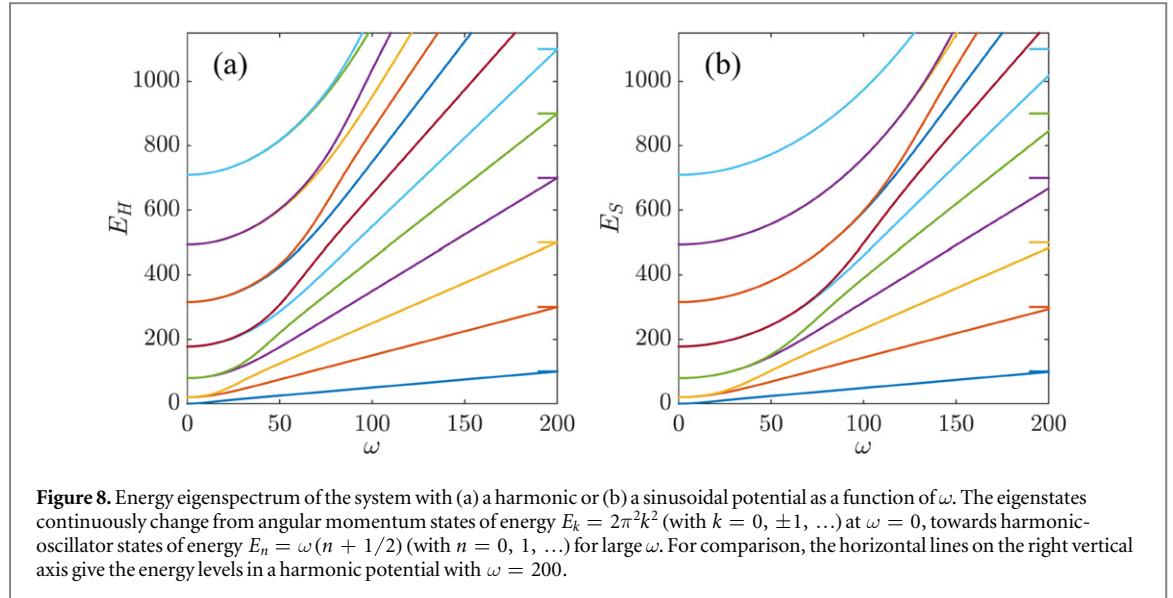
4.4. Harmonic and sinusoidal potentials

Both shortcuts described above are based on the presence of a harmonic potential of the form

$$V_H(x, t) = \frac{1}{2} \omega^2(t) (x - x_0(t))^2, \quad (21)$$

where ω is the frequency of the trap (in units of \hbar/mL^2) and x_0 the position of its minimum. Note that we require the potential to be symmetric around x_0 so that the potential is continuous at $x = \pm 1/2$, and therefore the real form of $(x - x_0)$ must be $(x - x_0 + 1/2)(\text{mod } 1) - 1/2$. The potential V_H is then continuous everywhere on the ring, but its derivative is discontinuous at $x = x_0 + 1/2$ (the position diametrically opposite to x_0). From a theoretical perspective, V_H is ideal because of its simplicity and its numerous known properties, particularly concerning STA, but it can also be considered a low energy approximation to any experimentally realistic potential. To show that the shortcut approach also works in experimentally realistic potentials, we discuss in the following its application to a sinusoidal potential [25, 26] of the form

$$V_S(x, t) = \frac{\omega^2(t)}{2\pi^2} \sin^2(\pi(x - x_0(t))), \quad (22)$$



where the notation is the same as before. Note that the pre-factor is chosen in such a way that V_H is an approximation of V_S around x_0 .

To visualise the difference between the two potentials, we first compute the energy spectra of both Hamiltonians by using a straightforward discrete variable representation method [27, 28]. The results as a function of ω are shown in figure 8 and one can see that the eigenstates at $\omega = 0$ are the angular momentum states $e^{i2\pi kx}$, with the clockwise and counter-clockwise momentum states of opposite quantum number k being degenerate. The degeneracy is lifted as ω becomes non-zero and the spectrum asymptotically approaches that of a harmonic oscillator. Note that for the sinusoidal case, even for large ω , the difference with the asymptotic harmonic spectrum increases with the quantum number n .

4.5. Single particle acceleration

In the following, we first show the results obtained from numerically simulating our protocol for a single particle initially in the ground state, where the free parameters of the protocol and the lengths of the different steps were chosen to allow for high fidelities. Note that the STA raising/lowering times can in principle be made arbitrarily short for fixed ω_f , unlike the adiabatic or the accelerating steps. In figure 9(a) we show the values for $\omega(t)$ and $\Omega(t)$ which define our chosen protocol, and in figure 9(b) we show the infidelities for the state preparation of plane waves $e^{i\Omega_f x}$ with $\Omega_f = 1 \dots 10 \times 2\pi$. One can see that the even for a large amount of angular momentum the fidelities remain very high, for both the harmonic and the sinusoidal potential.

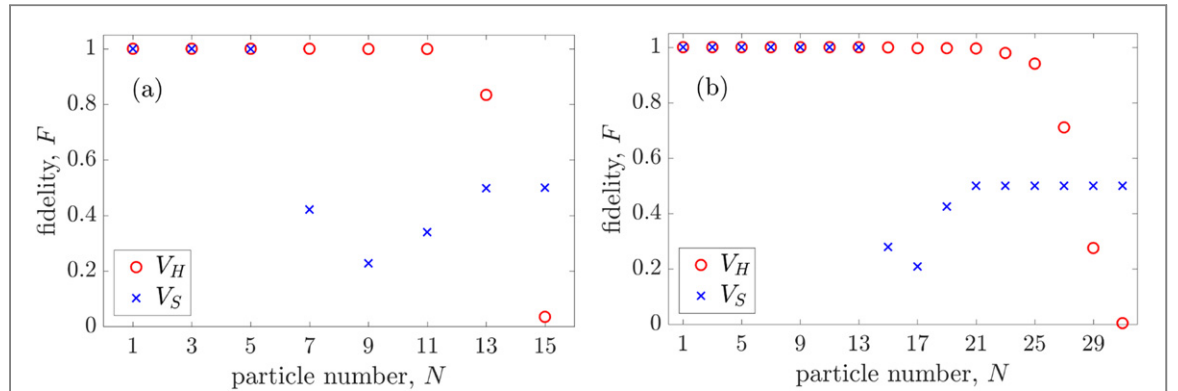


Figure 10. Final fidelities F of TG states of increasing particle number for the protocol shown in figure 9(a) with $\Omega_f = \pi$ for V_H (red circle) and V_S (blue cross). Plot (a) shows the fidelity of the protocol with $\omega_f = 100$ and (b) with $\omega_f = 200$.

4.6. TG gas acceleration

We now consider the multi-particle case in the TG regime. As this protocol does not include a δ -barrier, the target NOON state is slightly different from the one considered in the optimal control case. It corresponds to the state originating from adiabatically removing the barrier once the system is rotating at velocity $\Omega_f = \pi$. Similarly, the initial states for the particles will be eigenstates of free space, which are simply plane waves $e^{i2\pi kx}$ with integer k . Since the states with $\pm k$ are degenerate, however, it is equally valid to consider the initial eigenstates

$$\phi_0^i(x) = 1, \quad (23)$$

$$\phi_{2l-1}^i(x) = \frac{1}{\sqrt{2}}(e^{i2\pi lx} - e^{-i2\pi lx}) = i\sqrt{2} \sin(2l\pi x), \quad (24)$$

$$\phi_{2l}^i(x) = \frac{1}{\sqrt{2}}(e^{i2\pi lx} + e^{-i2\pi lx}) = \sqrt{2} \cos(2l\pi x), \quad (25)$$

for $l = 1, 2, \dots$. These states have the property of having a total angular momentum of zero and are well suited for our STA protocol. When an odd number of particles occupies the lower eigenstates, the sin/cos pairs are guaranteed to be both populated.

For $\Omega_f = \pi$, the plane wave of quantum numbers $k + 1$ and $-k$ are degenerate and we can construct the target states

$$\phi_{2l}^t(x) = \frac{1}{\sqrt{2}}(e^{i2\pi(l+1)x} + e^{-i2\pi lx}) = \sqrt{2} \cos[(2l+1)\pi x]e^{i\pi x}, \quad (26)$$

$$\phi_{2l+1}^t(x) = \frac{1}{\sqrt{2}}(e^{i2\pi(l+1)x} - e^{-i2\pi lx}) = i\sqrt{2} \sin[(2l+1)\pi x]e^{i\pi x}, \quad (27)$$

for $l = 0, 1, 2, \dots$. These states, of total angular momentum π , are very similar to the the eigenstates considered in the previous sections and NOON states can be constructed from them.

Any initial state $|\phi_l^i\rangle$ can be brought to the target state $|\phi_l^t\rangle$ (up to a possible shift in position) with high fidelity using our STA protocol. This process also works for TG gases, and we show in figure 10 the fidelity for TG gases of increasing (odd) particle numbers N submitted to our protocol. In figure 10(a) for the harmonic potential, the fidelities remain very high (infidelities of the order of 10^{-4}) for $N \leq 11$ after which they decrease. This is due to the finite maximum height of the potential (which, in turn, is due to the periodic boundary conditions), which affects the effectiveness of the STA acceleration scheme. The fidelities can be improved by increasing the maximum trapping frequency ω_f as we demonstrate in figure 10(b) where the value of ω_f is doubled and the fidelities remain high until $N \leq 21$. When using the sinusoidal potential, the fidelity drops for smaller particle numbers compared to the harmonic potential (although it also increases with ω_f), due to the lower height V_S has compared to V_H .

5. Conclusion

We have investigated the possibility of creating NOON states with ultracold quantum gases in the TG regime on a ring by using optimal control and STA techniques. Both these techniques were shown to allow to evolve the system into high-fidelity NOON states non-adiabatically.

In the case of optimal control, we used the CRAB technique with the Nelder–Mead minimisation method, for both a single particle and multiple particles by modifying either the potential barrier strength, its rotational velocity, or both. In all cases NOON states can be generated in finite time and with high fidelity. In particular, we have shown that it is sufficient to optimise for the particle closest to the Fermi edge to achieve high TG fidelities. In a second approach, we have generalised two known STA techniques to a ring system, and shown that STA techniques may also be used to create rotational states with high fidelity for both single particles and strongly correlated TG gases. The STA protocol we have applied is composed of five steps, where only the first and final steps required adiabaticity. Thus we have demonstrated that it is also possible to implement STA techniques on a one-dimensional ring system and generate NOON states between ultracold bosons without a potential barrier in the end.

The results presented here clearly show that it is possible to create macroscopic superposition states in TG gases on experimentally realistic timescales. They may therefore lead to a method of generating NOON states on a ring of ultracold atoms for use in quantum information systems.

References

- [1] Israel Y, Afek I, Rosen S, Ambar O and Silberberg Y 2012 *Phys. Rev. A* **85** 022115
- [2] Afek I, Ambar O and Silberberg Y 2010 *Science* **328** 1188172
- [3] Hallwood D, Ernst T and Brand J 2010 *Phys. Rev. A* **82** 063623
- [4] Girardeau M 1960 *J. Math. Phys.* **1** 516
- [5] Hallwood D, Burnett K and Dunningham J 2007 *J. Mod. Opt.* **54** 2129–48
- [6] Caneva T, Calarco T and Montangero S 2011 *Phys. Rev. A* **84** 022326
- [7] Torrontegui E, Ibáñez S, Martínez-Garaot S, Modugno M, del Campo A, Guéry-Odelin D, Ruschhaupt A, Chen Xi and Muga J G 2013 *Adv. At. Mol. Opt. Phys.* **62** 117–69
- [8] Das K K, Girardeau M D and Wright E M 2002 *Phys. Rev. Lett.* **89** 170404
- [9] Girardeau M D and Minguzzi A 2009 *Phys. Rev. A* **79** 033610
- [10] Girardeau M D, Wright E M and Triscari J M 2001 *Phys. Rev. A* **63** 033601
- [11] Girardeau M D and Wright E M 2000 *Phys. Rev. Lett.* **87** 050403
- [12] Shenke C, Minguzzi A and Hekking F 2012 *Phys. Rev. A* **85** 053627
- [13] Nunnenkamp A, Rey A M and Burnett K 2008 *Phys. Rev. A* **77** 023622
- [14] Nelder J and Mead R 1965 *Comput. J.* **7** 308–13
- [15] Martínez-Garaot S, Ruschhaupt A, Gillet J, Busch T and Muga J G 2015 *Phys. Rev. A* **92** 043406
- [16] del Campo A 2011 *Phys. Rev. A* **84** 012113
- [17] Lelas K, Ševa T and Buljan H 2011 *Phys. Rev. A* **84** 063601
- [18] Lewis H R and Riesenfeld W B 1969 *J. Math. Phys.* **10** 1485
- [19] Chen X, Ruschhaupt A, Schmidt S, del Campo A, Guéry-Odelin D and Muga J G 2010 *Phys. Rev. Lett.* **104** 063002
- [20] del Campo A and Boshier M G 2012 *Sci. Rep.* **2** 648
- [21] Chen X and Muga J G 2010 *Phys. Rev. A* **82** 053403
- [22] Masuda S and Nakamura K 2010 *Proc. R. Soc. A* **466** 1135–54
- [23] Torrontegui E, Ibáñez S, Chen X, Ruschhaupt A, Guéry-Odelin D and Muga J G 2011 *Phys. Rev. A* **83** 013415
- [24] Masuda S 2012 *Phys. Rev. A* **86** 063624
- [25] Phelan C F, Hennessy T and Busch T 2013 *Opt. Express* **21** 27093–101
- [26] Masuda S, Nakamura K and del Campo A 2014 *Phys. Rev. Lett.* **113** 063003
- [27] Light J C and Carrington T 2000 *Adv. Chem. Phys.* **114** 263–310
- [28] Baye D and Heenen P H 1986 *J. Phys. A: Math. Gen.* **19** 2041

GPUE: Graphics Processing Unit Gross–Pitaevskii Equation solver

James R. Schloss¹ and Lee J. O’Riordan¹

¹ Okinawa Institute of Science and Technology Graduate University, Onna-son, Okinawa 904-0495, Japan.

DOI: [10.21105/joss.01037](https://doi.org/10.21105/joss.01037)

Software

- [Review ↗](#)
- [Repository ↗](#)
- [Archive ↗](#)

Submitted: 15 October 2018

Published: 11 December 2018

License

Authors of papers retain copyright and release the work under a Creative Commons Attribution 4.0 International License ([CC-BY](#)).

Summary

Bose–Einstein Condensates (BECs) are superfluid systems consisting of bosonic atoms that have been cooled and condensed into a single, macroscopic ground state (Fetter, 2009; Pethick & Smith, 2008). These systems can be created in an experimental laboratory and allow for the exploration of physical phenomenon such as superfluid turbulence (Navon, Gaunt, Smith, & Hadzibabic, 2016; Roche & Barenghi, 2008; White, Anderson, & Bagannato, 2014), chaotic dynamics (Gardiner, 2002; Kyriakopoulos, Koukouloyannis, Skokos, & Kevrekidis, 2014; Zhang, 2017), and analogues of other quantum systems (Dalibard, Gerbier, Juzeliūnas, & Öhberg, 2011). Numerical simulations of BECs that directly mimic experiments are valuable to fundamental research in these areas and allow for theoretical advances before experimental validation. The dynamics of BEC systems can be found by solving the non-linear Schrödinger equation known as the Gross–Pitaevskii Equation (GPE),

$$i\hbar \frac{\partial \Psi(\mathbf{r}, t)}{\partial t} = \left(-\frac{\hbar^2}{2m} \nabla^2 + V(\mathbf{r}) + g|\Psi(\mathbf{r}, t)|^2 \right) \Psi(\mathbf{r}, t),$$

where $\Psi(\mathbf{r}, t)$ is the three-dimensional many-body wavefunction of the quantum system, $\mathbf{r} = (x, y, z)$, m is the atomic mass, $V(\mathbf{r})$ is an external potential, $g = \frac{4\pi\hbar^2 a_s}{m}$ is a coupling factor, and a_s is the scattering length of the atomic species. Here, the GPE is shown in three dimensions, but it can easily be modified to one or two dimensions (Pethick & Smith, 2008). One of the most straightforward methods for solving the GPE is the split-operator method, which has previously been accelerated with GPU devices (Bauke & Keitel, 2011; Ruf, Bauke, & Keitel, 2009). No software packages are available using this method on GPU devices that allow for user-configurable simulations and a variety of different system types; however, several software packages exist to simulate BECs with other methods and on different architectures, including GPELab (Antoine & Duboscq, 2014) the Massively Parallel Trotter-Suzuki Solver (Wittek & Cucchietti, 2013), and XMDS (Dennis, Hope, & Johnsson, 2013).

GPUE is a GPU-based Gross–Pitaevskii Equation solver via the split-operator method for superfluid simulations of both linear and non-linear Schrödinger equations, emphasizing superfluid vortex dynamics in two and three dimensions. GPUE is a fast, robust, and accessible software suite to simulate physics for fundamental research in the area of quantum systems and has been used to manipulate large vortex lattices in two dimensions (O’Riordan & Busch, 2016; O’Riordan, White, & Busch, 2016) along with ongoing studies of vortex dynamics.

For these purposes, GPUE provides a number of unique features: 1. Dynamic field generation for trapping potentials and other variables on the GPU device. 2. Vortex tracking in 2D and vortex highlighting in 3D. 3. Configurable gauge fields for the generation of

artificial magnetic fields and corresponding vortex distributions (Dalibard et al., 2011; Ghosh & Sachdeva, 2014). 4. Vortex manipulation via direct control of the wavefunction phase (Dobrek et al., 1999).

All of these features enable GPUE to simulate a wide variety of linear and non-linear dynamics of quantum systems. GPUE additionally features a numerical solver that improves on other available suites (O’Riordan, 2017; Wittek, 2016). All of GPUE’s features and functionality have been described in further detail in the documentation (Schloss & O’Riordan, 2018).

Acknowledgements

This work has been supported by the Okinawa Institute of Science and Technology Graduate University and by JSPS KAKENHI Grant Number JP17J01488. We would also like to thank Thomas Busch, Rashi Sachdeva, Tiantian Zhang, Albert Benseney, and Angela White for discussions on useful physical systems to simulate with the GPUE codebase, along with Peter Wittek and Tadhg Morgan for contributions to the code, itself. These acknowledgements can be found in `GPUE/acknowledgements.md`.

References

- Antoine, X., & Duboscq, R. (2014). GPELab, a Matlab toolbox to solve Gross–Pitaevskii equations I: Computation of stationary solutions. *Computer Physics Communications*, 185(11), 2969–2991. doi:[10.1016/j.cpc.2014.06.026](https://doi.org/10.1016/j.cpc.2014.06.026)
- Bauke, H., & Keitel, C. H. (2011). Accelerating the Fourier split operator method via graphics processing units. *Computer Physics Communications*, 182(12), 2454–2463. doi:[10.1016/j.cpc.2011.07.003](https://doi.org/10.1016/j.cpc.2011.07.003)
- Dalibard, J., Gerbier, F., Juzeliūnas, G., & Öhberg, P. (2011). Colloquium: Artificial gauge potentials for neutral atoms. *Rev. Mod. Phys.*, 83(4), 1523–1543. doi:[10.1103/RevModPhys.83.1523](https://doi.org/10.1103/RevModPhys.83.1523)
- Dennis, G., Hope, J., & Johnsson, M. (2013). XMDS2: Fast, scalable simulation of coupled stochastic partial differential equations. *Computer Physics Communications*, 184(1), 201–208. doi:[10.1016/j.cpc.2012.08.016](https://doi.org/10.1016/j.cpc.2012.08.016)
- Dobrek, Ł., Gajda, M., Lewenstein, M., Sengstock, K., Birk, G., & Ertmer, W. (1999). Optical generation of vortices in trapped Bose-Einstein condensates. *Phys. Rev. A*, 60(5), R3381–R3384. doi:[10.1103/PhysRevA.60.R3381](https://doi.org/10.1103/PhysRevA.60.R3381)
- Fetter, A. L. (2009). Rotating trapped Bose-Einstein condensates. *Rev. Mod. Phys.*, 81(2), 647–691. doi:[10.1103/RevModPhys.81.647](https://doi.org/10.1103/RevModPhys.81.647)
- Gardiner, S. A. (2002). (Quantum) chaos in Bose-Einstein condensates. *Journal of Modern Optics*, 49(12), 1971–1977. doi:[10.1080/09500340210140777](https://doi.org/10.1080/09500340210140777)
- Ghosh, S., & Sachdeva, R. (2014). Synthetic Gauge Fields for Ultra Cold Atoms: A Primer. *Journal of the Indian Institute of Science*, 94(2), 217–232. Retrieved from <http://journal.iisc.ernet.in/index.php/iisc/article/view/4502>
- Kyriakopoulos, N., Koukouloyannis, V., Skokos, C., & Kevrekidis, P. G. (2014). Chaotic behavior of three interacting vortices in a confined Bose-Einstein condensate. *Chaos*, 024410. doi:[10.1063/1.4882169](https://doi.org/10.1063/1.4882169)
- Navon, N., Gaunt, A. L., Smith, R. P., & Hadzibabic, Z. (2016). Emergence of a turbulent cascade in a quantum gas. *Nature*, 539, 72. doi:[10.1038/nature20114](https://doi.org/10.1038/nature20114)

- O'Riordan, L. J. (2017). *Non-equilibrium vortex dynamics in rapidly rotating Bose-Einstein condensates* (PhD thesis). Okinawa Institute of Science; Technology Graduate University. Retrieved from <http://ci.nii.ac.jp/naid/500001054902>
- O'Riordan, L. J., & Busch, T. (2016). Topological defect dynamics of vortex lattices in Bose-Einstein condensates. *Phys. Rev. A*, *94*(5), 053603. doi:[10.1103/PhysRevA.94.053603](https://doi.org/10.1103/PhysRevA.94.053603)
- O'Riordan, L. J., White, A. C., & Busch, T. (2016). Moiré superlattice structures in kicked Bose-Einstein condensates. *Phys. Rev. A*, *93*(2), 023609. doi:[10.1103/PhysRevA.93.023609](https://doi.org/10.1103/PhysRevA.93.023609)
- Pethick, C. J., & Smith, H. (2008). *Bose-Einstein Condensation in Dilute Gases*. Cambridge University Press. doi:[10.1017/CBO9780511802850](https://doi.org/10.1017/CBO9780511802850)
- Roche, P.-E., & Barenghi, C. F. (2008). Vortex spectrum in superfluid turbulence: Interpretation of a recent experiment. *EPL (Europhysics Letters)*, *81*(3), 36002. Retrieved from <http://stacks.iop.org/0295-5075/81/i=3/a=36002>
- Ruf, M., Bauke, H., & Keitel, C. H. (2009). A real space split operator method for the Klein-Gordon equation. *Journal of Computational Physics*, *228*(24), 9092–9106. doi:[10.1016/j.jcp.2009.09.012](https://doi.org/10.1016/j.jcp.2009.09.012)
- Schloss, J., & O'Riordan, L. J. (2018). GPUE documentation website. <https://gpue-group.github.io/>.
- White, A. C., Anderson, B. P., & Bagnato, V. S. (2014). Vortices and turbulence in trapped atomic condensates. *Proceedings of the National Academy of Sciences*. doi:[10.1073/pnas.1312737110](https://doi.org/10.1073/pnas.1312737110)
- Wittek, P. (2016). Comparing three numerical solvers of the Gross-Pitaevskii equation. <https://web.archive.org/web/20171120181431/https://peterwittek.com/gpe-comparison.html>.
- Wittek, P., & Cucchietti, F. M. (2013). A second-order distributed Trotter-Suzuki solver with a hybrid CPU-GPU kernel. *Computer Physics Communications*, *184*(4), 1165–1171. doi:[10.1016/j.cpc.2012.12.008](https://doi.org/10.1016/j.cpc.2012.12.008)
- Zhang, T. (2017). *Chaotic Vortex Dynamics in Bose-Einstein Condensates* (Master's thesis). Norwegian University of Science; Technology, Norway. Retrieved from <http://hdl.handle.net/11250/2467021>

Chaotic few-body vortex dynamics in rotating Bose-Einstein condensates

Tiantian Zhang,^{1,2} James Schloss,¹ Andreas Thomasen,¹ Lee James O’Riordan,¹ Thomas Busch,¹ and Angela White^{1,3}

¹*Okinawa Institute of Science and Technology Graduate University, Onna-son, Okinawa 904-0495, Japan*

²*Institute of Atomic and Subatomic Physics, Technische Universität Wien, Stadionallee 2, Vienna 1020, Austria*

³*Department of Quantum Science, Research School of Physics and Engineering, The Australian National University, Canberra ACT 2601, Australia*



(Received 11 December 2018; published 9 May 2019)

We investigate a small vortex-lattice system of four corotating vortices in an atomic Bose-Einstein condensate and find that the vortex dynamics display chaotic behavior after a system quench introduced by reversing the direction of circulation of a single vortex through a phase-imprinting process. By tracking the vortex trajectories and Lyapunov exponent, we show the onset of chaotic dynamics is not immediate, but occurs at later times and is accelerated by the close approach and separation of all vortices in a scattering event. The techniques we develop could potentially be applied to create locally induced chaotic dynamics in larger lattice systems as a stepping stone to study the role of chaotic events in turbulent vortex dynamics.

DOI: [10.1103/PhysRevFluids.4.054701](https://doi.org/10.1103/PhysRevFluids.4.054701)

I. INTRODUCTION

Dynamical systems that are highly sensitive to their initial conditions are often referred to as chaotic. Consequently, some of the hallmark indicators of chaotic evolution are a rapid divergence between two trajectories given a small change in initial conditions and a mixing of trajectories in phase space [1]. Many characteristics of chaos are exhibited in turbulent flows [2], including, for example, the exponential separation of pairs of particles in homogeneous isotropic turbulence [3]. It has recently been shown that in classical forced turbulence, the degree of chaos depends only on the Reynolds number [4]. The importance of chaotic events in classical turbulence and the similarities that can be drawn between classical and quantum turbulence strongly indicate that chaotic events will also contribute to turbulent quantum vortex dynamics, however the nature of these events remains largely unexplored [5].

Understanding the chaotic nature of vortex dynamics is therefore an important aspect of developing a detailed understanding of vortex turbulence. At the same time, it also remains an inherently interesting problem in systems composed of such small numbers of vortices that turbulence is absent. Chaotic few-vortex systems have been known to display intriguing dynamics since the seminal work of Aref and Pompfrey [6–9], who showed that although the two-dimensional hydrodynamics of the classical three vortex system in an infinite plane is integrable, this is not true for the case of four identical vortices which can exhibit chaotic dynamics [7]. The simple nature of quantum vortices in comparison to their classical counterparts has also led to interest in the chaotic nature of quantum vortices in superfluids, such as Bose-Einstein condensates (BECs) and superfluid He [10–13]. Unlike in the classical case, the onset of chaos in quantum vortices appears with fewer vortices present, and early experiments have explored corotating few-vortex clusters in harmonically trapped BECs, both for the integrable two-vortex problem as well as the nonintegrable three- and four-vortex cases where chaotic trajectories can occur [13]. In harmonically trapped two-dimensional BECs, the crossover from regular to chaotic motion in a system of three interacting

vortices, with two corotating vortices and an antivortex rotating in the opposite direction has also been explored theoretically through a reduced Hamiltonian approach [11,12].

Vortex dynamics in superfluid systems draw remarkable analogies to classical point-vortex systems and classical vortex turbulence in spite of the striking differences between quantum and classical fluids. In BECs, the superfluid velocity, $\mathbf{v} = \hbar \nabla \theta / m$, is dependent purely on the gradient of the condensate phase θ , which means quantum vortices possess a well-defined strength and quantized circulation, making them simpler than their classical counterparts which can be of any strength and arbitrary circulation. Although quantum and classical vortices are very different, hallmarks of classical turbulence, such as the Kolmogorov spectrum, have been shown to emerge in quantum vortex turbulence on scales larger than the average intervortex spacing [14–17]. Vortex turbulence in two-dimensional BECs has become a subject of increasing experimental interest, due to the controllable nature of BECs and quantum vortices. Experimental techniques have advanced, resulting in accessible methods to detect vortex circulation [18], image vortices *in-situ* [19], and build a picture of vortex dynamics at different times in a single experiment [20,21]. Recent times have seen experiments exhibiting the von Kármán vortex street [22], as well as investigations into decaying two dimensional turbulence [23,24] and demonstration of Onsager vortex clusters [25,26] in Bose-Einstein condensates.

In this work we will exploit the finely controllable nature of vortices in BECs to extend the picture of chaotic vortex dynamics in systems consisting of small numbers of quantum vortices. Vortex lattices in rotating BECs are extremely robust and have proven to be stable against externally applied perturbations, such as periodic kicking [27]. One way to capitalise on this stability and generate repeatable and well-controlled initial conditions is to engineer lattice defects by applying the technique of phase imprinting. Phase imprinting can be used to control both the number and location of defects in vortex lattices [28] and is also experimentally feasible [29]. Phase imprinting has been applied in a variety of BEC experiments, ranging from transferring orbital angular momentum to atoms from a Laguerre-Gaussian beam [30,31], to using a pulsed light shift with a tailored intensity pattern to create a soliton [32], vortex [29], or states with quantized circulation [33].

In the following, we show that phase imprinting one vortex defect in a small vortex lattice system can be used to controllably create chaotic vortex dynamics in an experimentally accessible way. We also find that even though chaotic dynamics is confirmed by a positive Lyapunov exponent immediately after the quench, other signals of chaotic dynamics are boosted only at later times by the close approach and consequent scattering of all vortices. Applying this technique to more than one vortex in the lattice may potentially be used to induce chaotic vortex dynamics in systems of larger numbers of vortices, enabling one to control the number of vortices with chaotic trajectories and the location of locally induced vortex chaos in larger lattice systems.

This manuscript is organized as follows. In Sec. II we discuss the theoretical model we apply to study the small vortex lattice systems in BECs, introducing the Gross-Pitaevskii equation and describing the technique of phase imprinting. Section III presents the resulting condensate dynamics after phase imprinting, and discusses how this leads to regular and chaotic vortex dynamics in systems of four corotating vortices and three corotating vortices and one antivortex, respectively. In Sec. IV, by tracking vortex trajectories and calculating the Lyapunov spectrum, we further quantify the onset of chaos. Finally, our conclusions are presented in Sec. V.

II. THEORETICAL MODEL

The dynamics of vortices in a BEC near zero Kelvin are well described in the mean-field regime by a two-dimensional Gross-Pitaevskii equation (GPE), which can be written as

$$i\hbar \frac{\partial}{\partial t} \Psi = \left(-\frac{\hbar^2}{2m} \nabla^2 + \frac{1}{2} m \omega_{\perp}^2 \mathbf{r}^2 + g |\Psi|^2 - \Omega L_z \right) \Psi, \quad (1)$$

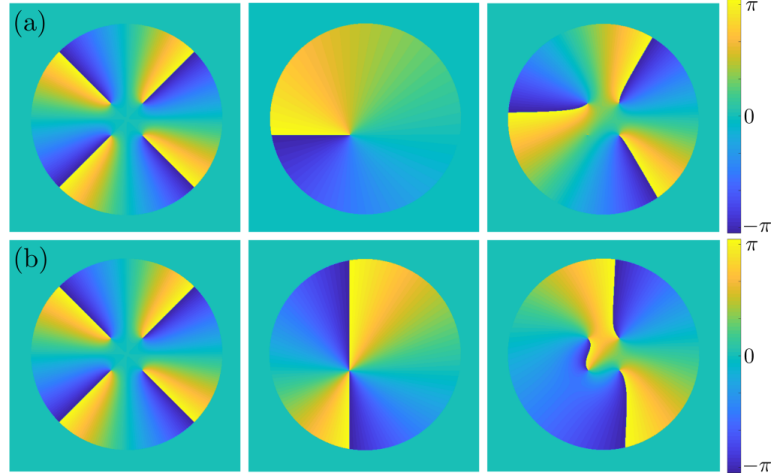


FIG. 1. From left to right both rows depict the phase profile of the initial corotating four-vortex system (left), the phase mask applied to change the circulation of the lower-left vortex (center) and the resulting four-vortex system after the phase imprinting process. (a) Imprinting of a 2π antivortex creates a system of three corotating vortices and removes the phase singularity in the lower-left quadrant. (b) Imprinting of a 4π antivortex creates a system of three corotating vortices and an antivortex in the lower-left quadrant.

in the rotating frame. Here $L_z = xp_y - yp_x$ is the angular momentum operator, and we choose a realistic value of $\Omega = 0.3 \times 2\pi$ Hz as the frequency of an externally applied rotation around the z axis. We model a condensate of $N = 10^6$ ^{87}Rb atoms with an s-wave scattering length $a_s \approx 90a_0$, confined in an oblate harmonic trapping potential, $(\mathbf{V}_\perp, \mathbf{V}_z) = \frac{1}{2}m(\omega_\perp^2 \mathbf{r}^2, \omega_z^2 \mathbf{z}^2)$, with typical trapping frequencies $(\omega_\perp, \omega_z) = (2\pi, 32\pi)$ Hz and \mathbf{r} is a position vector. The effective two-dimensional interaction strength is $g = (4\pi\hbar^2 a_s N/m) \sqrt{m\omega_z/2\pi\hbar} = 6.8 \times 10^{-40} \text{ m}^4 \text{ kg/s}^2$.

For the evolution of our BEC system, we use the split-step method [34]. In order to find the ground states in the rotating frame, we employ imaginary time propagation by substituting $t = -i\tau$ in Eq. (1) [35]. We then solve this equation efficiently on a spatial grid of $2^{10} \times 2^{10}$ points covering an extent of $700 \mu\text{m} \times 700 \mu\text{m}$, using graphics processing units (GPUs) by making use of the open-source GPE solver, GPUE [36].

Under large, externally imposed rotation, the ground state of a BEC can consist of a triangular lattice of quantum vortices, with the number of constituent vortices dependent on the rotation strength [37–39]. However, for smaller rotation strengths other configurations are known [40] and we will concentrate on the regime where four vortices appear in the ground state in a square configuration [41]. While the direction of rotation of the individual vortices is usually the same as that of the applied external rotation, this can be changed by phase imprinting [28].

Through phase imprinting, a phase profile corresponding to a vortex with 2π phase winding can be introduced into the condensate by $\Psi_{\text{IMP}}(\mathbf{r}, t) = |\Psi(\mathbf{r}, t)| \exp^{i[\theta(\mathbf{r}, t) + \theta_{\text{IMP}}(\mathbf{r})]}$ where the four-quadrant arctan defines $\theta_{\text{IMP}}(\mathbf{r}) = \arctan(y - y_0, x - x_0)$, which centers the singularity of the vortex phase profile at the position (x_0, y_0) in the condensate. Imprinting a phase mask of 2π winding centered on an existing vortex of 2π winding in the same direction will create a doubly charged vortex (of 4π winding) at that location, which will subsequently decay into two singly charged vortices [42]. Imprinting a vortex-centered phase mask of 2π winding in the opposite direction to the vortex circulation will result in vortex annihilation [see Fig. 1(a)], removing the circulation in that region. Finally, imprinting a phase mask with 4π winding in the opposite direction to the direction of circulation of a vortex on that vortex center [see Fig. 1(b)] will reverse the direction of circulation of that vortex. To annihilate or change the direction of circulation of a vortex through phase imprinting, the imprinted phase mask must be centered on a vortex in the lattice close to the vortex core at a distance of less than twice the condensate healing length [28].

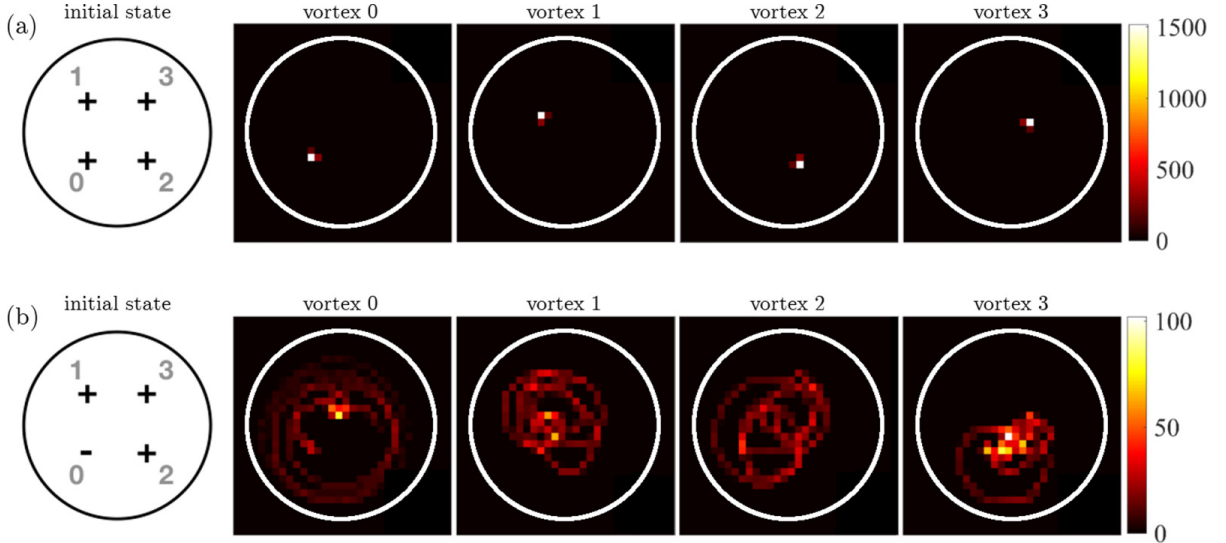


FIG. 2. Histograms of the positions of each vortex in the x - y plane, tracked over an evolution time of 20 s in the corotating frame. The vortex in the lower left has been annihilated by phase imprinting and reimprinted with (a) the same and (b) the opposite direction of rotation, exactly on the vortex core. The area of each plot is $400 \mu\text{m} \times 400 \mu\text{m}$, and the white circles are contour lines at 40% of the maximum density, indicating extent of vortex motion for a rotationally symmetric condensate. (a) For four vortices with the same circulation direction, regular trajectories at constant radius appear, while in panel (b), disordered vortex trajectories can be seen.

III. REGULAR AND IRREGULAR VORTEX DYNAMICS

In this work, we reverse the direction of circulation of a single vortex in a lattice through phase imprinting and investigate if the resulting vortex dynamics are regular or chaotic. To engineer slightly different initial conditions, we vary the distance from the existing vortex core at which the phase imprint has its singularity, while staying within a healing length, and compare the resulting trajectories. It is well established that a lattice of vortices with the same direction of rotation exhibits regular dynamics [39], and in Fig. 2(a) we confirm this for a system of four vortices. The graphs show the histograms of the positions of each individual vortex (labeled 0 to 3 from left to right), where vortex 0 has been erased and reimprinted with the original winding. One can clearly see that they remain stationary in the corotating frame over 20 s of evolution, even though a small residual movement from their initial position arises, which stems from the presence of small phonon excitations that were not fully damped out in the numerical ground-state finding process. However, when the direction of circulation of a single vortex is reversed in the reimprinting process, this regularity disappears, and the vortex dynamics become more disordered, with vortices traversing the width of the condensate [shown in Fig. 2(b)], where the heavily weighted histogram cells indicate more likely vortex positions during evolution. Reversing the direction of rotation of a single vortex can therefore lead to dramatically different results. It is worth noting that such histograms of vortex position evolution could readily be constructed in experiments with available *in-situ* imaging techniques [19,20].

Although introducing an antivortex results in disordered dynamics, one could imagine that this disordered motion is irregular but stable, and any small perturbation in vortex position might give rise to the same irregular trajectories around the condensate. To check this we compare two sets of perturbed vortex trajectories with slightly different shifts in the initial position of the antivortex, \mathbf{r}_0 and \mathbf{r}'_0 , and show the differences in trajectories defined as $\Delta\mathbf{r}_i(t) = \mathbf{r}_i(t) - \mathbf{r}'_i(t)$ in Fig. 3, where \mathbf{r} refers to the position of the i th vortex from the center of the condensate and $i \in \{1, 2, 3\}$ corresponds to the vortex number. One can see that this difference is initially small, but starts to diverge significantly at around $t \approx 10$ s, which is a strong indication of chaotic dynamics in this system.

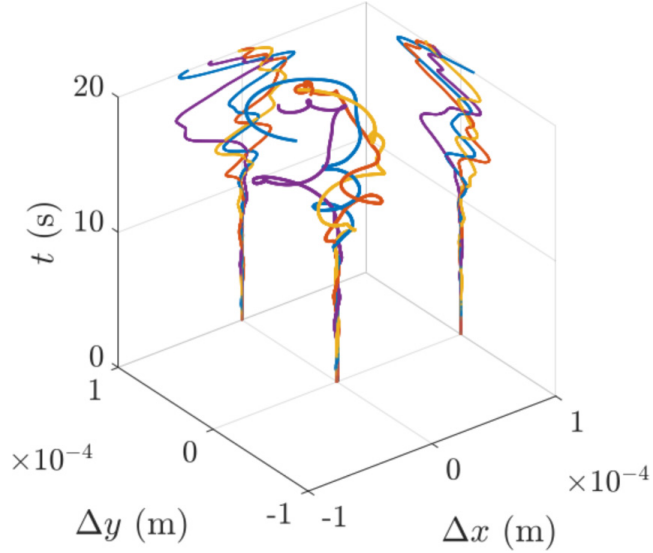


FIG. 3. Evolution of the difference in trajectories $\Delta\mathbf{r}_i = \mathbf{r}_i - \mathbf{r}'_i$ with \mathbf{r} corresponding to the position of the i th vortex from the center of the condensate and $i \in \{0, 1, 2, 3\}$ labeling each individual vortex for the four-vortex system as shown in Fig. 2. A small change in the initial position of the antivortex arises from a phase imprint at (x_0, y_0) and $(x_0 - \xi/3, y_0)$ where (x_0, y_0) denotes the preexisting corotating vortex core position. The curves show that even though the onset of disorder is immediate, a strong divergence of trajectories is observed at about $t \approx 10$ s (see projections onto the x - t and y - t planes). The difference in trajectory of the antivortex, $\Delta\mathbf{r}_0$, is shown in blue, while yellow, orange, and purple lines depict the three corotating vortices.

A close inspection of the vortex dynamics (see supplemental movie [43]) shows that the strong divergence in trajectories appears to be accelerated when all four vortices move close to each other and are minimally separated. Because the velocity fields of each vortex decays as $1/r$, where r is the distance from each vortex core, the vortices experience stronger velocity fields when they are closer to each other; moreover, the point of minimal separation can be interpreted as a multivortex *scattering* event. Such a scattering event is highly nonlinear and accelerates the divergence between the vortex trajectories. In Fig. 4 we show snapshots of the full condensate density before ($t = 6$ s), at ($t = 10$ s) and after ($t = 15$ s) the scattering event. One can see that the differences between $\Delta x = 0$ [Fig. 4(a)] and $\Delta x = \xi/3$ [Fig. 4(b)] are small before, but large after multivortex scattering. By tracking the distance between each corotating vortex and the antivortex, we show in Fig. 4(c) that a clear minimum around $t = 10$ s exists, indicating vortex scattering at this time. In our calculations, we track vortex positions numerically, by finding the positions in the condensate where the condensate density $|\Psi|^2$ goes to zero, with a 2π winding in the condensate phase around the grid plaquette surrounding that position, signaling the position of a vortex. As long as the distance between two vortices is large, the velocity field of one vortex seen by the other vortex will be small, and consequently any small difference stemming from the small change in the initial condition will not have a large effect on the vortex dynamics. However, a closer approach of the vortex cores leads to stronger interactions and therefore differences in the velocity fields have a larger influence on the ensuing vortex dynamics, leading to the observed boost in the divergence of the resulting trajectories. In order to determine if this disordered motion is indeed chaotic, it is necessary to analyze the vortex dynamics in more detail and to do this we proceed to calculate the Lyapunov exponent.

IV. CHARACTERIZING CHAOTIC VORTEX DYNAMICS

Lyapunov exponents give the rates of divergence of nearby orbits in phase space [44]. For the two neighboring trajectories in four-dimensional phase space we consider, $\mathbf{P}(t) = (x(t), y(t), v_x(t), v_y(t))$ and $\mathbf{P}'(t) = (x'(t), y'(t), v'_x(t), v'_y(t))$, with separation defined as $\delta\mathbf{P}(t) =$

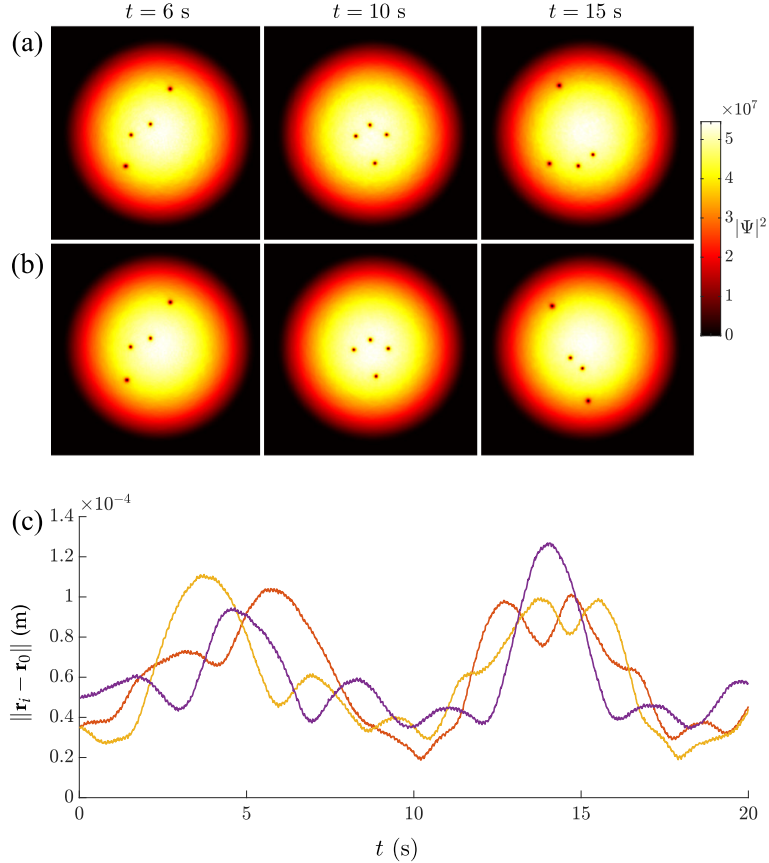


FIG. 4. Density plots of condensate for (a) $\Delta x = 0$ and (b) $\Delta x = \xi/3$ at times $t = \{6, 10, 15\}$ s. The densities before the scattering event differ only on small scales (see $t = 6$ s), whereas for times after the event large deviations are visible (see $t = 15$ s). At $t = 10$ s the vortices make their closest approach. The area plotted is $500 \mu\text{m} \times 500 \mu\text{m}$. (c) Distances between the vortices at positions \mathbf{r}_i with \mathbf{r} corresponding to the position of the i th vortex from the center of the condensate and $i \in \{1, 2, 3\}$ corresponding to the vortex number as shown in Fig. 2 and antivortex at \mathbf{r}_0 for $\Delta x = 0$. A minimum around $t = 10$ s is clearly visible.

$(\delta x(t), \delta y(t), \delta v_x(t), \delta v_y(t))$ where $\delta x(t) = x(t) - x'(t)$, etc. The resulting four-dimensional Lyapunov exponent, λ , can then be calculated as

$$\lambda = \lim_{t \rightarrow \infty} \frac{1}{t} \ln \frac{\|\delta \mathbf{P}(t)\|}{\|\delta \mathbf{P}(0)\|}, \quad (2)$$

where $\|\cdot\|$ denotes the Euclidean norm. If one or more Lyapunov exponents are positive, the system is chaotic, with unpredictable dynamics developing at a timescale which can be determined from the magnitude of the Lyapunov exponent. While it is difficult numerically to isolate the evolution of the momentum of each vortex in time, we can build up a representative picture of the phase-space trajectories of individual vortices in our vortex system by tracking both the position and velocity of each vortex. The Lyapunov exponents can then be calculated by comparing two trajectories with slightly perturbed initial conditions.

In order to define a phase-space measure for the total system of vortices instead of for each constituent vortex individually, we use a center of mass (COM) variable defined by $\mathbf{R}_M = \frac{1}{n+1} \sum_{i=0}^n \mathbf{r}_i$, where $n+1$ is the number of vortices. Similarly, the center of mass velocity is expressed as $\mathbf{v}_M = \frac{1}{n+1} \sum_{i=0}^n \mathbf{v}_i$. To calculate the Lyapunov exponent using the center of mass variables in Eq. (2), we define the separation of the trajectories in four-dimensional phase-space as $\delta \mathbf{P}(t) = (\delta x_M(t), \delta y_M(t), \delta v_{Mx}(t), \delta v_{My}(t))$ where $\delta x_M(t) = x_M(t) - x'_M(t)$, etc.

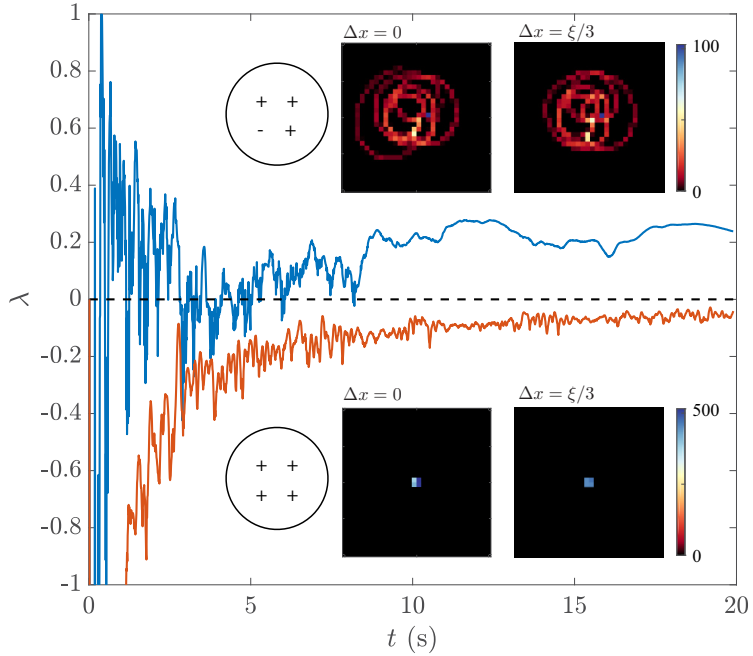


FIG. 5. The insets show the histograms of the COM trajectories calculated over 20 s of evolution for the system of four vortices when the position of a single vortex has been shifted by $\Delta x = 0\xi$ and $\Delta x = \xi/3$. The upper two panels depict the corresponding trajectories after the direction of rotation of a single vortex has been reversed, whereas the lower row displays the trajectories for the case where all vortices corotate. The main curve plots the corresponding Lyapunov exponents, calculated from the shown COM trajectories. The negative Lyapunov exponents (orange) indicate that shifting the vortex about the initial position still ensures the stability of vortex trajectories. Reversing the direction of circulation of a single vortex (blue) however leads to fluctuations about zero, eventually leading to a fully positive exponent.

The insets of Fig. 5 show the histogram in time (and in the corotating frame) of the center of mass trajectories, which confirm similar irregular dynamics of the system with the antivortex (upper row) and regular trajectories of the system with four corotating vortices (lower row). It is worth noting that one could also consider using a global measure which takes into account the direction of circulation of the vortices, and instead consider a *center of charge* variable [11]. As we find both quantities give similar qualitative results for calculating the Lyapunov exponents, we only consider the COM of the vortex system here.

As expected, this COM Lyapunov exponent spectrum, calculated for both regular and disordered four vortex systems, shows that the regular corotating system always maintains a negative value for the Lyapunov exponent, indicating nonchaotic behavior (orange curve in Fig. 5). However, for the system where a vortex of opposite sign is introduced, we observe that the Lyapunov exponent initially strongly oscillates but later settles and grows to maintain a positive value, indicating chaotic behavior. The time of onset of the constantly positive exponent corresponds to the appearance of the scattering event and the boost in the difference in trajectories. The strong oscillations before that time can therefore most likely be attributed to the finite resolution of our numerics and consequently limited accuracy of the vortex velocities. Such a Lyapunov exponent spectrum could be experimentally constructed through *in-situ* measurements [19,20], where vortex positions (and consequently velocities) are tracked in a single experimental run.

V. DISCUSSION AND CONCLUSIONS

We have demonstrated that applying phase imprinting techniques to a small lattice of vortices can change the dynamics of the system from being regular to being chaotic. By simply reversing

the direction of rotation of a single vortex, the Lyapunov exponent of the COM trajectories for the vortices clearly indicates the chaotic nature of the vortex trajectories after an initial adjustment phase. In fact, we have found that the chaotic dynamics are accelerated at late times by the close approach and consequent scattering of vortices in a multivortex scattering event. This scattering event amplifies the small initial difference in trajectories and results in vortices scattering at different angles while also seeding the ensuing chaotic divergence of trajectories. This method is potentially scalable to larger lattices of vortices and is realisable in cold-atom experiments.

We have also checked that reversing the direction of circulation of a single vortex in small lattices of five and six vortices still exhibit chaotic dynamics [45], and find they exhibit a similar degree of chaotic motion with Lyapunov exponents of 0.24, 0.24, and 0.27 for the four, five and six vortex cases, respectively after 20 s of evolution. This result contrasts to the limit of rapidly rotating condensates, where large Abrikosov vortex lattices develop and phase engineering a single vortex defect is known to only induce localized disturbance [28]. Studying this crossover from chaotic to regular dynamics, and engineering a crossover from regular to turbulent dynamics is an exciting extension we leave to future work.

ACKNOWLEDGMENTS

This work has been supported by the Okinawa Institute of Science and Technology Graduate University and used the computing resources of the Scientific Computing and Data Analysis section. This work has also been supported by JSPS KAKENHI-16K05461 and JP17J01488. We also thank Carlo F. Barenghi and Makoto Tsubota for useful discussions.

-
- [1] S. H. Strogatz, *Nonlinear Dynamics and Chaos, with Applications to Physics, Biology, Chemistry, and Engineering* (Reading, MA: Addison-Wesley, 1994).
 - [2] E. A. Spiegel, Chaos: A mixed metaphor for turbulence, *Proc. R. Soc. Lond. A* **413**, 87 (1987).
 - [3] L. Biferale, G. Boffetta, A. Celani, B. J. Devenish, A. Lanotte, and F. Toschi, Lagrangian statistics of particle pairs in homogeneous isotropic turbulence, *Phys. Fluids* **17**, 115101 (2005).
 - [4] A. Berera and R. D. J. G. Ho, Chaotic Properties of a Turbulent Isotropic Fluid, *Phys. Rev. Lett.* **120**, 024101 (2018).
 - [5] A. C. White, B. P. Anderson, and V. S. Bagnato, Vortices and turbulence in trapped atomic condensates, *Proc. Natl. Acad. Sci. USA* **111**, 4719 (2014).
 - [6] H. Aref and N. Pomphrey, Integrable and chaotic motions of four vortices, *Phys. Lett. A* **78**, 297 (1980).
 - [7] H. Aref and N. Pomphrey, Integrable and chaotic motions of four vortices I. The case of identical vortices, *Proc. R. Soc. Lond. A* **380**, 359 (1982).
 - [8] H. Aref, Integrable, chaotic, and turbulent vortex motion in two-dimensional flows, *Annu. Rev. Fluid Mech.* **15**, 345 (1983).
 - [9] B. Eckhardt and H. Aref, Integrable and chaotic motions of four vortices II. Collision dynamics of vortex pairs, *Proc. R. Soc. Lond. A* **326**, 655 (1988).
 - [10] S. K. Nemirovskii and W. Fiszdon, Chaotic quantized vortices and hydrodynamic processes in superfluid helium, *Rev. Modern Phys.* **67**, 37 (1995).
 - [11] N. Kyriakopoulos, V. Koukouloyannis, C. Skokos, and P. G. Kevrekidis, Chaotic behavior of three interacting vortices in a confined Bose-Einstein condensate, *Chaos* **24**, 024410 (2014).
 - [12] V. Koukouloyannis, G. Voyatzis, and P. G. Kevrekidis, Dynamics of three non-corotating vortices in Bose-Einstein condensates, *Phys. Rev. E* **89**, 042905 (2014).
 - [13] R. Navarro, R. Carretero-González, P. J. Torres, P. G. Kevrekidis, D. J. Frantzeskakis, M. W. Ray, E. Altuntaş, and D. S. Hall, Dynamics of a Few Corotating Vortices in Bose-Einstein Condensates, *Phys. Rev. Lett.* **110**, 225301 (2013).
 - [14] C. Nore, M. Abid, and M. E. Brachet, Kolmogorov Turbulence in Low-Temperature Superflows, *Phys. Rev. Lett.* **78**, 3896 (1997).

- [15] S. R. Stalp, L. Skrbek, and R. J. Donnelly, Decay of Grid Turbulence in a Finite Channel, *Phys. Rev. Lett.* **82**, 4831 (1999).
- [16] T. Araki, M. Tsubota, and S. K. Nemirovskii, Energy Spectrum of Superfluid Turbulence with no Normal-Fluid Component, *Phys. Rev. Lett.* **89**, 145301 (2002).
- [17] J. Salort, C. Baudet, B. Castaing, B. Chabaud, F. Daviaud, T. Didelot, P. Diribarne, B. Dubrulle, Y. Gagne, F. Gauthier *et al.*, Turbulent velocity spectra in superfluid flows, *Phys. Fluids* **22**, 125102 (2010).
- [18] S. W. Seo, B. Ko, J. H. Kim, and Y. Shin, Observation of vortex-antivortex pairing in decaying 2D turbulence of a superfluid gas, *Sci. Rep.* **7**, 4587 (2017).
- [19] K. Wilson, Z. L. Newman, J. D. Lowney, and B. P. Anderson, In situ imaging of vortices in Bose-Einstein condensates, *Phys. Rev. A* **91**, 023621 (2015).
- [20] D. V. Freilich, D. M. Bianchi, A. M. Kaufman, T. K. Langin, and D. S. Hall, Real-time dynamics of single vortex lines and vortex dipoles in a Bose-Einstein condensate, *Science* **329**, 1182 (2010).
- [21] S. Serafini, L. Galantucci, E. Iseni, T. Bienaimé, R. Bisset, C. F. Barenghi, F. Dalfovo, G. Lamporesi, and G. Ferrari, Vortex Reconnections and Rebounds in Trapped Atomic Bose-Einstein Condensates, *Phys. Rev. X* **7**, 021031 (2017).
- [22] W. J. Kwon, J. H. Kim, S. W. Seo, and Y. Shin, Observation of von Kármán Vortex Street in an Atomic Superfluid Gas, *Phys. Rev. Lett.* **117**, 245301 (2016).
- [23] T. W. Neely, A. S. Bradley, E. C. Samson, S. J. Rooney, E. M. Wright, K. J. H. Law, R. Carretero-González, M. J. Davis, and B. P. Anderson, Characteristics of Two-Dimensional Quantum Turbulence in a Compressible Superfluid, *Phys. Rev. Lett.* **111**, 235301 (2013).
- [24] W. J. Shin, G. Moon, J. Choi, S. W. Seo, and Y. Shin, Relaxation of superfluid turbulence in highly oblate Bose-Einstein condensates, *Phys. Rev. A* **90**, 063627 (2014).
- [25] G. Gauthier, M. T. Reeves, X. Xu, A. S. Bradley, M. Baker, T. A. Bell, H. Rubinsztein-Dunlop, M. J. Davis, and T. W. Neely, Negative-temperature Onsager vortex clusters in a quantum fluid, [arXiv:1801.06951 \[cond-mat.quant-gas\]](https://arxiv.org/abs/1801.06951).
- [26] S. P. Johnstone, A. J. Groszek, P. T. Starkey, C. J. Billington, T. P. Simula, and K. Helmerson, Order from chaos: Observation of large-scale flow from turbulence in a two-dimensional superfluid, [arXiv:1801.06952 \[cond-mat.quant-gas\]](https://arxiv.org/abs/1801.06952).
- [27] L. J. O’Riordan, A. C. White, and T. Busch, Moiré superlattice structures in kicked Bose-Einstein condensates, *Phys. Rev. A* **93**, 023609 (2016).
- [28] L. J. O’Riordan and T. Busch, Topological defect dynamics of vortex lattices in Bose-Einstein condensates, *Phys. Rev. A* **94**, 053603 (2016).
- [29] Ł. Dobrek, M. Gajda, M. Lewenstein, K. Sengstock, G. Birkl, and W. Ertmer, Optical generation of vortices in trapped Bose-Einstein condensates, *Phys. Rev. A* **60**, 3381(R) (1999).
- [30] M. F. Andersen, C. Ryu, P. Cladé, V. Natarajan, A. Vaziri, K. Helmerson, and W. D. Phillips, Quantized Rotation of Atoms from Photons with Orbital Angular Momentum, *Phys. Rev. Lett.* **97**, 170406 (2006).
- [31] C. Ryu, M. F. Andersen, P. Cladé, V. Natarajan, K. Helmerson, and W. D. Phillips, Observation of Persistent Flow of a Bose-Einstein Condensate in a Toroidal Trap, *Phys. Rev. Lett.* **99**, 260401 (2007).
- [32] J. Denschlag, J. E. Simsarian, D. L. Feder, C. W. Clark, L. A. Collins, J. Cubizolles, L. Deng, E. W. Hagley, K. Helmerson, W. P. Reinhardt, S. L. Rolston, B. I. Schneider, and W. D. Phillips, Generating solitons by phase engineering of a Bose-Einstein condensate, *Science* **287**, 97 (2000).
- [33] A. Kumar, R. Debussey, T. Badr, C. De Rossi, M. de Goér de Herve, L. Longchambon, and H. Perrin, Producing superfluid circulation states using phase imprinting, *Phys. Rev. A* **97**, 043615 (2018).
- [34] J. Javanainen, and J. Ruostekoski, Symbolic calculation in development of algorithms: Split-step methods for the Gross-Pitaevskii equation, *J. Phys. A* **39**, L179 (2006).
- [35] M. L. Chiofalo, S. Succi, and M. P. Tosi, Ground state of trapped interacting Bose-Einstein condensates by an explicit imaginary-time algorithm, *Phys. Rev. E* **62**, 7438 (2000).
- [36] J. Schloss and L. J. O’Riordan, GPUE: Graphics Processing Unit Gross-Pitaevskii Equation solver, *J. Open Source Softw.* **3**, 1037 (2018).
- [37] F. Chevy, K. W. Madison, and J. Dalibard, Measurement of the Angular Momentum of a Rotating Bose-Einstein Condensate, *Phys. Rev. Lett.* **85**, 2223 (2000).

-
- [38] K. W. Madison, F. Chevy, W. Wohlleben, and J. Dalibard, Vortex Formation in a Stirred Bose-Einstein Condensate, *Phys. Rev. Lett.* **84**, 806 (2000).
 - [39] J. R. Abo-Shaeer, C. Raman, J. M. Vogels, and W. Ketterle, Observation of vortex lattices in Bose-Einstein condensates, *Science* **292**, 476 (2001).
 - [40] A. Aftalion and Q. Du, Vortices in a rotating Bose-Einstein condensate: Critical angular velocities and energy diagrams in the Thomas-Fermi regime, *Phys. Rev. A* **64**, 063603 (2001).
 - [41] A. V. Zampetaki, R. Carretero-González, P. G. Kevrekidis, F. K. Diakonos, and D. J. Frantzeskakis, Exploring rigidly rotating vortex configurations and their bifurcations in atomic Bose-Einstein condensates, *Phys. Rev. E* **88**, 042914 (2013).
 - [42] Y. Shin, M. Saba, M. Vengalattore, T. A. Pasquini, C. Sanner, A. E. Leanhardt, M. Prentiss, D. E. Pritchard, and W. Ketterle, Dynamical Instability of a Doubly Quantized Vortex in a Bose-Einstein Condensate, *Phys. Rev. Lett.* **93**, 160406 (2004).
 - [43] See Supplemental Material at <http://link.aps.org/supplemental/10.1103/PhysRevFluids.4.054701> for an example movie of the multivortex scattering event that seeds the onset of irregular dynamics.
 - [44] A. Wolf, J. B. Swift, H. L. Swinney, and J. A. Vastano, Determining Lyapunov exponents from a time series, *Physica D* **16**, 285 (1985).
 - [45] T. Zhang, Chaotic vortex dynamics in Bose-Einstein condensates, Master's thesis, NTNU, 2017.

Controlled creation of three-dimensional vortex structures in Bose–Einstein condensates using artificial magnetic fields

James Schloss,¹ Peter Barnett,^{1,2} Rashi Sachdeva,¹ and Thomas Busch¹

¹⁾ OIST Graduate University, 904-0495 Okinawa, Japan

²⁾ Department of Physics, University of Otago, Dunedin 9054, New Zealand

The physics of quantized vortex excitations in atomic Bose–Einstein condensates has been extensively studied in recent years. Although simple vortex lines are relatively easy to create, control, and measure in experiments, it is a lot more difficult to do the same for vortex ring structures. Here we suggest and explore a method for generating and controlling superfluid vortex rings, vortex ring lattices, and other three dimensional vortex structures in toroidally-trapped superfluid Bose–Einstein condensates by using the artificial magnetic field produced by an optical nanofiber. The presence of the fiber also necessitates a multiply-connected geometry and we show that in this situation the presence of these vortex structures can be deduced from exciting the scissors mode of the condensate.

PACS numbers: 03.75.Lm, 05.30.Jp, 78.67.-n, 42.81.-i

I. INTRODUCTION

Atomic Bose–Einstein condensates (BECs) are superfluids consisting of neutral, bosonic atoms that have been cooled and condensed into the macroscopic ground state of an external potential¹. They have been shown to support a large number of flow-related excitations, with the most common ones being quantized vortex lines and vortex rings^{2–9}. However, vortices with higher winding numbers are unstable in singly-connected condensates, which means that increasing the amount of angular momentum imparted on the superfluid will lead to an increasing number of vortices with a winding number of one. These vortex lines interact repulsively and larger numbers will eventually arrange themselves in the form of a triangular, Abrikosov lattice³, similar to the behaviour known for Type II superconductors¹⁰. Due to the quantization and the homogeneity in winding numbers, single component condensates are often suggested and used for studying superfluid turbulence^{11–14}.

In a finite-sized atomic condensate without dissipative effects, all vortex lines must have a finite length and either start and end at the cloud surface² or reconnect onto themselves¹². Complex, three dimensional vortex topologies beyond vortex lines cannot be easily created by stirring or rotating a BEC because the vortex lines generated in this way must follow the axis of rotation; therefore, to consistently control and generate vortex rings or other topological structures, methods beyond stirring are required and only a small number of experimental realizations of these have been reported^{5,9}.

In most cases, including in most theoretical proposals, vortex ring generation in BECs relies on dynamic processes that do not create eigenstates of the system. These include using the decay of dark solitons in multicomponent condensates⁵ via the snake instability¹⁵, direct density engineering^{16,17}, or the collision of symmetric defects¹⁸. Other theoretical proposals have considered interfering two BECs¹⁹, using spatially dependent Feschbach resonances²⁰, or direct phase imprinting

methods¹⁵. It should be noted that for inhomogeneously trapped BECs, vortex ring structures are known to be unstable, which has led to difficulties in their experimental observation²¹. In addition, the direct absorption imaging techniques employed in the field of BECs are not well suited to determine whether a three dimensional vortex structure is present in an experimental system or not.

Another method to induce rotational effects in a BEC is through the introduction of artificial magnetic fields, which can be created, for example, by the interaction between an atomic system in a dressed state and an electric field that is tuned near an atomic resonance frequency²². In this case, instead of following an axis of rotation, the vortices follow along the artificial magnetic field lines, which allows one to stably generate complex vortex structures by modulating the geometry of the magnetic field profiles.

In this work we will discuss a system that allows for the tunable creation of artificial magnetic fields based on electromagnetic fields that vary strongly over short distances. Such behavior can be found in the near-field regime on the surface of a dielectric system, when light undergoes total internal reflection²³. For the generation of vortex rings, a suitable dielectric system is the optical nanofiber, which is an optical element that has several propagation modes to allow for the configurable generation of evanescent fields. Nanofiber systems can be created by heating and stretching optical fibers until their thinnest region is roughly hundreds of nanometers in diameter^{24,25}. At this scale, the wavelength of light is larger than the diameter of the fiber and the strength of the evanescent field is significantly enhanced²⁶. The form of the evanescent field varies significantly depending on the optical modes propagating through the nanofiber, and we will show that this can be used to generate interesting and tunable artificial magnetic fields.

Optical nanofibers are already used in many different experiments with ultracold atoms^{27–32}, and trapping potentials at around 200nm from the fiber surface can be created by using two differently detuned input fields^{33,34}. Our proposed setup will allow for the creation of vortex

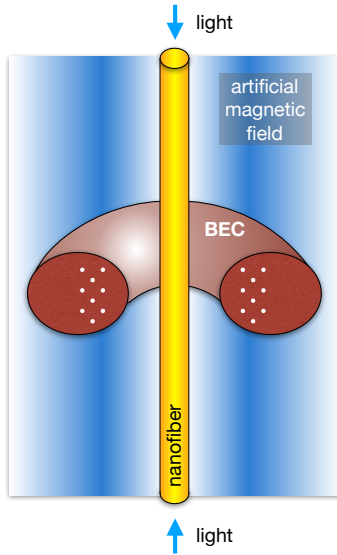


FIG. 1. Schematic of the system. Blue or red-detuned light is sent into the nanofiber (yellow), creating an evanescent field and artificial magnetic field (blue) that influences the BEC (maroon) held by a toroidal trapping potential. If the artificial magnetic field strength is greater than a threshold value, vortex rings (white) will appear and begin to arrange themselves into a triangular lattice.

rings in BECs that are trapped toroidally around the fiber at roughly the same distance by coupling the BEC to the evanescent field created by different modes propagating through the nanofiber³⁵. A schematic of system is depicted in Fig. 1.

In addition, we also discuss a mechanism to detect vortex rings by exciting the scissors mode in an elliptic-toroidal system^{36–38}. This can be done by slightly tilting the trapping geometry radially from the center of the torus, which will cause the BEC to oscillate in and out due to the new potential. Without a vortex present, this oscillation possesses a single frequency, whereas in the presence of a vortex ring it will contain two frequencies that average to the vortex-less oscillation frequency, similar to scissors mode oscillation frequencies in two dimensional, elliptically-trapped BECs^{39–41}. While in simply-connected condensates, vortex rings cannot be detected by this method, we show that in our multiply-connected, elliptic-toroidal geometry, this mode allows for the detection of three dimensional vortex structures.

The manuscript is organized as follows: In Section II, we will discuss how BECs interact with the evanescent field profiles generated by the optical nanofiber. Then, in Section III, we will show simulated results of the vortex configurations that can be generated and discuss in Section IV how to detect whether a vortex ring exists by exciting the scissors mode in an elliptic-toroidal geometry. Finally, in Section V, we will discuss potential

extensions of the suggested system.

II. BOSE-EINSTEIN CONDENSATES IN THE PRESENCE OF AN OPTICAL NANOFIBER

The superfluid properties of atomic Bose-Einstein condensates are captured by the Gross-Pitaevskii Equation (GPE), which describes the evolution of the condensate wave-function in the mean field limit as¹

$$i\hbar \frac{\partial \Psi}{\partial t} = \left[\frac{(p - m\mathbf{A}(\mathbf{r}))^2}{2m} + V_{\text{trap}}(\mathbf{r}) + g|\Psi|^2 \right] \Psi. \quad (1)$$

Here $p = -i\hbar \frac{\partial}{\partial \mathbf{r}}$ is the standard momentum operator and the kinetic energy term also accounts for the presence of a spatially inhomogeneous artificial vector potential, $\mathbf{A}(\mathbf{r})$. The potential term $V_{\text{trap}}(\mathbf{r})$ describes an external trap and the non-linear term accounts for the scattering interaction between the atoms. Its strength is given by $g = \frac{4\pi\hbar^2 a_s}{m}$, where a_s is the scattering length of the atomic species and m its mass. The artificial vector potential can take many forms, and for our purpose we choose a description in terms of Berry's connection²²

$$\mathbf{A} = i\hbar \langle \Psi_l | \nabla \Psi_l \rangle, \quad (2)$$

where Ψ_l is the atomic wavefunction in some dressed state l . Since we will be considering two-state atoms in the presence of an optical field, the relevant dressed states can be written within the rotating wave approximation as²³

$$|\Psi_1(\mathbf{r})\rangle = \begin{pmatrix} \cos[\Phi(\mathbf{r})/2] \\ \sin[\Phi(\mathbf{r})/2] e^{i\phi(z)} \end{pmatrix}, \quad (3)$$

$$|\Psi_2(\mathbf{r})\rangle = \begin{pmatrix} -\sin[\Phi(\mathbf{r})/2] e^{-i\phi(z)} \\ \cos[\Phi(\mathbf{r})/2] \end{pmatrix}, \quad (4)$$

where $\phi(z)$ is the phase of the optical field and $\Phi(\mathbf{r}) = \arctan(|\kappa(\mathbf{r})|/\Delta)$, with $\Delta = \omega_0 - \omega$ being the detuning and $\kappa(\mathbf{r}) = \mathbf{d} \cdot \mathbf{E}(\mathbf{r})/\hbar$ being the Rabi frequency. The atomic dipole moment is given by \mathbf{d} and $\mathbf{E}(\mathbf{r})$ is the electric field.

The form of the artificial vector potential, $\mathbf{A}(\mathbf{r})$, is therefore determined by the form of the optical fields, and for the nanofiber system it can be controlled by choosing specific optical modes to travel through the fiber. The artificial magnetic field associated with the spatially varying artificial vector potential is then given by $\mathbf{B} = \nabla \times \mathbf{A}$, and when the magnetic field lines penetrate the condensates, an artificial Lorentz force will lead to the creation of vortices around these field lines.

To determine which modes will propagate in an optical fiber, one needs to calculate the V -number, which is given by $V = k_0 a \sqrt{n_1^2 - n_2^2}$. Here a is the fiber radius, n_1 is the refractive index of the fiber, n_2 is the refractive index of the cladding, and $k_0 = \omega/c$ with ω being the frequency of the input light beam. In this case, the fiber has been tapered such that the cladding has become

the vacuum with $n_2 = 1$. Higher order modes can only be sustained if $V > V_c \simeq 2.405$, and below this value only the fundamental HE_{11} mode can propagate. The V -number can easily be controlled by choosing the fiber radius^{29,32}

Using cylindrical coordinates, the evanescent field around the nanofiber corresponding to the $\text{HE}_{\ell m}$ mode with circular polarization is given by⁴²

$$E_r = iC[(1-s)K_{\ell-1}(qr) + (1+s)K_{\ell+1}(qr)]e^{i(\omega t - \beta z)}, \quad (5)$$

$$E_\phi = -C[(1-s)K_{\ell-1}(qr) - (1+s)K_{\ell+1}(qr)]e^{i(\omega t - \beta z)}, \quad (6)$$

$$E_z = 2C(q/\beta)K_\ell(qr)e^{i(\omega t - \beta z)}, \quad (7)$$

where

$$s = \frac{1/h^2 a^2 + 1/q^2 a^2}{J'_\ell(ha)/[haJ_\ell(ha)] + K'_\ell(qa)/[qaK_\ell(qa)]}, \quad (8)$$

$$C = \frac{\beta}{2q} \frac{J_\ell(ha)/K_\ell(qa)}{\sqrt{2\pi a^2(n_1^2 N_1 + n_2^2 N_2)}}, \quad (9)$$

and

$$\begin{aligned} N_1 = & \frac{\beta^2}{4h^2} \left[(1-s)^2 [J_{\ell-1}^2(ha) + J_\ell^2(ha)] \right. \\ & \left. + (1+s)^2 [J_{\ell+1}^2(ha) - J_\ell(ha)J_{\ell+2}(ha)] \right] \\ & + \frac{1}{2} [J_\ell^2(ha) - J_{\ell-1}(ha)J_{\ell+1}(ha)], \end{aligned} \quad (10)$$

$$\begin{aligned} N_2 = & \frac{J_\ell^2(ha)}{2K_\ell^2(qa)} \left(\frac{\beta^2}{4q^2} \left[(1-s)^2 [K_{\ell-1}^2(qa) - K_\ell^2(qa)] \right. \right. \\ & \left. \left. - (1+s)^2 [K_{\ell+1}^2(qa) - K_\ell(qa)K_{\ell+2}(qa)] \right] \right. \\ & \left. - \frac{1}{2} [K_\ell^2(qa) + K_{\ell-1}(qa)K_{\ell+1}(qa)] \right). \end{aligned} \quad (11)$$

The mode geometry is given by $J_n(x)$, the Bessel function of the first kind, $K_n(x)$, the modified Bessel function of the second kind, and β , the propagation constant of the fiber. The scaling factors are given by $q = \sqrt{\beta^2 - n_2^2 k_0^2}$ and $h = \sqrt{n_1^2 k_0^2 - \beta^2}$, the normalisation constant is C and s is a dimensionless parameter.

When the input light field is linearly polarized, it is convenient to write the cartesian components of the evanescent electric field as

$$\begin{aligned} E_x = & \sqrt{2}C \left[(1-s)K_{\ell-1}(qr) \cos(\phi_0) \right. \\ & \left. + (1+s)K_{\ell+1}(qr) \cos(2\phi - \phi_0) \right] e^{i(\omega t - \beta z)}, \end{aligned} \quad (12)$$

$$\begin{aligned} E_y = & \sqrt{2}C \left[(1-s)K_{\ell-1}(qr) \sin(\phi_0) \right. \\ & \left. + (1+s)K_{\ell+1}(qr) \sin(2\phi - \phi_0) \right] e^{i(\omega t - \beta z)}, \end{aligned} \quad (13)$$

$$E_z = 2\sqrt{2}iC(q/\beta)K_\ell(qr) \cos(\phi - \phi_0) e^{i(\omega t - \beta z)}. \quad (14)$$

Here ϕ_0 determines the orientation of polarization, with $\phi_0 = 0$ being along the x axis and $\pi/2$ being along the y axis. The artificial vector potential produced by such evanescent fields around an optical nanofiber is then given by³⁵

$$\mathbf{A} = \hat{z}\hbar\kappa_0(n_1 + 1)\tilde{s} \left[\frac{|d_r E_r + d_\phi E_\phi + d_z E_z|^2}{1 + \tilde{s}^2|d_r E_r + d_\phi E_\phi + d_z E_z|^2} \right], \quad (15)$$

where $\tilde{s} = \frac{|\mathbf{d} \cdot \mathbf{E}|}{\hbar|\Delta|}$ and the corresponding magnetic field $\mathbf{B} = \nabla \times \mathbf{A}$ can be calculated to be

$$\begin{aligned} \mathbf{B} = & \frac{\hbar\kappa_0 s^2 (n_1 + 1)}{(1 + \tilde{s}^2|d_r E_r + d_\phi E_\phi + d_z E_z|^2)^2} \\ & \times \left[\hat{\phi} \frac{\partial}{\partial r} |d_r E_r + d_\phi E_\phi + d_z E_z|^2 \right. \\ & \left. - \hat{r} \frac{1}{r} \frac{\partial}{\partial \phi} |d_r E_r + d_\phi E_\phi + d_z E_z|^2 \right]. \end{aligned} \quad (16)$$

This shows that the \mathbf{B} field has only components in the $\hat{\phi}$ and \hat{r} directions, which means that all field lines lie in the horizontal plane if the fiber is aligned along the vertical \hat{z} direction.

For a BEC that is trapped cylindrically around a nanofiber one can therefore expect to find vortex structures that wrap around the nanofiber and potentially close in on themselves in the form of vortex rings; however, depending on the exact form of the evanescent mode other structures are possible as well. Modulating the value of \tilde{s} allows one to change the amplitude and range of the magnetic field and thereby change the size and shape of the generated vortex structures³⁵. In the following we will focus on three different evanescent field configurations: the fundamental HE_{11} mode with circular polarization, the HE_{11} mode with linear polarization, and the HE_{21} mode with linear polarization. The electric field configurations and their corresponding artificial magnetic fields can be seen in Fig. 2. It is notable that using the circularly polarized fundamental HE_{11} mode leads to cylindrically symmetric electric (Fig. 2(a)) and artificial magnetic field configurations (Fig. 2(b)), whereas using linearly polarized light leads to a lobed structure for both quantities (see Figs. 2(c) and (d)). When using linearly-polarized light with the higher-order HE_{21} mode, an even more complex structure composed of four petals appears (see Figs. 2(e) and (f)) and the broken rotational symmetry suggests these fields will lead to the appearance of non-standard flow excitations. While using even higher order modes or interfering different modes can lead to even more complicated fields³⁵, we concentrate here on the three examples above, as they demonstrate the large range of fundamental possibilities the system allows for.

III. VORTEX CONFIGURATIONS

To determine the vortex states that can be created by the evanescent fields around a nanofiber we solve the full

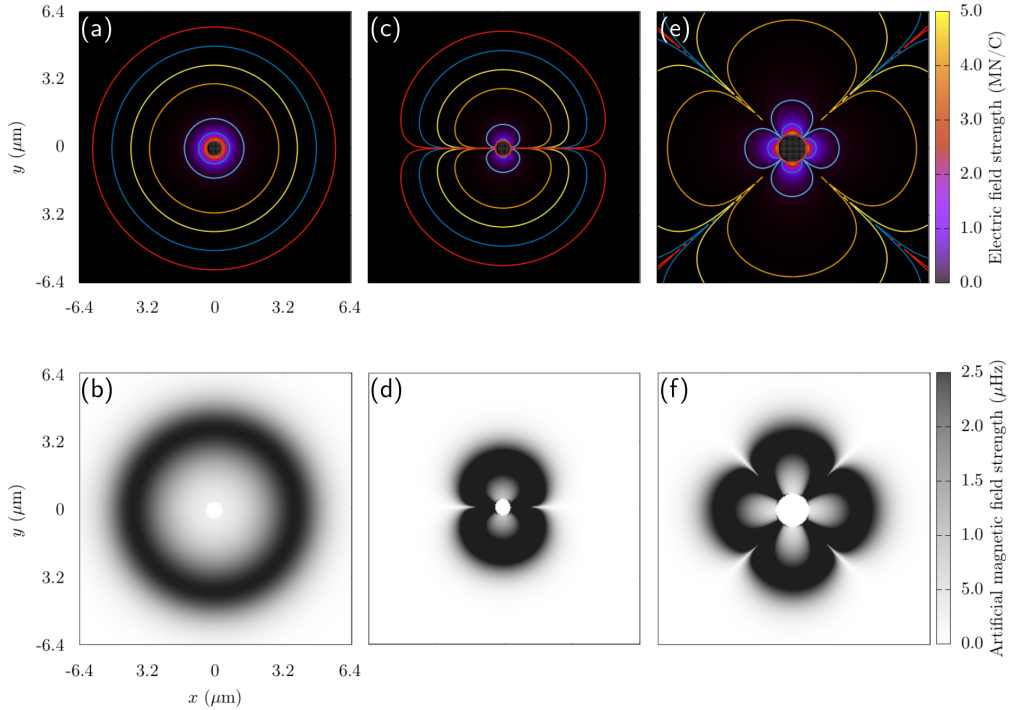


FIG. 2. Images of electric and artificial magnetic field profiles for [(a) and (b)] the fundamental HE₁₁ mode with circular polarization, [(c) and (d)] the HE₁₁ mode with linear polarization, and [(e) and (f)] the HE₂₁ mode with linear polarization. For these calculations, the input power is 372 nW in (a) and (b) , 16 nW in (c) and (d), and 418 nW in (e) and (f). For the HE₁₁ mode, the nanofiber radius is 200 nm with blue-detuned light of 700 nm, and for the HE₂₁ mode, the nanofiber radius is 400 nm with red-detuned light of 980 nm

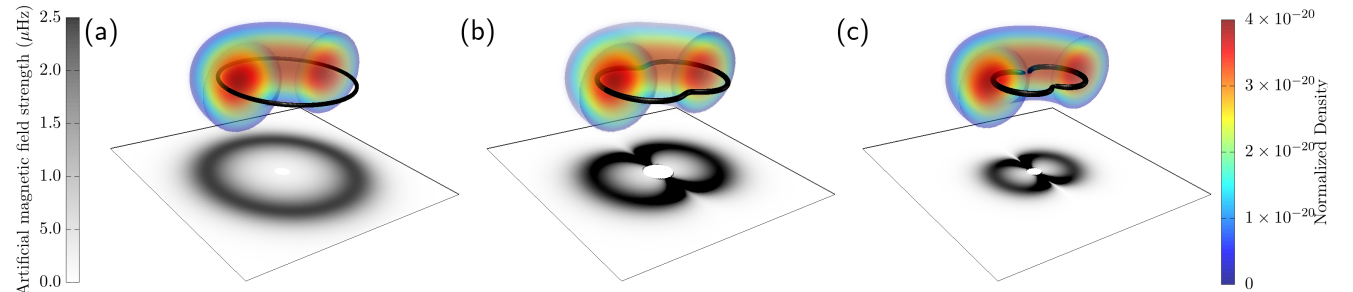


FIG. 3. Vortex configurations for different magnetic field profiles from the nanofiber for the fundamental HE₁₁ mode with (a) circular polarization, (b) elliptical polarization, and (c) linear polarization along the \hat{y} direction. The vortex distributions have been found via an isosurface on the Sobel filtered wavefunction density for a ⁸⁷Rb BEC and all optical fiber fields are normalized and for a nanofiber of 200 nm in radius with blue-detuned light of 700nm. The magnetic field profiles shown in the shaded region beneath wavefunction density are similar to those in Figure 2(b) and (d).

three-dimensional Gross-Pitaevskii equation for a condensate trapped toroidally around the fiber. For this, we use the GPUE codebase⁴³ to describe a ⁸⁷Rb condensate with 1×10^5 atoms with a scattering length of $a_s = 4.76 \times 10^{-9}$ m on a three-dimensional grid of 256^3 points with a spatial resolution of 50 nm. To clearly highlight the effects of the artificial magnetic fields, we assume a generic, external toroidal trapping around the

fiber given by

$$V_{\text{trap}} = m(\omega_r^2(r - \eta)^2 + \omega_z^2 z^2), \quad (17)$$

where we chose the trapping frequencies in the r and z directions to be $\omega_r = \omega_z = 7071$ Hz to match typical experimental conditions in fiber trapping²⁷. The parameter η defines the distance of the center of the toroidal condensate from the center of the fiber and is chosen such that the atoms are trapped outside the reach of the van-der-Waals potential of the fiber. For simulations of the

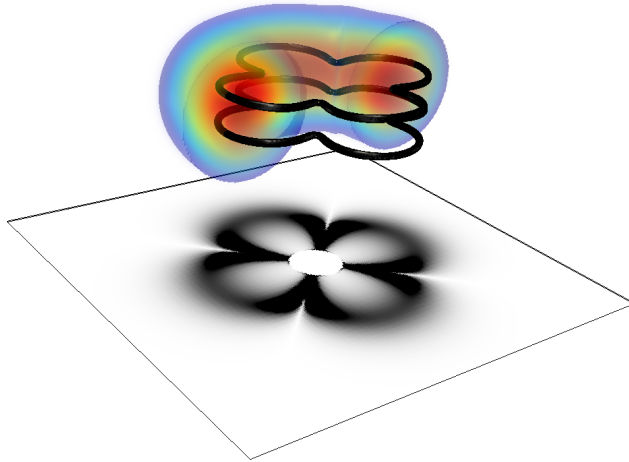


FIG. 4. Vortex configuration for the HE₂₁ mode with linear polarization along the \hat{y} direction. The vortex distributions have been found via an isosurface on the Sobel filtered wavefunction density for a ⁸⁷Rb BEC and the optical fiber fields are for a nanofiber of 400 nm in diameter for the bottom image with red-detuned light of 980 nm. The magnetic field profile is similar to the one shown in Figure 2(f), and has been calculated for a nanofiber of 400 nm in radius with red-detuned light of 980 nm.

HE₁₁ mode, we assume a fiber radius of 200 nm and we use $\eta = 3.20 \mu\text{m}$ to create a toroidal BEC with an inner radius roughly 300 nm from the fiber surface. To simulate the effects of higher-order HE₂₁ modes, we assume an increased fiber radius of 400 nm, with all other parameters remaining the same. This creates a toroidal BEC with an inner radius roughly 150 nm from the fiber surface.

As a first example, we study the fundamental HE₁₁ mode with circular polarization, which is perfectly azimuthally symmetric. One can therefore expect to find vortex lines that wrap around the fiber at a constant radius and reconnect onto themselves. This is confirmed in Fig. 3(a), where we show the equilibrium solution for a field strength that leads to exactly one vortex ring. For linearly polarized HE₁₁ modes, the circular symmetry is broken and one can see from Fig. 3(c) that the vortex lines bend towards the inner edge of the condensate, creating two vortex lobes. This can be easily understood by realizing that the vortex lines have to follow lines of constant magnetic fields, which in these areas also bend towards and vanish into the fiber surface. However, this also means that the field lines come very close when approaching the surface and careful examination of the condensate density shows that the vortex lines do not follow the field lines into the fiber surface, but rather connect to the neighbouring lobe when they approach each other within a healing length. In fact, one can continuously go from the circular to the linear setting by considering elliptically polarized light, which leads to vortex rings that are deformed and interpolate between the azimuthally symmetric and fully folded in structure (see Fig. 3(b)).

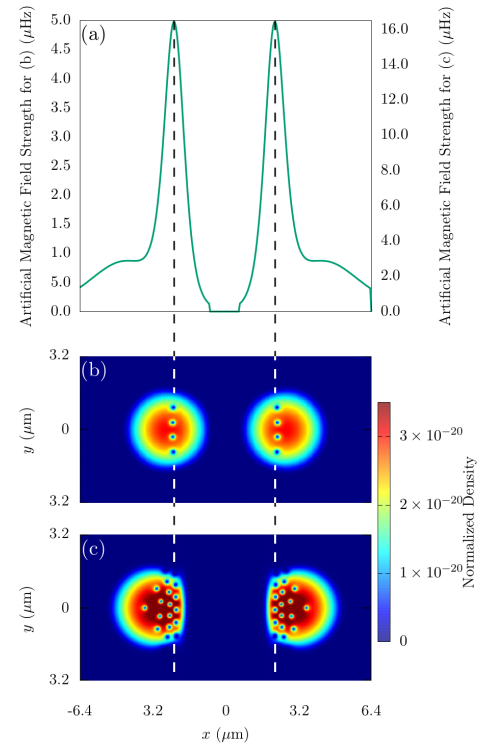


FIG. 5. (a) The magnetic field profile along the x -direction for the fundamental HE₁₁ mode with circular polarization outside a fibre of 200 nm radius. Note that for this mode and polarization the whole system is azimuthally symmetric. For weak fields (see (b)) this leads to a small number of vortices that align along the line at which the magnetic field is maximal and for larger fields (see (c)) more vortex rings appear that form the beginning of an Abrikosov lattice. The optical fiber field and wavefunction density have been normalized and are for a nanofiber of 200 nm in diameter with blue-detuned light of 700nm and a ⁸⁷Rb BEC respectively.

Finally, for the linearly polarized HE₂₁ mode, the superfluid system responds by creating vortex lines arranged in a four-petal shape, again mimicking the geometry of the artificial magnetic field (see Fig. 4(a)). For this situation we also show it is possible to create multiple of these vortex structures by increasing the field strength and that for low densities of these structures, they arrange themselves on top of the maximum of the inhomogeneous B-field inside the condensate (see Fig. 5(b) for the HE₁₁ mode).

To study control of multiple vortex structures with this system, we show that by increasing the B-field strength even further for the HE₁₁ mode, we can create an even larger number of vortex rings, which at a certain density, make a transition to arranging themselves in a triangular geometry, forming the equivalent of the famous Abrikosov lattice (see Figs. 5(a), (b) and (c)). However, as the artificial magnetic field is strongly inhomogeneous, this lattices forms close to and around the maximum of

the magnetic field.

It is therefore clear that one can control the shape of each vortex structure and their number by purely controlling the optical fields that are fed into the fiber, and that artificial magnetic fields around optical fibers provide unprecedented control for the creation of vortex ring-like structures. In fact, because all optical fields can also be time dependent, this system can potentially be used for studies of the dynamical properties of these rings; however, in the latter case, additional care needs to be taken as high magnetic field values change the potential geometry of the atoms in the BEC due to a coupling between the artificial vector potential \mathbf{A} , and the trapping potential, V_{trap} . In this case, the external potential V_{trap} gets modified by a term proportional to \mathbf{A}^2 , which has an effect on the condensate density beyond exciting rotation. Time-dependent changes to the \mathbf{A} field through changes in the laser intensity therefore also lead to phonon excitations, which in turn have an influence on the vortex line dynamics. However, studies of the response of the wavefunction density to time-dependent artificial magnetic fields go beyond the scope of this work. Nevertheless, let us stress, that for constant optical fields these (deformed) vortex-ring structures are stable and unique to creating vortex rings with artificial magnetic fields. They cannot be excited using simple rotation in singly connected potentials.

IV. DYNAMIC VORTEX DETECTION AND SCISSOR MODES

Observing the presence of vortex rings in a three dimensional BEC is a difficult problem, as absorption spectroscopy usually only provides a picture of an integrated two-dimensional density. However, due to the unique geometry of the system we describe here, one can identify whether vortex rings are present by exciting the scissors mode of the condensate^{36–38}. This works for systems trapped in elliptically toroidal geometries ($\omega_z < \omega_r$), which is a simple generalization of the above discussion. The scissors mode then gets excited by modifying the external potential with a rotation in the rz -plane

$$V = V_{\text{trap}}(r, \theta, z) - m\omega_0^2 \alpha r z, \quad (18)$$

where $\alpha = 2\epsilon\theta$ is a coefficient related to the tilting angle, ϵ is the deformation of the trap in the rz plane and θ is the angle at which the original trap was aligned at. For a small initial angle of θ_0 this change in the potential causes a BEC without rotation to oscillate back and forth in the trap with a frequency given by⁴¹

$$\omega_{\text{scissors}} = \sqrt{\omega_r^2 + \omega_z^2}. \quad (19)$$

If, however, this mode is excited for a BEC that contains a vortex line, the oscillation will be strongly influenced by the currents inside the condensate and two different frequencies (ω_+ and ω_-) appear in the oscillation

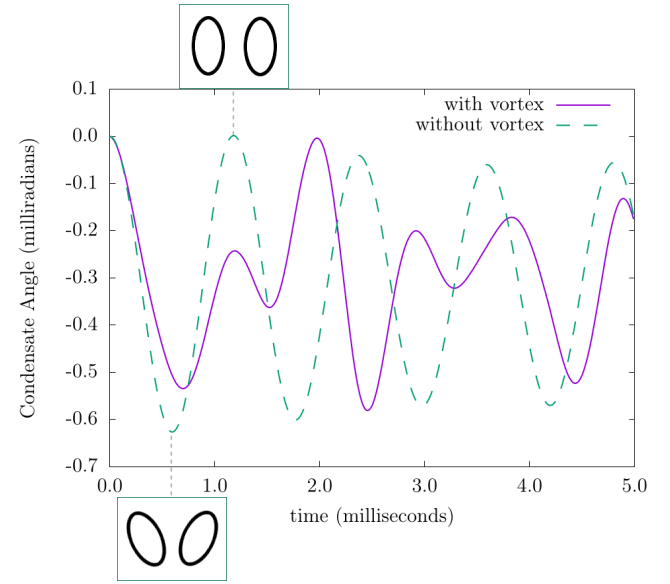


FIG. 6. Angle of the condensate axis after excitation of the toroidal scissors mode for an elliptic-toroidal BEC with a single vortex ring (purple, solid) and without a vortex present (cyan, dashed). Depictions of two dimensional slices for the scissors mode without a vortex are shown in the insets. Here we see that the scissors mode causes oscillation in and out towards the center of the system, and that two distinct frequencies are present in the curve for the condensate carrying a vortex ring.

spectrum^{39–41}. The splitting of these two frequencies, when small compared to the frequency of the scissors mode without a vortex present, can be written as⁴⁰

$$\omega_+ - \omega_- = \frac{\langle l_z \rangle}{m(r^2 + z^2)}, \quad (20)$$

where $\langle l_z \rangle$ is the average angular momentum per particle. Calculating these values for our system for $\omega_r = 4242\text{Hz}$, and $\omega_z = 2828\text{Hz}$ then leads to $\omega_{\text{scissors}} = 5090\text{Hz}$, $\omega_- = 3765\text{Hz}$, and $\omega_+ = 6415\text{Hz}$, which are very close to the values observed in the numerical simulations shown in Fig. 6. However, one can also see from this figure that the oscillation is not perfect and seems to decay over time. This is due to the above mentioned modification of the trapping potential by the artificial vector potential, which leads to a deviation from the perfect elliptical toroidal shape used in the derivation of eq. (20). Nevertheless, it does not effect the main argument.

It is worth noting that this method cannot be used to detect a vortex ring inside a simply connected condensate, as in this situation the flow around the vortex line has no preferred direction. However, in the toroidal shape each radial slice can be seen as a two-dimensional elliptical BEC with a single vortex, and the system will therefore exhibit the scissors mode frequency as expected. While in principle the excitation of the scissors mode can

also be used to detect Abrikosov vortex-ring lattice, the fact that the inhomogeneous artificial magnetic field leads to an inhomogeneous vortex ring distribution will have an effect on the expected oscillation frequencies.

V. DISCUSSION

We have shown that it is possible to create and control vortex rings and more complicated vortex structures in three dimensions using the artificial magnetic field around an optical nanofiber. In addition, and to the best of our knowledge, there is currently no other known method to generate the the structures obtained from non-azimuthally symmetric modes from the linearly and elliptically polarized evanescent fields shown in Figs. 3(b,c) and 4. We have also shown that the scissors mode of the condensate can be used to detect whether connected vortex structures are present in an elliptic toroidal system. The structures generated by these fiber-based systems therefore allow one to deterministically design experiments from which one can study complicated superfluid mechanisms, like the kelvin-mode cascade, superfluid turbulence, or reconnection events between superfluid vortex lines. Being able to stably create these non-trivial vortex configurations may be first step to creating more complex structures like vortex knots in a single-component superfluid BEC system with the optical nanofiber; however, to generate these structures, the magnetic field must have a dependence on \hat{z} , which is not present in our current model.

VI. ACKNOWLEDGEMENTS

This work has been supported by the Okinawa Institute of Science and Technology Graduate University and used the computing resources of the Scientific Computing and Data Analysis section. This work has also been supported by JSPS JP17J01488.

- ¹C. J. Pethick and H. Smith. *Bose-Einstein Condensation in Dilute Gases*. Cambridge University Press, 2 edition, 2008.
- ²K. W. Madison, F. Chevy, W. Wohlleben, and Jl. Dalibard. Vortex formation in a stirred bose-einstein condensate. *Physical Review Letters*, 84(5):806, 2000.
- ³J. R. Abo-Shaeer, C. Raman, J. M. Vogels, and W. Ketterle. Observation of vortex lattices in bose-einstein condensates. *Science*, 292(5516):476–479, 2001.
- ⁴D. H. Wacks, A. W. Baggaley, and C. F. Barenghi. Large-scale superfluid vortex rings at nonzero temperatures. *Phys. Rev. B*, 90:224514, Dec 2014.
- ⁵B. P. Anderson, P. C. Haljan, C. A. Regal, D. L. Feder, L. A. Collins, C. W. Clark, and E. A. Cornell. Watching dark solitons decay into vortex rings in a bose-einstein condensate. *Phys. Rev. Lett.*, 86:2926–2929, Apr 2001.
- ⁶A. Bulgac, M. MN. Forbes, M. M. Kelley, K. J. Roche, and G. Wlazłowski. Quantized superfluid vortex rings in the unitary fermi gas. *Phys. Rev. Lett.*, 112:025301, Jan 2014.
- ⁷M. J. H. Ku, B. Mukherjee, T. Yefsah, and M. W. Zwierlein. Cascade of solitonic excitations in a superfluid fermi gas: From planar solitons to vortex rings and lines. *Phys. Rev. Lett.*, 116:045304, Jan 2016.
- ⁸M. R. Matthews, B. P. Anderson, P. C. Haljan, D. S. Hall, C. E. Wieman, and E. A. Cornell. Vortices in a bose-einstein condensate. *Phys. Rev. Lett.*, 83:2498–2501, Sep 1999.
- ⁹T. Yefsah, A. T Sommer, M. JH Ku, L. W Cheuk, W. Ji, W. S Bakr, and M. W Zwierlein. Heavy solitons in a fermionic superfluid. *Nature*, 499(7459):426, 2013.
- ¹⁰A. A. Abrikosov. The magnetic properties of superconducting alloys. *Journal of Physics and Chemistry of Solids*, 2(3):199–208, 1957.
- ¹¹M. Tsobota. Turbulence in quantum fluids. *Journal of Statistical Mechanics: Theory and Experiment*, 2014(2):P02013, 2014.
- ¹²C. F. Barenghi, L. Skrbek, and K. R. Sreenivasan. Introduction to quantum turbulence. *Proceedings of the National Academy of Sciences*, 111(Supplement 1):4647–4652, 2014.
- ¹³S. W Seo, B. Ko, J. H. Kim, and Y. Shin. Observation of vortex-antivortex pairing in decaying 2d turbulence of a superfluid gas. *Scientific reports*, 7(1):4587, 2017.
- ¹⁴N. Navon, A. L Gaunt, R. P Smith, and Z. Hadzibabic. Emergence of a turbulent cascade in a quantum gas. *Nature*, 539(7627):72, 2016.
- ¹⁵J. Ruostekoski and J. R Anglin. Creating vortex rings and three-dimensional skyrmions in bose-einstein condensates. *Physical review letters*, 86(18):3934, 2001.
- ¹⁶I. Shomroni, E. Lahoud, S. Levy, and J. Steinhauer. Evidence for an oscillating soliton/vortex ring by density engineering of a bose-einstein condensate. *Nature Physics*, 5(3):193, 2009.
- ¹⁷J. Ruostekoski and Z. Dutton. Engineering vortex rings and systems for controlled studies of vortex interactions in bose-einstein condensates. *Physical Review A*, 72(6):063626, 2005.
- ¹⁸N. S Ginsberg, J. Brand, and L. V. Hau. Observation of hybrid soliton vortex-ring structures in bose-einstein condensates. *Physical review letters*, 94(4):040403, 2005.
- ¹⁹B. Jackson, J. F McCann, and C. S Adams. Vortex line and ring dynamics in trapped bose-einstein condensates. *Physical Review A*, 61(1):013604, 1999.
- ²⁰F. Pinsker, N. G Berloff, and V. M Pérez-García. Nonlinear quantum piston for the controlled generation of vortex rings and soliton trains. *Physical Review A*, 87(5):053624, 2013.
- ²¹M. Abad, M. Guilleumas, R. Mayol, and M. Pi. Vortex rings in toroidal bose-einstein condensates. *Laser Physics*, 18(5):648–652, 2008.
- ²²J. Dalibard, F. Gerbier, G. Juzeliūnas, and Patrik Öhberg. Colloquium. *Rev. Mod. Phys.*, 83:1523–1543, Nov 2011.
- ²³M. Mochol and K. Sacha. Artificial magnetic field induced by an evanescent wave. *Scientific reports*, 5, 2015.
- ²⁴J. M Ward, D. G O’Shea, B. J Shortt, M. J Morrissey, K. Deasy, and S. G. Nic Chormaic. Heat-and-pull rig for fiber taper fabrication. *Review of scientific instruments*, 77(8):083105, 2006.
- ²⁵L. Tong, R. R Gattass, J. B Ashcom, S. He, J. Lou, M. Shen, I. Maxwell, and E. Mazur. Subwavelength-diameter silica wires for low-loss optical wave guiding. *Nature*, 426(6968):816, 2003.
- ²⁶A. Yariv. *Introduction to optical electronics*. Holt, Rinehart and Winston, Inc., New York, NY, 1976.
- ²⁷E. Vetsch, D. Reitz, G. Sagué, R. Schmidt, S. T. Dawkins, and A. Rauschenbeutel. Optical interface created by laser-cooled atoms trapped in the evanescent field surrounding an optical nanofiber. *Physical review letters*, 104(20):203603, 2010.
- ²⁸C. Lacroute, K. S. Choi, A. Goban, D. J Alton, D. Ding, N. P. Stern, and H. J. Kimble. A state-insensitive, compensated nanofiber trap. *New Journal of Physics*, 14(2):023056, 2012.
- ²⁹T. Nieddu, V. Gokhroo land, and S. Nic Chormaic. Optical nanofibres and neutral atoms *Journal of Optics*, 18(5):053001, 2016.
- ³⁰E. Sagué, E. Vetsch, W. Alt, D. Meschede, and A. Rauschenbeutel. Cold-Atom Physics Using Ultrathin Optical Fibers: Light-Induced Dipole Forces and Surface Interactions. *Phys. Rev. Lett.*, 99(16):163602, 2007

- ³¹L. Russell, K. Deasy, M. J. Daly, M. J. Morrissey, and S. Nic Chormaic. Sub-Doppler temperature measurements of laser-cooled atoms using optical nanofibres. *Measurement Science and Technology* 23(1):015201, 2011
- ³²R. Kumar, V. Gokhroo1, K. Deasy, A. Maimaiti, M. Frawley, C. Phelan, and S. Nic Chormaic. Interaction of laser-cooled ^{87}Rb atoms with higher order modes of an optical nanofibre. *New Journal of Physics* 17(1):013026, 2015.
- ³³F. Le Kien, V. I. Balykin, and K. Hakuta. Atom trap and waveguide using a two-color evanescent light field around a subwavelength-diameter optical fiber. *Physical Review A*, 70(6):063403, 2004.
- ³⁴C. F. Phelan, T. Hennessy, and Th. Busch. Shaping the evanescent field of optical nanofibers for cold atom trapping. *Optics Express*, 21(22):27093–27101, 2013.
- ³⁵R. Sachdeva and Th. Busch. Creating superfluid vortex rings in artificial magnetic fields. *Physical Review A*, 95(3):033615, 2017.
- ³⁶M. Cozzini, S. Stringari, V. Bretin, P. Rosenbusch, and J. Dalibard. Scissors mode of a rotating bose-einstein condensate. *Physical Review A*, 67(2):021602, 2003.
- ³⁷D. Guéry-Odelin and S. Stringari. Scissors mode and superfluidity of a trapped bose-einstein condensed gas. *Physical review letters*, 83(22):4452, 1999.
- ³⁸O. M. Marago, S. A. Hopkins, J. Arlt, E. Hodby, G. Hechenblaikner, and C. J. Foot. Observation of the scissors mode and evidence for superfluidity of a trapped bose-einstein condensed gas. *Physical review letters*, 84(10):2056, 2000.
- ³⁹N. L. Smith, W. H. Heathcote, J. M. Krueger, and C. J. Foot. Experimental observation of the tilting mode of an array of vortices in a dilute bose-einstein condensate. *Physical review letters*, 93(8):080406, 2004.
- ⁴⁰F. Zambelli and S. Stringari. Quantized Vortices and Collective Oscillations of a Trapped Bose-Einstein Condensate *Phys. Rev. Lett.*, 81:1754, 1998.
- ⁴¹S. Stringari. Superfluid Gyroscope with Cold Atomic Gases *Phys. Rev. Lett.*, 86:4725, 2001.
- ⁴²V. Georgievich Minogin and S. Nic Chormaic. Manifestation of the van der waals surface interaction in the spontaneous emission of atoms into an optical nanofiber. *Laser Physics*, 20(1):32–37, 2010.
- ⁴³J. Schloss and L. J. O’Riordan. Gpue: Graphics processing unit gross-pitaevskii equation solver. *Journal of Open Source Software*, 3:1037, 2018.